The University Of Sheffield.

Optical quantitative phase microscopy: novel methods and applications

By:

Samuel McDermott

Supervised By:

Dr Andrew Maiden

and Prof Alejandro Franji

A thesis submitted in partial fulfilment of the requirements for the degree of Doctor of Philosophy

The University of Sheffield

Faculty of Engineering

Department of Electronic and Electrical Engineering

July 29, 2019

Abstract

Quantitative Phase Imaging (QPI) techniques are a set of microscopy techniques that allow us to observe transparent samples, such as biological cells and optical components, in a way that standard optical microscopes cannot. Although these samples do not absorb light they do cause a significant change to the phase of the incident light. QPI techniques map these optical path length variations across a transparent sample to produce high contrast phase images. Additionally, the quantitative nature of the phase images allows for further information, such as sample thickness and refractive index, to be deduced. The purpose of this thesis is to develop and test novel QPI methods and applications based on a diffractive imaging technique called ptychography.

The thesis starts with an overview of key QPI techniques before showing the development and testing of a novel QPI technique called optical near-field ptychography. The phase image produced is shown to be accurate and artefact free, while reducing the quantity of data needed for image acquisition, when compared to existing techniques.

It is identified that Spatial Light Modulators (SLMs), digital optical devices that modulate a light wavefront's phase or amplitude across a two-dimensional surface, are increasingly important as components in QPI techniques. To utilise an SLM effectively it is necessary to characterise the modulation response of the device. A novel application of ptychography in characterising an SLM is demonstrated, generating a subpixel resolution of the display over the device's entire active area.

Further developments are then explored in the integration of an SLM with ptychography, with the ultimate aim of developing a new QPI technique with no

moving parts. The application of this technology is envisioned in high quality quantitative phase videos.

Acknowledgements

I would like to express my gratitude to those people who have supported me throughout my academic studies. I have appreciated all the opportunities afforded to me; to meet new people, and learn new things.

Firstly, I would like to express my thanks to my supervisor, Dr Andrew Maiden. He has provided me with the opportunity to fulfil a long-held dream of mine to pursue my PhD studies. I am very grateful for all his advice, support, and guidance throughout my time at Sheffield, and his calm dedication to achievement. In addition to the subject knowledge, he has taught me much about the process and application of research.

I would like to thank my second supervisor, Prof Alejandro Franji. I have enjoyed my conversations with him, and valued his 'big picture' advice for life and work as a researcher. I have also learned many things from Prof John Rodenburg, and have appreciated his advice, discussions, and trips to the pub.

I have met many excellent colleagues and friends at the University of Sheffield. In particular, I would like to thank Dr Gavin Williams and Dr Peng Li for their assistance with the work in Chapter 4. For providing an enjoyable office environment, I would like to thank Dr Darren Batey, Dr Shaohong Cao, Daniel Johnson, Zhuoqun Zhang, Yangyang Mu, Freddrick Allars, and Liam Pennington.

I am grateful to the Engineering and Physical Sciences Research Council (EPSRC) for funding my DTA scholarship.

Finally, I would like to thank my parents, Bill and Carolyn McDermott, who have

always supported my academic endeavours. I am very grateful for the opportunities in life they have given me.

This thesis is dedicated to the memory of my grandma, Pam Boar.

Contents

List of Figures

List of Tables

List of acronyms

CCD Charge-Couple Device

CG Conjugate Gradient

DIC Differential Interence Contrast

DM Difference Map

DVI Digital Visual Interface

ePIE Extended Ptychographical Iterative Engine

FFT Fast Fourier Transform

FPM Fourier Phase Microscopy

GLIM Gradient Light Interference Microscopy

GPU Graphical Processing Unit

LCD Liquid Crystal Display

LCoS Liquid Crystal on Silicon

LUT Look Up Table

MEMS Microelectromechanical Systems

mPIE Momentum-accelerated Ptychographical Iterative Engine

MTF Modulation Transfer Function

NA Numerical Aperture

OTF Optical Transfer Function

PALM Photo Activated Localization Microscopy

PCM Phase Contrast Microscopy

PIE Ptychographical Iterative Engine

PSF Point Spread Function

PSI Phase-shifting interferometry

QPI Quantitative Phase Imaging

RAAR Relaxed Averaged Alternating Reflections

RI Refractive Index

SIM Structured Illumination Microscopy

SLIM Spatial Light Interference Microscopy

SLIT Spatial Light Interference Tomography

SLM Spatial Light Modulator

SNR Signal to Noise Ratio

STED Stimulated Emission Depletion

STORM Stochastic Optical Reconstruction Microscopy

TIE Transport of Intensity Equation

Chapter 1

Introduction

Microscopy has enhanced research in many scientific fields by allowing us to directly see the structure of natural and man-made objects. In biology, microscopy has granted us a view of cellular and sub-cellular information. In material sciences, new materials can be observed with atomic level precision. In electronics, microscopes have enabled us to construct smaller and smaller devices. In many fields, scientific discoveries can be linked with the development of new microscopes.

However, many objects are hard to directly observe with conventional microscopes. They have low intrinsic contrast, because they do not absorb or scatter light sufficiently and so appear almost transparent. Some key examples of these objects include the majority of biological samples such as cells; optical components such as lenses; and electronic components such as Microelectromechanical Systems (MEMS) devices.

In the field of biology, fluorescence microscopes have been an important development, enabling scientists to observe cellular structures. Chemicals are used to stain targeted cell structures, increasing their contrast. However, these chemicals can damage the cells they are enhancing, and tend to decrease in effectiveness over time. As such, it is important to develop techniques that enhance the contrast of these transparent objects without modifying them.

Quantitative Phase Imaging (QPI) microscopy increases the contrast of an object by mapping the optical path length variations of the illumination as it passes through the object. These optical path length variations appear as phase delays to the exit wave of the object – that is, the wavefront immediately after the object in the optical system. Unfortunately, the phase delay of the light cannot be directly observed with detectors in the same way that the intensity of the light can be measured, so techniques have to be developed that can calculate it. This has become an exciting area of research, with the advancement of new algorithms, faster computers, and improved optical components.

One such new optical component that is improving QPI is the Spatial Light Modulator (SLM). An SLM is a small electro-optical device that can modify the phase and amplitude of an incoming light beam across its two-dimensional array. As an SLM is controlled by a computer, in a similar way to a digital display, its properties can be changed dynamically. This creates a digital interface to optics, allowing for more advanced operations.

The field of QPI techniques is large and increasing. This thesis focusses primarily of the family of QPI techniques called ptychography, a conceptually elegant coherent diffractive method that can produce high quality, accurate phase images over a large field of view. However, these high quality images come at a cost: ptychography methods tend to require a large amount of acquisition time and generate large datasets for reconstruction. This makes them less suited for biological applications, where high frame-rates and near real-time images are expected.

The overarching form of this thesis is illustrated by Figure 1.1. Ptychography and SLMs were identified as key future trends in QPI. A new method in ptychography was developed and a new application of ptychography was used to investigate the SLM. This thesis investigates the interplay between these two technologies and explores how they can be combined.

In Chapter 2, the theoretical background for optics, and Fourier optics is described

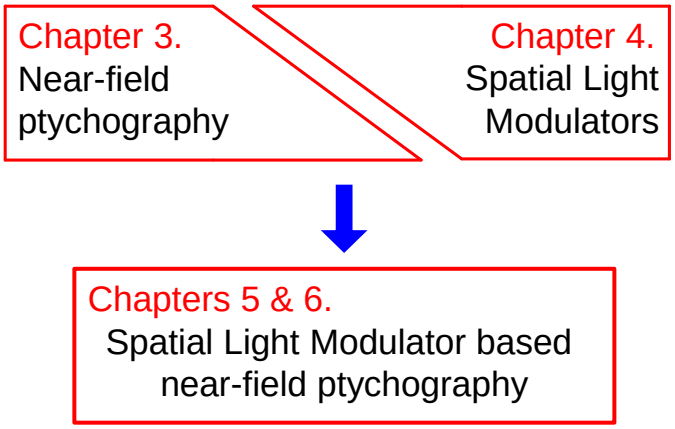

Figure 1.1: This thesis starts with the development of optical near-field ptychography. Spatial Light Modulators are introduced and are then characterised using ptychography. The final chapter explores how Spatial Light Modulators can be integrated with near-field ptychography.

from Maxwell's equations. The context to optical microscopy and bio-imaging is outlined before detail is given on key QPI techniques. Additionally, more recent QPI techniques that use an SLM are explained and the field of QPI is analysed. Finally, the operation and use of an SLM is summarised, and its limitations and potential impact are assessed.

In Chapter 3, the development of a novel QPI method is described. This method, called optical near-field ptychography, builds on the set of QPI methods known as ptychography. The setup and operation is explained, and it is tested on several phase objects.

In Chapter 4, standard ptychography is given a new application in characterising an SLM. Errors with the SLM are identified and shown to be corrected using this method.

In Chapter 5, investigations are made into whether an SLM can be integrated with near-field ptychography to create a new QPI technique with no moving parts. New algorithms are proposed and experimental demonstrations are made.

In Chapter 6, a new algorithm is described that adds constraints to the phase profile displayed on the SLM to improve its characterisation procedure in a new high-speed QPI technique.

1.1 Main contributions of thesis

The main contributions of this thesis are as follows:

- Development of a novel optical quantitative phase imaging technique, called optical near-field ptychography. The new technique maintains a high quality phase image while reducing acquisition and reconstruction time. It is demonstrated on artificial and biological objects.
- Development and demonstration of a new characterisation technique for a phase Spatial Light Modulator. This novel application of ptychography creates high quality sub-pixel images across the entire surface of the Spatial Light Modulator.
- Investigation into the use of a Spatial Light Modulator with ptychography, to create a high quality phase image with no moving parts.

1.2 Publications

Parts of the work published in this thesis were previously published as the following journal paper publications:

1. **Samuel McDermott**, Andrew Maiden, "Near-field ptychographic microscope for quantitative phase imaging", *Optics Express*, 26.19 (Sep. 2018), p. 25471.
2. **Samuel McDermott**, Peng Li, Gavin Williams, and Andrew Maiden, "Characterizing a spatial light modulator with ptychography", *Optics Letters*, 42.3 (Feb. 2017), pp. 371-374.

Parts of the work published in this thesis were previously presented at a conference:

1. **Samuel McDermott**, Andrew Maiden, "Optical near-field ptychography", *Focus on Microscopy*, (Mar. 2018), Singapore.

Parts of the work published in this thesis were previously presented as posters at conferences:

1. **Samuel McDermott**, Andrew Maiden, "Imaging the invisible: Implementing optical near-field ptychography for faster quantitative phase imaging", *Engineering Researcher Symposium*, (Jun. 2018), The University of Sheffield.

2. **Samuel McDermott**, Andrew Maiden, "First steps towards high speed quantitative phase imaging of cells", *Biophotonics and Imaging Summer School*, (Sep. 2016), National University of Ireland Galway.

Chapter 2

Background

The ultimate aim of this research is to develop and improve quantitative phase retrieval techniques. This chapter will start with a brief historical introduction to optics. Some of the key mathematical ideas used in this field will then be derived. Next, the theory around standard microscopy and its relation to bio-imaging will be explored. A 'state of play' of the field of QPI will be addressed to lay the foundations of this contribution. A Venn diagram showing the relations between all the contrast enhancing microscopy techniques discussed in this chapter is shown in Figure 2.1. At the end of this chapter SLMs–electro-optical components that were used extensively in this research–will be introduced. They are small devices used for modulating the phase and intensity of light across their display. The operation and characterisation of these devices will be expanded, setting out the need for an improved characterisation method.

2.1 The foundations of optics

Optics is a vast subject, with a lengthy history [1]. The interaction of an electromagnetic wave with matter has been considered for many years, and with a huge variety of models. The most obvious initial dilemma in optics is whether light can be considered

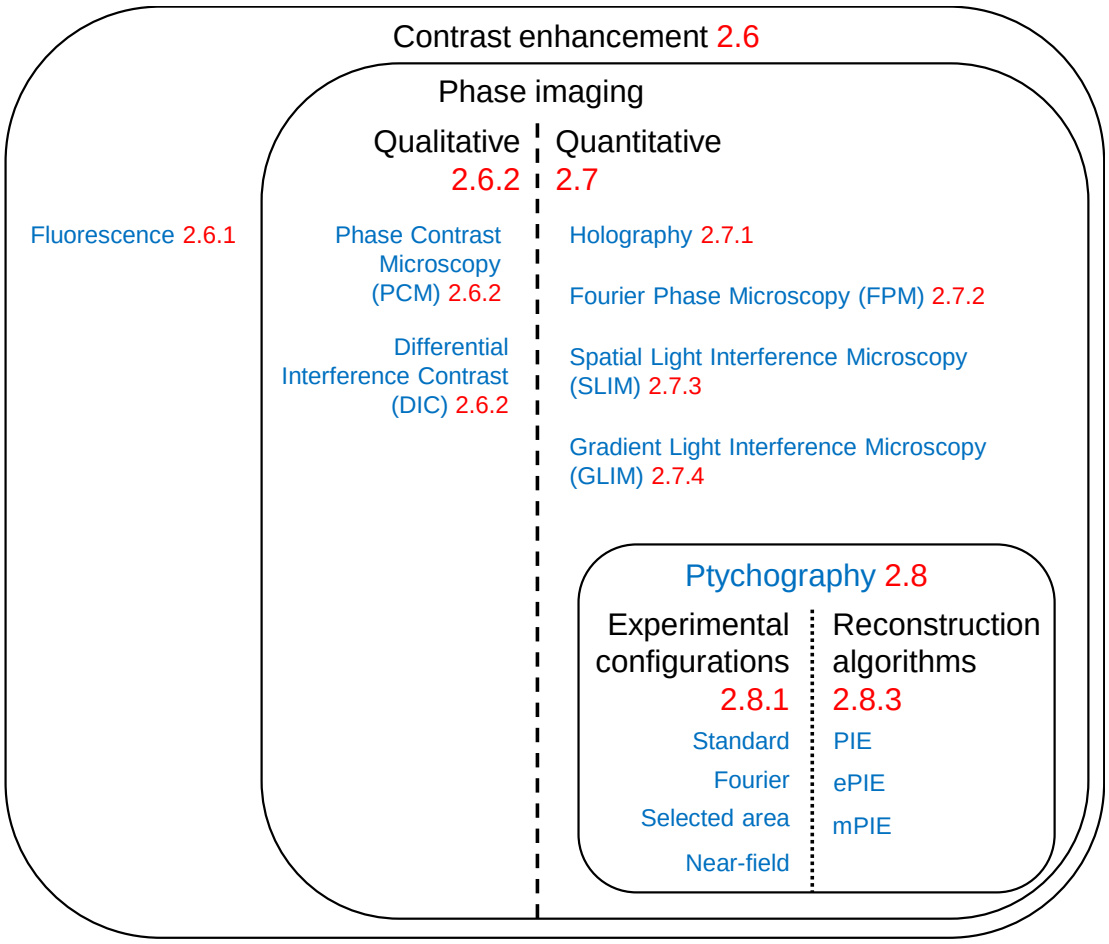

Figure 2.1: A Venn diagram showing the relations between the contrast enhancing microscopy techniques (in blue) described in this chapter with their section number in red.

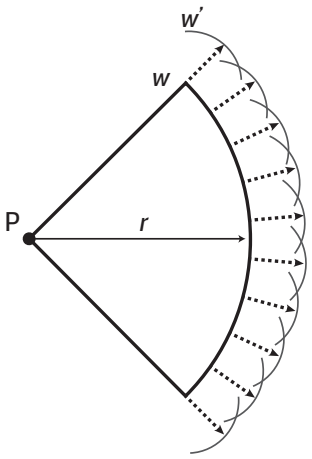

Figure 2.2: Huygen's secondary wavelets. A wavefront propagating from point P at time t has a radius $r = ct$ in position w, where c is the speed of light. Huygen's secondary wavelets originating at every point on w have a radius of $c(t - t')$, forming a new wavefront w' at time t'.

a particle, a ray, or a wave. The answer tends to depend on the scenario.

Whilst Newton expounded a particle theory of light, with *Opticks*, Thomas Young was a key promoter of the wave theory of light, his double slit experiment could only be explained in terms of waves. This was further explored by Fresnel, showing that the wave must be a transverse oscillation. Fresnel also developed theories of diffraction at shallow edges. Maxwell's four equations finally cemented the concept of the wave theory of light, by combining the physics of electricity and magnetism and deducing that an electromagnetic wave would travel at the speed of light.

Huygens developed a theory about how light could be represented as a ray. He proposed that light is propagated as a wavefront, and that instantaneously every point on the wavefront is the source of a wavelet, a secondary wave that propagates outward as a spherical wave, as shown in Figure 2.2. Each wavelet has infinitesimal amplitude, but on the common envelope where the wavelets intersect, a new wavefront of finite amplitude is formed. This envelope of the wavelets is perpendicular to the radius of each wavelet, such that the ray of light is the normal to the wavefront. This theory can

account for basic ray optics such as reflection, refraction, and diffraction.

However, all was not complete. Issues remained around the interaction of light with matter, particularly the 'blackbody spectrum' of thermal radiation and the photoelectric effect. Max Planck and Albert Einstein developed theories around the quantification of light, where radiation could be explained as discrete units.

2.2 Maxwell's equations

As this work deals purely with electromagnetic radiation, a suitable place to start the mathematical foundation of the work in this thesis are the Maxwell equations[1]:

$$\begin{aligned} \nabla \times \boldsymbol{\mathcal{E}} &= -\mu \frac{\partial \boldsymbol{\mathcal{B}}}{\partial t} \\ \nabla \times \boldsymbol{\mathcal{B}} &= \epsilon \frac{\partial \boldsymbol{\mathcal{E}}}{\partial t} \\ \nabla \cdot \epsilon \boldsymbol{\mathcal{E}} &= 0 \\ \nabla \cdot \mu \boldsymbol{\mathcal{B}} &= 0, \end{aligned} \tag{2.1}$$

where $\boldsymbol{\mathcal{E}}$ is the electric field, and $\boldsymbol{\mathcal{B}}$ is the magnetic field. μ is the permeability, and ϵ the permittivity of the medium in which the wave is propagating [2].

If the medium is linear, isotropic (properties are independent of polarization of the wave), homogeneous (permittivity is constant throughout the region of propagation), and non-dispersive (the permittivity is independent of wavelength), then the Maxwell's

[1] For the purposes of optics, it is assumed that there are no free charges or currents.

equations (2.1) can be reduced to two equations for the electric and magnetic fields:

$$\begin{aligned} \nabla^2 \boldsymbol{\mathcal{E}} - \frac{n^2}{c^2} \frac{\partial^2 \boldsymbol{\mathcal{E}}}{\partial t^2} = 0 \\ \nabla^2 \boldsymbol{\mathcal{B}} - \frac{n^2}{c^2} \frac{\partial^2 \boldsymbol{\mathcal{B}}}{\partial t^2} = 0. \end{aligned} \tag{2.2}$$

For these vector wave equations, n is the refractive index of the medium:

$$n = \sqrt{\frac{\epsilon}{\epsilon_0}}, \tag{2.3}$$

and c is the velocity of propagation in a vacuum:

$$c = \frac{1}{\sqrt{\mu_0 \epsilon_0}}, \tag{2.4}$$

where ϵ_0 and μ_0 are the permittivity and permeability in a vacuum, respectively.

As these vector wave equations are obeyed by all the orthogonal scalar components of $\boldsymbol{\mathcal{E}}$ and $\boldsymbol{\mathcal{B}}$, all of their behaviour can be combined into a single scalar wave equation:

$$\nabla^2 u(\mathbf{r}, t) = \frac{n^2}{c^2} \frac{\partial^2 u(P, t)}{\partial t^2}, \tag{2.5}$$

where $u(\mathbf{r}, t)$ is the scalar field component at position $\mathbf{r}$ at time t.

2.3 The light wave equation and the Helmholtz equation

A wave of any quantity u travelling in a position direction z with velocity v has the form [1]:

$$u = f(z - vt). \tag{2.6}$$

The function f describes the shape of u at time $t = 0$. The shape does not change with time, but only moves along the z-axis. At any one time, the variation of u with z is $\partial u/\partial z$ and in any one place the rate of change of u is $\partial u/\partial t$. Substituting for the variable $z' = (z - vt)$ we get:

$$\frac{\partial u}{\partial z} = \frac{\partial u}{\partial z'}\frac{\partial z'}{\partial z} = \frac{\partial u}{\partial z'} \tag{2.7}$$

$$\frac{\partial u}{\partial t} = \frac{\partial u}{\partial z'}\frac{\partial z'}{\partial t} = -v\frac{\partial u}{\partial z'}. \tag{2.8}$$

In the same way, the second differential of u with respect to z can be shown to be:

$$\frac{\partial^2 u}{\partial t^2} = v^2\frac{\partial^2 u}{\partial z^2}. \tag{2.9}$$

This is the one-dimensional wave equation, and applies to any wave propagating in the z direction with uniform velocity. It can be generalised to three dimensions:

$$\frac{\partial^2 u}{\partial x^2} + \frac{\partial^2 u}{\partial y^2} + \frac{\partial^2 u}{\partial z^2} = \frac{1}{v^2}\frac{\partial^2 u}{\partial t^2}. \tag{2.10}$$

or more concisely:

$$\nabla^2 u = \frac{1}{v^2}\frac{\partial^2 u}{\partial t^2} \tag{2.11}$$

which is the three dimensional wave equation. The similarity between (2.11) and (2.5) shows that:

$$v = \frac{c}{n}. \tag{2.12}$$

Although the form of the wave $f(z - vt)$ can be of any form, it is convenient to use complex exponentials. For completeness, it can be shown that any continuous function can be created from the superposition of these harmonic solutions using Fourier analysis.

Now looking at a monochromatic wave's scalar field u at position $\mathbf{r}$ and time t, it

can be written as [2]:

$$u(\mathbf{r},t) = \Re\left\{\psi(\mathbf{r})\exp(-i2\pi\nu t)\right\}, \tag{2.13}$$

where ν is the optical frequency and $\Re$ signifies to take the real part. $\psi(\mathbf{r})$ is known as the phasor:

$$\psi(\mathbf{r}) = A(\mathbf{r})\exp\left[-i\phi(\mathbf{r})\right], \tag{2.14}$$

where $A(\mathbf{r})$ and $\phi(\mathbf{r})$ are the amplitude and phase, respectively, of the wave at position $\mathbf{r}$. As $\psi(\mathbf{r},t)$ is an optical wave, it must satisfy the scalar wave equation (2.5). Substituting (2.13) into the scalar wave equation shows that ψ must obey the time independent equation:

$$(\nabla^2 + k^2)\psi = 0, \tag{2.15}$$

where k is defined as the *wave number*:

$$k = \frac{2\pi n\nu}{c} = \frac{2\pi}{\lambda}. \tag{2.16}$$

λ is the wavelength in the dielectric medium ($\lambda = \frac{c}{n\nu}$). It should be noted that (2.15) is known as the *Helmholtz equation* and that this formulation is particularly useful for Fourier optics.

2.4 Fourier optics

The mathematical basis for the computational optics employed in this thesis for propagation is in Fourier optics. In this section we move from the wave theory of optics, into useful mathematical functions to describe the propagation of wave-fields.

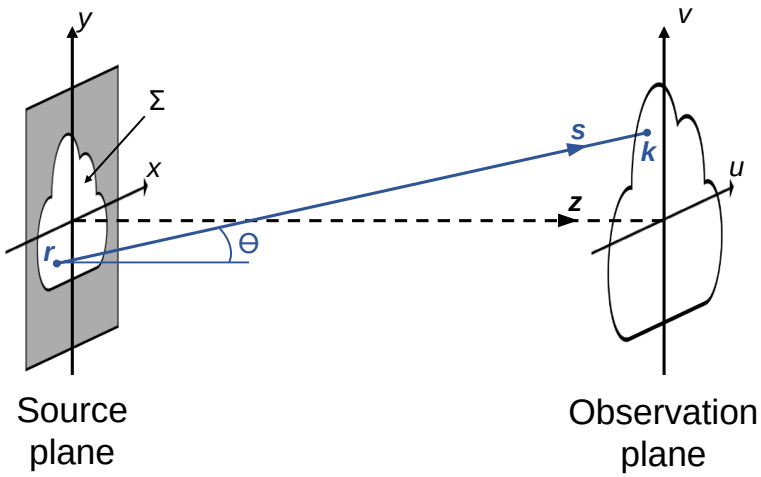

Figure 2.3: The coordinate basis for wave propagation.

2.4.1 The Huygens-Fresnel principle

From the Helmholtz equation derived previously, we use *Green's theorem* to deduce a general solution, known as the *Rayleigh-Sommerfield* solutions [2], [3]. From the first Rayleigh-Sommerfield solution, the Huygens-Fresnel principle in rectangular coordinates is identified:

$$\psi(u,v,z) = \frac{1}{i\lambda}\iint_{\Sigma} \psi(x,y,0)\frac{e^{iks}}{s}\cos(\mathbf{z},\mathbf{s})dxdy, \tag{2.17}$$

where $\psi(x,y,0)$ is the wavefield in the source plane, and $\psi(u,v,z)$ is the wavefield in the observation plane. Σ is the aperture in the source plane. $\cos(\mathbf{z},\mathbf{s}) = \cos\theta$ is the cosine of the angle between the propagation direction, $\mathbf{z}$, and the vector $\mathbf{s}$ joining a point on the source plane with a point on the observation plane, as can be seen in Figure 2.3.

The term $\cos\theta$ is therefore defined as:

$$\cos\theta = \frac{z}{s}, \tag{2.18}$$

and so the Huygens-Fresnel principle can be written as:

$$\psi(u,v,z) = \frac{z}{i\lambda}\iint_{\Sigma}\psi(x,y,0)\frac{\exp(iks)}{s^2}dxdy, \tag{2.19}$$

where

$$s = \sqrt{z^2 + (u-x)^2 + (v-y)^2}. \tag{2.20}$$

This is visually demonstrated in Figure 2.2. It shows that the observed field ($\psi(u,v,z)$) is a superposition of diverging spherical waves ($\frac{\exp(iks)}{s^2}$) originating from secondary sources located at all points (x,y) within the aperture Σ. The Rayleigh-Sommerfield diffraction formula is difficult and computationally expensive to analytically evaluate [4], and so some simplifications can be made in order that propagation of wavefields can be calculated efficiently. These propagators will be used in this thesis, as part of propagation expressions in simulations and reconstruction algorithms. Examples of MATLAB code to implement these propagators are also given in Appendix A.

2.4.2 Fresnel propagation

The Fresnel approximation reduces the Huygens-Fresnel principle to something that is more computationally simple by approximating the distance r given by (2.20) using a binomial expansion [2], [3]. Letting b be a number < 1, the binomial expansion is:

$$\sqrt{1+b} = 1 + \frac{1}{2}b - \frac{1}{8}b^2 + \dots. \tag{2.21}$$

Factor z out of (2.20) to give:

$$s = z\sqrt{1 + \left(\frac{u-x}{z}\right)^2 + \left(\frac{v-y}{z}\right)^2}. \tag{2.22}$$

Apply the binomial expansion and keep the first two terms of the expansion:

$$s \approx z\left[1+\frac{1}{2}\left(\frac{u-x}{z}\right)^2+\frac{1}{2}\left(\frac{v-y}{z}\right)^2\right]. \tag{2.23}$$

Substituting this approximation into the Huygens-Fresnel principle ((2.19)) gives the Fresnel approximation:

$$\psi(u,v,z)=\frac{e^{ikz}}{i\lambda z}\iint_{\Sigma}\psi(x,y,0)\exp\left\{\frac{ik}{2z}\left[(u-x)^2+(v-y)^2\right]\right\}dxdy \tag{2.24}$$

Here, the error introduced when dropping all the terms of the expansion of r apart from z in the denominator of (2.19) is considered acceptably small. Additionally, if the term $\exp\left[\frac{ik}{2z}(u^2+v^2)\right]$ is factored outside of the integral of (2.24):

$$\psi(u,v,z)=\frac{e^{ikz}}{i\lambda z}e^{\frac{ik}{2z}(u^2+v^2)}\iint_{\Sigma}\psi(x,y,0)e^{\frac{ik}{2z}\left(x^2+y^2\right)}e^{-\frac{ik}{2z}(ux+vy)}dxdy \tag{2.25}$$

then the Fresnel approximation can be seen to be a Fourier transform of the wavefield and a quadratic phase exponential. Alternatively, and the form used for computation purposes due to the successive Fourier and inverse Fourier transforms, this Fresnel approximation can be written as a convolution integral, given by:

$$\psi(u,v,z)=\mathcal{F}^{-1}\left\{\mathcal{F}\left\{\psi(x,y,0)\right\}H(f_X,f_Y)\right\}, \tag{2.26}$$

with the transfer function H:

$$H(f_X,f_Y)=e^{ikz}\exp\left[-i\pi\lambda z(f_X^2+f_Y^2)\right]. \tag{2.27}$$

To determine the accuracy of the Fresnel approximation, firstly it should be noted that the spherical secondary wavelets of the Huygens-Fresnel principle have been

replaced with parabolic wavefronts, due to dropping the higher terms of the binomial expansion. Therefore, a sufficient condition for the accuracy of this approximation is that the maximum phase change induced by dropping the $\frac{b^2}{8}$ term is much less than 1 radian. This is expressed as:

$$z^3 \gg \frac{\pi}{4\lambda}\left[(u-x)^2+(v-y)^2\right]^2_{\max}. \tag{2.28}$$

If this condition is met, then the observation plane is said to be in the near-field of the source plane, and as such the Fresnel propagator should be used in the near-field.

A looser criterion, known as the Fresnel number, is also used to determine whether the Fresnel approximation is valid:

$$N_F = \frac{w^2}{\lambda z}, \tag{2.29}$$

where w is the radius of the circular aperture in the source plane. If the Fresnel number is greater than 1, then it is commonly accepted that the Fresnel approximation is valid [4]. The MATLAB implementation of Fresnel propagation can be found in Appendix A.1.

2.4.3 Fraunhofer propagation

Alternatively, if the parabolic phase term $\left(\exp\left[\frac{ik}{2z}\left(x^2+y^2\right)\right]\right)$ in the Fresnel approximation (2.25) can be assumed to be flat, i.e.:

$$z \gg \frac{k(x^2+y^2)_{\max}}{2}, \tag{2.30}$$

then the wavefield can be found from a direct Fourier transform of the aperture itself (up to a multiplicative phase factor in (u,v)) [2]:

$$\psi(u,v,z) = \frac{e^{ikz}}{i\lambda z} e^{\frac{ik}{2z}(u^2+v^2)} \iint_{\Sigma} \psi(x,y,0) \exp\left[-\frac{i2\pi}{\lambda z}(ux+vy)\right] dxdy. \tag{2.31}$$

This propagator cannot be written as a convolution integral. However, it can be seen that apart from the multiplicative phase factors outside the integral, it is just a Fourier transform of the wavefield, evaluated at frequencies:

$$f_u = \frac{u}{\lambda z} \tag{2.32}$$

$$f_v = \frac{v}{\lambda z}. \tag{2.33}$$

This approximation is considered valid in the far-field, such that the Fresnel number (2.29) is much less than 1. The MATLAB implementation of Fraunhofer propagation can be found in Appendix A.2.

2.4.4 Angular spectrum propagation

An alternative to the Fresnel approach of propagation is to consider that a wavefield consists of plane waves (as opposed to spherical waves) travelling in different directions from that plane [2], [3]. The *angular spectrum* of a wavefield is given by a two dimensional Fourier transform of the wavefield. Considering a wavefield ψ, incident on a transverse (x,y) plane, travelling in the positive z direction. At the $z=0$ plane, the wavefield has an angular spectrum:

$$A(f_X, f_Y; 0) = \int_{-\infty}^{\infty}\int \psi(x,y,0) \exp\left[-i2\pi\left(f_X x + f_Y y\right)\right] dxdy \tag{2.34}$$

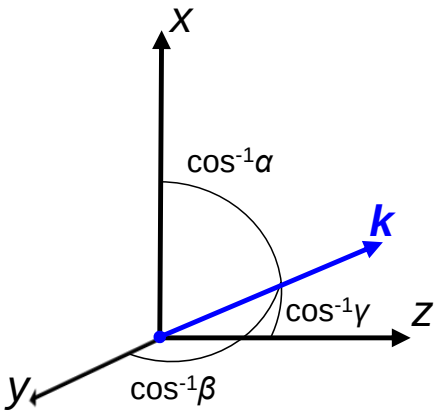

Figure 2.4: The wave vector **k** in terms of direction cosines.

Using the Fourier integral theorem, the wavefield ψ can be equally described as a collection of simple complex exponential functions:

$$\psi(x,y,0) = \int_{-\infty}^{\infty}\int A(f_X x, f_y y; 0) \exp\left[i2\pi\left(f_X x + f_Y y\right)\right] df_X df_Y. \tag{2.35}$$

Now, considering a plane wave, p, as in Figure 2.4, propagating with wave vector **k**, where **k** has magnitude $2\pi/\lambda$ and direction cosines (α, β, γ):

$$p(x,y,z;t) = \exp\left[\left(i(\mathbf{k}\cdot\mathbf{r} - 2\pi\nu t\right], \tag{2.36}$$

where $\mathbf{r} = x\hat{x} + y\hat{y} + z\hat{z}$ is the position vector and $\mathbf{k} = \frac{2\pi}{\lambda}\left(\alpha\hat{x} + \beta\hat{y} + \gamma\hat{z}\right)$. The direction cosines are related by $\gamma = \sqrt{1-\alpha^2-\beta^2}$. The time independent complex phasor amplitude across a constant z-plane is therefore:

$$P(x,y,z) = \exp(i\mathbf{k}\cdot\mathbf{r}) = \exp\left[i\frac{2\pi}{\lambda}(\alpha x + \beta y)\right]\exp\left[i\frac{2\pi}{\lambda}\gamma z\right]. \tag{2.37}$$

Therefore, at $z = 0$, the complex exponential function in (2.35) $\left(\exp\left[i2\pi\left(f_X x + f_Y y\right)\right]\right)$

can also be described as a plane wave propagating with direction cosines:

$$\alpha = \lambda f_X \tag{2.38}$$

$$\beta = \lambda f_Y \tag{2.39}$$

$$\gamma = \sqrt{1 - (\lambda f_X)^2 - (\lambda f_Y)^2}. \tag{2.40}$$

And so the angular spectrum of the wavefield at z = 0 can be written in terms of direction cosines as:

$$A\left(\frac{\alpha}{\lambda}, \frac{\beta}{\lambda}; 0\right) = \iint_{-\infty}^{\infty} \psi(x, y, 0) \exp\left[-i2\pi\left(\frac{\alpha}{\lambda}x + \frac{\beta}{\lambda}y\right)\right] dxdy. \tag{2.41}$$

Considering that the wavefield has travelled a distance z to a plane parallel to the (x, y) plane, the angular spectrum of the wavefield at this point is:

$$A\left(\frac{\alpha}{\lambda}, \frac{\beta}{\lambda}; z\right) = \iint_{-\infty}^{\infty} \psi(x, y, z) \exp\left[-i2\pi\left(\frac{\alpha}{\lambda}x + \frac{\beta}{\lambda}y\right)\right] dxdy. \tag{2.42}$$

As previously, we can write the wavefield as an inverse Fourier transform of its spectrum:

$$\psi(x, y, z) = \iint_{-\infty}^{\infty} A\left(\frac{\alpha}{\lambda}, \frac{\beta}{\lambda}; z\right) \exp\left[i2\pi\left(\frac{\alpha}{\lambda}x + \frac{\beta}{\lambda}y\right)\right] d\frac{\alpha}{\lambda}d\frac{\beta}{\lambda}. \tag{2.43}$$

Remembering that the wavefield must satisfy the Helmholtz equation (2.15) at all source-free points:

$$(\nabla^2 + k^2)\psi = 0, \tag{2.44}$$

and applying this requirement to (2.43), A must satisfy the differential equation:

$$\frac{d^2}{dz^2} A\left(\frac{\alpha}{\lambda}, \frac{\beta}{\lambda}; z\right) + \left(\frac{2\pi}{\lambda}\right)^2 \left[1 - \alpha^2 - \beta^2\right] A\left(\frac{\alpha}{\lambda}, \frac{\beta}{\lambda}; z\right) = 0. \tag{2.45}$$

A solution to this differential equation can be written as:

$$A\left(\frac{\alpha}{\lambda},\frac{\beta}{\lambda};z\right)=A\left(\frac{\alpha}{\lambda},\frac{\beta}{\lambda};0\right)\exp\left(i\frac{2\pi}{\lambda}\sqrt{1-\alpha^2-\beta^2}z\right). \tag{2.46}$$

This solution gives two classes of results:

1. $$\alpha^2+\beta^2<1 \tag{2.47}$$

   The effect of the propagation over the distance z is a change of the relative phases of the various components of the angular spectrum. As each component plane wave is travelling at a different angle, each one will travel a different distance between the two parallel planes, introducing relative phase delays.

2. $$\alpha^2+\beta^2>1 \tag{2.48}$$

   This makes the square root imaginary, so that (2.46) becomes:

   $$A\left(\frac{\alpha}{\lambda},\frac{\beta}{\lambda};z\right)=A\left(\frac{\alpha}{\lambda},\frac{\beta}{\lambda};0\right)\exp\left(-\frac{2\pi}{\lambda}\sqrt{\alpha^2+\beta^2-1}z\right). \tag{2.49}$$

   This is the non-propagating solution, which decays to zero rapidly. These components are called *evanescent waves*, and because we can assume that the distance z is larger than a few wavelengths, can be disregarded.

Combining these results, the wavefield at a parallel plane at a distance z from the initial plane $z=0$ can be written by substituting (2.46) into (2.43):

$$\psi(x,y,z)=\int_{-\infty}^{\infty}\!\!\int A\left(\frac{\alpha}{\lambda},\frac{\beta}{\lambda};0\right)\exp\left(i\frac{2\pi}{\lambda}\sqrt{1-\alpha^2-\beta^2}z\right) \tag{2.50}$$

$$\times\,\mathrm{circ}\left(\sqrt{\alpha^2+\beta^2}\right)\exp\left[i2\pi\left(\frac{\alpha}{\lambda}x+\frac{\beta}{\lambda}y\right)\right]d\frac{\alpha}{\lambda}d\frac{\beta}{\lambda}. \tag{2.51}$$

This is known as the angular spectrum propagator. Computationally it is implemented by:

1. Fourier transform the starting wavefield.

2. For $\alpha^2 + \beta^2 < 1$, multiply by the phase term

$$\exp\left(i\frac{2\pi}{\lambda}\sqrt{1-\alpha^2-\beta^2}z\right)$$

3. Inverse Fourier transform to the propagated wavefield.

The angular spectrum propagator is mathematically valid for any propagation distance, but in practice is only suited to short propagation distances, where the Fresnel number is much greater than 1. This is because the starting and propagated wavefields have the same spatial sampling, due to the Fourier and inverse Fourier transformations. Over a large propagation distance the size of the wavefield will increase, and will exceed the calculation window, creating aliasing. The MATLAB implementation of the angular spectrum propagation can be found in Appendix A.3.

2.5 Light microscopy and bio-imaging

The connection between biological research and light microscopy is strong [5], [6]. Many of the microscopy tools that cell biologists now rely on were once breakthroughs in microscope technology. From the first observations by Hooke and van Leeuwenhoek in the 17^{th} century, starting the field of biological imaging, to the dyes discovered in the late 1800s for staining cells, early technologies were crucial in the understanding of cells and diseases. More recently, the digital revolution has enabled the development of huge advances in microscope technology, using the Charge-Couple Device (CCD) to capture and algorithms to enhance images, revealing more details of the cellular structures.

One of the key problems addressed by this research is that biological cells appear transparent unless contrast enhancing techniques are developed and as such are known as 'phase objects'. The next section will start by explaining the theory behind a basic microscopes, before giving a background to two fields of contrast enhancement: a brief look at fluorescence; and the main focus of this thesis, phase imaging.

2.5.1 Microscopy basics

The compound microscope was invented by Galileo in about 1610 [3]. It was invented because if only a single magnifier is used, the distance between the object and eye will become inconveniently small if larger fields of view are required with large magnification. In a microscope, the magnification is achieved in two stages, providing higher magnification of nearby objects. In this section, some of the key concepts around microscopy will be introduced.

Compound microscopes

The most basic model of a compound microscope is shown in Figure 2.5a [3]. This is known as a finite microscope. The objective lens forms a real, inverted, magnified image of the object. This image lies in the plane of the field stop of the eyepiece. The diverging rays from each point in this image will emerge parallel to each other from the eyepiece lens. The eye's lens itself forms the virtual image on the retina.

An infinity compound microscope is a more modern type of microscope, having been adopted in the last few decades [7], [8]. A basic model is shown in Figure 2.5b. Instead of the objective lens projecting the intermediate image onto the intermediate image plane, infinity-corrected objective lenses are designed so that the light emerging from the lens is focussed to infinity. The tube lens then forms the image at its focal plane. In the same way, an eyepiece lens and the eye can be used to focus a virtual image on the back of the retina. Alternatively a detector, such as a CCD, can be placed

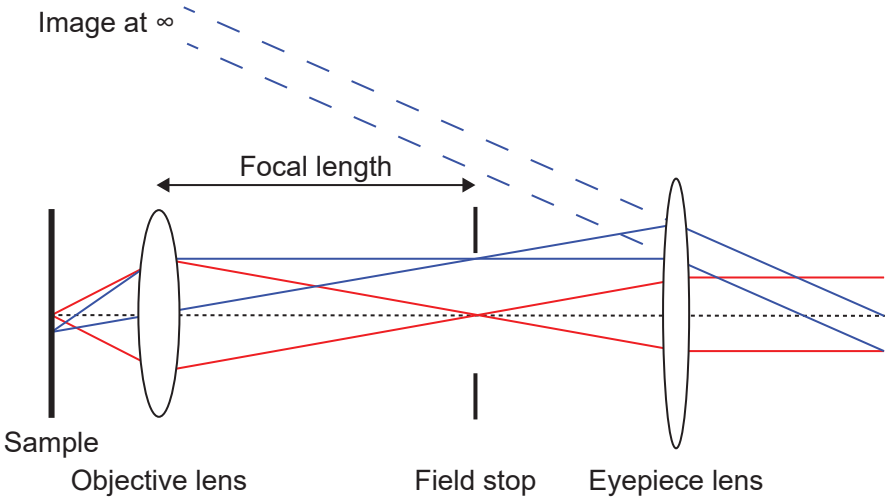

(a) Finite microscope.

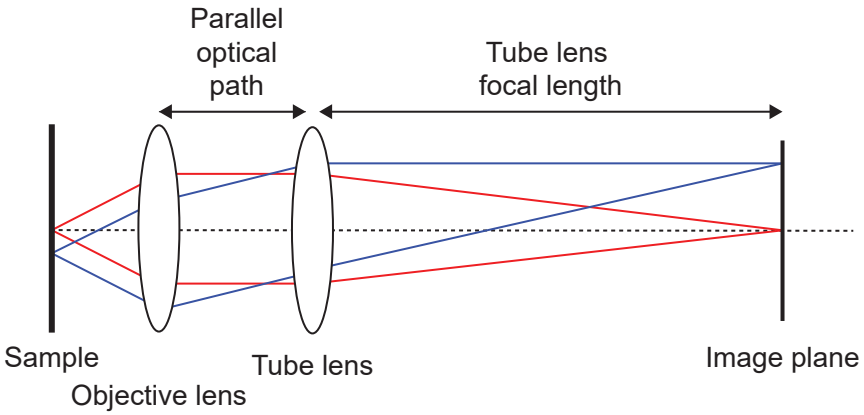

(b) Infinity corrected microscope.

Figure 2.5: Two compound microscopes.

in the image plane. A key feature of this setup is the light rays in the region between the objective and tube lens are collimated, or parallel. This gives several advantages over a finite microscope. Firstly, the magnification does not change when the distance between the objective and tube lens changes (to a reasonable degree). This means additional components (such as polarisers, or Wollaston prisms) can be placed in the infinity region. Secondly, parfocality between different infinity-corrected objective lenses can be easily maintained.

Coherent and incoherent illumination

The illumination of the microscope shall now be considered [2]. We can either have a *coherent* imaging system, which is linear in complex amplitude, or an *incoherent* imaging system, which is linear in intensity. An example of a coherent light source is one where the light appears to originate from a single point, such as a laser, whereas an incoherent source is one where the light appears from diffuse sources, such as the sun, or a white light bulb. The phase of a spatially coherent light source varies in time in unison across its field. The phase of a spatially incoherent light source randomly changes in time across the field. These different types of system are discussed further below.

Instead of thinking about the microscope as a series of lenses, Figure 2.6 shows that all the elements of the system can be put in a black box–the 'imaging system'. The properties of this imaging system can be defined by the entrance and exit pupils of the combined system, assuming perfect geometrical optics. To analyse the frequency responses of this system, we will return to a Fourier optics approach.

Firstly, we shall look at the frequency response of a coherent illumination on the imaging system.

Imaging with a coherent illumination (such as a monochromatic laser), is described

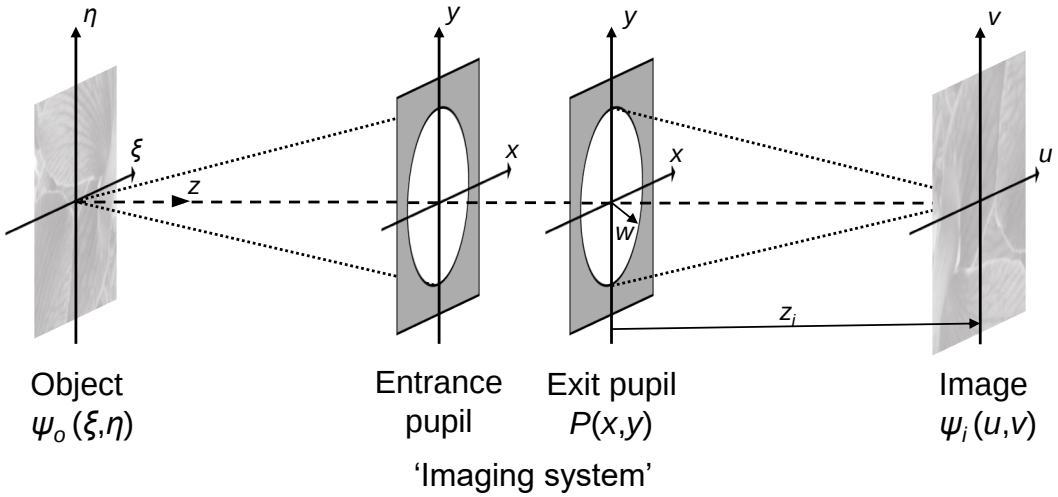

Figure 2.6: The general imaging model used for frequency analysis, with coordinate definitions.

as a convolution, using the coordinates shown in Figure 2.6 [2], [4]:

$$\psi_i(u,v) = h(u,v) \otimes \psi_g(u,v), \tag{2.52}$$

where h is the coherent impulse response for the imaging system, which in a diffraction-limited system (one with a perfect pupil function where only the boundaries of the pupil are involved with diffractive effects) is the Fraunhofer diffraction pattern of the exit pupil:

$$h(u,v) = \frac{A}{\lambda z_i} \iint_{-\infty}^{\infty} P(x,y) \exp\left[-i\frac{2\pi}{\lambda z_i}(ux+vy)\right] dxdy. \tag{2.53}$$

ψ_g is the ideal geometrical-optics predicted field, which is a copy of the object field, scaled by the transverse magnification M_t:

$$\psi_g(u,v) = \frac{1}{|M_t|}\psi_o\left(\frac{u}{M_t}, \frac{v}{M_t}\right). \tag{2.54}$$

In the frequency domain (where the subscripts X and Y are used regardless of the space variables that they correspond to) using the convolution theorem, Equation 2.52

becomes:

$$G_i(f_X, f_X) = H(f_X, f_Y)G_g(f_X, f_Y), \tag{2.55}$$

where H is Fourier transform of h, which for a diffraction limited imaging system, is in effect the pupil function, giving:

$$H(f_X, f_Y) = (A\lambda z_i)P(-\lambda z_i f_X, -\lambda z_i f_Y), \tag{2.56}$$

which, with choice of A such that $A\lambda z_i$ is equal to unity, gives:

$$H(f_X, f_Y) = P(\lambda z_i f_X, \lambda z_i f_Y). \tag{2.57}$$

Equation (2.57) (the *coherent transfer function*, or *amplitude transfer function*) shows the key information about diffraction-limited coherent imaging systems. If the pupil function, P, is unity within a region and zero outside, there is a finite passband in the frequency domain within which the imaging system passes through all frequency components without altering their phase or amplitude (for a perfect system without aberrations). Outside this passband, the frequency response drops to zero, meaning that those frequency components are blocked.

In many cases, the pupil function is circular (for example, a lens). For a circular pupil with diameter $2w$:

$$P(x, y) = \text{circ}\left(\frac{\sqrt{x^2 + y^2}}{w}\right), \tag{2.58}$$

the coherent image transfer function is:

$$H(f_X, f_Y) = \text{circ}\left(\frac{\sqrt{f_X^2 + f_Y^2}}{\frac{w}{\lambda z_i}}\right). \tag{2.59}$$

This is a circular function, as shown as the blue line in Figure 2.7, with a cutoff

frequency

$$f_0 = \frac{w}{\lambda z_i}. \tag{2.60}$$

Next, the analysis of the frequency response on the imaging system with incoherent illumination.

For a incoherent imaging system, using the same imaging system in Figure 2.6, the intensity convolution integral is obeyed [2]. In contrast to the coherent analysis, incoherent imaging is linear with irradiance.

$$I_i(u,v) = |h(u,v)|^2 \otimes I_g(u,v), \tag{2.61}$$

where h is the same coherent impulse response as (2.53), and I_g the ideal geometical-optics irradiance image of (2.54). $|h(u,v)|^2$ is also known as the *Point Spread Function (PSF)*. As with coherent imaging, we apply the convolution theorem to (2.61) to obtain the frequency domain relation:

$$\mathcal{G}_i(f_X, f_Y) = \mathcal{H}(f_X, f_Y)\mathcal{G}_g(f_X, f_Y). \tag{2.62}$$

The normalised frequency spectra of I_g and I_i are defined as:

$$\mathcal{G}_g(f_X, f_Y) = \frac{\int\int_{-\infty}^{\infty} I_g(u,v) \exp\left[-i2\pi(f_X u + f_Y v)\right] dudv}{\int\int_{-\infty}^{\infty} I_g(u,v) dudv} \tag{2.63}$$

$$\mathcal{G}_i(f_X, f_Y) = \frac{\int\int_{-\infty}^{\infty} I_i(u,v) \exp\left[-i2\pi(f_X u + f_Y v)\right] dudv}{\int\int_{-\infty}^{\infty} I_i(u,v) dudv}, \tag{2.64}$$

and the normalised transfer function is:

$$\mathcal{H}(f_X, f_Y) = \frac{\mathcal{F}\left(|h(u,v)^2|\right)}{\iint_{-\infty}^{\infty} |h(u,v)|^2 du dv} \tag{2.65}$$

$$= \frac{\iint_{-\infty}^{\infty} |h(u,v)|^2 \exp\left[-i2\pi(f_X u + f_Y v)\right] du dv}{\iint_{-\infty}^{\infty} |h(u,v)|^2 du dv} \tag{2.66}$$

$\mathcal{H}$ is known as the Optical Transfer Function (OTF), and its modulus $|\mathcal{H}|$ is the Modulation Transfer Function (MTF).

Finally, it is helpful to notice that the OTF is the normalised autocorrelation function of the coherent transfer function:

$$\mathcal{H}(f_X, f_Y) = H(f_X, f_Y) \star H(f_X, f_Y)|_{\text{norm}}. \tag{2.67}$$

Once again, we shall analyse the frequency response of an 'imaging system' which consists of a circular exit pupil with diameter $2w$.

$$P(x,y) = \text{circ}\left(\frac{\sqrt{x^2+y^2}}{w}\right) \tag{2.68}$$

This is not as simple to calculate compared to the coherent case, but the OTF can be shown to be [2]:

$$\mathcal{H}(\rho) = \frac{2}{\pi}\left[\arccos\left(\frac{\rho}{2\rho_0}\right) - \frac{\rho}{2\rho_0}\sqrt{1-\left(\frac{\rho}{2\rho_0}\right)^2}\right] \qquad \rho \leq 2\rho_0 \tag{2.69}$$

$$= 0 \qquad \text{otherwise,} \tag{2.70}$$

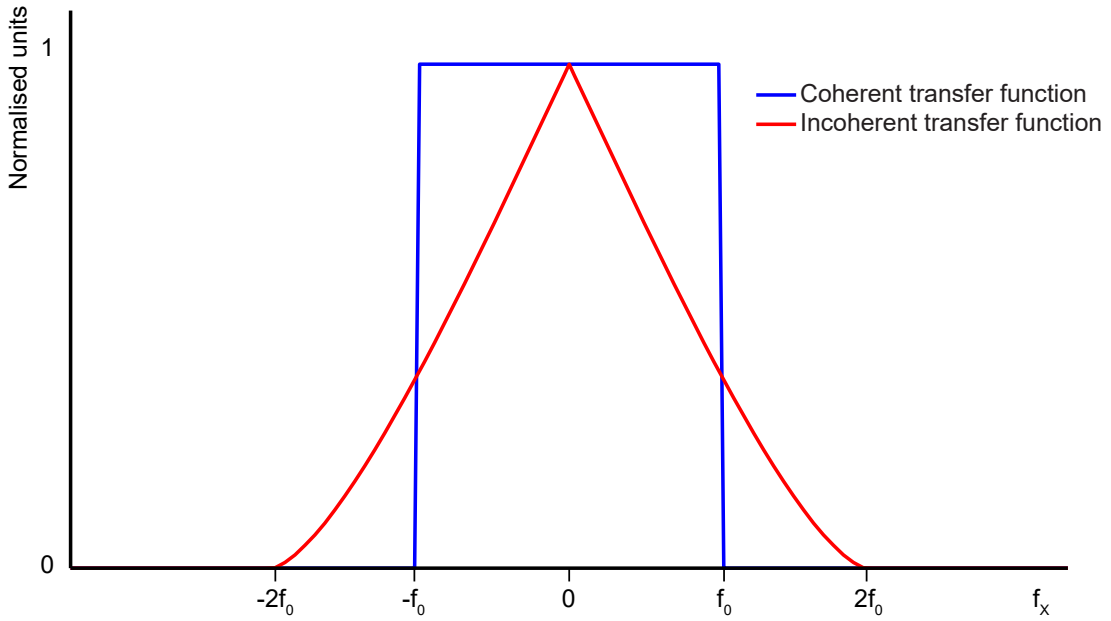

Figure 2.7: A comparison of the coherent and incoherent transfer functions for a circular pupil. A cross section is taken along the f_X axis, although both functions are rotationally symmetric.

where $\rho = \sqrt{f_X^2 + f_Y^2}$ and the cutoff frequency is:

$$2\rho_0 = \frac{2w}{\lambda z_i}, \tag{2.71}$$

which is twice the cutoff frequency of the coherent imaging system. The incoherent (OTF) transfer function can be seen as the red line in Figure 2.7.

Initially, it may appear that incoherent imaging generates a better resolution than coherent imaging. This is not necessarily the case as the coherent transfer function shows the frequency cutoff for the amplitude of the wavefield, whereas the incoherent transfer function shows the cutoff frequency of the intensity of the wavefield. It should also be noted that the coherent transfer function is flat, and so behaves as an ideal passband.

Another important consideration of coherent imaging systems is *speckle* [2]. When

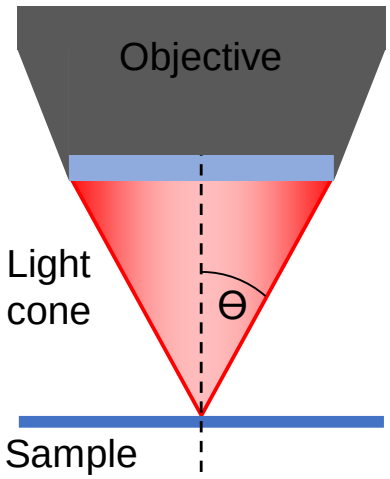

Figure 2.8: The light cone incident on the objective lens, showing the half angle for calculating the Numerical Aperture.

an object is illuminated by a coherent light source, its micro-surface structure have a considerable effect on the exit wavefield. The random bumps of a surface are large enough that a region of the coherent wavefield passing through one dip will have a significantly different phase offset from a neighbouring region. This causes a granularity and a random assortment of spots and dots across an image. This effect is not present in incoherent imaging, where the speckles change rapidly and randomly in time, effectively averaging and cancelling themselves out. Highly coherent illumination is also susceptible to pronounced diffraction patterns caused by optical imperfections, such as dust [2].

Numerical Aperture

The Numerical Aperture (NA) of a microscope is a dimensionless number that measures the performance of the objective lens in collecting light:

$$\mathrm{NA} = n \sin\theta \tag{2.72}$$

where n is the refractive index of the medium in contact with the objective lens (for air $n = 1$), and θ is the half angle of the light cone entering the objective as shown in Figure 2.8.

One way to increase the NA of a microscope is to change the refractive index of the medium in contact with the objective lens. For example, an oil-immersed microscope objective can have a refractive index of $n = 1.51$. In practice, the highest NA a dry objective can have is 0.95, whereas with oil, the highest in practice is 1.4 [1].

Resolution

Resolution is defined as the shortest distance between two points on the sample that can be separately distinguished by an observer or sensor. There are however, several interpretations of this definition [9].

It was shown by Abbe [10] that the smallest distance between two points that can be resolved by a diffraction limited lens is:

$$d = \frac{\lambda}{2n \sin \theta} \tag{2.73}$$

where d is the resolving power of the lens, λ is the wavelength of light, n is the refractive index of the transmitting medium, and θ is the maximum semi-angle captured by the lens. It can then be seen that its relation to the NA is:

$$d = \frac{\lambda}{2\text{NA}}. \tag{2.74}$$

The Sparrow criterion for incoherent illumination in two dimensions for the imaging system in Figure 2.6 is defined as [11]:

$$d = \frac{2.976 z_i \lambda}{2\pi w}, \tag{2.75}$$

and for coherent illumination is:

$$d = \frac{4.600 z_i \lambda}{2\pi w}, \tag{2.76}$$

where d is the smallest resolvable distance between two point objects that results in a uniform intensity gradient of two sinc^2 functions centred at those points.

For digital sensors, such as a CCD, it is also important to consider the Nyquist-Shannon sampling theorem which states that for a continuous function $x(t)$, bandlimited to a finite range of frequencies $< B$, the function can be recovered exactly if the sampling interval, Δx is:

$$\Delta x < \frac{1}{2B}. \tag{2.77}$$

If this requirement is not met, then there will be aliasing in the image, where under-sampled high-frequency components appear as low-frequency content [4].

2.6 Contrast enhancement

Many biological samples, such as cells and thin tissue samples, when imaged using conventional microscopes have little absorption contrast in the visible light spectrum (other than haemoglobin). Their scattering contrast is also small, meaning that unmodified cellular structures are difficult to observe. Biologists can use stains that attach themselves to macromolecules (proteins and DNA) to enable structural features to be visualised. Alternatively, cellular structures have higher refractive indices than their surroundings and so produce relative phase delays in the transmitted light. These phase variations can be converted into intensity variations which can be observed [6]. These two techniques of contrast enhancement are described in greater detail in the following two sections.

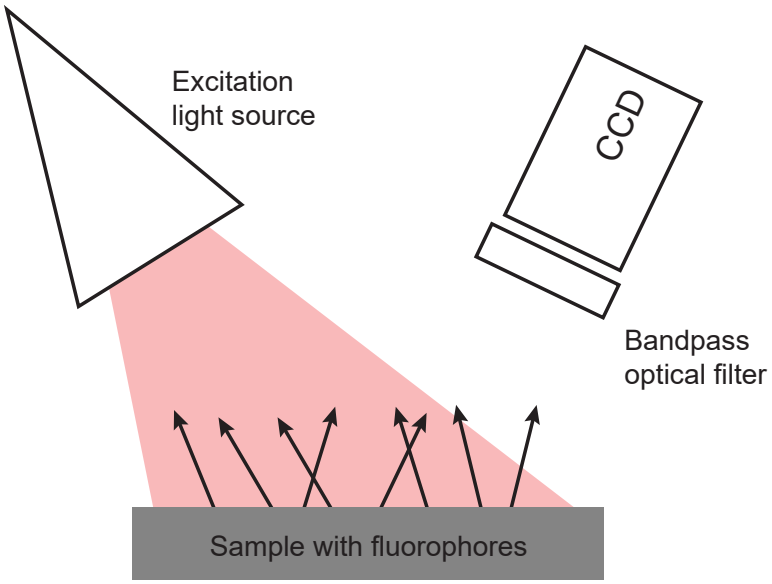

Figure 2.9: An example setup for fluorescence imaging. The fluorescent molecules near the surface of the sample are irradiated using the excitation light source with the required wavelength. They emit light of a higher wavelength in all directions. The bandpass optical filter removes the irradiating wavelength and passes the fluorescent wavelength of light through to the CCD where it is captured.

2.6.1 Fluorescence

Fluorescence techniques are a way of increasing contrast of microscopy bio-images. Fluorescence imaging is one of the major ways that biologists examine cells, proteins, and tissues [13]. Fluorophores are chemicals that when illuminated with a light with a specific wavelength, will emit light with a longer wavelength. The source illumination is separated from the fluorescence by filtering. There are two types of fluorescent molecules: endogenous, which are naturally occurring in tissues, and exogenous, which are not naturally occurring in the body. These exogenous fluorophores can be formulated to bind preferentially to certain tissue types, or cells in a specific disease state. A simple geometry for imaging the fluorescence emission from sources near the surface of tissue is shown in Figure 2.9 [6]. Figure 2.10 shows how information about the locations of different molecules in a cell can be achieved using three colour

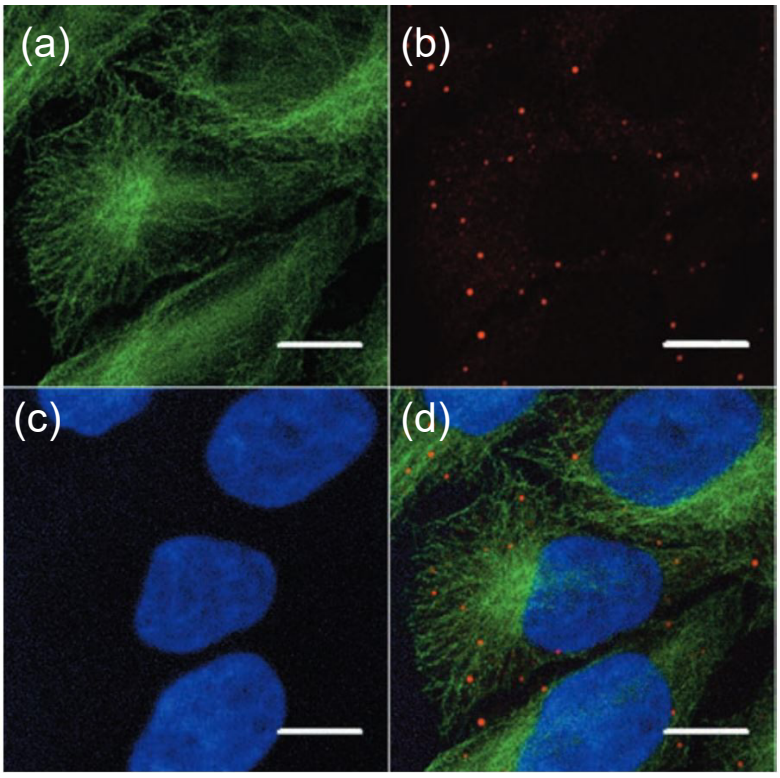

Figure 2.10: Three colour fluorescence image of HeLa cells. It can be seen that the different fluorophores attach to different molecules. (a) Microtubuli are stained in green. (b) P-bodies are stained in red (c) DNA is stained in blue. (d) An overlay of all three spectral channels. Scale bar = 10 µm. [Reproduced from [12]]

fluorescence.

One of the major advantages of fluorescence imaging is that they produce background-free measurements. This means that fluorophores can be sensed at extremely small concentrations. In addition, they have led to techniques that reach past the diffraction limit as described by Abbe [10] in the 19th century. The 2014 Nobel Prize in Chemistry was awarded to Eric Betzig, William Moerner, and Stefan Hell, for 'the development of super-resolved fluorescence microscopy'. Examples of these techniques are Stimulated Emission Depletion (STED) [14], Structured Illumination Microscopy (SIM) [15], Photo Activated Localization Microscopy (PALM) [16], and Stochastic Optical Reconstruction Microscopy (STORM) [17].

However, fluorescence imaging has several disadvantages. The images are often qualitative and require specific targeting of the protein and fluorophores. This means that it is not possible to deduce additional numerical information about the sample, and observe everything about a cell at once. In addition, fluorophores suffer from photobleaching, where the fluorescent effects decrease over time. This can limit longer term observations of cells. Phototoxicity can cause damage or even kill cells, as the excitation light illumination needs to be very strong to excite the fluorophores. Adding fluorophores into samples can alter the normal physiology of the cells, and so there are strong controls over whether they can be used for live observation [18].

2.6.2 Phase imaging

Phase imaging is another way we can increase the contrast of an image of an object with low intrinsic contrast. As light passes through an object it is slowed down due to the change in refractive index. This changes its phase relative to light that has not passed through the object. Phase imaging techniques observes these phase shifts produced as light interacts with the object at each point within the field of view, and so can create contrast. However, it is not possible to directly observe these phase shifts due the phase

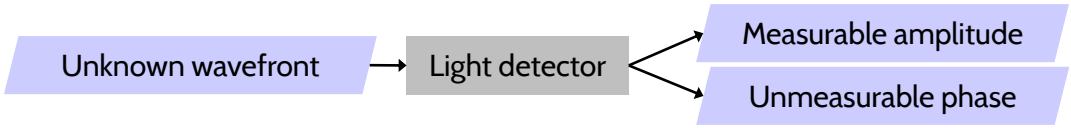

Figure 2.11: The phase problem. Light detectors are only able to measure the intensity of incident light. The phase is unmeasurable and so the overall measurement of the object is incomplete. Valuable information about the object is lost when it is observed.

problem.

The phase problem

Light detectors, such as CCDs, can measure only the intensity of the light that interacts with them. The actual phase of the light varies too fast to be directly recorded–at the scale of femtoseconds for visible light [19].

As previously shown, a monochromatic light wave can be described as the complex scalar function

$$\psi(\mathbf{r}) = |\psi(\mathbf{r})| \exp(i\phi(\mathbf{r})). \tag{2.78}$$

The detector can only capture the power of the intensity, I, of the wave,

$$I(\mathbf{r}) = |\psi(\mathbf{r})|^2 = \psi(\mathbf{r})\psi(\mathbf{r})^*. \tag{2.79}$$

The asterisk denotes the complex conjugate of the function, such that

$$\psi(\mathbf{r})^* = |\psi(\mathbf{r})| \exp(-i\phi(\mathbf{r})). \tag{2.80}$$

This means that when the intensity of the wave is captured, all the phase information is lost.

This is known as the phase problem, and is a classic inverse problem, as illustrated in Figure 2.11. If we know the complex-valued wave at one position, we can easily

calculate the wave downstream, using a propagator, and measure the intensity using a detector. However, starting with the recorded intensity data, it is seemingly intractable to reverse. Any phase value can be guessed at the detector, but knowing what are the single correct phase values that gave rise to this intensity data is seemingly impossible. In addition, intensities do not add linearly, creating a solution space that is highly non-linear.

This is the main problem that phase imaging attempts to solve. When we can only capture intensity information about a wave, how can we uncover its underlying phase information?

Qualitative phase imaging techniques can be used to increase the contrast of samples with low intrinsic contrast by providing an intensity image derived from phase shifts across samples. They do not, however, fully solve the phase problem as the phase changes across samples cannot be retrieved quantitatively.

Phase Contrast Microscopy

Phase Contrast Microscopy (PCM) is one of the most commonly used phase imaging techniques [20]. Phase imaging started with the physical explanation of image information given by Abbe [10] that an image field is formed as the interference effect between plane waves moving in different directions. By exploiting the concept that the image field is the superposition of fields originating from the sample, Zernike developed PCM in the 1930s [21]. This was an important advancement in endogenous contrast, as it revealed inner details of transparent objects without staining.

An optical setup for PCM is given in Figure 2.12. A small metal film is placed in the Fourier plane of the objective, such that it covers the DC component and both attenuates and shifts the phase of the unscattered field. This is known as a phase contrast filter.

Assuming that the sample under investigation is a phase object and its image field

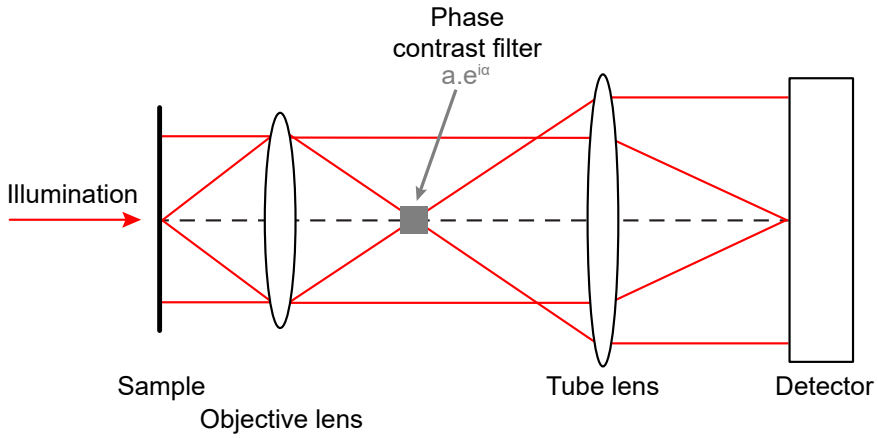

Figure 2.12: The optical setup for Phase Contrast Microscopy.

is normalised, the image field takes the form

$$\psi(\mathbf{r}) = e^{i\phi(\mathbf{r})} = 1 + \psi_1(\mathbf{r}) \tag{2.81}$$

where the first term is the unscattered field, and the second component is the fluctuating field and ϕ is the endogenous contrast, or phase shift. Also assuming that the transmission function of the phase contrast filter is $ae^{i\alpha}$ where a is the attenuation of the filter and α the phase shift, the new field becomes

$$\begin{aligned} \psi(\mathbf{r}) &= ae^{i\alpha} + \psi_1(\mathbf{r}) \\ &= ae^{i\alpha} + e^{i\phi(\mathbf{r})} - 1 \end{aligned} \tag{2.82}$$

The intensity of this phase contrast image is

$$\begin{aligned} I(\mathbf{r}) &= |\psi(\mathbf{r})|^2 \\ &= a^2 + 1 + 1 + 2\left[a\cos\left(\alpha + \phi(\mathbf{r})\right) - a\cos\alpha - \cos\phi(\mathbf{r})\right] \\ &= a^2 + 2\left[1 - \cos\phi(\mathbf{r}) - a\cos\alpha + a\cos\left(\alpha + \phi(\mathbf{r})\right)\right] \end{aligned} \tag{2.83}$$

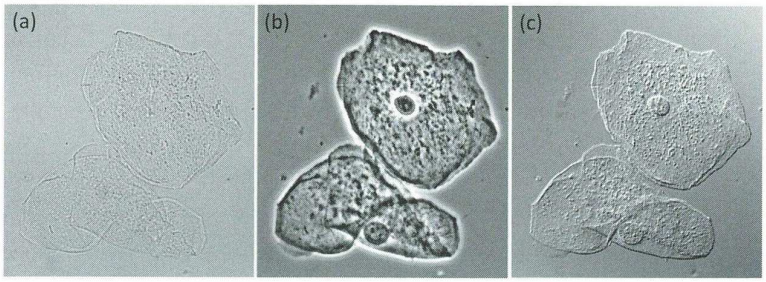

Figure 2.13: Comparative microscope images of a hamster cheek cell: (a) standard bright field microscopy image, (b) Phase Contrast Microscopy image, (c) Differential Interference Contract microscopy image. [Reproduced from [7]]

As $(1 - \cos x)$ is negligible for small x, and choosing $\alpha = \pm\frac{\pi}{2}$

$$\begin{aligned} I(\mathbf{r}) &= a^2 \pm 2a \sin\phi(\mathbf{r}) \\ &\approx a^2 \pm 2a\phi(\mathbf{r}) \end{aligned} \tag{2.84}$$

where in (2.84), we similarly approximate that $sinx \approx x$ for small x. By choosing our phase contrast filer to have $\alpha = \pm\frac{\pi}{2}$, this shift has produced an intensity which is approximately proportional to ϕ, meaning that we are able to observe the endogenous contrast.

This was a such a breakthrough technique for observing cell biology, that its inventor, Frits Zernike, was awarded the Nobel Prize for Physics in 1953. (2.13) shows how a PCM image compares to a standard brightfield image. It can be seen that the contrast is much higher in the PCM image than the bright field image, but has a characteristic 'halo' glowing edge effect. This happens because the phase filter is of finite size and so low frequency components of the sample's spectrum are phase shifted along with the DC component. There is therefore no contrast resulting from the low frequencies of the sample, and the halos are a low frequency artefact. The PCM requires spatially coherent light, and as such, can create additional image noise of speckle [6], [20].

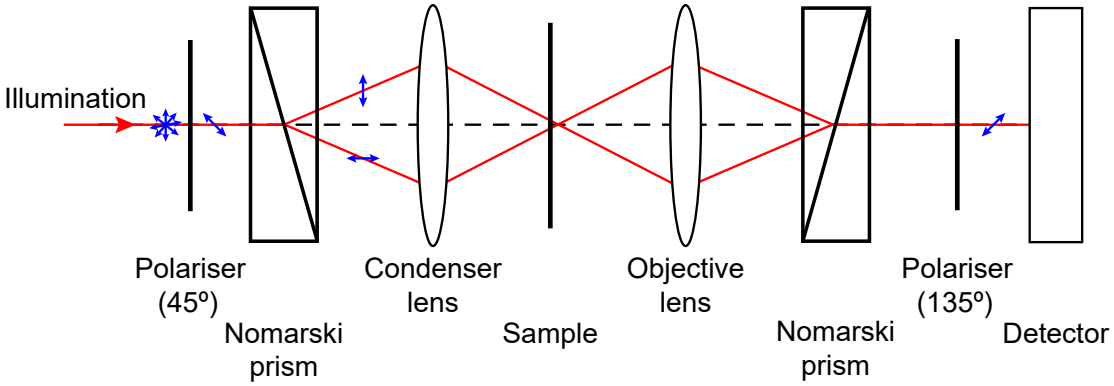

Figure 2.14: The optical setup for Differential Interference Contrast microscopy. The blue arrows indicate the polarity of the light.

Differential Interference Contrast

Differential Interence Contrast (DIC), developed by George Nomarski [22], uses interferometry to enhance the contrast of transparent objects [7]. As with PCM, DIC transforms the phase shift of light through the object into a detectable intensity image, although the contrast is proportional to the optical path length gradient in one direction, not the path length itself. These images are generated by interfering an image field with a duplicate of itself that is slightly shifted.

A diagram of how DIC operates is given in Figure 2.14. The light is first polarised at 45° and enters a Nomarski-modified Wollaston prism. This component separates light into two orthogonal linearly polarised beams. These two beams are focused by the condenser such that they pass through the sample, through separate but adjacent points. This is now the equivalent of illuminating it with two coherent sources, one with 0° polarisation and the other with 90° polarisation. Because the sample has spatially varying thickness, the optical path length of these two slightly offset beams will be different. Because of the different polarisations, these two beams do not interact with each other at this point. The beams pass through the objective lens and are focussed onto a second Nomarski-modified Wollaston prism. Being used the other

way round, the prism combines the two beams into one polarised at 135°. This overlays the two images and aligns their polarisation such that they can interfere. As the two images were spatially offset, interference in the final image occurs between adjacent locations in the sample which have slightly different phase. This phase difference is due to the relative difference in optical path length of the adjacent locations of the sample, therefore producing an intensity image approximately equal to the differential of the refractive index of the sample.

Figure 2.13 shows a characteristic DIC image of a hamster cheek cell for comparison. DIC does not produce the diffraction halo present in PCM. However, as the image is proportional to the differential of the optical path length relative to the orientation of the Wollaston prisms, it is important to recognise that features parallel to the gradient will not be visible. This can be corrected by rotating the sample for comparison. As with PCM, it is not possible to quantitatively extract the phase information from images produced by DIC.

2.7 Quantitative phase imaging techniques

A quantitative phase image contains a numerical map of all path length shifts across the field of view and is more useful than just a conventional intensity, or phase, image as they allow further numerical information to be gleaned. The length of these path shifts is changed by the thickness of the object and its refractive index. This information can be used for further measurements, such as calculating the topology of an object. A quantitative complex image, which contains both the phase and amplitude of the exit wave from an object, provides us with all the information needed about the exit wave. However, as will be discussed in the next section, it is not simple to obtain.

The natural application of QPI is in imaging transparent objects. In biological applications, this allows us to non-invasively image live cells without staining [20],

[23]–[26]. Additionally, QPI images tend to have higher contrast than the qualitative techniques discussed in Section 2.6.2, aiding with segmentation and tracking of cells [18].

One of the most impactful uses of QPI in bioimaging is in measuring single-cell volume and mass, non destructively, over long timescales [13]. This ability comes from the fact that refractive index is linearly proportional to cell density for some cells, as shown by Davies and Barer [27], [28]. As a QPI technique's output is a phase map of the cell with respect to the culture medium, it can be converted into the cell's dry mass. Mathematically, the spatially dependent phase shift can be described as:

$$\phi(\mathbf{r}) = \frac{2\pi}{\lambda} h(\mathbf{r}) n(\mathbf{r}), \tag{2.85}$$

where λ is the wavelength of the illumination, h is the thickness of the sample at position, $\mathbf{r}$, with its refractive index at that position, n. However, if the refractive index of a cell is not well known, or non-uniform, it is difficult to decouple the thickness and refractive index. QPI has also been shown to be a good tool for real time blood testing [29], stem cell differentiation [30], cancer drug screening [31], and observing cell growth [32]–[34]. One of the big aims in this field is to develop microscopy techniques with sufficient temporal phase stability and spatial resolution for sub-cellular, dynamic imaging [35].

In materials science, QPI has been used to characterise contact lenses [36], and lenslet arrays [37], [38]. These are key applications due to the transparent nature of these objects. Following broader trends in engineering, QPI has also shown to be useful in microelement studies [39], and characterising nano materials [40].

This section will begin by looking at some of the standard QPI techniques. I will then focus on a new grouping of QPI techniques, those that benefit from using an SLM. An SLM is an electro-optical device that converts a digital signal into two-dimensional

spatially varying modulation (amplitude or phase) on a beam of light. The operation of an SLM will be given in detail in Section 2.11.

2.7.1 Standard quantitative phase imaging techniques

QPI techniques attempt to solve the phase problem, however, the equipment setups of these techniques tend to be more complex. While this field is large and always expanding, this section will describe a few key techniques used by biologists and their applications.

Interferometry is a large family of techniques [41], of which detail is given about Young's interferometer and Twyman-Green interferometry in Section 2.11.4 in particular. In addition, lateral shearing interferometry [42] has been used to image cells. Interferometric techniques use the superimposition of light waves to create interference. However, interferometric methods tend to suffer from noise in their phase sensitivity, due to the reference beam travelling a separate path to the sample path.

Digital holography

Based on optical techniques introduced by Dennis Gabor [43], and Leith and Upatniek [44], digital holography obtains the phase information from an object as intensity variations in the detector plane [45]. Since its inception, holography has expanded into a vast field, including as a powerful tool in biology, and in 1971 Gabor was awarded a Nobel Prize in Physics for his development of the technique. As the name suggests (*holo* from the Greek *holos* meaning 'whole') the technique records the entire object field–the amplitude *and* phase.

Holography is a two step process: writing the hologram, and reading the hologram. There are many variants of holography, but the Mach-Zehnder interferometry setup is one the most common, as shown in Figure 2.15 [46]. A laser

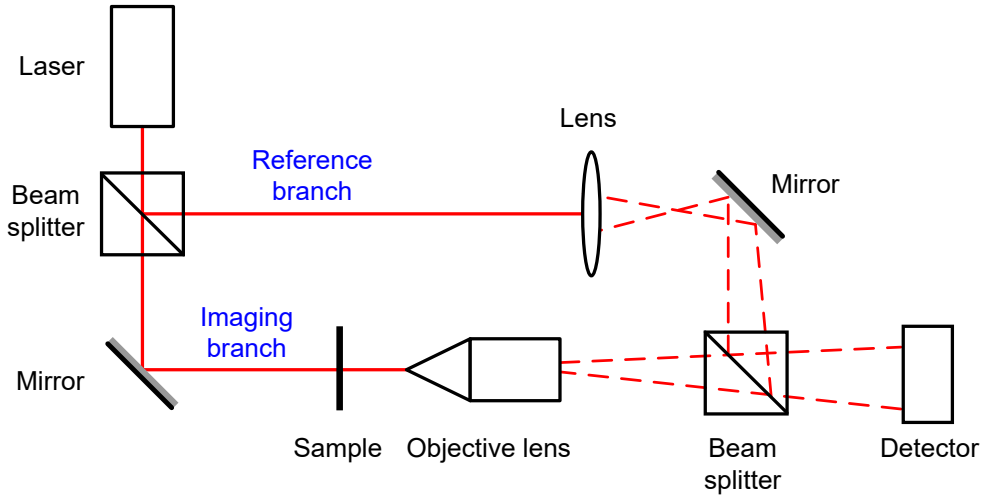

Figure 2.15: The optical setup for digital holography.

beam is split into two. On the imaging branch, the microscope objective produces a magnified image of the sample. The other branch is used as a reference branch. The two beams interfere and form a hologram. The original object is reconstructed numerically, using the Fast Fourier Transform (FFT) algorithm acting on the intensity distribution of the recorded image. This is analogous to optical holography, where the hologram is illuminated by a plane wave and observed at the same Fresnel distance as it was captured. Digital holography is one of the most widely used label free cell imaging techniques, however, it typically requires a specifically designed machine in order to support the stability of an reference beam. It has been used to image live cells in vitro by Marquet [46]. In the same way as described, the setup used is essentially a Mach-Zehnder interferometer. A comparison of results of an *in vitro* mouse neuron are shown in Figure 2.16. It can again be seen that the PCM image (a) has a halo in the background as a bright zone surrounding the neuron which can make some structures invisible. The DIC image suffers from the shadow-cast effect where the contrast of the image is not symmetrical. The digital holography image exhibits some coherence noise but it is possible to extract the morphology and refractive index of the sample.

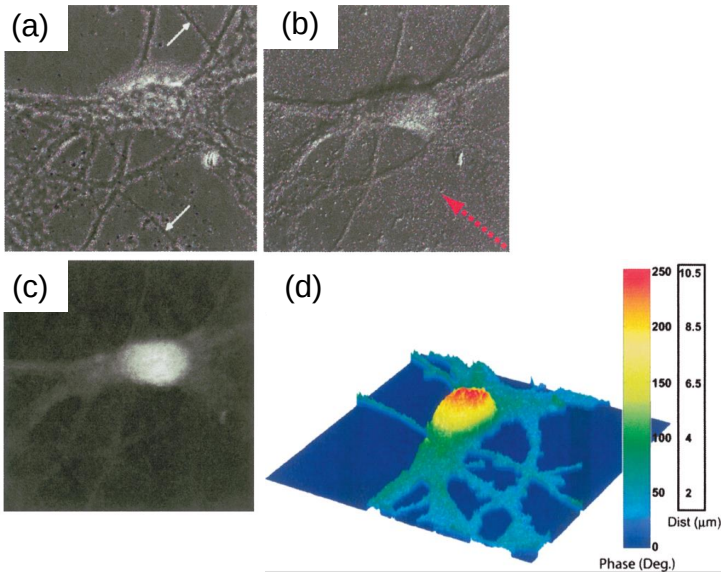

Figure 2.16: Comparison of images from a living mouse neuron in culture. (a) Phase Contrast image (Section 2.6.2) (b) Differential Interference Contrast image (Section 2.6.2) (c) Raw digital holography image (d) Perspective image of phase distribution obtained with digital holography. [Reproduced from [46]]

Transport of Intensity Equation (TIE)

QPI using the TIE is a method that does not use interferometric geometry, but uses the Abbe's theory that the image field itself is an interferogram [10]. It was introduced by Pagnin and Nugent [48], based on theory by Teague [49]. It operates using a standard bright field microscope, using white light. Several intensity measurements are taken as the object moves through focus, and a quantitative phase image is generated of the in-focus field.

In order to use the TIE for quantitative phase imaging, start with a wavefield incident on the detector of a microscope shown in Figure 2.17 [20] . The scalar image field has the form:

$$\psi(\mathbf{r}) = \sqrt{I(\mathbf{r})}\exp[i\phi(\mathbf{r})], \tag{2.86}$$

where $\mathbf{r} = (x, y)$ are the transverse coordinates, I is the intensity, ϕ is the phase

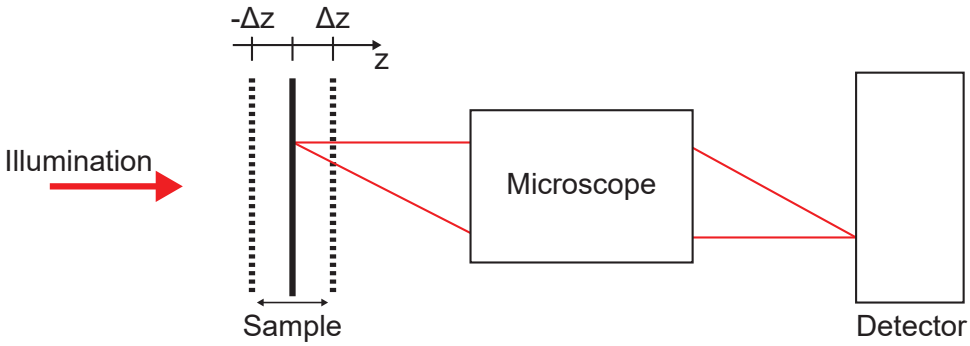

Figure 2.17: The basic setup for phase imaging with the transport of intensity equation. The microscope can be any standard optical microscope.

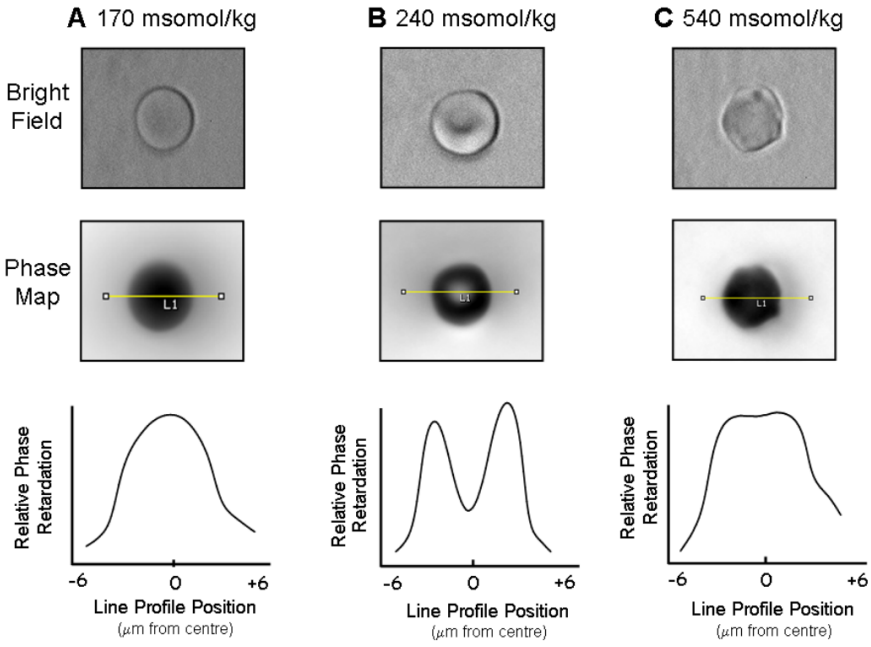

Figure 2.18: Transport of Intensity Equation (TIE) was used to compare the morphology of rat red blood cells in buffer solutions of differing osmolarity. The quantitative phase image allows biologists to easily view the shape of the cells compared to the bright field image. [Reproduced from [47]]

distribution of the wavefield at that plane. The TIE as derived by Teague [49] is defined as:

$$k_0 \frac{\partial I(\mathbf{r})}{\partial z} = -\nabla[I(\mathbf{r})\nabla\phi(\mathbf{r})], \tag{2.87}$$

where $k_0 = \frac{2\pi}{\lambda}$ is the wavenumber, and $\nabla = (\partial/\partial x, \partial/\partial y)$.

It can be seen from this equation that by knowing how the intensity of the wavefield changes along the optic axis (along z), the transverse phase distribution of the wavefield can be recovered. With the assumption of a weakly scattering object, the transverse intensity can be approximated as uniform, giving:

$$\frac{\partial I(\mathbf{r})}{\partial z} = -\frac{I_0}{k_0}\nabla^2\phi(\mathbf{r}). \tag{2.88}$$

I_0 is the uniform transverse intensity distribution at the plane of focus ($z = 0$). (2.88) shows that the Laplacian of ϕ can be accessed using measurements of the longitudinal gradient of I along z. This gradient can be measured experimentally by moving the sample over small distances (Δz, a fraction of a wavelength) around the focal plane, as demonstrated in Figure 2.17:

$$\frac{\partial I(\mathbf{r},0)}{\partial z} \approx \frac{1}{2\Delta z}\left[I(\mathbf{r},\Delta z) - I(\mathbf{r},-\Delta z)\right] \tag{2.89}$$

$$= g(\mathbf{r}). \tag{2.90}$$

Using the measured derivative, $g(\mathbf{r})$, with (2.88), the inverse Laplace operation can be carried out in the frequency domain, using the differentiation formula of the Fourier Transform[2]:

$$\tilde{\phi}(\mathbf{k}) = \frac{k_0}{I_0}\frac{\tilde{g}(\mathbf{k})}{\mathbf{k}^2}, \tag{2.91}$$

[2]
$$\left(\frac{\partial}{\partial x}\right)^m \left(\frac{\partial}{\partial y}\right)^n \rightarrow (ik_x)^m (ik_y)^n \tilde{f}(k_x, k_y),$$
where (k_x, k_y) are the conjugate variables to (x, y), and $\tilde{f}$ is the Fourier transform of f.

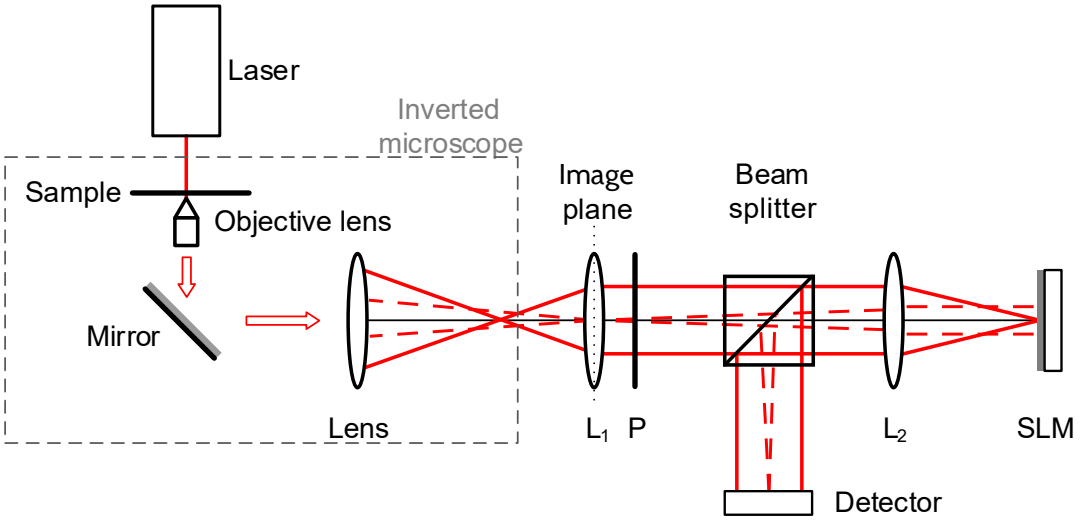

Figure 2.19: The optical setup for Fourier Phase Microscopy. The area inside the grey box is a standard inverted microscope. The scattered field component is indicated with a dotted line, and the unscattered field is the solid line. Lens L_1 is placed in the image plane of the microscope. Polariser P ensures the field polarisation is in line with the SLM. Lens L_2 projects the Fourier transform of the field onto the SLM.

where $\mathbf{k} = (k_x, k_y)$ is the conjugate variable to $\mathbf{r}$, and $\tilde{\phi}$ and $\tilde{g}$ are the Fourier transforms of ϕ and g, respectively.

Applying an inverse Fourier transform to (2.91), back to the spatial domain, creates the quantitative phase image, $\phi(\mathbf{r})$, of the sample.

The benefits of this technique are that it uses a standard bright field microscope, and that as there are no reference beams required, is inherently more stable. As it is a white light technique, it reduces the effect of speckle, improving image quality. However, the technique requires that there are no phase discontinuities, or phase vortices [50].

This technique has been used for non-invasive imaging of cells, such as cheek cells [51] and red blood cells [47]. Figure 2.18 shows how useful a QPI image obtained using TIE is to compare the morphology of the red blood cells.

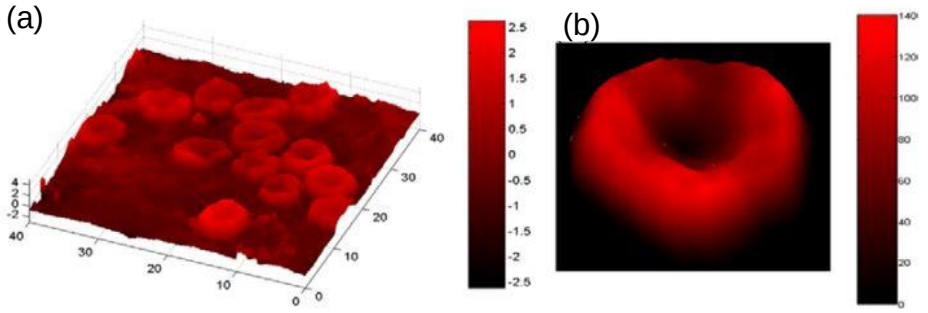

Figure 2.20: (a) Quantitative phase image of a blood smear using Fourier Phase Microscopy (FPM); the colour bar indicates thickness in microns. (b) Surface image of a single red blood cell; the colour bar shows the phase shift in nanometres. [Reproduced from [52]]

2.7.2 Fourier Phase Microscopy (FPM)

FPM [53], a common path method QPI method, uses the idea that the scattered and unscattered light from a sample are used as the object and reference fields of an interferometer. An extension of PCM [21] and Phase-shifting interferometry (PSI) [54], FPM Fourier decomposes an image field into two spatial components that can be shifted in phase with respect to each other with an SLM, obtaining a quantitative phase image of a sample [19].

The experimental setup for Fourier Phase microscopy is shown in Figure 2.19. The SLM is used to controllably shift the phase of the scattered field component $\psi_1(\mathbf{r})$ (dotted line) with the respect to the average field $\psi_0(\mathbf{r})$ (solid line) in four increments of $\pi/2$. This is similar to typical phase-shifting interferometry measurements [55]. The phase difference between ψ_1 and ψ_0 is calculated by combining four recorded interferograms using [19]:

$$\Delta\phi(\mathbf{r}) = \tan^{-1}\left[\frac{I(\mathbf{r};3\pi/2) - I(\mathbf{r};\pi/2)}{I(\mathbf{r};0) - I(\mathbf{r};\pi)}\right] \tag{2.92}$$

where $I(\mathbf{r};\alpha)$ is the interferogram captured by the CCD at the phase shift generated by

the SLM, α. Defining $\beta(\mathbf{r}) = |\psi_1(\mathbf{r})|/|\psi_0(\mathbf{r})|$, then the phase of the image field $\psi(\mathbf{r})$ can be calculated using:

$$\phi(\mathbf{r}) = \tan^{-1}\left[\frac{\beta(\mathbf{r})\sin(\Delta\phi(\mathbf{r}))}{1+\beta(\mathbf{r})\cos(\Delta\phi(\mathbf{r}))}\right]. \tag{2.93}$$

The results of FPM show higher contrast than a standard PCM image, and also provides quantitative information about the sample thickness [53]. The retrieval rate is limited by the refresh rate of the SLM. Four captures are required for each image, corresponding to the four phase shifts required. A faster version of FPM has since been developed, known as *fast* Fourier phase microscopy [56] and using a transmission mode SLM, which gives path length stability of 2 nm at acquisition rates of 10fps. As a common-path method, it also shows high temporal sensitivity.

FPM has been used to demonstrate the existence of dynamic sub-domains within a human blood cell [52]. A typical wide-field FPM image of a fresh human blood smear is shown in Figure 2.20(a). In order to analyse the cell dynamics, the individual cells were segmented from the background, as (b). Other applications include the measurement of cell growth [57], and observing other dynamic phenomena in transparent systems, such as dissolving sugar crystals [56].

2.7.3 Spatial Light Interference Microscopy (SLIM)

SLIM [20] is an add-on module for existing white light Phase Contrast Microscopes (Section 2.6.2) as shown in Figure 2.21. It combines the two ideas of PCM and inline holography [43] to generate a quantitative phase map overlaying the image produced by a phase contrast microscope. In addition to the $\pi/2$ phase shift introduced by the phase contrast microscope, SLIM generates additional phase shifts using the SLM, in increments of $\pi/2$ and records these four images. The phase across the image field

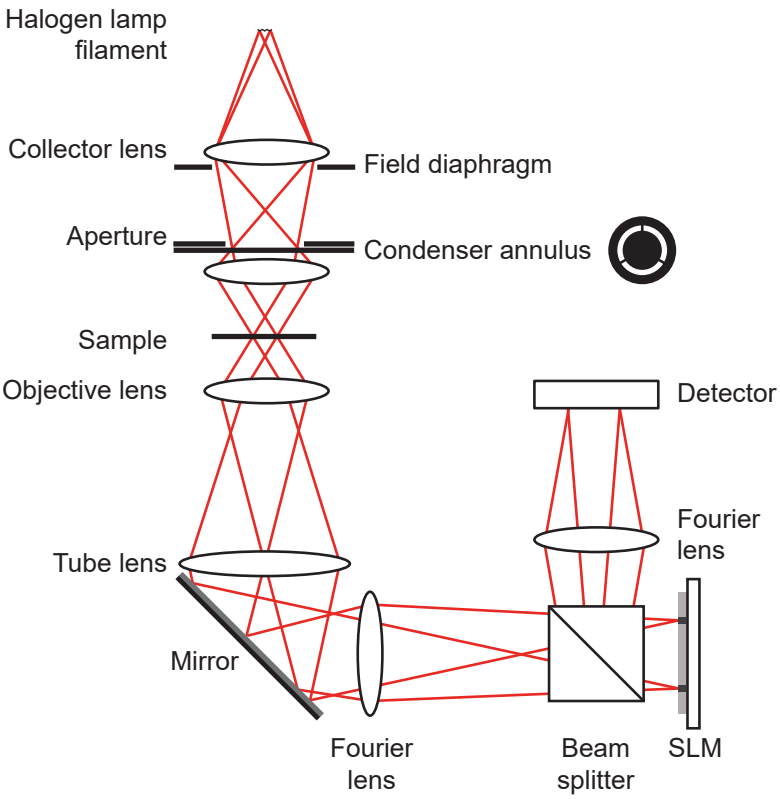

Figure 2.21: The optical setup for Spatial Light Interference Microscopy.

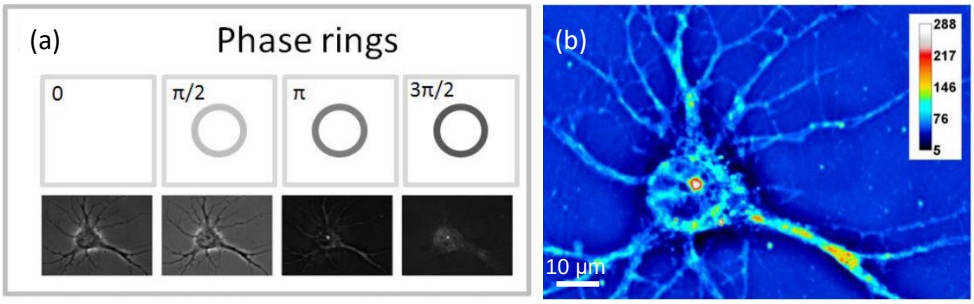

Figure 2.22: Spatial Light Interference Microscopy (SLIM) images of a hippocampal neuron. (a) shows the phase rings which are displayed on the SLM and the corresponding images recorded by the CCD. (b) shows the quantitative phase image produced by SLIM with the colour bar indicating the optical path length in nanometres. [Reproduced from [20]]

cross correlation function is calculated by combining these four images using:

$$\Delta\phi(\mathbf{r}) = \arg\left[\frac{I(\mathbf{r};-\pi/2) - I(\mathbf{r};\pi/2)}{I(\mathbf{r};0) - I(\mathbf{r};-\pi)}\right] \tag{2.94}$$

where $I(\mathbf{r};\alpha)$ is the interferogram captured by the CCD at the phase shift generated by the SLM, α. Defining $\beta(x,y) = |U_1(x,y)|/|U_0|$, i.e. the non-zero frequency component of U divided by the zero frequency component of U, then the phase of the image field $U(x,y)$ can be calculated using:

$$\phi(x,y) = \arg\left[\frac{\beta(x,y)\sin(\Delta\phi(x,y))}{1+\beta(x,y)\cos(\Delta\phi(x,y))}\right]. \tag{2.95}$$

The derivation of that result is as follows [45]:

A homogeneous field, $\psi(\mathbf{r})$, is split into its scattered and unscattered components, as described earlier with Phase Contrast Microscopy (Section 2.6.2):

$$\begin{aligned}\psi(\mathbf{r};\omega) &= \psi_0(\omega) + \psi_1(\mathbf{r};\omega) \\ &= |\psi_0(\omega)|\, e^{i\phi_0(\omega)} + |\psi_1(\mathbf{r};\omega)|\, e^{i\phi_1(\mathbf{r};\omega)}.\end{aligned} \tag{2.96}$$

Interpreting this result as the interference between the spatial average of the field and the spatially varying component, we can then describe the image field as an interferogram, as with Gabor's in-line holography [43]. The cross-spectral density in the space frequency domain can then be written as:

$$W_{01}(\mathbf{r};\omega) = \langle \psi_0(\omega)\cdot\psi_1^*(\mathbf{r};\omega)\rangle\,, \tag{2.97}$$

where * is the complex conjugate and the angular brackets indicate ensemble average. If the power spectrum, $S(\omega) = \left\langle |U_0(\omega)|^2 \right\rangle$, has a mean frequency ω_0, (2.97) can be

factorised as:

$$W_{01}(\mathbf{r};\omega-\omega_0) = |W_{01}(\mathbf{r};\omega-\omega_0)|\, e^{i[\Delta\phi(\mathbf{r};\omega-\omega_0)]}. \tag{2.98}$$

Using the *Wiener-Khintchine* theorem (which proves that the autocorrelation function of a random signal has a Fourier transform, which is also shown to be the power spectrum of the random signal), the temporal cross-correlation function is obtained by Fourier transforming (2.98) as:

$$\Gamma_{01}(\mathbf{r};\tau) = |\Gamma_{01}(\mathbf{r};\tau)|\, e^{i[\omega_o\tau+\Delta\phi(\mathbf{r};\tau)]}, \tag{2.99}$$

where $\Delta\phi(\mathbf{r}) = \phi_0 - \phi_1(\mathbf{r})$ represents the spatially varying phase difference of the cross-correlation function. We can interpret (2.97) by seeing that the spatially varying phase of the cross-correlation function can be retrieved by measuring the intensity at various time delays, τ. This phase information is the same as that of monochromatic light at frequency ω_0. It can be experimentally shown that the autocorrelation function of white light does behave as a monochromatic field oscillating at a mean frequency, ω_0.

When the delay between ψ_0 and ψ_1 is varied, the interference is obtained simultaneously by every pixel of the detector, and so we can consider the detector array to be an array of interferometers. The average ψ_0 is constant across the entire plane and so can serve as a common reference field. As the two fields share a common path, they minimise any vibrational noise in the phase measurement.

From (2.99), the intensity of the field at the image plane is expressed as a function of time delay:

$$I(\mathbf{r};\tau) = I_0 + I_1(\mathbf{r}) + 2\,|\Gamma_{01}(\mathbf{r};\tau)|\cos\left[\omega_0\tau + \Delta\phi(\mathbf{r})\right]. \tag{2.100}$$

Therefore, to quantitatively retrieve the phase, the time delay is varied to get phase

delays of $-\pi, -\pi/2, 0$, and $\pi/2$ (as $\omega_0\tau_k = k\pi, k = 0,1,2,3$). An intensity map is recorded for each delay, and combined as:

$$I(\mathbf{r};0) - I(\mathbf{r};-\pi) = 2\left[\Gamma(0) + \Gamma(-\pi)\right]\cos\left[\Delta\phi(\mathbf{r})\right] \tag{2.101}$$

$$I(\mathbf{r};-\frac{\pi}{2}) - I(\mathbf{r};\frac{\pi}{2}) = 2\left[\Gamma(-\frac{\pi}{2}) + \Gamma(\frac{\pi}{2})\right]\cos\left[\Delta\phi(\mathbf{r})\right]. \tag{2.102}$$

For time delays around $\tau = 0$ that are comparable to the optical period, $|\Gamma|$ can be assumed to vary slowly, and that $\Gamma(0) + \Gamma(-\pi) = \Gamma(-\frac{\pi}{2}) + \Gamma(\frac{\pi}{2})$. Equations (2.101) and (2.102) can be combined and rearranged to give the spatially varying phase of the cross correlation function Γ:

$$\Delta\phi(\mathbf{r}) = \arg\left[\frac{I(\mathbf{r};-\pi/2) - I(\mathbf{r};\pi/2)}{I(\mathbf{r};0) - I(\mathbf{r};-\pi)}\right]. \tag{2.103}$$

Defining $\beta(\mathbf{r}) = |U_1(\mathbf{r})|/|U_0|$ then the phase across the image field, U(**r**) is:

$$\phi(\mathbf{r}) = \arg\left[\frac{\beta(\mathbf{r})\sin(\Delta\phi(\mathbf{r}))}{1 + \beta(\mathbf{r})\cos(\Delta\phi(\mathbf{r}))}\right]. \tag{2.104}$$

Wang [20] has developed SLIM as a QPI technique for observing cell cultures from rat brains. As it is a white light technique, the short coherence length of the light source used means that the images produced are speckle free. Because the quantitative information can be overlayed on a fluorescent image, it can also enable multimodal investigations, such as molecular specificity. Figure 2.22 shows a quantitative phase image generated using SLIM. The technique is also relatively fast, with a frame rate of 2.6 frames/s that could be increased with a faster phase modulator and camera.

SLIM has already found a large number of applications, mainly in the biological sciences. It has been used in areas such as measuring density fluctuations to provide mechanical information on cellular structures [58], and topography of cells [59]. Through slight modification, known as Spatial Light Interference Tomography (SLIT),

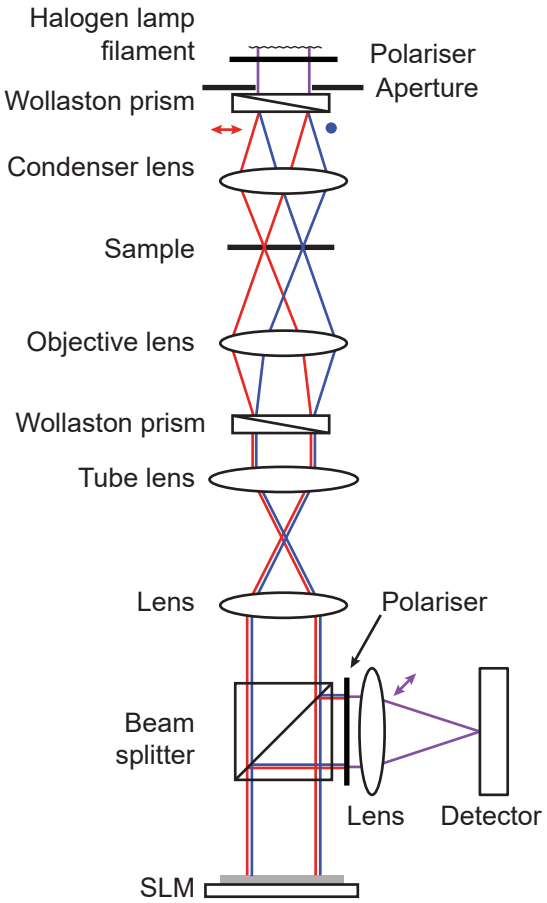

Figure 2.23: The optical setup for Gradient Light Interference Microscopy (GLIM).

it has been used to perform three dimensional tomography on living cells [60]. As it is an add on module for conventional phase contrast microscopes, it is possible to perform long term cell imaging [32]. Clinical applications have also started to be explored, with blood screening [61] and cancer diagnosis [62], [63].

2.7.4 Gradient Light Interference Microscopy (GLIM)

GLIM [64] is a relatively new technique, advancing the DIC method described in Section 2.6.2. The technique is an add-on to a standard DIC microscope, as in Figure 2.23. The added module contains an SLM, which displays 4 different phase

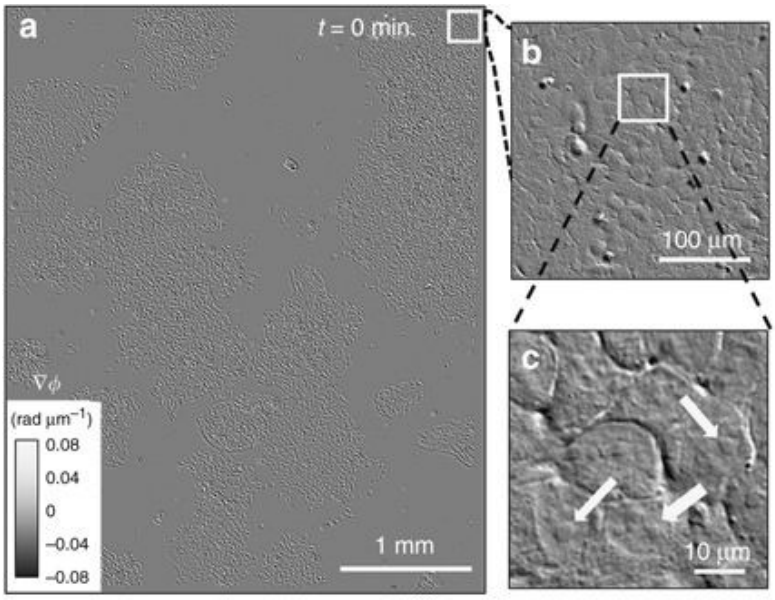

Figure 2.24: A quantitative phase image of HeLa cells produced with GLIM. (b) and (c) are zoomed in regions of (a), which shows a mosaicked field of view composed of 16×20 tiles. The colour bar applies to all the figures. [Reproduced from [64]]

retardations ($\phi_n = n\pi/2$, with n = 0,1,2,3). The camera then captures an image for each phase change on the SLM. By combining the four images with the following equation, the phase gradient for the sample can be generated.

$$\nabla\phi(\mathbf{r}) = \frac{\arg\{[I_4(\mathbf{r}) - I_2(\mathbf{r})], [I_3(\mathbf{r}) - I_1(\mathbf{r})]\}}{\delta r} \tag{2.105}$$

The mathematical basis for GLIM is as follows. In the same way as DIC, the GLIM microscope generates two replicas of the image field, cross-polarised and shift transversely by a distance smaller than the diffraction spot. GLIM, however, removes the second polariser and instead spatially Fourier transforms the fields onto an SLM. This SLM has its active axis parallel to one of the fields. It then applies a phase retardation to that field of $\phi_n = n\pi/2$, with n = 0, 1, 2, 3. The other field, polarised at a different angle, is left unmodified. Both fields are again Fourier transformed onto the detector plane. A linear polariser, at 45^o to both fields, combines both fields at the

detector, resulting in a coherent superposition:

$$\psi_n(\mathbf{r}) = \psi(\mathbf{r}) + \psi(\mathbf{r} + \delta\mathbf{r})e^{i\phi_n}, \tag{2.106}$$

where $\delta\mathbf{r}$ is the spatial offset between both fields and $\psi(\mathbf{r})$ is the image field. The intensity image, as captured by the detector, at each phase shift applied to the SLM, n, is given as:

$$I_n(\mathbf{r}) = |\psi_n(\mathbf{r})|^2 \tag{2.107}$$

$$I_n(\mathbf{r}) = I(\mathbf{r}) + I(\mathbf{r} + \delta\mathbf{r}) + 2|\gamma(\mathbf{r}, \delta\mathbf{r})| \cos\left[\phi(\mathbf{r} + \delta\mathbf{r}) - \phi(\mathbf{r}) + \phi_n\right], \tag{2.108}$$

where $I(\mathbf{r})$ and $\phi(\mathbf{r})$ are the intensity and phase of the image field, respectively. γ is the mutual intensity between the two spatially offset fields:

$$\gamma(\mathbf{r}, \delta\mathbf{r}) = \langle \psi^*(\mathbf{r})\psi(\mathbf{r} + \delta\mathbf{r})\rangle. \tag{2.109}$$

Given the four intensity images, for $n = 0, 1, 2, 3$, it is possible to solve for the phase gradient. Identifying that the phase difference, $\Delta\phi = \phi(\mathbf{r} + \delta\mathbf{r}) - \phi(\mathbf{r}) \approx \nabla(\phi)\delta\mathbf{r}$, where $\nabla(\phi)$ is the gradient of the phase in the direction of the shift, the four intensity frames can be combined to give:

$$\nabla\phi(\mathbf{r}) = \frac{\arg\{[I_4(\mathbf{r}) - I_2(\mathbf{r})], [I_3(\mathbf{r}) - I_1(\mathbf{r})]\}}{\delta r} \tag{2.110}$$

This equation can therefore be used to calculate quantitatively the gradient of the phase along the direction of the shift. The phase value, $\phi(\mathbf{r})$ can be obtained by integrating along the gradient direction, relative to a known position $\phi(0, y)$, for example along the x-axis:

$$\phi(\mathbf{r}) = \int_0^x \left[\nabla_x\phi(x', y)\right] dx' + \phi(0, y). \tag{2.111}$$

As a common-path white light method, it also has nanometre path-length stability and is speckle free. However, as it produces a phase gradient, some integration, with a known reference point, is required in order to obtain a phase image. It is also strongly reliant of the phase accuracy of the SLM.

GLIM has been demonstrated as a useful tool for imaging bovine embryos over several days [13], [64]. This is a particularly good use of QPI as it is a non-destructive way of performing tomography of living cells. Figure 2.24 shows a quantitative phase image of a HeLa cell culture produced by GLIM.

2.8 Ptychography

The technique used predominately in this thesis is Ptychography, and so greater detail into the ideas behind this technique are given here. Ptychography is a coherent diffractive imaging technique that uses a source of radiation, a object that scatters the illumination, and a detector to generate several diffraction patterns in order to recover the complex representation of the object.

There are two procedures required in generating a QPI image using ptychography, which can also be thought of as an information based way to solve the phase problem:

1. **Ptychographic data collection.** Carried out on an optical bench or in a purpose-built microscope. This part of ptychography generates the ptychographical dataset from a sample. In this step the optics *encodes* the complex information about the object.

2. **Ptychographic data reconstruction.** This part is carried out on a computer, using algorithms to reconstruct the sample from the ptychographic al dataset. In this step the algorithms *decode* the dataset to generate the complex image of the object.

These can be considered essentially separate operations, and many different procedures have been invented for both. One technique for data collection can be used

with any of the techniques for reconstruction, and *vice versa*. In general, for a technique to be considered as ptychography, Rodenburg and Maiden [65] consider that these five properties need to be met:

1. One of the optical components (generally the object) must move laterally relative to the other components.

2. The detector must be placed in an optical plane in which the exit-wave from the illumination and object has intermixed to create an interference pattern.

3. The detector collects at least two interference patterns, arising from at least two known different lateral physical offsets of the illumination with respect to the object.

4. The source of the radiation must be substantially (but not necessarily wholly) coherent. This means that the interference is stable.

5. The complex image of the object is generated by a computer algorithm, which solves for the complex wavefield incident on the detector, solving the phase problem.

The development of ptychography started with this line of thought [66]: a small region of an object is illuminated by a probe (utilising language of the electron microscope), creating an exit wave originating from the other side of the object. Downstream from the object, the diffraction pattern is recorded (in reciprocal space), allowing the amplitudes of adjacent points of the exit wave to interfere with each other. From this single diffraction pattern, the phase difference between these amplitudes (with an uncertainty of the complex conjugate) can be estimated. By moving the probe to a new position, but retaining some overlap with the previous position, the complex conjugate ambiguity can be resolved. This is because a shift in probe position is equivalent to introducing a phase ramp in reciprocal space. This

concept was first proposed by Hoppe [67], [68]. Although the language of this setup originates from electron microscopy, the 'probe' can refer to any mode of localised illumination (visible light, x-ray, or electron).

This idea was expanded from two diffraction patterns to multiple overlapping diffraction patterns. This can be achieved by moving the illumination across a grid of overlapping positions over the object. Using these multiple overlapping positions allows a wide field of view over the object, but also requires the algorithm to find a solution that is consistent between the positions, which is computationally difficult. The first ptychography experiment of this kind was performed by Rodenburg *et al.* [69]. Iterative algorithms have made ptychography with multiple diffraction patterns computationally viable, and result in a high resolution, large field of view images.

The next two sections will investigate some of the different experimental configurations that fulfil the above requirements, before looking at the iterative algorithms used to decode the dataset.

2.8.1 Ptychographical experimental configurations

One of the features of ptychography is that it can adopt different configurations. Each configuration has its own advantages and disadvantages, which generally should be chosen to match experimental requirements. This section will describe four experimental configurations used to generate a ptychographic dataset that are relevant to this work.

Standard ptychography

The concept of standard ptychography is to scan a localised coherent probe beam over the object, as shown in Figure 2.25 [65]. This probe illuminates a small region of the object. The diffraction pattern at this scan position is captured by the detector some

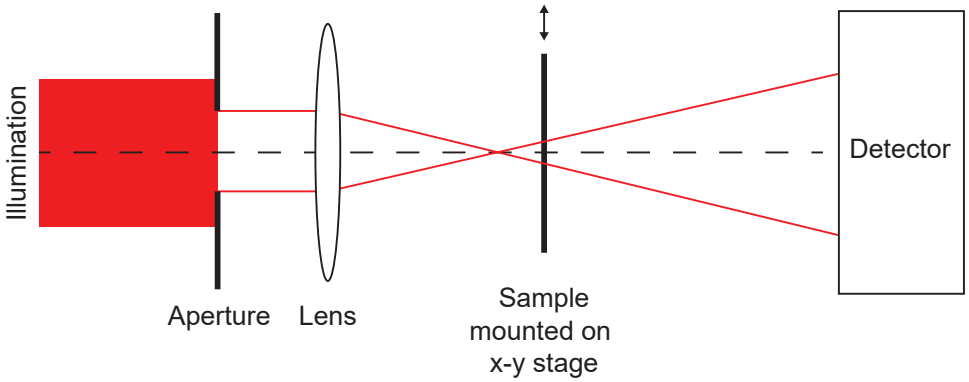

Figure 2.25: A typical setup for standard transmissive ptychography. A uniform coherent illumination passes though an aperture to create a focussed 'probe' using a lens. The sample is positioned slightly downstream of the focus of the beam. The probe illuminates a small region of the sample, which is mounted on an $x - y$ stage. Further downstream, the detector collects the interference pattern. The sample is then moved laterally by an amount smaller than the probe size, until all the interference patterns are captured.

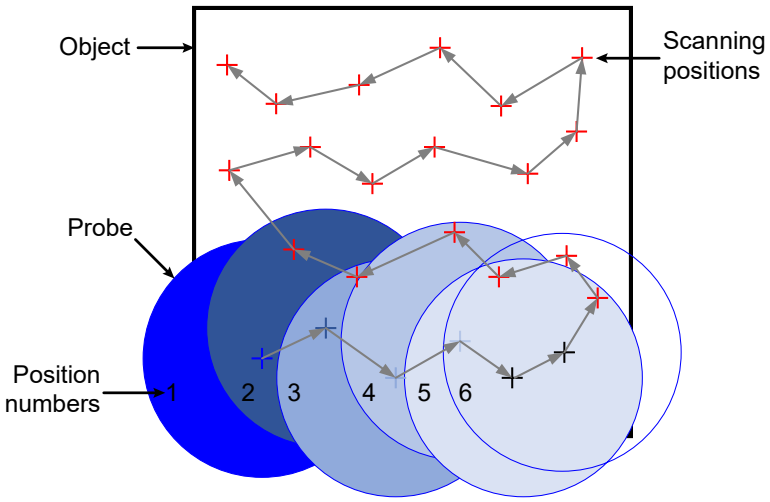

Figure 2.26: An example ptychographical scan pattern of 24 (6×4) diffraction pattens. The probe scans across the object in pseudo-random positions within a grid. Each probe overlaps with the previous position. The diffraction pattern is captured by the detector after each movement.

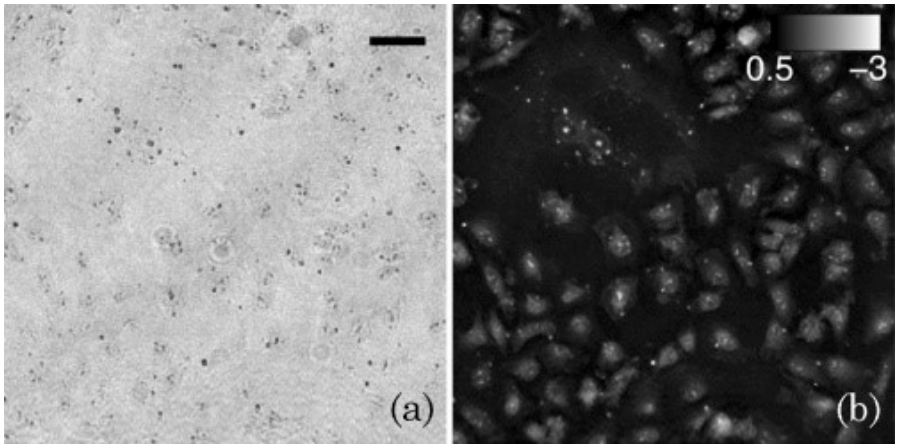

Figure 2.27: Reconstructed image of cancerous human lung cells from standard ptychography. (a) is the amplitude of the reconstruction, showing very little contrast. (b) is the phase of the reconstruction, clearly showing the structure of the cells. Scale bar = 50 µm. [Reproduced from [70]]

distance downstream. The sample is then laterally translated, relative to the probe, through a known discrete grid of positions. In order to gain redundancy between the measurements, the step size between positions must be smaller than the size of the probe. This forms an overlapping patchwork of illumination over the object, as shown in Figure 2.26. This technique is also known as defocused probe ptychography, for obvious reasons.

Standard ptychography tends not to be used for bio-imaging as the time taken to scan the probe across the sample takes too long. However, Maiden *et al.* [70] have demonstrated ptychography with cancerous human lung cells, in Figure 2.27. These images demonstrate the clear advantage in a phase image, when wanting to observe cell structures.

Fourier ptychography

Fourier ptychography [72]–[74] inverts the principle of traditional ptychography by positioning the probe in reciprocal space and recording the intensity patterns in real

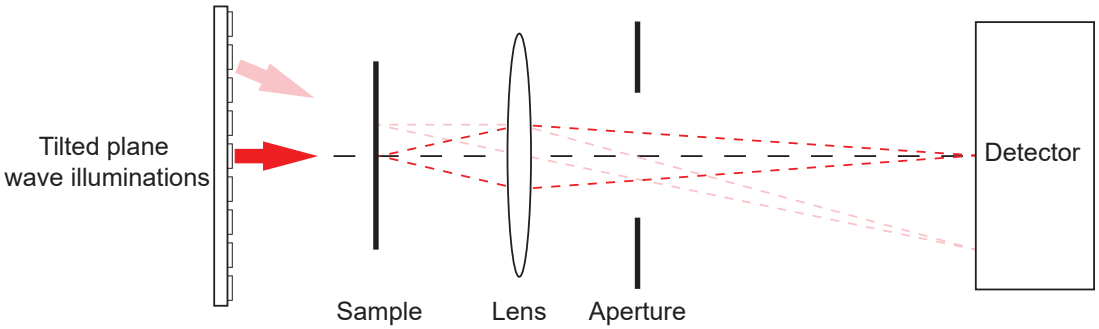

Figure 2.28: The experimental setup for Fourier Ptychography. Instead of moving the sample, like in standard ptychography, the thin sample is illuminated by several plane waves with different angles. This is typically done using an array of LEDs. The aperture is located in the back focal plane of the lens, and the detector in the image plane. This means that tilting the illumination angle has the effect of shifting the diffraction pattern across the aperture.

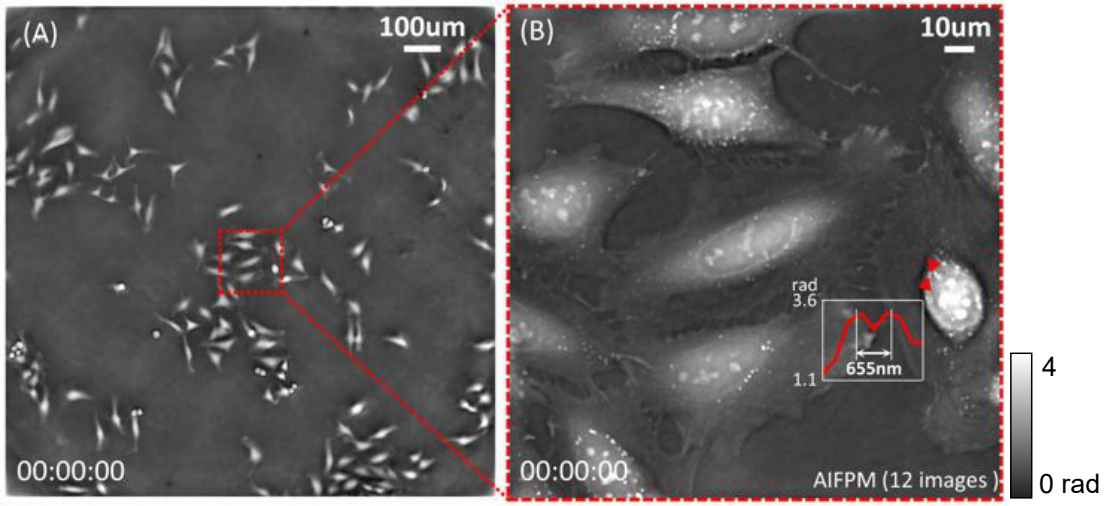

Figure 2.29: (A) Phase reconstruction of human cervical adenocarcinoma epithelial (HeLa) cells captured using Fourier ptychography. (B) Enlarged image of the red-boxed region in (A). [Reproduced from [71]]

space [65]. The probe is formed in reciprocal space by illuminating the object from different angles (most commonly by using an array of LEDs) and placing an aperture in the back focal plane of the lens, as shown in Figure 2.28. Tilting the illumination corresponds to a translation of the frequency spectrum in the back focal plane of the lens. The aperture filters out the high frequencies from the spectrum and the detector, located in the image plane of the lens, captures a low resolution image of the object. By choosing the angles of the illumination so that there is sufficient overlap of the spectrum at the aperture, a ptychographic scan can be performed. It can therefore be seen that the aperture behaves as the reciprocal of the localised illumination in standard ptychography, and the object is the frequency spectrum of the sample.

As this is the inverted form of ptychography, some of the properties are also reversed. The field of view is determined by the size of the detector. Each of the captured images by the detector contain the different frequency information of the sample, as the spectrum 'probe' is scanned. This means that the larger the angle of the illumination, the higher the frequency captured.

There are several key differences between Fourier and standard ptychography, that are useful to know when deciding which technique to use. In Fourier ptychography, as the detector captures an image of the sample, rather than its diffraction pattern, the dynamic range requirement on the detector is reduced. However, at the higher tilted angles, the amplitude of the scattered illumination reaching the detector is reduced, meaning that exposures at these angles will need to be higher. One of the assumptions required by the Fourier ptychography setup is that the sample is optically thin. This is because at the higher tilt angles it would not be possible to model the interaction of a thicker sample with the illumination with a multiplication. This may limit the type of samples used, unless multi-slice methods are employed [75]. One of the key advantages of Fourier ptychography is that the different angles of illumination can be created by an array of LEDs. This means that neither the illumination or the object need to move. This

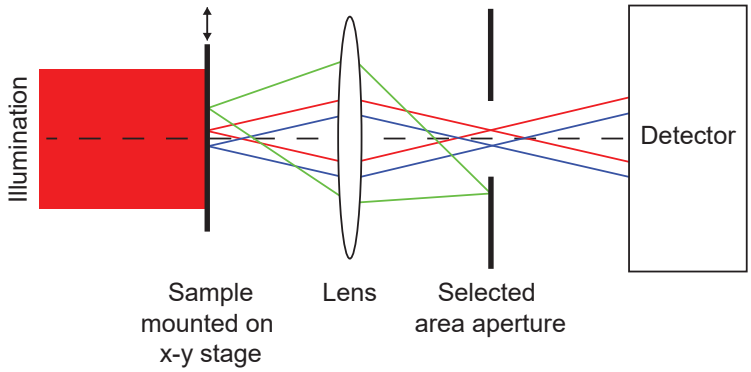

Figure 2.30: The experimental setup for selected area ptychography. The sample is uniformly illuminated and the lens focuses an image at the plane where the selected area aperture is located. The resulting diffraction pattern is recorded downstream by the detector. The sample is moved laterally, so that its wavefield moves across the aperture, which acts as a virtual probe.

saves time, as motorised stages take time to move positions. Additionally, mechanical stages tend to suffer from hysteresis, although this can be corrected in software (see Section 2.8.3). For bioimaging, it is useful to keep samples still or to prevent sudden rapid movements which may disrupt the sample.

In the area of bioimaging, for the reasons described above, Fourier ptychography has been demonstrated to be particularly good at capturing high-speed in vitro quantitative phase videos of cells, achieving maximum frame rates of 1.25Hz [76]. 3D Fourier ptychography has begun to reduce the limitation on the thickness requirements of the sample, with a multislice approach [75]. Fourier ptychographic images however, tend to be prone to low spatial frequency artefacts [71], as can be seen in Figure 2.29.

Selected area ptychography

In selected area ptychography, a standard microscope with coherent uniform illumination forms a conventional image. An aperture is placed in the image plane of the microscope, and the diffraction pattern is recorded some distance downstream, as

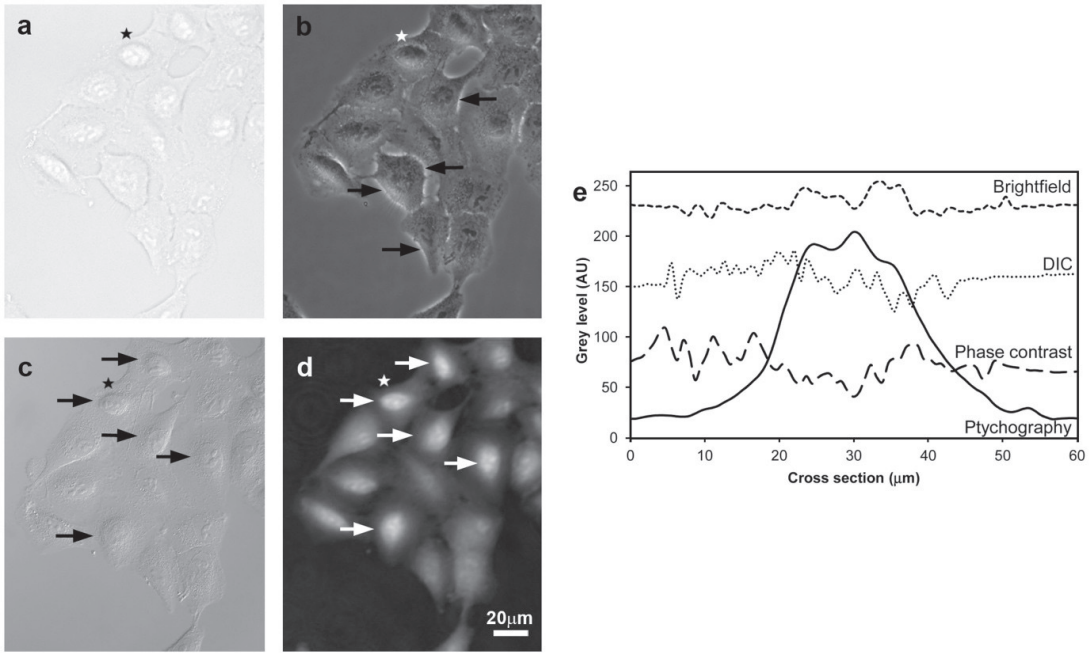

Figure 2.31: A comparison of contrast enhancing techniques of Adherent human alveolar epithelial (A549) cells (a) Brightfield image defocused to reveal cell edges. (b) Phase Contrast Microscopy (PCM) image. (c) Differential Interference Contrast (DIC) microscopy image. (d) Selected area ptychographic image. All images (a-d) are recorded from the same field of view. (e) The variation in grey level across a cell (marked by an asterisk) for all 4 imaging modalities. [Reproduced from [25]]

shown in Figure 2.30. The sample is mounted on a motorised stage, and is laterally translated so that the image of the sample moves across the aperture. This image of the sample is therefore the 'object', and the aperture is the illumination function.

Selected area ptychography can image a very large field of view, whilst retaining the full coherent resolution capability of the objective lens to give high resolution images [65].

Marrison [25] uses selected area ptychography and the Extended Ptychographical Iterative Engine (ePIE) algorithm to image cells. Their experimental setup is typical for transmissive selected area ptychography. They report that this technique is particularly suitable for reporting cell changes, such as mitosis, apoptosis and cell differentiation, especially with the ability to image cells in tissue culture plastic ware

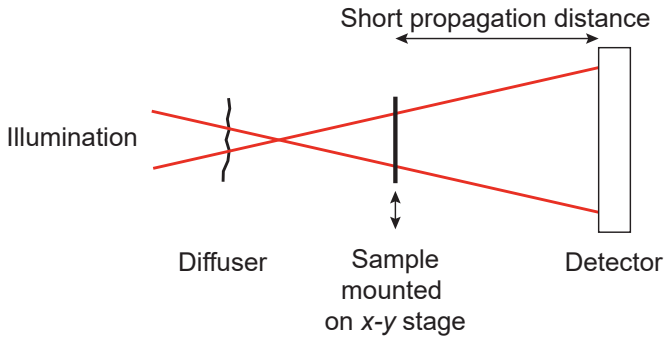

Figure 2.32: The experimental setup for near-field ptychography in the X-ray domain, as demonstrated by Stockmar *et al.* [77]. A diffuser is illuminated and projected onto the sample.

and focus after acquisition. In addition, as the images are high contrast and artefact free, it is possible to use them for segmentation and image analysis. A comparison of the contrast enhancement techniques discussed earlier in this thesis alongside the selected area ptychography result for a bio-image can be seen in Figure 2.31.

Near-field ptychography

Near-field ptychography has been developed in the x-ray regime [77], [79]. There are a few key differences between standard ptychography and near-field ptychography [65].

1. The propagation distance between the exit wave of the combined sample and illumination is greatly reduced. This requires that the Fresnel number of the diffraction is high.

2. The illumination, whilst remaining static, must deviate strongly from a uniform plane wave. This can be done be placing a diffuser in the path of the illumination. This is necessary as it the source of the diversity between diffraction patterns.

3. A larger area of the sample is illuminated at one time.

The experimental setup to achieve these aims in x-ray near-field ptychography is shown by Stockmar *et al.* [77], [80], [81] in Figure 2.32. The wavefield emitted from

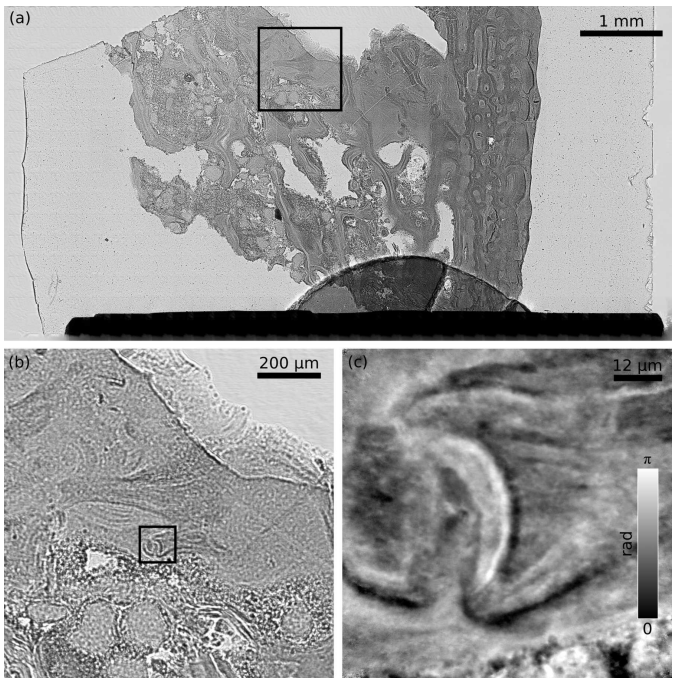

Figure 2.33: X-ray reconstructions of a fossil fish bone. (a) Transmission image obtained with parallel-beam holography data; arbitrary units. (b) Magnified view from box in (a). (c) Phase image from the near-field ptychographic reconstruction of a scan performed on the area in the box of (b). [Reproduced from [78]]

a diffuser, illuminated by the x-rays, is focussed to create a virtual point source. The expanding beam illuminates a large area of the sample to create a combined exit-wave that is propagated a short distance to the detector. It can therefore be seen why there must be a diffuser in place–if the sample was just illuminated by a plane wave, then was moved laterally with respect to the illumination, the interference pattern on the detector would also just move laterally, not giving any additional information. The diffuser provides the diversity between the diffraction patterns. In this work they demonstrate that by using ptychography in the near-field they can reduce the number of interference patterns needed to just 16, in order to image an optically thick sample. The field of view is large, even when only a few diffraction patterns are captured. Simulation work [82] has further demonstrated that at least 6 interference patterns are required, as well as some other key experimental parameters.

2.8.2 The key experimental parameters

For all these different experimental configurations, there is a set of core experimental parameters that should be considered when designing a ptychographic experiment [65]:

1. **Number of diffraction patterns:** As has been shown, ptychography can work with a minimum of two diffraction patterns. There is no theoretical upper limit on the number of diffraction patterns. It may be useful to capture more diffraction patterns to extend the field of view of the sample in real-space ptychography, or to increase the frequencies captured in Fourier ptychography. However, the obvious trade off is that the more diffraction patterns captured, the more data is collected. This means that the acquisition time required for a single ptychographic image is lengthened, and that the reconstruction time is increased. There may also be memory limitations for very large datasets.

2. **Scan pattern:** In which pattern should the sample be moved to with relation to the illumination? The most obvious, and simplest arrangement is a grid, or raster scan. This allows for easy analysis of the amount of overlap between diffraction patterns. However, this can suffer from the 'raster scan pathology' [83], where a periodic scan will tend to produce image artefacts at that periodicity. This should be avoided if possible, by randomly offsetting the positions on the grid (whilst maintaining a suitable overlap), or by using a circular pattern. It might also be important to consider how to increase the efficiency of the stage movements, by creating the shortest path between the set of points, to reduce the movement of the sample.

3. **Scan step size:** As was shown previously, the diffraction patterns need to overlap. The amount of overlap can affect the reconstruction results and is defined as:

$$\text{Overlap}(\%) = \left(\frac{\text{(Diameter of probe)-(Step size)}}{\text{(Diameter of probe)}} \right) * 100. \tag{2.112}$$

   At the extremes, at 100% overlap all the probe positions are the same, and so all the diffraction patterns are identical, meaning that there is no diversity between them but considerable redundancy. This dataset contains no probe shift information and so there is difficulty in reconstruction. For large amounts of overlap, the field of view would also be small. At 0% overlap, the diffraction patterns will not overlap, and so do not fulfil the requirements of ptychography. Smaller amounts of overlap will generate larger fields of view, but because of the geometry of overlapping circles, the overlap must be at least 30% so that each pixel of the object is illuminated once.

4. **Probe size:** The size of the probe on the sample does not constrain the minimum sampling condition, as long as the sampling condition at the detector is maintained [65]. Using a smaller probe size will however require more

diffraction patterns to cover the same field-of-view.

5. **Exposure time:** This is the amount of time that the detector captures the diffraction pattern. It is important to set this correctly with the brightness of the illumination so as not to over- or under-expose the captured image. The main balance to be struck when choosing an exposure time are reducing the signal to noise ratio of the images while increasing the frame rate of acquisition. For diffraction images with a high dynamic range requirement, such as focus probe ptychography, it may be necessary to capture images with different length exposures and combine them to generate a final image.

6. **Camera length:** This refers to the propagation distance between the exit wave and the detector. A shorter camera length means that the angle subtended by one detector pixel will be bigger, reducing the maximum probe size allowed for sufficient sampling (Section 2.5.1). It also means that the angle subtended by the whole detector will be bigger, causing a decrease in the pixel size of the reconstructed image; from (2.38) and using the paraxial approximation ($\theta \approxeq \sin\theta = U/z$)

$$\Delta x = 1/f \tag{2.113}$$

$$= \frac{\lambda z}{U}, \tag{2.114}$$

where z is the camera length and U is the size of the detector.

Once the Fresnel number, N_F of the setup has been calculated using (2.29), the type of propagator for use in the reconstruction algorithms can be determined:

- $N_F > 1$: Fresnel propagator (Section 2.4.2)
- $N_F \ll 1$: Fraunhofer propagator (Section 2.4.3)
- $N_F \gg 1$: Angular spectrum propagator (Section 2.4.4)

2.8.3 Iterative ptychographical reconstruction algorithms

There are many different ways to process a ptychographical dataset in order to recover a complex image of an object A survey by Marchesini demonstrates the variety of these techniques [84]. Important reconstruction techniques include Difference Map (DM) [83], Conjugate Gradient (CG) [85] and Relaxed Averaged Alternating Reflections (RAAR) [86]. This thesis will just focus on a subset of iterative ptychographical reconstruction algorithms, the Ptychographical Iterative Engine (PIE) family.

Ptychographical Iterative Engine (PIE)

In order to solve the inverse problem to retrieve the complex image of the object from the ptychographical dataset, it is necessary to apply some constraints to the problem. These constraints include the data itself and also *a priori* information (which includes the positions of the illumination relative to the object), and are used to help the algorithm find the solution. The first algorithm developed in the PIE family was by Faulkner and Rodenburg [87], but required that the probe consisted of a hard edge. This is very rarely the case and so it was further expanded to create the PIE algorithm [69]. This algorithm can work with a probe that doesn't have a hard edge, which is more realistic, but the probe must be accurately determined in both amplitude and phase prior to reconstruction. The probe needs to computationally estimated from knowledge of the aperture, and a physical measurement of the distance between the aperture and the object. The algorithm for PIE is shown below, as well as a flowchart in Figure 2.34.

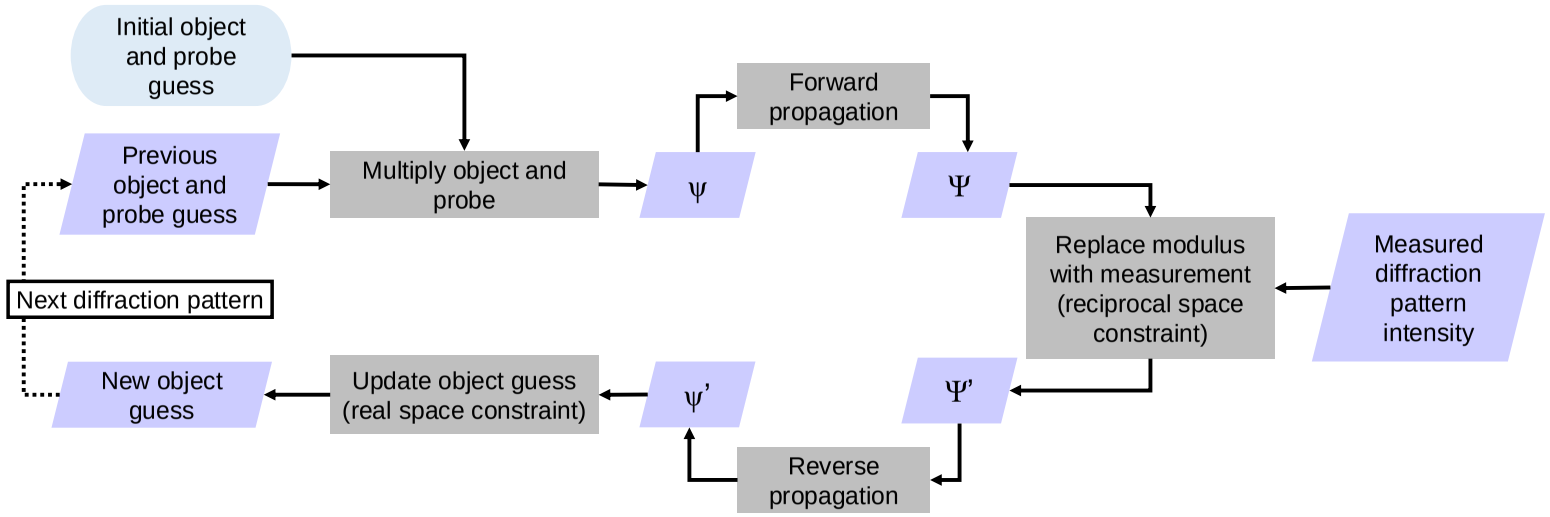

Figure 2.34: Algorithm flowchart of the Ptychographical Iterative Engine. Starting with an initial guess of the probe and object, the algorithm repeats until the error in the diffraction plane is sufficiently low.

PIE algorithm:

The following symbols are assigned:

P	Known illumination function (historically the probe)
O	Object transmission function
ψ	Exit wave (with ′ to indicate the updated wave)
Ψ	Diffraction pattern (with ′ to indicate the updated wave)
I	Measured intensity (from the detector)
$j \in [0 \dots J]$	Diffraction pattern number
	(usually after the J diffraction patterns have been ordered randomly)
n	Iteration number
$\mathbf{r}$	Real space coordinates
$\mathbf{R_j}$	Known position for diffraction pattern j (e.g. the stage position)
$\mathbf{k}$	Reciprocal space coordinates
$\mathcal{P}_z$	Propagator (e.g. Fresnel, Fraunhofer, Fourier, Angular Spectrum), over a distance z
α	Object update parameter

1. For iteration $n = 0$, make initial guess of the object transmission function $O_j(\mathbf{r})$.

2. Multiply the current guess of the object by the illumination at the current position ($P(\mathbf{r} - \mathbf{R}_j)$) to produce the guessed exit wave at position $\mathbf{R}_j$:

$$\psi_j(\mathbf{r}, \mathbf{R}_j) = O_j(\mathbf{r})P(\mathbf{r} - \mathbf{R}_j). \tag{2.115}$$

   This multiplicative assumption can be considered valid for 'thin' objects [88].

3. Propagate the exit wave to the detector to create a guessed diffraction pattern. The choice of propagator, as well as the distance to propagate will depend on the experimental setup, as outlined in Section 2.4.2, Section 2.4.3, or Section 2.4.4.

$$\Psi_j(\mathbf{k}) = \mathcal{P}_z \left[\psi_j(\mathbf{r}, \mathbf{R}_j)\right]. \tag{2.116}$$

4. Apply a reciprocal space constraint by replacing the modulus of the guessed diffraction pattern with the square root of the measured intensity at position $\mathbf{R}_j$, while retaining the phase, $\theta_j(\mathbf{k}) = \arg(\Psi_j(\mathbf{k}))$:

$$\Psi'_j(\mathbf{k}) = \sqrt{I_j(\mathbf{k})} e^{i\theta_j(\mathbf{k})}. \tag{2.117}$$

5. Reverse propagate this updated diffraction pattern to give an updated exit wave:

$$\psi'_j(\mathbf{r}) = \mathcal{P}_z^{-1} \left[\Psi'_j(\mathbf{k})\right] \tag{2.118}$$

6. Update the guess of the object in the area covered by the illumination, using the object update function:

$$O_{j+1}(\mathbf{r}) = O_j(\mathbf{r}) + \alpha \frac{|P(\mathbf{r} - \mathbf{R}_j)|}{|P(\mathbf{r} - \mathbf{R}_j)|_{\max}} \frac{P^*(\mathbf{r} - \mathbf{R}_j)}{(|P(\mathbf{r} - \mathbf{R}_j)|^2 + \epsilon)} \left[\psi'_j(\mathbf{r} - \mathbf{R}_j) - \psi_j(\mathbf{r} - \mathbf{R}_j)\right] \tag{2.119}$$

This update equation is the key to the PIE algorithm. ϵ is a small constant to avoid division by zero. $\alpha \in [0, 1]$ is known as the object update parameter, and controls the feedback loop. A larger value of α will speed convergence, at the higher risk of being caught in a local minima.

7. Get the next recorded diffraction pattern, $j = j + 1$, or if $j = J$ then start the next

iteration:

$$n = n + 1$$

$$j = 0$$

8. Repeat steps 2-7 for a fixed number of iterations, or until the error is sufficiently small. A suitable measure for the error is the sum squared error (SSE):

$$\text{SSE} = \frac{(I_j(\mathbf{k}) - |\Psi_j(\mathbf{k})|^2)}{N}, \tag{2.120}$$

where N is the number of pixels of the measured diffraction pattern.

The PIE algorithm was demonstrated with visible light [89], [90], however any errors in the initial model of the probe wavefront result in errors in the final reconstruction. Additionally, there may be some scenarios where it is not possible to accurately characterise the probe before the experiment.

Extended Ptychographical Iterative Engine (ePIE)

In order to remove the requirement of a known probe, the ePIE algorithm was developed [91]. This algorithm, similar in form to the PIE algorithm solves for both the object and the probe.

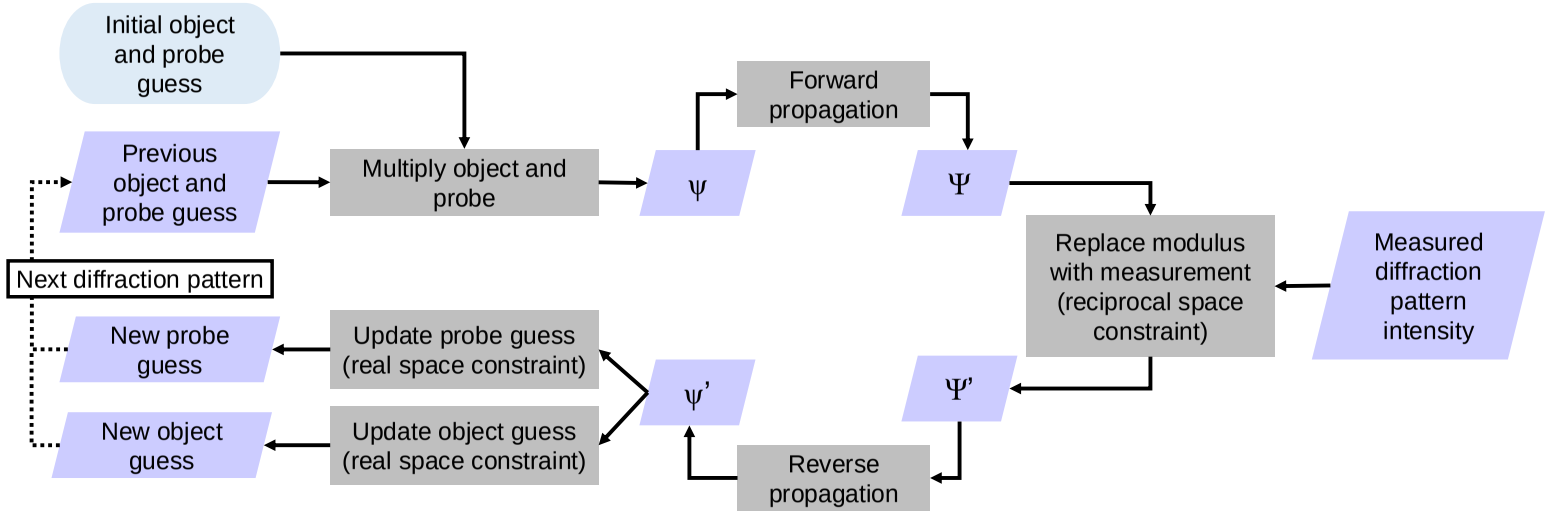

Figure 2.35: Algorithm flowchart of the extended Ptychographical Iterative Engine. Starting with an initial guess of the probe and object, the algorithm repeats until the error in the diffraction plane is sufficiently low.

ePIE algorithm:

The following symbols are assigned:

P	Illumination function (historically the probe)
O	Object transmission function
ψ	Exit wave (with ′ to indicate the updated wave)
Ψ	Diffraction pattern (with ′ to indicate the updated wave)
I	Measured intensity (from the detector)
$j \in [0 \dots J]$	Diffraction pattern number
	(usually after the J diffraction patterns have been ordered randomly)
n	Iteration number
$\mathbf{r}$	Real space coordinates
$\mathbf{R}$	Known current position (e.g. the stage position)
$\mathbf{k}$	Reciprocal space coordinates
$\mathcal{P}_z$	Propagator (e.g. Fresnel, Fraunhofer, Fourier, Angular Spectrum), over a distance z
α	Object update parameter
β	Probe update parameter

1. For iteration $n = 0$, make initial guess of the object transmission function $O_j(\mathbf{r})$.

2. Multiply the current guess of the object by the illumination at the current position ($P_j(\mathbf{r} - \mathbf{R}_j)$) to produce the guessed exit wave at position $\mathbf{R}_j$:

$$\psi_j(\mathbf{r}) = O_j(\mathbf{r})P_j(\mathbf{r} - \mathbf{R}_j). \tag{2.121}$$

   This multiplicative assumption can be considered valid for ‘thin’ objects.

3. Propagate the exit wave to the detector to create a guessed diffraction pattern. The choice of propagator, as well as the distance to propagate will depend on the experimental setup, as outlined in Section 2.4.2, Section 2.4.3, or Section 2.4.4.

$$\Psi_j(\mathbf{k}) = \mathcal{P}_z\left[\psi_j(\mathbf{r})\right]. \tag{2.122}$$

4. Apply a reciprocal space constraint by replacing the modulus of the guessed diffraction pattern with the square root of the measured intensity at position $\mathbf{R}_j$, while retaining the phase, $\theta_j(\mathbf{k}) = \arg(\Psi_j(\mathbf{k}))$:

$$\Psi'_j(\mathbf{k}) = \sqrt{I_j(\mathbf{k})}e^{i\theta_j(\mathbf{k})}. \tag{2.123}$$

5. Reverse propagate this updated diffraction pattern to give an updated exit wave:

$$\psi'_j(\mathbf{r}) = \mathcal{P}_z^{-1}\left[\Psi'_j(\mathbf{k})\right] \tag{2.124}$$

6. Update the guess of the object in the area covered by the illumination, using the object update function:

$$O_{j+1}(\mathbf{r}) = O_j(\mathbf{r}) + \alpha\frac{P_j^*(\mathbf{r}-\mathbf{R}_j)}{|P_j(\mathbf{r}-\mathbf{R}_j)|^2}\left[\psi'_j(\mathbf{r}) - \psi_j(\mathbf{r})\right] \tag{2.125}$$

Update the guess of the probe, using the probe update function:

$$P_{j+1}(\mathbf{r}) = P_j(\mathbf{r}) + \beta\frac{O_j^*(\mathbf{r}+\mathbf{R}_j)}{|O_j(\mathbf{r}+\mathbf{R}_j)|^2}\left[\psi'_j(\mathbf{r}) - \psi_j(\mathbf{r})\right] \tag{2.126}$$

In this algorithm, $\beta \in [0,1]$ is introduced, and is the feedback parameter for the probe.

7. Get the next recorded diffraction pattern, $j = j + 1$, or if $j = J$ then start the next iteration:

$$n = n + 1$$
$$j = 0$$

8. Repeat steps 2-7 for a fixed number of iterations, or until the error is sufficiently small. A suitable measure for the error is the sum squared error (SSE):

$$\text{SSE} = \frac{(I_j(\mathbf{k}) - |\Psi_j(\mathbf{k})|^2)}{N}, \tag{2.127}$$

where N is the number of pixels of the measured diffraction pattern.

This algorithm has been demonstrated in visible light [25], [92], [93], x-rays [94] and electron microscopy [95], [96]. It is intuitive to code efficiently, and generally converges quickly and robustly for well conditioned ptychographic data.

Rational for the update equations

Mathematically, the update equations can be justified as follows [97]. Considering an error metric for the object, E_j:

$$E_j = \sum_{\mathbf{r}} \left| P_j(\mathbf{r} - \mathbf{R}_j) O_j(\mathbf{r}) - \psi_j'(\mathbf{r}) \right|^2, \tag{2.128}$$

the goal is to change the object reconstruction such that the error is reduced and the exit wave, $P_j(\mathbf{r} - \mathbf{R}_j)O_j(\mathbf{r})$, is closer to the exit wav,e having been updated with the diffraction pattern, $\psi_j'(\mathbf{r})$. The gradient of this error with respect to the object is:

$$\nabla E_j(\mathbf{r}) = 2P_j^*(\mathbf{r} - \mathbf{R}_j) \left[P_j(\mathbf{r} - \mathbf{R}_j) O_j(\mathbf{r}) \right]. \tag{2.129}$$

As the error increases in the direction of this gradient, it can be reduced by moving the current object in the negative gradient direction by a small step, γ:

$$O_{j+1}(\mathbf{r}) = O_j(\mathbf{r}) - \frac{\gamma}{2}\nabla E_j(\mathbf{r}) \tag{2.130}$$

$$= O_j(\mathbf{r}) + \gamma P_j^*(\mathbf{r} - \mathbf{R}_j)[\psi_j'(\mathbf{r}) - \psi_j(\mathbf{r})]. \tag{2.131}$$

Setting $\gamma = \frac{\alpha}{\left|P_j(\mathbf{r}-\mathbf{R}_j)\right|^2}$ gives the object update function as (2.125).

Further extensions

As has been shown, the ePIE algorithm is widely used as it is robust in a variety of modalities, whilst being quick to converge. There have been further extensions to this algorithm, which haven't affected the core aspect of the algorithm, but are still used to improve its outcomes. The two that used in this thesis are annealing, and Momentum-accelerated Ptychographical Iterative Engine (mPIE), which are described below.

Position annealing One of the key pieces of *a priori* information used in ptychography is the positions of the object relative to the illumination. For a standard ptychography optical setup this information will be given by the *x*-*y* translation stage that the sample is mounted on. Issues such as backlash, where there is no output motion when the direction is reversed, mean that the position reported by the stage is not completely accurate. Further issues include when inaccuracies in the known positions are exaggerated by a large scan pattern, when the alignment of the stage is not precisely perpendicular to the optic axis, or when the magnification of the system is not precisely measured. An annealing algorithm [98] provides corrections for these errors by simultaneously trialling a set of stage positions within a provided radius for each diffraction pattern. If one of these corrections gives a lower error between the measured and guessed diffraction patterns than the previous position, it is accepted as

the new position. This can be repeated for a fixed number of iterations, or until the change in position is sufficiently small.

Momentum-accelerated PIE Despite the fact the ePIE converges at a reasonable rate, there are some scenarios in which it may take a long time to converge, or maybe converges to an incorrect solution. A further improvement was made to the ePIE algorithm, which borrowed ideas of momentum from machine learning. This extra step is known as mPIE [97]. The probe and object are updated with ePIE for a fixed number of times, T. A velocity map $v_{j\mathbf{r}}$ is created, which uses the current object estimate and the object estimate after the $(j-T)^{\text{th}}$ update:

$$v_j\mathbf{r} = \eta_{\text{obj}} v_{(j-T)}(\mathbf{r}) + O_{(j+1)}(\mathbf{r}) - O_{(j+1-T)}(\mathbf{r}), \tag{2.132}$$

where $v_0(\mathbf{r}) = 0$, and $\eta_{\text{obj}} \in [0, 1]$ is a update constant which is equivalent to a 'friction' in the momentum. In this equation, the velocity is increase in the direction of a general trend in its updates, whereas pixel that oscillates around a value will have a velocity term that averages to zero.

Once this velocity map is calculated once every T iterations, it can be added to update the new object estimate:

$$O_{(j+1)}(\mathbf{r}) = O_{(j+1)}(\mathbf{r}) + \eta_{\text{obj}} v_j(\mathbf{r}). \tag{2.133}$$

The effect of this addition is that the algorithm converges to a solution much more quickly, and has the ability to 'roll out' of local minima.

2.8.4 Reconstruction errors and ambiguities

One of the inherent questions asked when using a reconstruction algorithm to create an image of a physical object is how can you know whether the image reflects reality.

One way to identify the error in a reconstruction has been given earlier, as a diffraction plane sum squared error:

$$\text{SSE} = \frac{(I(\mathbf{k},\mathbf{R}) - |\Psi_n(\mathbf{k},\mathbf{R})|^2)}{N}. \tag{2.134}$$

This is useful as a way to measure the convergence of an algorithm, however may not be suitable for an overall measure of the quality of a solution. A detector measurement could contain random shot noise or thermal noise when it uses the photoelectric effect to convert photons into electrons. Additionally, there may be ambient light, or issues caused by unwanted reflections that means that the measurement itself may have error.

It would therefore be appropriate to test the reconstruction against a known object. In simulations it is obvious that the object will be known, as so the same sum squared error can be calculated between the reconstructed object and the known object. Experimentally, a known physical sample can be used as a test object, which has been measured externally to this system. In both cases, there may still ambiguities present in the reconstructed object that must be considered, such as phase offset and phase ramps.

2.8.5 Advantages of ptychography

Ptychography is a common path technique, meaning that a reference beam is not required like in interferometry or holography. This makes it a technique that is easier to set up, and does not suffer phase sensitivity issues such as mechanical vibrations. Many of the experimental setups can be added to a standard microscope, facilitating ease of use. It produces high quality complex images–as the probe can be separated from the object, many inhomogeneities in the illumination can be removed. In addition, because there is a considerable amount of redundancy in the ptychographic dataset, errors caused by the detector can be corrected. For the standard

ptychographic setups, a large field of view is possible, suitable for characterising larger optical components. The reconstruction techniques are simple to code and optimise, and are robust at reconstructing accurate images.

2.8.6 Issues with ptychography

One of the most important issues with ptychographical techniques is that they are not immediate, such as a standard microscope, or the PCM and DIC techniques. This tends to be trend across QPI techniques: the data takes time to collect, and even more time to reconstruct. Ptychography can also produce large datasets for large fields of view, that require storage and processing capability.

2.9 Characterising phase retrieval techniques

As with all 'measurement' instruments, we can characterise different QPI techniques by key parameters to assess their performance. These key parameters are: acquisition rate, transverse resolution, and phase sensitivity [45]:

Acquisition rate

A higher acquisition rate means that faster phenomena can be studied by a QPI technique. As per the Nyquist sampling theorem [99], the sampling (or acquisition) frequency must be at least twice the frequency of the signal of interest to be resolved corrected. For QPI systems the acquisition rate largely depends on the number of camera exposures needed for each phase image. This can vary from a single exposure, for example for interferometry, to tens of exposures, for ptychography.

Transverse resolution

For intensity-based imaging systems, transverse resolution is the shortest distance between points on the sample that can be distinguished by the technique [45]. Calculating the transverse resolution of QPI techniques can be more complicated than for conventional microscopy. It is however the aim of QPI to maintain the diffraction-limited resolution given by the microscope part of the system. This was shown by Abbe in 1873 [10] that, for most purposes, the theoretical resolution limit for far field imaging is half the wavelength of the light:

$$d = \frac{\lambda}{2n \sin \alpha} \tag{2.135}$$

where d is the resolving power of the lens, λ is the wavelength of light, n is the refractive index of the transmitting medium, and α is the maximum semi-angle captured by the lens. The main issue is that any lens used in an optical system will never be ideal and will introduce aberrations which increase the minimum resolving power of the lens. In addition, any Fourier transforms in a QPI system will introduce some spatial filtering, which can reduce its transverse resolution.

QPI techniques bring some additional challenges, as they are complex images. In the case of coherent imaging, transverse resolution is not as obvious as the contrast and resolution appear entangled [2], [20]. For phase only imaging the intensity definition of transverse resolution is not possible, as there is no intensity profile. This is still an ongoing research problem.

Phase sensitivity

In QPI, phase sensitivity can refer to two domains: temporal phase sensitivity and spatial phase sensitivity [45]. With temporal phase sensitivity, we are looking for the smallest phase change that can be detected at a given point in the field of view. As an

example [19], to detect red blood cell membranes fluctuations we require a path-length displacement sensitivity of approximately 1 nm. This corresponds to a temporal phase sensitivity of 5 mrad to 10 mrad. These signals can be easily lost in the phase noise produced by QPI systems–from air fluctuations, or mechanical vibrations of optical components. A good QPI system will attenuate the noise as much as possible, for example by stabilising the components, either actively or passively. Active stabilisation could involve a feedback loop that provides continuous cancellation of noise. Passive stabilisation could involve damping mechanical oscillations by using a air supported table. Common path techniques where the two fields travel down the same path, utilising Abbe's theory that an image itself is an inteferogram [10], automatically cancel the noise in the interference term as the noise in both fields is similar.

Whereas temporal phase sensitivity refers to the 'frame to frame' phase noise, spatial phase sensitivity corresponds to the 'point to point' phase noise that affects QPI systems. This is in effect the smallest path length change that QPI techniques can measure. Spatial phase sensitivity is not as easy to isolate but key ways to reduce the spatial phase noise are to keep the optics clean and to decrease the coherence length of the light source. This is because these non-uniformities are produced from random 'speckle', where random interference patterns are created by fields scattered from impurities [19]. Using white light instead of highly coherent sources can also reduce the effect of speckle.

2.10 Reflections on these techniques

Using the key performance parameters given in Section 2.9, Table 2.1 shows a comparison of some of the different QPI techniques. A few of the general positive traits across these techniques can be identified [45]:

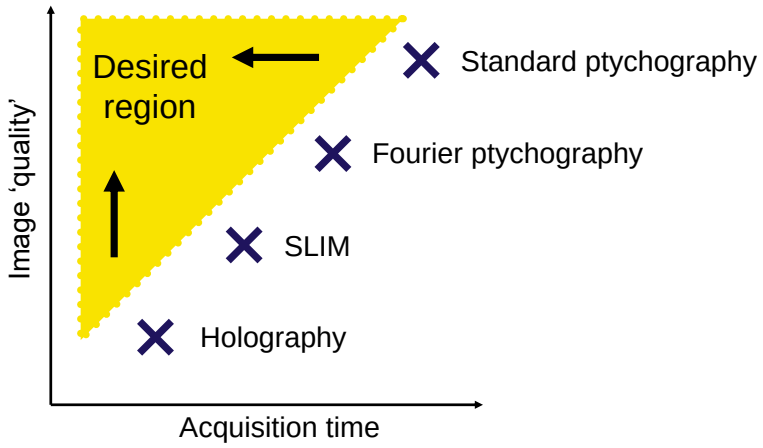

Figure 2.36: A rough guide to the current field of QPI. Image quality isn't rigorously defined here, but in general the higher the quality of the phase image, the longer that image took to acquire. A suitable future development area is in the yellow 'desired region', with high image quality and low acquisition time.

- **White light:** Techniques that use white light as an illumination source suffer less from speckle, and generate images that are spatially more uniform. (TIE, SLIM, GLIM)
- **Add on for standard microscope:** Techniques that can be added on to a standard microscope are more convenient for the end user. (TIE, FPM, Fourier ptychography)
- **Common path:** Techniques that share a path for the reference and sample beams are inherently more stable, with improved phase sensitivity. (All ptychographic techniques, SLIM, GLIM, FPM, TIE)
- **Illumination removal:** Techniques that are able to separate the illumination from the object produce higher quality images. (All ptychographic techniques)
- **SLM:** Techniques that use an SLM do not need moving parts, and can operate faster. (GLIM, SLIM, FPM)

In general, there tends to be a trade-off between final image quality and the amount

of acquisition time and data required. A generalised view of the field looks like the chart shown in Figure 2.36. Although there are many directions in which to focus new technique development, this thesis prioritises developing techniques that have a high image quality with a low acquisition time.

It is clear that although the SLM has become an important component in improving QPI techniques, all the techniques outlined above that use one make one key assumption: the SLM is a perfect optical component. This incorrect assumption, as will be shown in Chapter 4, means that the image quality will be lower than expected. A suitable avenue of exploration will be a technique that uses an SLM (for speed, and a common path method) but isolates the SLM's non-ideal response from the final reconstruction (to improve image quality).

Table 2.1: A comparison of the key figures of merit for some of the optical QPI techniques discussed.

Technique	**Acquisition time**	**Field of View**	**Transverse resolution (m)**	**Phase sensitivity**	**Other points of note**
Digital holography [100]	Framerate	Limited by NA of microscope	μ	$2\pi/60$	Alignment difficult, sensitive to environmental noise
Standard ptychography	1 min to 1 hour	Limited by translation stage	μ	$2\pi/330$ [101]	Contains moving parts, creates large amounts of data
Fourier ptychography [72]	10 sec to several mins	Limited by NA of illumination	μ	Not available	Alignment of illumination difficult, creates large amounts of data
Fourier phase microscopy [53]	$4\times$ framerate	Limited by NA of microscope	μ	$2\pi/35000$	Assumes a perfect SLM
SLIM [20]	$4\times$ framerate	Limited by NA of microscope	μ	$2\pi/12600$	Add on for standard phase contrast microscopes, assumes a perfect SLM

2.11 Spatial light modulation

As has been seen in Section 2.7, SLMs are increasing being used as tools in QPI techniques. A key aim of this research is to combine SLM with microscope to produce improved techniques. Many optical devices are static. Lenses, mirrors and the like remain fixed during optical experiments, unless they are mounted on an independent mechanical stage. This means that optical information contained within the light cannot be altered quickly. A direct connection between data processing and application to the optics bench is therefore a useful tool. Many of these devices are commonplace, for example a CCD can capture light information for digital processing. However, a device that can convert electronic data into spatially modulated coherent optical signals are currently of particular interest [2]. These devices are known as Spatial Light Modulators.

There are two main categories of SLMs [2]:

- **Electrically written SLM:** Electrical signals representing the information to input to the system directly drive a device that can control its spatial distribution of absorption or phase shift of light.

- **Optically written SLM:** Optical signals are input on one side of the device which can sense the brightness of each pixel so that the pattern can be replicated.

An electrically written SLM was used in this work. An SLM display generally consists of an array of pixels, where each pixel is able to impose its own modulation on the incident light, as shown in Figure 2.37. This means the device can control the phase and/or amplitude of the incident light wavefront in two dimensions. They are smaller than usual display technologies, with an active area of approximately 1.5cm $\times$ 1cm, but can have up to high definition resolution (1080 $\times$ 1920 pixels.)

There are a range of SLM technologies, the most promising are [2]:

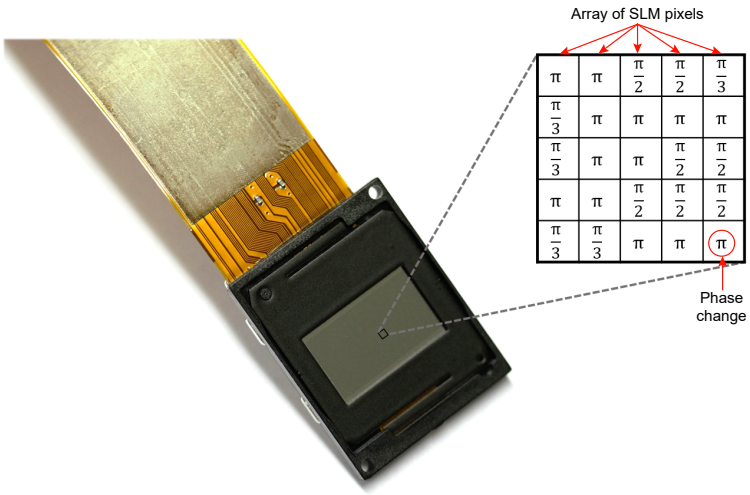

Figure 2.37: An example of a phase only Liquid Crystal Spatial Light Modulator. Each pixel of the reflective display can alter the phase of the incident light.

- **Liquid Crystal** Liquid Crystal spatial light modulators are switched by either thin-film transistors, or silicon backplanes. Can be used for a range of applications, but tend to be slow. They are readily commercially available and affordable [102].

- **Magneto-Optic** Made using pixelated crystals of Aluminium Garnet, switched by an array of magnetic coils using the magneto-optic effect [103], [104]

- **Deformable Mirror** Consists of an array of sprung mirrors, constructed using nano-technology techniques. They provide a continuous phase distortion with large amplitude, but typically contain a low number of 'pixels' [105], [106].

- **Multiple Quantum Well** Utilises the Quantum Stark Effect in a very thin layer. They are extremely fast, but have poor contrast, are difficult to make in large arrays and difficult to drive, but are the future of fast optical switching [2].

Throughout this thesis, a reflective Liquid Crystal on Silicon (LCoS) SLM was used, produced by Holoeye. The unit used, a Pluto Phase only SLM, is addressed using a

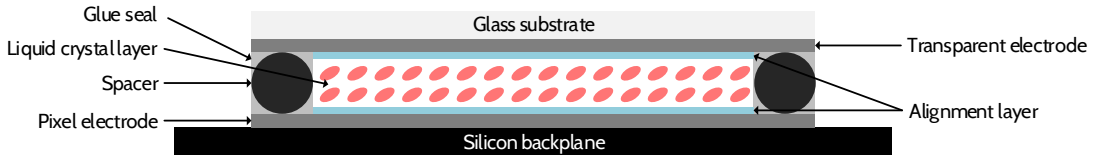

Figure 2.38: A simplified structure of an Liquid Crystal SLM. The rod-like molecules in the liquid crystal layer change their refractive index when their surrounding electric field is changed.

standard Digital Visual Interface (DVI) signal from a computer's graphics card and so behaves as an external monitor. The SLM driver unit converts this incoming 256-bit grey level signal using a Look Up Table (LUT) to a phase modulation value. When a field of visible light (in the range 420 nm to 700 nm) is incident on the display, the phase across the two dimensions is altered according to the phase modulation value.

2.11.1 How does a liquid crystal on silicon phase only spatial light modulator work?

A Liquid Crystal Display (LCD) is one of the most commonly used optical modulation components as they are cheap, commercially available and can be controlled electronically. The display contains liquid crystals, which are rod like molecules that are in a state of matter between a solid and a liquid. The liquid crystal is a uniaxial, birefringent material with extraordinary refractive index $\mathbf{n}_e$ and ordinary refractive index $\mathbf{n}_o$. The optical properties of this liquid crystal are modified using an alternating electric field such that the liquid crystal molecules tilt to align with the electric field. This means the extraordinary refractive index $\mathbf{n}_e$ decreases and the path length through that region is decreased, resulting in a spatial phase change [107].

2.11.2 Uses of liquid crystal spatial light modulators

Although LCD SLM devices are at an early stage of maturity, they are emerging as a useful technology in optics research with several uses. As a way of digitally creating

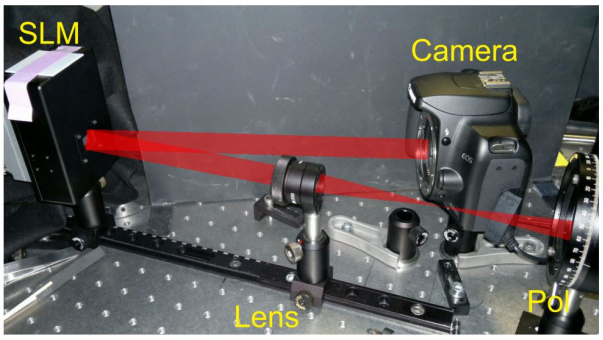

(a) The setup used for investigating using SLMs for head-up displays.

(b) An example image of an heads-up display image projected by the SLM.

Figure 2.39: SLMs are used for generating head-up displays. [Reproduced from [108]]

holograms they can be used as head-up displays [108]–[110]. This type of technology is used where we want the user to get more information whilst not distracting them from their current task, like when driving. Figure 2.39 shows how the SLM is an integral component in such technologies. SLMs are also used for telecommunication devices [111], [112], adaptive optics [106], [113], and holographic 3D displays [108], [114], [115]. They can also be used for beam shaping, for example for optical tweezers [116], and aberration correction [117].

The most useful thing that an SLM brings to microscopy is an additional dimension – time. Because it is possible to change the properties of an SLM instantly with a computer, a lot more applications become available. SLMs also provide a digital interface to optics, meaning that more complex operations can be achieved. This is further helped by the recent advances in Graphical Processing Unit (GPU) technology, which can perform large parallel calculations quickly. Complex patterns–such as holograms–can then be displayed on the SLM with a quicker calculation time, resulting in more 'intelligent' imaging.

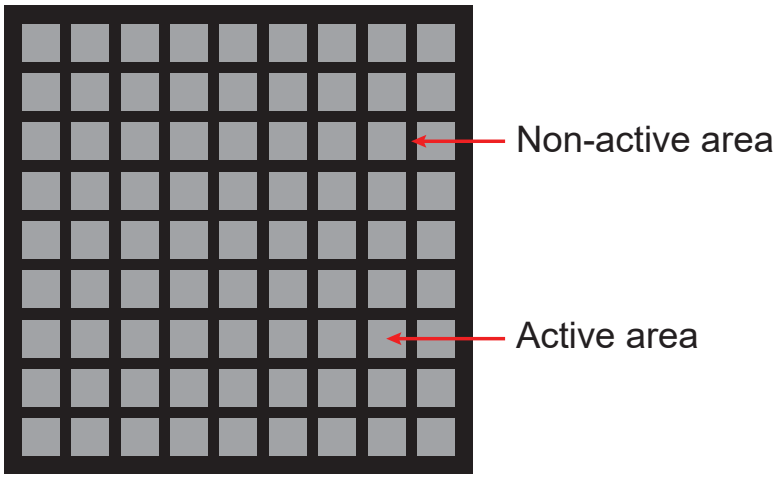

Figure 2.40: A LCD consists of an array of square pixels of active area surrounded by a grid of non-active area which creates light absorption and diffraction into higher orders.

2.11.3 Limitations of liquid crystal spatial light modulators

There are a few imperfections with SLM devices that need to be considered before their use as an optical tool. As the technology is developing, some of these issues will be reduced in severity, but others can be characterised and compensated for.

The fill factor of the device–the ratio of active area to the total area of the aperture–is the most significant limitation to the performance of SLM devices [118]. Because each pixel of the device is surrounded by a non-active area, as illustrated in Figure 2.40, there is light absorption in the darker areas. Additionally, the grating like structure can lead to diffraction into higher orders and diffraction losses.

Due to the design of a LCD SLM, neighbouring pixels cannot have a large change in orientation. This means that sudden phase change between adjacent pixels is not possible. Intermediate regions, known as flyback, or crosstalk, regions [119], are present between regions of large phase change, as illustrated in Figure 2.41. The size of this region will depend on the phase difference between these neighbouring regions, and may extend to several pixels [39]. In addition, due to the slope of the phase profile in this region, light passing through will be diffracted to higher orders leading to

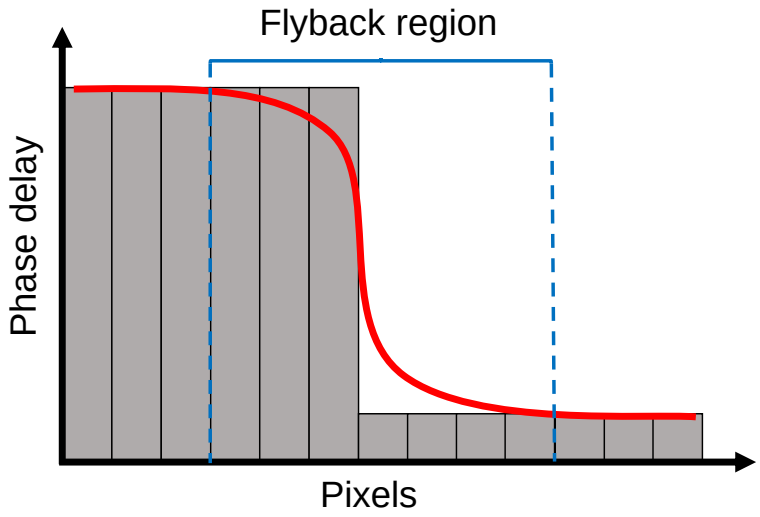

Figure 2.41: An illustration of the flyback region on a LCD SLM. The grey bars are the expected phase profile across an SLM in one dimension. The red line shows the real phase profile, highlighting the flyback region between adjacent pixels with a large phase difference.

diffraction losses [119].

As a display technology, it is also important to consider the response time of the device. This can vary between devices, and depending on the application, a slow refresh rate and flickering might cause issues.

Another challenge presented is the precise characterisation of the phase response of the SLM. The linearity of the phase response of the SLM needs to be optimised for a given wavelength [120], [121], which is not a trivial task. Various techniques have been identified to measure the phase response of an SLM, of which more detail is given in Chapter 4.

As shown in Figure 2.38, at the front of the SLM device is a thin layer of glass. This layer of glass has a slight spherical deformation to it [107], [121]. This curvature can be of the order of a couple of wavelengths, so for some purposes is negligible, but can present problems where highly accurate phase responses are needed.

Many of the imaging technologies described previously in Section 2.7 make the

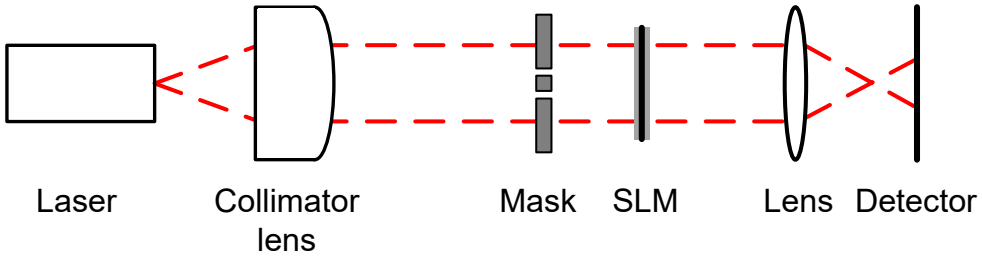

Figure 2.42: The setup for Young's interferometry to characterise a transmissive SLM. The mask has two pinholes placed in front of the SLM.

assumption that an SLM provides a perfect phase display. As a result, many of the techniques have less than perfect reconstruction results.

2.11.4 Characterising a Spatial Light Modulator

In this section, existing techniques used to characterise some aspects of the SLM will be described, and their limitations.

Interferometry

Interferometry is often to measure the profile of the SLM's phase modulation. Traditionally, techniques based on Mach-Zehnder interferometers were used, however this method is sensitive to environmental conditions and can only give a rough idea of the behaviour of the SLM [122].

Young's interferometer One of the more simple techniques to characterise phase is Young's interferometer. Bergeron [122] demonstrated this method, which is based on Young's fringes, using a setup as shown in Figure 2.42. A mask with two pin holes is placed in front of the transmissive SLM. The SLM is split into two, one half is kept constant, and the other half is varied to characterise the SLM in the given range. Both signals are uniform over each pin hole aperture. When the two regions have the same

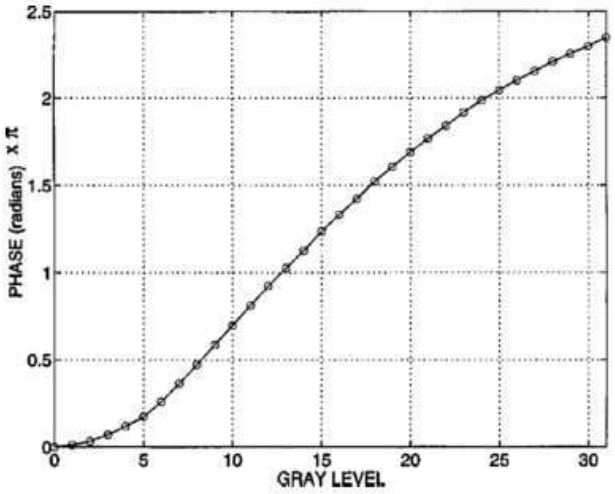

Figure 2.43: Results of the phase response of the SLM using Young's interferometer. [Reproduced from [122]]

value, the Fourier transform shows a co-sinusoidal function modulated by an Airy spot. If the phase value of one is varied, the co-sinusoidal function will translate according to the phase difference between both regions. Bergeron's results are shown in Figure 2.43. They show the non-linear behaviour of the SLM and reflect the robustness of the characterisation technique. However, this technique can only characterise a small region of the SLM.

Twyman-Green interferometry Interferometry was used by Villalobos-Mendoza *et al.* [123], [124] to characterise an SLM. In particular, they used a Twyman-Green interferometer (a variant of the Michelson interferometer), as shown in Figure 2.44.

The display of the SLM was again split into two, the top half's grey level was varied, and the bottom half remained fixed as a reference. This change in grey level produces a phase shift in the wavefront that can be seen in a fringe shift in the interference pattern. Their algorithm then finds the position of each maximum in the interferograms and finds the phase differences between the top row (corresponding to the varying half of the SLM) and the bottom row (corresponding to the reference half of the SLM) and

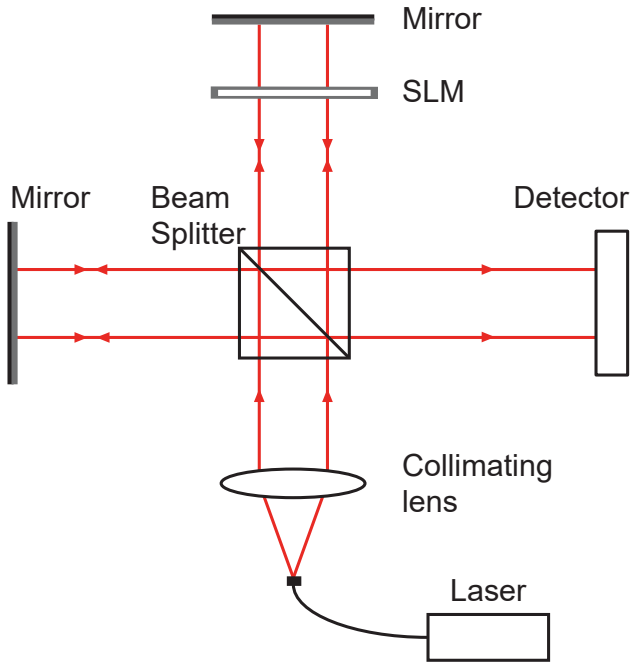

Figure 2.44: Experimental configuration for Twyman-Green interferometry with a transmissive SLM.

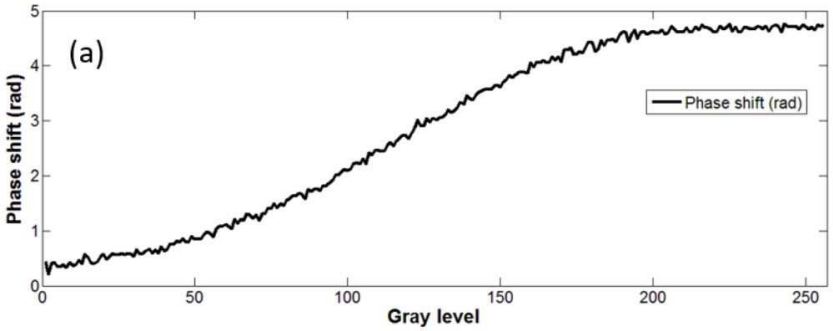

Figure 2.45: The characterisation of an SLM's phase shifts for each grey level using Twyman-Green interferometry. [Reproduced from [123]]

averaging, giving a graph such as Figure 2.45.

However, as in general with double path interferometric methods, alignment of the components can be difficult, and instability between the two arms can lead to low phase sensitivity.

Holography

As described in Section 2.7.1, digital holography obtains the phase information of the object as intensity variations in the detector plane. Panezai [125] used lens-less Fourier transform digital holography to reconstruct the phase of an SLM. The experimental setup is shown in Figure 2.46.

Having been polarised and split into two, the laser beams are expanded and collimated. The SLM is used as the object, and the light reflected is the object wave. The reference wave is turned into a point source using the microscopic objective. The two waves interfere with each other through the beam splitter and the digital hologram is recorded on the CCD.

A double exposure technique was used to remove phase aberration. The first hologram is recorded by setting the SLM at 0 grey level. The second hologram is recorded by splitting the SLM into two, such that one half has a fixed level, and the other half has varying grey level. The phase images were reconstructed using the Fresnel transfer algorithm. The phase without aberration was obtained by subtracting the two reconstructed phase images from each other. The phase image will show the contrast between the two regions, the reference and the constant test. The phase difference is calculated by first averaging the phase value in the two regions and then calculating the difference between them.

This technique can also be used to characterise the phase of the active region, and the authors demonstrate this with a phase grating loaded onto the SLM as shown in Figure 2.47.

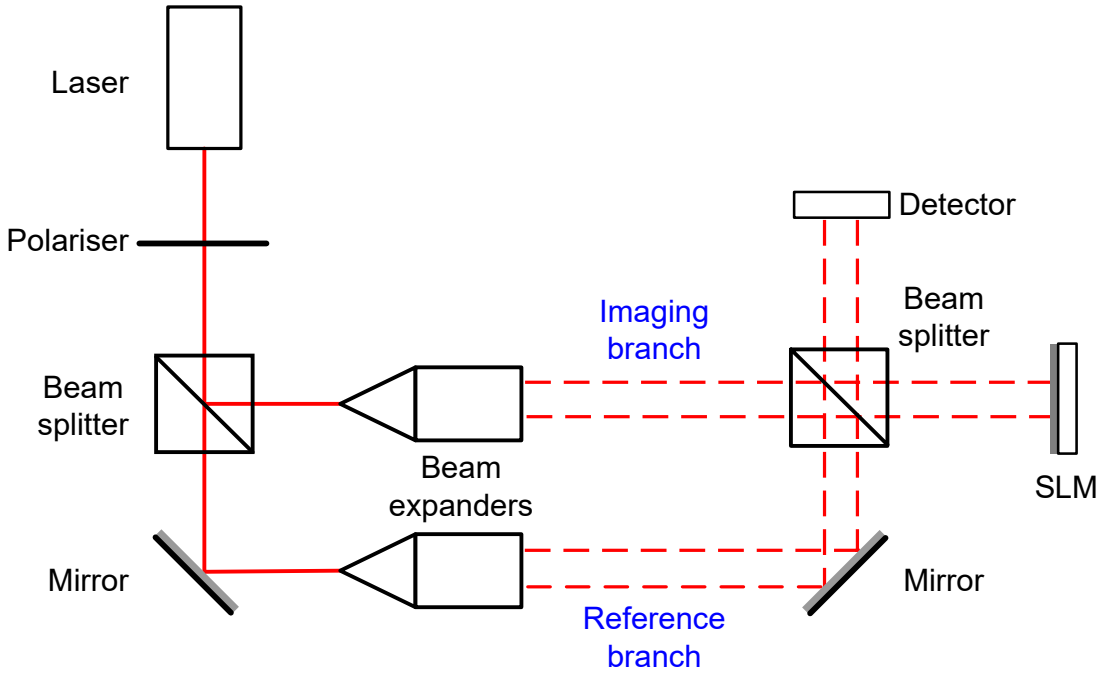

Figure 2.46: Optical setup for holography phase characterisation of an SLM.

Spread Spectrum Phase Retrieval

Spread-Spectrum Phase Retrieval (SSPR) was used by Kohler *et al.* [126] to characterise an SLM. Their experimental set up is as Figure 2.48.

M diffraction patterns are collected, as the phase plate is shifted transversely. An iterative algorithm similar to the PIE algorithm (Section 2.8.3) is utilised. The algorithm starts with a random estimate of $\psi(\mathbf{r})$ at $(n = 0)$, the wave front before the phase plate, and proceeds iteratively:

1. Modulate the current estimate of $\psi_n(\mathbf{r})$ with the plate phase, at the current plate position m (= 0,1,...,M):

$$\tilde{\psi}_n(\mathbf{r}) = \psi_n(\mathbf{r}) \exp(j\phi_m(\mathbf{r})), \quad m = \text{mod}(n, M) \tag{2.136}$$

where $\phi_m(\mathbf{r})$ is the phase distribution of the plate offset in position m.

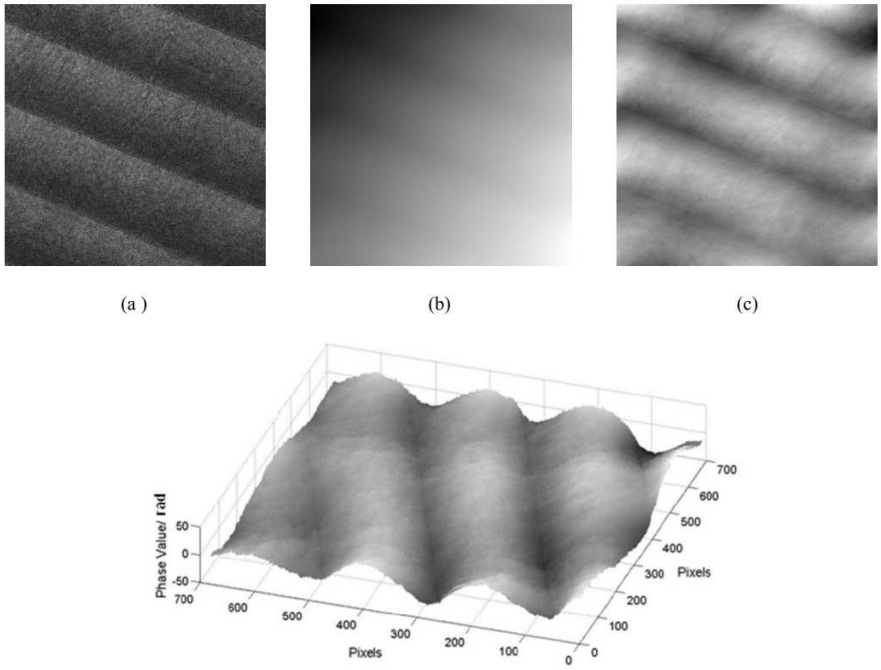

Figure 2.47: Imaging a phase grating loaded onto an SLM using holography. (a) Reconstruction amplitude image, (b) reconstructed phase image with aberration, (c) unwrapped phase image, (d) 3-D phase image [Reproduced from [125]]

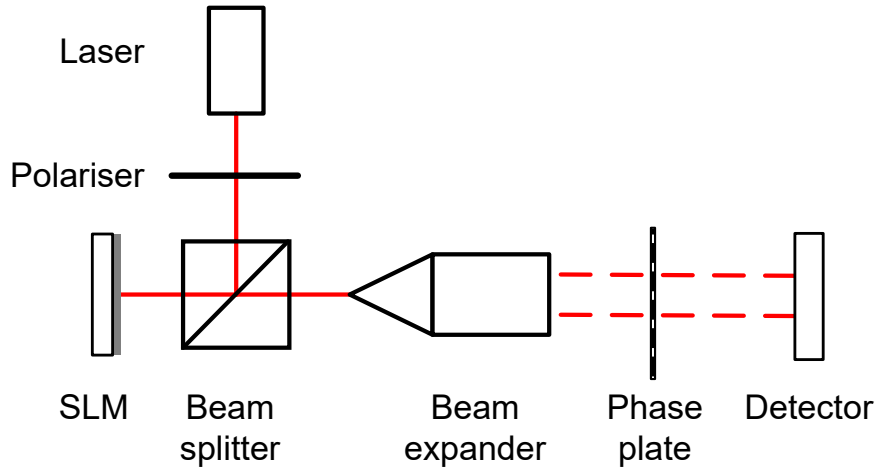

Figure 2.48: The optical setup for phase retrieval of a reflective SLM using Spread Spectrum Phase Retrieval.

2. Propagate the wavefront, $\tilde{\psi}_n(\mathbf{r})$, using Fresnel propagation (Section 2.4.2) to the CCD to obtain an estimate $\Psi_n(\mathbf{k})$ at the diffraction plane.

3. Replace the magnitude of $\Psi_n(\mathbf{k})$ with the diffraction pattern measured by the detector.

4. Propagate the corrected wavefront, $\tilde{\Psi}_n(\mathbf{k})$, back to plate plane.

5. Remove the plate phase modulated in step 1 to obtain a new estimate of the wavefront before the plate:

$$\psi_{n+1}(\mathbf{r}) = \tilde{\psi}_n(\mathbf{r}) \exp(-j\phi_m(\mathbf{r})) \tag{2.137}$$

6. Repeat steps 1-5 for the next plate position (i.e. n+1).

Once the change in amplitude between successive retrieved waves has become sufficiently small, the process ends. The object field is recovered by further propagation to the object plane.

The authors identify several sources of error in the experiment:

- variations of the input intensity,
- movement of the object,
- the difference between the propagation distance used in the phase, retrieval and the real distance,
- inaccurate movement of the modulator,
- errors in the modulator's phase function,
- detector noise.

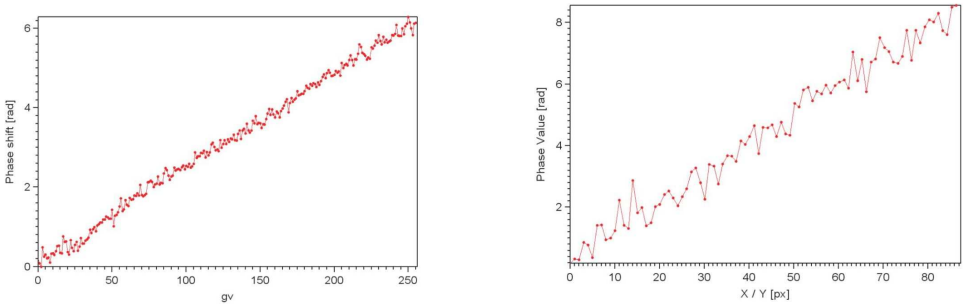

(a) Phase shift of the SLM measured with a double slit setup.

(b) Phase retrieved from an SLM with a blazed grating with a period of 12 pixels obtained using SSPR.

Figure 2.49: Comparative results from Kohler's work. [Reproduced from [126]]

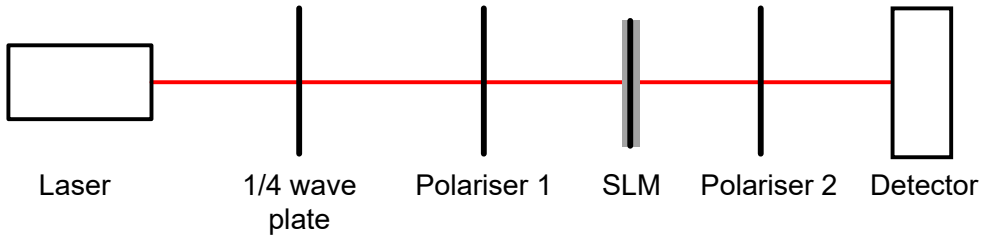

Figure 2.50: The optical setup for Burman's characterisation with polarisers. The Microdisplay is a transmissive SLM. The 1/4 wave plate is used to obtain right-handed circularly polarized light, from which the characterisation equations are derived.

The results from this work are compared with double slit interferometry for the retrieved phase of a blazed grating written into the SLM, as shown in Figure 2.49. This technique has useful results, although suffers from comparatively high noise.

Polarisers

Burman *et al.* [127] characterise a phase only SLM using polarisers. Their technique uses two polarisers, at fixed angles, with the transmissive SLM in-between, as shown in Figure 2.50.

The combination of the two polariser angles that give the maximum phase modulation with the minimum amplitude modulation is found. By changing the grey

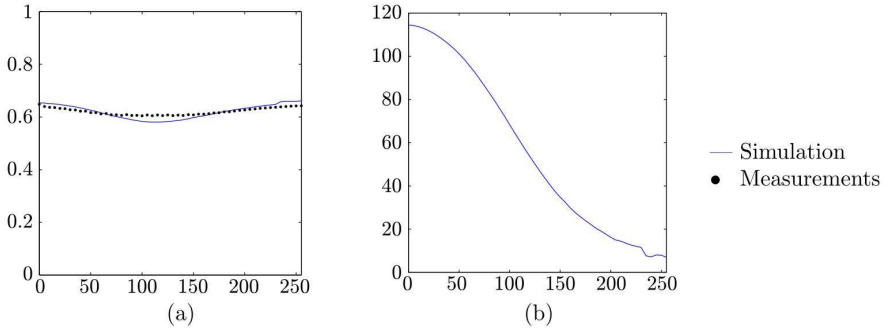

Figure 2.51: The results of using polarisers to characterise a SLM (a) Amplitude modulation vs Grey level; (b) Phase modulation[°] vs Grey level. In this case, the maximum phase modulation obtained is 115°. [Reproduced from [127]]

level of the SLM and measuring the intensity, the phase introduced by the SLM can be deduced via a Hilbert transform [20]. Their results are given as two graphs, shown in Figure 2.51.

Analysis of existing techniques

In Section 2.11.3, two main issues were identified about SLMs which can be characterised which might affect their use as components in QPI techniques: the phase response and the curvature of the SLM. Most of the techniques described are aimed at exclusively extracting the phase response of the SLM. They can produce a graph of the average phase change the device produces at each phase level that it can be programmed to display. They either can image the SLM over a small area, or over larger areas at a lower resolution. They are all susceptible to errors resulting from imperfect optical components in their characterisation, and those based on interference with a reference beam involve careful alignment and calibration.

Chapter 3

Optical near-field ptychographic microscope for quantitative phase imaging

This chapter focuses on my work developing a novel QPI technique called optical near-field ptychography. It starts with an introduction to the development, and the reasons behind it, before moving on to previous developments in the area. The experimental setup and image reconstruction procedures are described, followed by the results and discussion of the technique. Finally, future directions for the technique are expanded. This work was published in Optics Express [128].

3.1 Introduction

Ptychography has several benefits. It is able to generate high quality quantitative phase images; it does not suffer temporal phase issues as there is no separate reference beam; any illumination aberrations or dust are decoupled from image of the sample and it can generate complex images with large fields of view.

However, standard ptychography, as described in Section 2.8.1 does have some issues, particularly in the area of bio-imaging. As a beam must be scanned across the sample, it takes a reasonable amount of time to collect the data required to reconstruct one image. This can result in blurred images as samples move between captures. In addition, the sample is constantly moving on a mechanical stage, which can further increase blurring if the timing between the stage movement and camera is not accurately controlled. The frame rate of any video footage will be limited by this movement. Standard ptychography also produces large amounts of data, which takes time to reconstruct, limiting its ability as a 'live' technique.

Fourier ptychography (Section 2.8.1) deals with some of these issues. As the sample is not moving, blurring is reduced. The frame rate can also be increased, as it is limited by the changing positions of the LEDs. However, it is only suitable for thin samples, as the angles of the illumination assume a thin sample. In addition, the data requirement of Fourier ptychography is still high, requiring tens to hundreds of diffraction patterns. It is also prone to low-frequency artefacts [71].

The purpose of this research is to take the benefits of ptychography, but to try and improve the technique to be more suitable for bio-imaging. Using ideas from selected area ptychography and x-ray near-field ptychography (Section 2.8.1), this work develops optical near-field ptychography. The technique is then tested and analysed on a range of samples.

There are issues with the x-ray near-field setup as described in Section 2.8.1 that were changed in this setup of near-field ptychography. Firstly, as the sample itself is being imaged, rather than an image of the sample, restraints are placed on how optically thick the sample can be in order to imaged accurately. In addition, the diffuser is magnified as it is propagated onto the sample. This means is is not possible to know the exact diffuser-sample distance [82], since the diffuser appears before the mirrors used to focus. As the diffuser is magnified, it is difficult to predict whether the

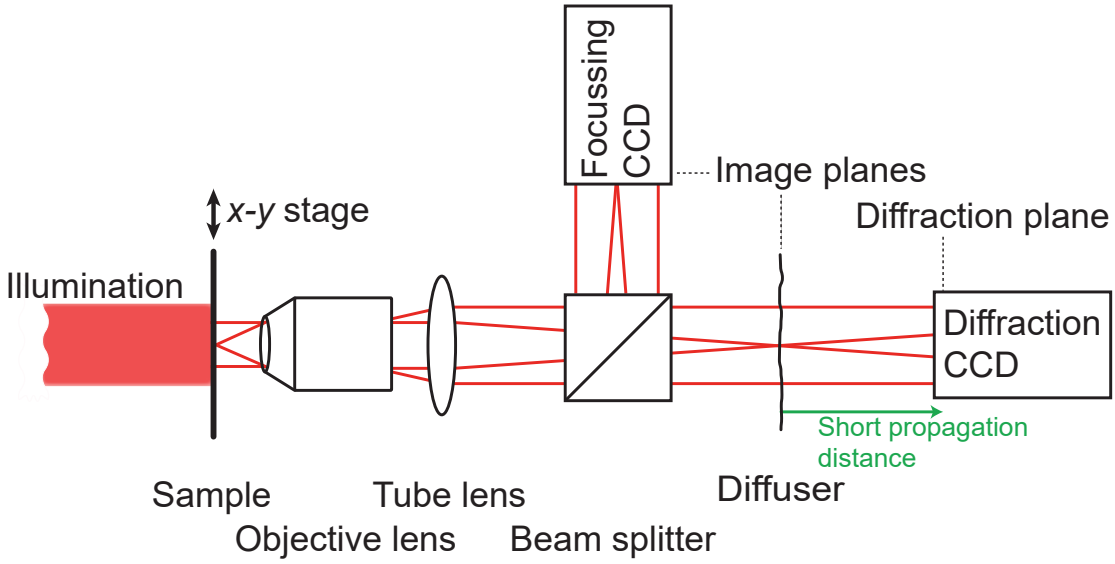

Figure 3.1: The experimental setup for optical near-field ptychography.

speckle pattern over the sample will change sufficiently in every location of the sample in order to have enough difference between the diffraction patterns in that region.

3.2 Dataset acquisition

Firstly, the experimental setup and ptychographical data collection procedure will be described. This includes some of the investigations performed to determine necessary characteristics of the technique.

3.2.1 Theoretical setup

The experimental setup for optical near-field ptychography is simple, as shown by Figure 3.1. A collimated laser illuminates more than the required field of view of the sample. A standard microscope (objective and tube lens) forms a magnified image of the sample onto an image plane, where a diffuser is located. The diffuser modulates the image and the resulting exit wave propagates a short distance onto a CCD. The

sample is then moved with small lateral offsets using the mechanical stage, and further diffraction patterns are captured. The setup for optical near-field ptychography was consciously designed with several characteristics:

1. **It can be added onto a standard optical microscope.** This is particularly useful in the area of bioimaging, as biologists will tend to have standard microscopes available for use. This technique can therefore be developed as an 'add-on' for these microscopes, with few technical difficulties.

2. **The image of the sample is projected onto the diffuser.** This means that the technique reconstructs the magnified image of the sample produced by the microscope.

3. **The CCD's dynamic range requirements are reduced.** As there is no aperture, as in selected area ptychography, there is not the associated dark- and bright-field areas in the diffraction pattern. This means that multiple exposures are not required to accurately capture the diffraction pattern.

4. **The full field of view can be captured with fewer diffraction patterns.** This means that the ptychographic dataset can be captured in a shorter amount of time, reducing blur and increasing the frame rate of quantitative phase videos, and speeding up the reconstruction time.

3.2.2 Optical bench setup

The particular setup used is shown in Figure 3.2. The illumination is formed by collimating a 675nm fibre-coupled laser beam. The sample is mounted on to a Newport XPS-Q4 x-y-z motorised stage. The objective lens is interchangable, a 20× (NA = 0.40) and 4× (NA = 0.10) magnification were used in our experiments. A fixed 18 cm tube lens completes the rest of the infinite microscope (described in

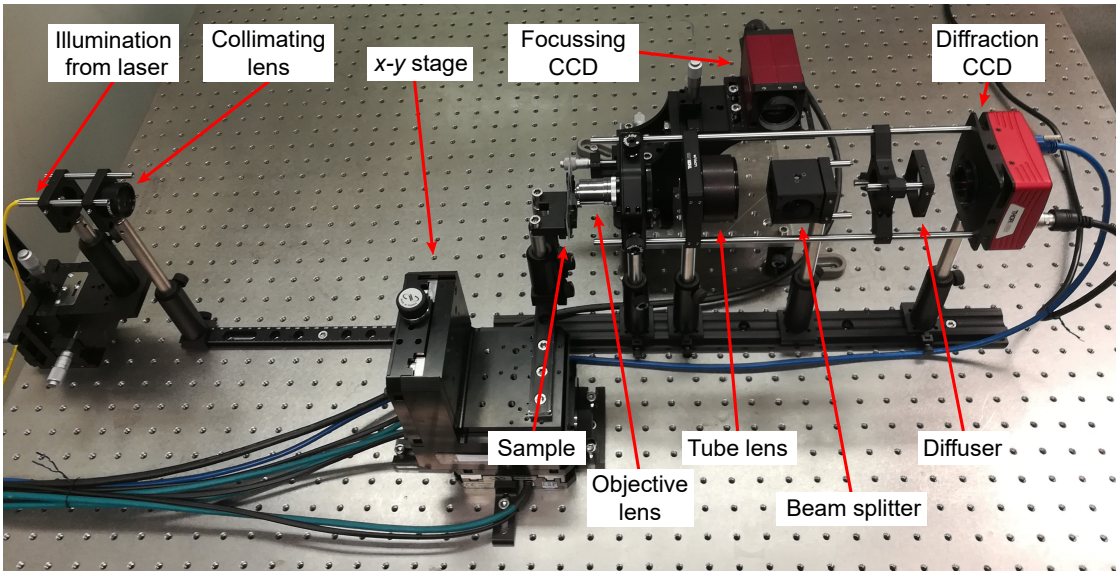

Figure 3.2: The optical bench setup for optical near-field ptychography.

Section 2.5.1), which forms the magnified image of the sample at its image plane. On this plane, a diffuser (a flat piece of transparent adhesive tape) is positioned, and 5 cm downstream of this, the Thorlabs 4070M USB CCD (2048 $\times$ 2048 pixels on a 7.4 µm pitch) is placed. The CCD is binned by a factor of 2, and the data is captured with a single 200 µs exposure. This gives a Fresnel number of:

$$\begin{aligned} N_F &= \frac{w^2}{\lambda z} \\ &= \frac{0.0152^2}{675 \times 10^{-9} \times 5 \times 10^{-2}} \\ &= 6.85 \times 10^3, \end{aligned} \tag{3.1}$$

which is $\gg 1$, placing the propagation distance from the diffuser to the CCD firmly in the near-field (see Section 2.4.4).

For alignment, as described below in Section 3.2.5 a secondary focussing CCD is placed perpendicular to the optic axis. A beamsplitter, or mirror, is placed so that the CCD detector is also in the image plane of the microscope. Once the sample has been

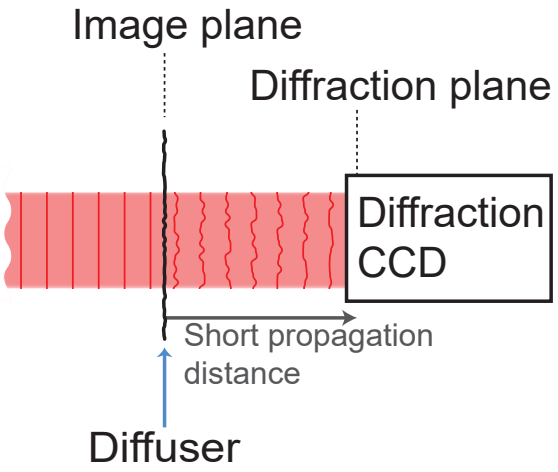

Figure 3.3: The diffuser modulates the image wave formed by the microscope.

focussed, this beamsplitter can be removed.

3.2.3 Investigations behind optical bench setup

There are several different components and parameters involved in optical near-field ptychography. Although throughout my experimentation, it proved a remarkably robust technique, working well over a range of step sizes, grid patterns and camera lengths, some of these parameters will result in better image quality or reconstruction speed. A helpful analysis of x-ray near-field ptychography was completed by Clare *et al.* [82], and although their setup was different, it was a useful starting point for this analysis. Parts of the experimental setup were investigated and chosen in the following ways:

Diffuser

The purpose of the diffuser is to modulate the image wave formed by the microscope, as shown in Figure 3.3. As such, when choosing a diffuser, the following should be considered. Firstly, it is necessary that the diffuser does not attenuate the light, so that it is not necessary to increase the exposure length of the CCD. Secondly, there is a

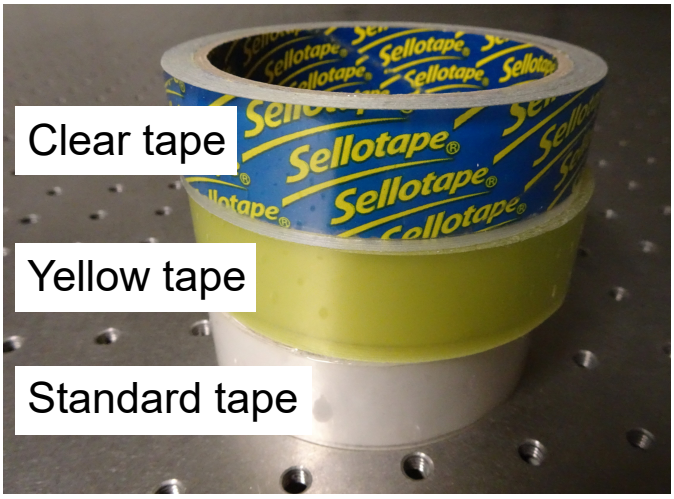

Figure 3.4: The three adhesive tapes used.

trade off regarding the phase altering properties of the diffuser. It is important for the diffuser to have enough 'features' in order that there is sufficient diversity in the diffraction patterns. (Remembering that at the extreme, without a diffuser, each diffraction image would be exactly the same, but laterally shifted. This makes the problem under-constrained and so not possible to reconstruct, as demonstrated in simulation by Clare [82].) In the other extreme, a diffuser that is too diffuse will overpower the signal, resulting in diffraction patterns that appear as random noise.

A range of diffusers (including three different transparent adhesive tapes shown in Figure 3.4), and two apertures were investigated:

- **Apertures:** This is, in effect, selected area ptychography. A 250 µm (Figure 3.5a) and a 480 µm (Figure 3.5b) diameter aperture were placed in the image plane of the microscope. As can be seen from the diffraction pattern, much of the camera's detector area is not used. This is therefore wasted data. In addition, the contrast between the centre of the diffraction pattern and the edges is large, meaning that a large dynamic range detector is needed, or multiple exposures. As the aperture is just a hole, the diffraction pattern at the centre is essentially just an out-of-

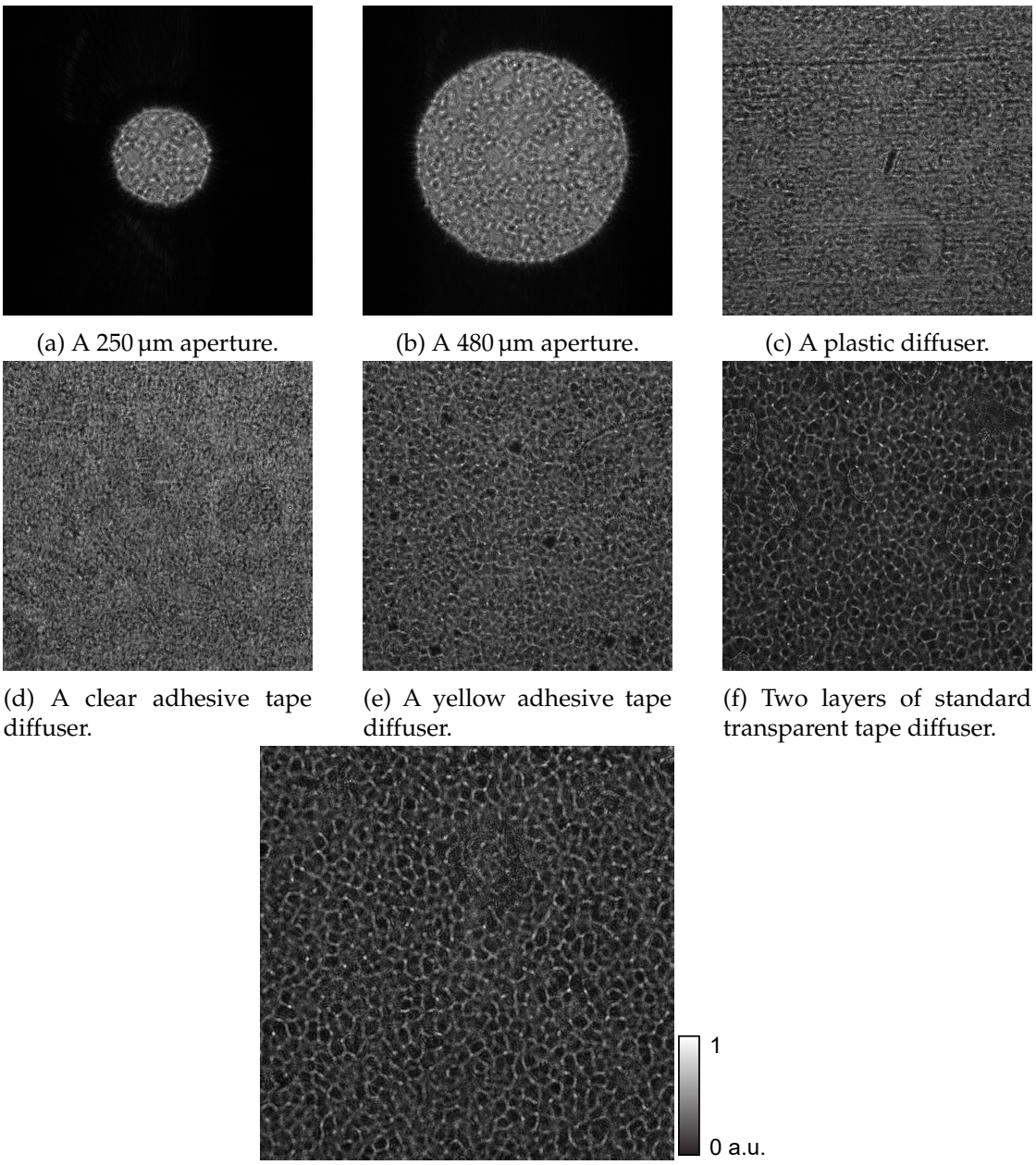

(a) A 250 µm aperture.

(b) A 480 µm aperture.

(c) A plastic diffuser.

(d) A clear adhesive tape diffuser.

(e) A yellow adhesive tape diffuser.

(f) Two layers of standard transparent tape diffuser.

(g) One layer of standard transparent adhesive tape diffuser.

Figure 3.5: The diffraction patterns observed when using a range of diffusers and apertures. The diffraction pattern captured was using the same sample of frog red blood cells and have been square-rooted to enhance contrast. Each figure shows the full field of view of the camera, which is 1.54 cm^2.

focus image from the microscope. The Fresnel integral relation shows that in the nearfield, there is no overlap between disparate regions of the sample; the only part of the diffraction pattern where diffraction effects have occurred is at the edge of the aperture. This means the sample needs to be moved so that every part of the object interacts with the boundary of the aperture.

- **Plastic:** (Figure 3.5c) This was taken from a plastic document wallet. The diffraction effects are not clear here as it looks like an out of focus image, but there are also some horizontal streaks in the material that appear in the diffraction pattern.

- **Clear adhesive tape:** (Figure 3.5d) The diffraction effects are limited here.

- **Yellow adhesive tape:** (Figure 3.5e) The diffraction pattern's power was attenuated by the yellow tape, but the diffraction effects are more apparent. There are darker 'blobs' from the glue on the tape.

- **Two layers of standard adhesive tape:** (Figure 3.5f) The diffraction effects are stronger here, but air bubbles are created in-between the two pieces of tape. This creates uneven effects caused by the change in refractive index through the bubbles and the increase in thickness of the tape.

- **Standard adhesive tape:** (Figure 3.5g) The diffraction effects are strong here, creating an even speckle across the whole detector.

Although the technique works with all the different varieties of diffuser investigated, the standard adhesive was chosen. This is a more qualitative analysis, but a quantitative analysis of diffusers could be investigated with the technique described in Section 5.2.2.

Camera length

The camera length in near-field ptychography is the propagation distance between the diffuser and the detector. In general, the camera length should be greater than the depth of field of the microscope [129]:

$$\text{Camera length} \geq \frac{\lambda}{\text{NA}^2}. \tag{3.2}$$

Scan pattern and step size

The scan pattern describes the positions that the mechanical stage takes for each diffraction pattern acquisition. As was discussed in Section 2.8.2, some choices of scan pattern can have a negative effect on the final reconstruction, such as the 'raster scan pathology' [83]. This has been further tested in simulation for the X-ray near-field case [82], where they identify a pseudo-random scan pattern to be the most effective. A spiral pattern has also been shown to work well [130], providing a high overlap per number of scan patterns. Tests were undertaken between a pseudo-random grid pattern and spiral pattern. Although early results indicated that the pattern choice was not critical due to the inherent redundancy in near-field ptychography from the large overlaps, the pseudo-random spiral was chosen as the basis of the approach taken here.

The minimum step size should be:

$$M \times \text{Step size} \geq \text{Probe resolution} \approx \frac{\lambda}{\text{NA}_{\text{probe}}}, \tag{3.3}$$

where M is the magnification of the objective lens. Small random offsets were added to a regular spiral pattern, as shown in a typical pattern in Figure 3.6. The positions, P,

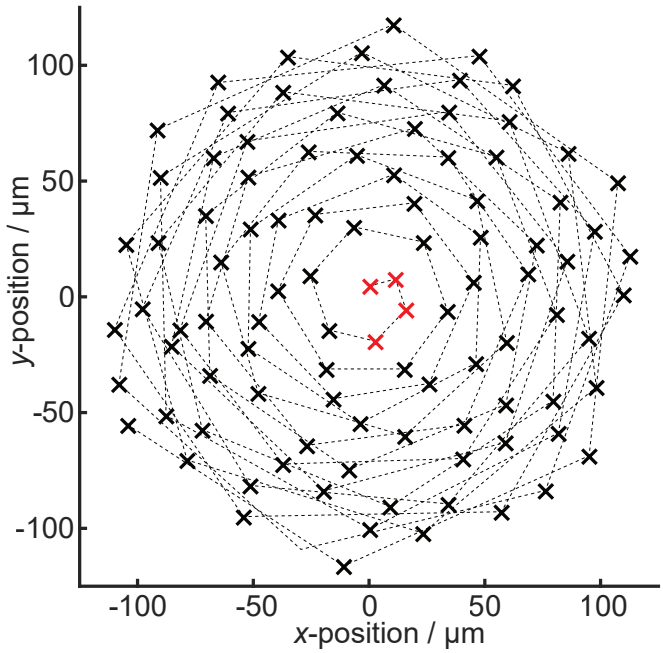

Figure 3.6: A typical pseudo-random spiral pattern of $x - y$ translation stage positions for the collection of the near-field ptychographical dataset. Data is collected from the centre of the region of interest outwards. The four red positions indicate the theoretical minimum number of stage positions required to create a suitable near-field ptychographical dataset.

were generated using the following equations:

$$P_0 = [0, 0] \tag{3.4}$$

$$P_{n+1} = P_n + [\Re(C), \Im(C)]\,, \tag{3.5}$$

where the complex value C for each position is given by:

$$C = s \times \sqrt{\frac{\theta_n}{2\pi}} \exp(i\theta_n). \tag{3.6}$$

In our setup, the step size, s, is 30 µm. θ was defined for each position as:

$$\theta_0 = 0.2R \tag{3.7}$$

$$\theta_n = \theta_{n-1} + 0.9 + 0.2R, \tag{3.8}$$

where R is a random number, $R \sim U([0, 1])$. This gives an average separation of 15.8 µm and maximum and minimum separation of (max: 23.2 µm, min: 7.94 µm) between scan positions.

Number of diffraction patterns

This is a parameter that can be investigated. However, as there is considerable overlap between the diffraction patterns, the number of diffraction patterns required is significantly fewer than standard, or Fourier ptychography. Simulation analysis indicates that at least 6 diffraction patterns are required [82].

3.2.4 Alignment procedure

Once the components are set up on the optical bench in their approximate locations, this procedure was followed to ensure correct alignment:

1. Ensure the illumination is collimated and uniformly illuminating more of the sample than required.
2. Place a CCD in the approximate location of the image plane of the microscope, located at the focal length of the tube lens.
3. Insert a sample with solid edges and known size, for example a USAF 1951 test chart.
4. Focus the sample onto the CCD with the z-direction of the mechanical stage.
5. Measure the magnification of the microscope by measuring the size of the known features on the test chart.
6. Move the camera to attempt to correct the magnification to the magnification of the objective lens.
7. Repeat steps 4, 5 and 6 until the measured and expected magnifications are identical. Confirm by measuring the size of the test chart features and comparing to their known sizes.
8. The CCD is now in the image plane of the microscope. Place the diffuser in this plane by measuring the distance between the tube lens and the location of the image plane.
9. Place the camera at 90° to the optical axis, between the tube lens and the image plane, add a mirror or beamspliter in the optical path to direct the illumination to this focussing CCD.
10. Repeat the magnification testing process to ensure the plane of the focussing CCD is in the image plane of the microscope.
11. Move the diffraction plane camera downstream of the diffuser by a short propagating distance, as discussed in Section 3.2.3.

12. Temporarily moving the diffuser, measure the magnification at the diffraction plane using the test card (this is the magnification required in the reconstruction algorithm).

13. The components are now correctly aligned for data collection. Once they have been aligned this process does not need to be repeated, even when changing the objective lens.

3.2.5 Ptychographic dataset collection

In order to collect a ptychographic dataset, the following steps are taken.

1. **Focus the sample onto the image plane.** The secondary focussing CCD is used for this. Once the sample is in focus on the focussing CCD, then it is also in focus on the diffuser. Remove the beam splitter to prevent unwanted reflections.

2. **Keep the sample in the starting position.**

3. **Capture the diffraction pattern using the diffraction plane CCD.** Ensure the exposure length is set so the image is not over or under exposed.

4. **Move sample to next position.** Further details about the position requirements are discussed below

5. **Repeat collection of diffraction images until all positions have been captured.** Depending on the field of view or image quality required, this can be from 4 to 100 diffraction patterns.

6. **If collecting a quantitative phase video, move back to starting position and repeat process.**

3.3 Image reconstruction

This section will describe how the collected ptychographical dataset can be processed to generate the complex images of the illumination with diffuser, and the sample. The ePIE (Section 2.8.3) was used to reconstruct the complex images of the illumination/diffuser and the sample. This is in contrast to the x-ray near-field ptychography research [77], [80]–[82], [131], which used the Difference Map algorithm [132], an alternative search algorithm that can be used for ptychography.

The ePIE algorithm was chosen as it tends to be a robust algorithm, that avoids local minima that cause issues such as phase vortices [81]. It was slightly modified to take account that the sample is magnified by the objective, and so is the sample's positions. The positions are multiplied by the magnification measured at the detector, M. Using the 20× objective gave a measured magnification of 26.85×, and the 4× gave 5.55×. The modified ePIE update functions are:

$$O_{j+1}(\mathbf{r} - M\mathbf{R_j}) = O_j(\mathbf{r} - M\mathbf{R_j}) + \alpha \frac{P_j^*(x,y)}{|P_j(\mathbf{r})|^2_{\max}} \left[\psi_j'(\mathbf{r}) - \psi_j(\mathbf{r})\right], \tag{3.9}$$

$$P_{j+1}(\mathbf{r}) = P_j(\mathbf{r}) + \beta \frac{O_j^*(\mathbf{r} - M\mathbf{R_j})}{|O_j(\mathbf{r})|^2_{\max}} \left[\psi_j'(\mathbf{r}) - \psi_j(\mathbf{r})\right], \tag{3.10}$$

where all the symbols are the same as Section 2.8.3 apart from the inclusion of M.

The angular spectrum propagator was used (as described in Section 2.4.4). This is because we are operating in the near-field, with a Fresnel number of 6.85×10^3. Clare *et al.* [82] use the Fresnel propagator, but as they are working in the X-ray domain, they will have smaller angles of diffraction, meaning that they can use this less accurate, paraxial solution (Section 2.4.2).

In addition, the camera length used in the propagation should also be scaled by the ratio of the measured magnification at the detector to the magnification of the microscope objective. This avoids a strong phase curvature appearing in the

reconstruction at the diffuser [77]. For the 20× objective used, and the measured camera length of 5 cm, the corrected camera length was 5.7 cm.

The image reconstruction procedure also used annealing (Section 2.8.3, to correct the mechanical stage positions; and background removal (which will be discussed further in Section 4.4.2, where it was first utilised). For samples that include multiple phase wraps (i.e. optically thick objects), it was also useful to use mPIE (Section 2.8.3).

3.4 Results

3.4.1 Example near-field ptychographic dataset and reconstruction

As a demonstration of the data input and output of the optical near-field ptychography's ePIE algorithm, Figure 3.7 shows a subset of 100 diffraction patterns that were captured using the optical bench setup. The sample used was pre-prepared frog red blood cells. These diffraction patterns were processed using the ePIE algorithm to give the results on the right. The output from the algorithm is a complex image of the diffuser, and the sample. These complex images are shown as the phase and modulus of the complex values. The following sections will show in detail the dataset collection and reconstruction for three samples. These samples were chosen assess the performance of the near-field ptychographic microscope:

1. **Red blood cells:** These pre-prepared frog red blood cells are a biological sample, one that represents the type of sample that would be a typical application of the microscope. They were used as a sample to show performance at different magnifications, and at small numbers of diffraction patterns.

2. **Glass microspheres:** This sample was made to evaluate the technique for optically thick samples. A small amount of index matching oil was dropped on the surface of a blank microscope slide. Several 210 µm-diameter glass

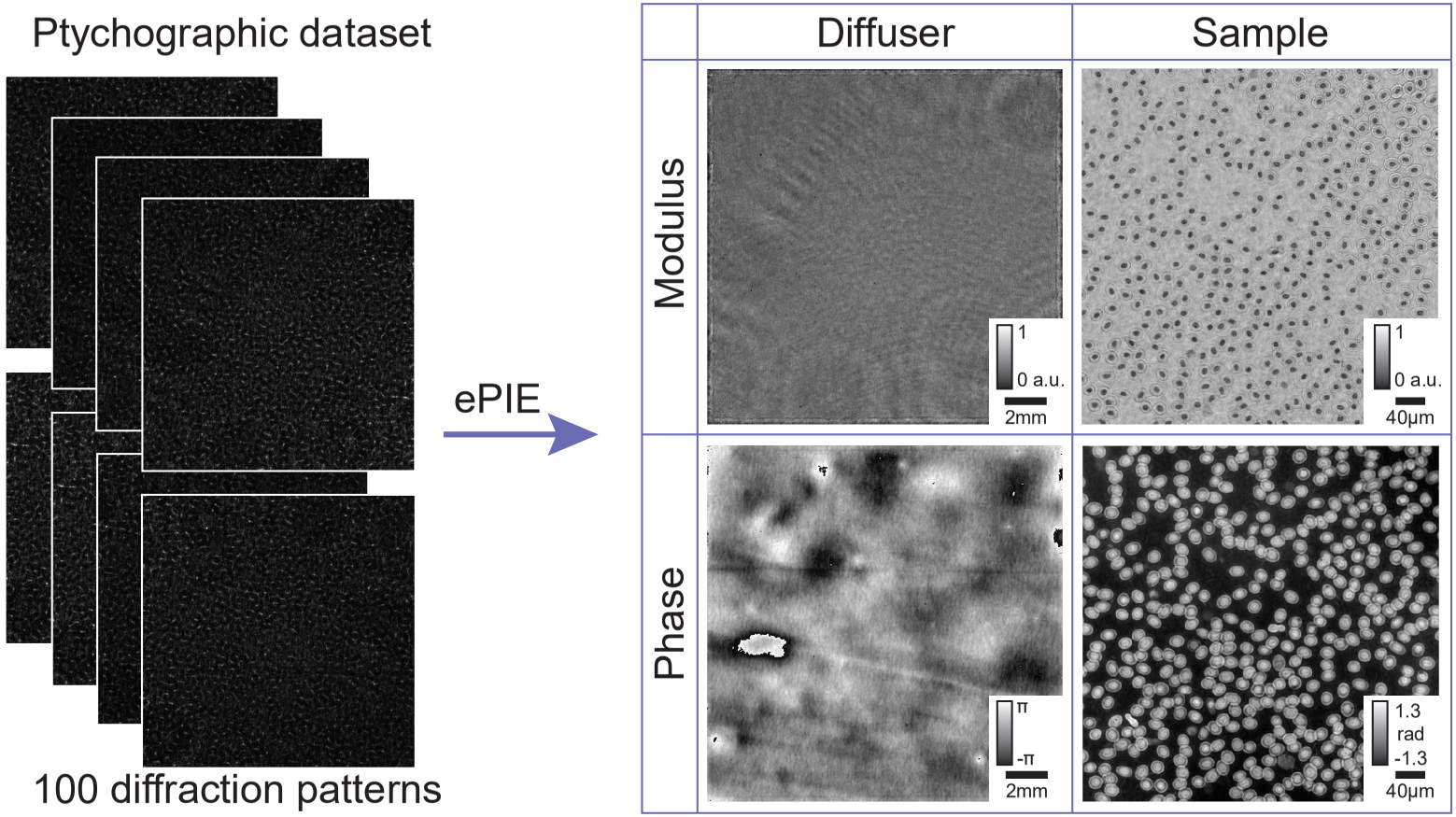

Figure 3.7: The 100 collected diffraction patterns are processed with the ePIE algorithm to generate complex images of the diffuser and sample

microspheres were sprinkled over the surface of the oil and a cover slip placed over the top and secured with transparent adhesive. As the microscope sample position is vertical the microspheres were allowed to settle before imaging.

3. **Singlet lens:** Lenses are important applications of QPI techniques. For example, contact lenses [36] have been characterised using a propriety ptychographic machine. A large field of view is required to get the most information from a lens characterisation. Lenses are transparent, and cannot be imaged using traditional microscopy techniques, but their thickness is proportional to their phase change. This means a lens can be used to assess the accuracy of the reconstructed phase as well as to test the technique's spatial phase sensitivity.

3.4.2 Results from red blood cells

The frog red blood cells were used as a sample to test the performance of the technique as the number of diffraction patterns were reduced. For this test, a 20× objective lens with NA=0.40 was used, whose magnification, M, at the plane of the diffraction CCD was measured as 26.85× using the USAF 1951 test chart. The first ptychographical dataset of 100 diffraction patterns were captured using the optical bench setup as shown in Figure 3.2.

This ptychographical dataset was processed using the ePIE algorithm as described in Section 2.8.3. The parameters for the probe and object update functions in the algorithm were $\alpha = \beta = 1$. The phase image shown in Figure 3.8(a) was reconstructed with 200 iterations of the algorithm. The complex-valued reconstruction of the diffuser shown in Figure 3.8(b), the 'probe' in the algorithm, was used as an initial estimate for all the subsequent tests. This calibration step reduces the number of iterations required for the algorithm to converge in future reconstructions. As the number of diffraction patterns used is reduced, using a better initial guess of the probe also aids

the phase retrieval process in avoiding stagnation in local minima.

Next, a second dataset of only 25 diffraction patterns was collected using the same setup. The reconstruction procedure was repeated, but this time using the diffuser profile reconstructed from the first dataset as an initial estimate of of the probe, $p(x, y)$. As the probe will change very little between experiments, the step size in the probe update function of the ePIE algorithm was reduced to $\beta = 10^{-4}$. ePIE this time generated the phase image shown in Figure 3.8(c). A further five diffraction patterns was discarded from the data set and the reconstruction repeated, producing the phase image in Figure 3.8(d). Discarding more and more of the diffraction patterns resulted in Figure 3.8(e)-Figure 3.8(g). Comparing these phase reconstructions visually with the reconstruction using 100 diffraction patterns, it can be seen that the image quality is good down to six diffraction patterns. The red blood cell substructures can be observed and the background is smooth. When using six diffraction patterns, the structures of the cells themselves can be observed clearly, but the background starts to become noisy. Below four diffraction patterns, the reconstruction becomes poorly conditioned and swamped by noise. To demonstrate the phase sensitivity (Section 2.9) of the technique when reducing the number of diffraction patterns, a cross-section dissecting the same single cell along the line in the magnified view in Figure 3.8(a) and Figure 3.8(c-g) was compared. Despite increasing background noise, the phase accuracy of the reconstructions remains consistent, even for the four diffraction pattern case.

In terms of data acquisition time, using unoptimised code running through the MATLAB image acquisition toolbox it took approximately 0.1s to move the sample and capture a diffraction pattern with a 200 µs exposure. The total time simply multiplies this figure by the number of diffraction patterns, giving a current usable maximum data collection rate of $\sim$ 2Hz. Data reconstruction using the ePIE algorithm was extremely fast when using the previously reconstructed image of the diffuser as

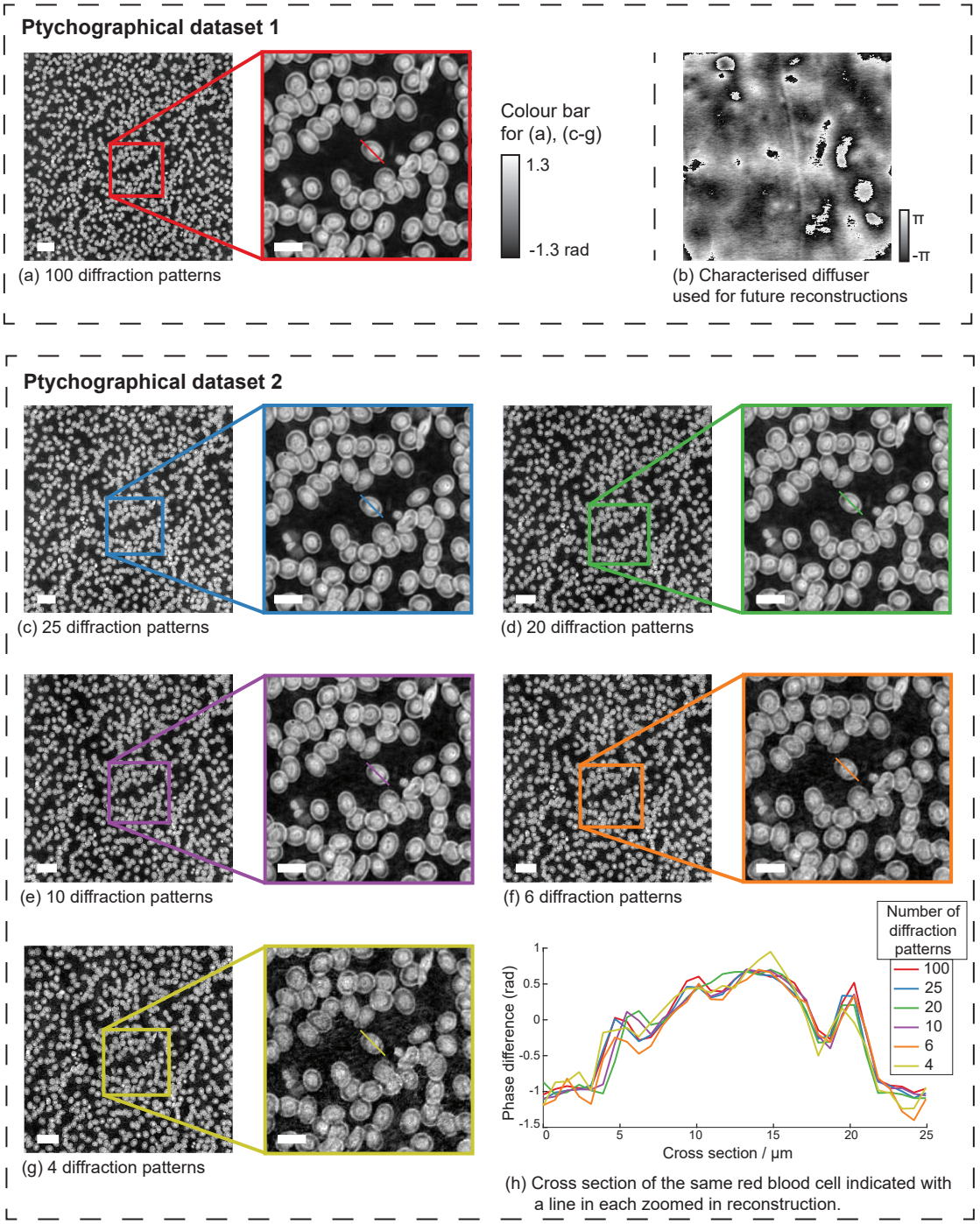

Figure 3.8: Phase reconstructions of frog red blood cells. For each subfigure (a), (c-g), the image on the left is the full field-of-view (Scale bar = 50 µm), and the image on the right is the zoomed-in portion indicated by the boxes (Scale bar = 20 µm). (h) shows cross-sections through a single red blood cell, taken along the lines indicated in each of subfigures (a), (c-g).

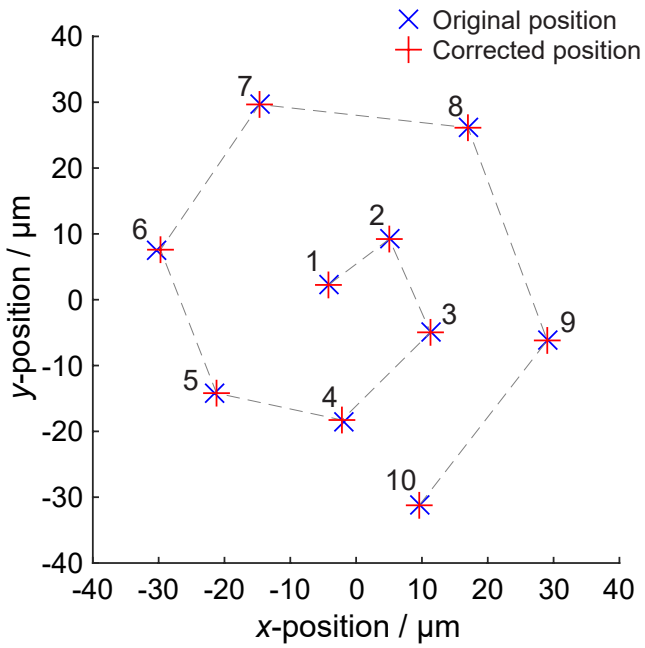

Figure 3.9: The position annealing corrects for errors between the measured and true stage positions.

an initial estimate of the probe. For the case of four diffraction patterns, using the MATLAB parallel processing toolbox and an Nvidia GeForce 1080 GPU, ePIE converged within ten to twenty iterations, which took between 0.7 and 1.2 s (including position annealing (Section 2.8.3 and background compensation (described later in Section 4.4.2). Figure 3.9 shows how the position annealing can make small adjustments between the position the stage reports it is in, compared to its true position. This addition makes the reconstruction algorithm robust to component misalignments.

One of the advantages of using near-field ptychography with a standard microscope platform is that it is very simple to change the magnification. To demonstrate this, the same red blood cells sample was used, and the 20× objective lens replaced by a 4× lens of NA=0.10 (whose magnification at the diffraction-capture CCD was calibrated as 5.55×). In this case, ten diffraction patterns (taking $\sim$ 1s) were collected using the same

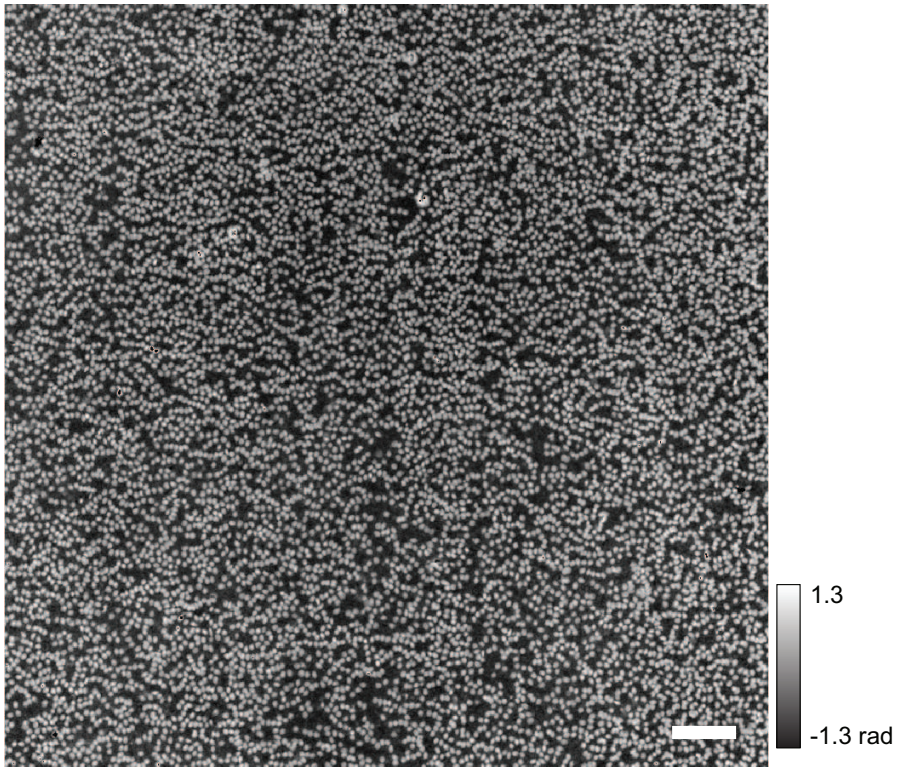

Figure 3.10: The same frog red blood cell from Figure 3.8, using an objective lens with 4× magnification. 10 diffraction patterns, captured in 1s, were used to obtain this image. (Scale bar = 200 µm).

scan positions as in the previous experiments. An identical reconstruction process, using the diffuser reconstruction from the previous experiments to seed the algorithm, generated the image in Figure 3.10. (Note that not all the cells are in focus in this large field-of-view.)

3.4.3 Results from glass microspheres

The sample thickness that can be handled by both ptychography and Fourier ptychography is limited to a region where the interaction of the sample with an illumination function is accurately modelled by a multiplication – the multiplicative approximation. Beyond this limit, conventional reconstruction algorithms fail and computationally expensive alternatives such as multi-slice ptychography must be

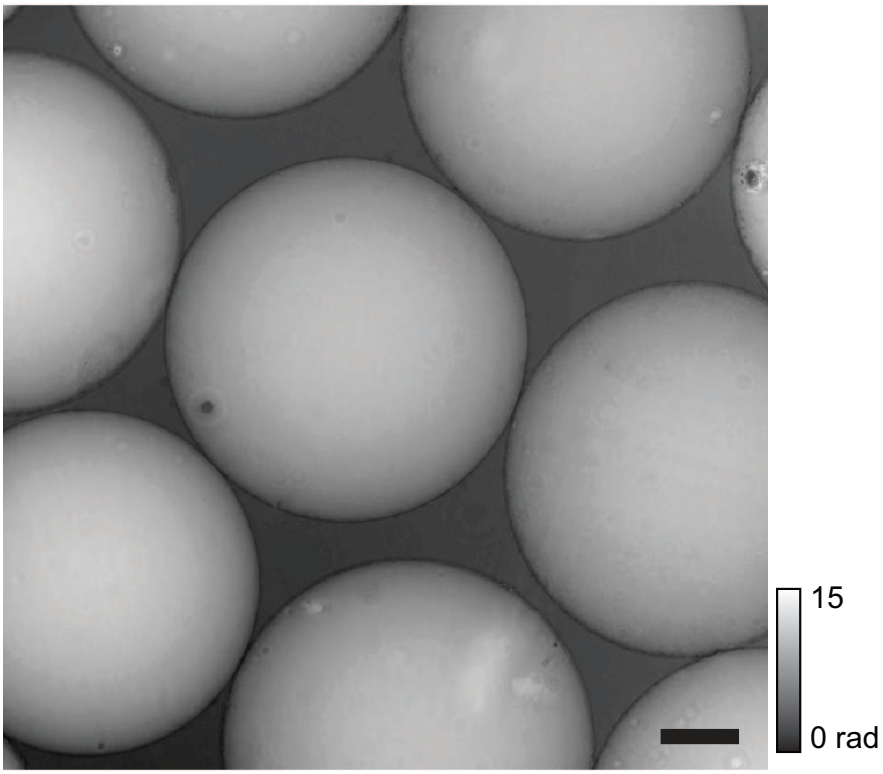

Figure 3.11: 210 µm diameter glass microspheres suspended in index matching oil. This image was reconstructed from 100 diffraction patterns, captured with a 20× magnification, 0.4NA objective lens. (Scale bar = 50 µm).

employed [75], [133]. In this near-field configuration, the equivalent interaction is between the image of the sample produced by the microscope and the optically thin diffuser, which can always be modelled by a multiplication. Consequently, thicker samples have no effect on the accuracy or success of the reconstruction process (although they may not be imaged entirely in focus). In this way the complex-valued images created by this setup are more like those of digital holography, and so can be propagated to different focal planes, and further processed to remove aberrations.

To show the capability of the technique when dealing with optically thick samples, a dataset of 25 diffraction patterns was collected in the same way, using the 20×, NA=0.4 objective lens. 210 µm-diameter glass microspheres (Refractive Index (RI) 1.51-1.52) suspended in index-matching oil (RI: 1.5124) were used as a sample. The thickness limit, T, for conventional ptychography can be approximated by:

$$T \leq \frac{(\delta r)^2}{\lambda} \tag{3.11}$$

$$\leq \frac{(14.8 \times 10^{-6})^2}{675 \times 10^{-9}} \tag{3.12}$$

$$\leq 30\,\mu\text{m}, \tag{3.13}$$

where δr is the image resolution [134]. This sample is therefore much thicker than the limit imposed on conventional ptychography, and suitable test sample.

mPIE [97], as described in Section 2.8.3, was required for this sample as its reconstructed image has multiple phase wraps due to its thickness. Reconstructions from ePIE are prone to phase vortices (as has also been noted in the case of the Difference Map algorithm for x-ray near-field ptychography [81]), and mPIE's ability to escape local minima reduces these artefacts substantially. The diffuser reconstruction from the red blood cell experiments was used as an initial guess of the probe to start the algorithm. The step size in the ePIE update functions were reduced

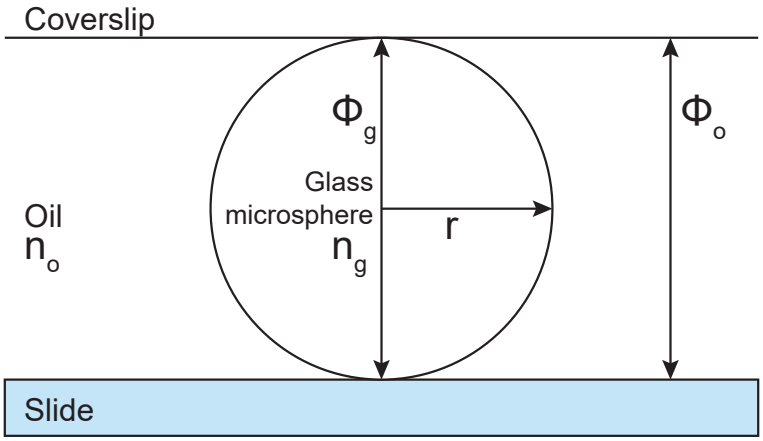

Figure 3.12: Graphical model of the glass microsphere (refractive index n_g, radius r, phase shift at the centre of the sphere ϕ_g) suspended in oil (refractive index n_o, phase shift ϕ_o.

to values of $\alpha = 0.2$ and $\beta = 10^{-4}$. For the momentum acceleration in mPIE a batch size, T, equal to the number of diffraction patterns in our experiment (25) was used and the update parameter $\eta = 0.99$. Figure 3.11 shows the resulting unwrapped phase reconstruction of the microspheres. They are imaged with both an excellent spherical profile and detailed high resolution features on the spheres' surface. The phase shift at the centre of the central sphere is 7.5 rad. Using (2.85) and with reference to Figure 3.12:

$$\phi_g = \frac{2\pi 2 r n_g}{\lambda}, \qquad \phi_o = \frac{2\pi 2 r n_o}{\lambda}, \qquad \phi_g - \phi_o = 7.5 \text{ rad} \tag{3.14}$$

$$\begin{aligned} \phi_g - \phi_o &= \frac{2\pi 2 r n_g}{\lambda} - \frac{2\pi 2 r n_o}{\lambda} \\ &= \frac{2\pi 2 r}{\lambda}(n_g - n_o) \\ (n_g - n_o) &= \frac{7.5 \times 675 \times 10^{-9}}{2\pi \times 210 \times 10^{-6}} \\ &= 0.0038. \end{aligned} \tag{3.15}$$

equating to a refractive index difference between the oil (n_o) and the glass (n_g) of 0.0038

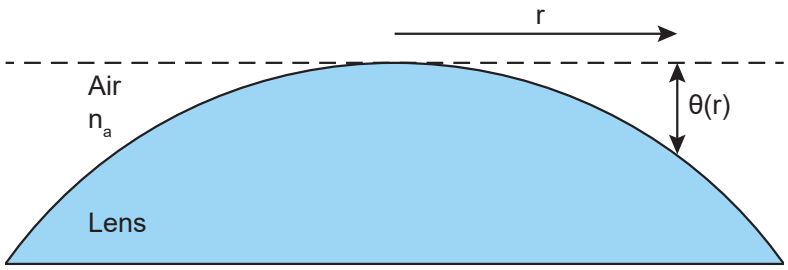

Figure 3.13: The model used to calculate the cross-section height of the lens from the phase reconstruction.

- well within the specified range. Dust and grease on the surfaces of the microscope slide are also reconstructed, although they are somewhat out of focus. Such features would cause artefacts in both conventional and Fourier ptychography.

3.4.4 Results from singlet lens

As a final analysis of the technique, a Thorlabs LA1131-A, 1 inch diameter, 50mm focal length plano-convex lens was chosen. The lens was secured to the $x-y$ translation stage such that the centre of the lens was approximately centred on the optical path of the microscope. 100 diffraction patterns were captured using the experimental procedure described above, but the step size in the scan position spiral was expanded by a factor of four to extend the field of view. Again, mPIE was used to reconstruct this data to avoid phase vortices associated with the large number of phase wraps, and the original diffuser reconstruction from the red blood cell experiment was used to initialise the probe in the reconstruction.

A central cut-out from the resulting reconstruction, of diameter 3000 pixels, is shown in Figure 3.14(a). The apparent centre of the lens is offset from the centre of the reconstructed field of view, due to a combination of a slight tilt and shift of the lens mount. Using (2.85) and with reference to Figure 3.13, we can convert from the radial average phase difference $\overline{\phi(r)}$ at radius r from centre, in the unwrapped reconstructed

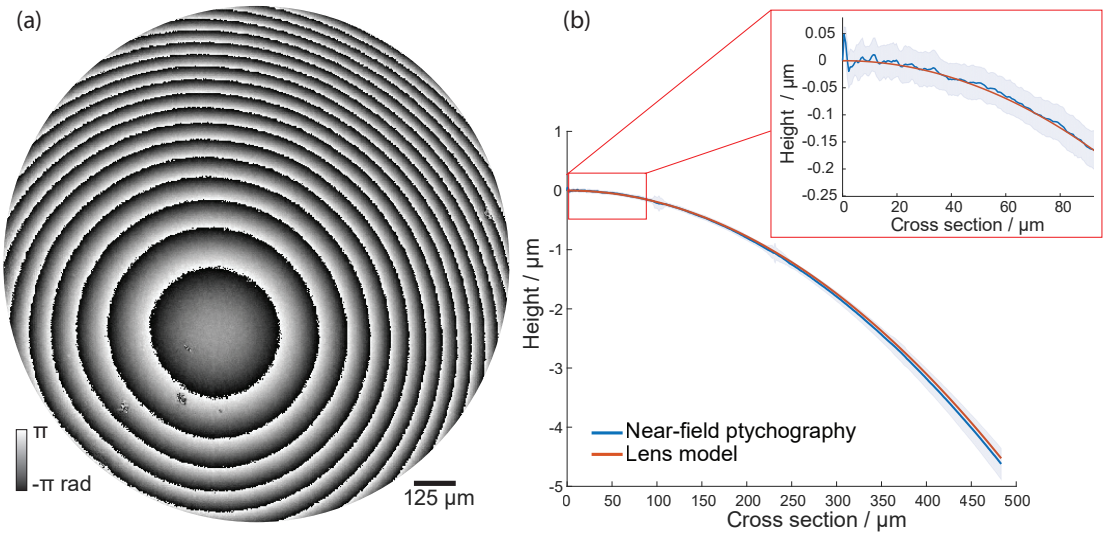

Figure 3.14: (a) A quantitative phase reconstruction of a singlet lens, focal length 50mm. (b) A comparison of the expected profile of the lens with the unwrapped reconstruction using near-field ptychography. The blue line is the radial average of the height change across the lens and the blue shaded surrounded is the radial standard deviation. The orange line is the model for the lens, based on its focal length.

image of the lens, to its cross-section height difference $h(r)$:

$$\overline{\phi(r)} = \frac{2\pi}{\lambda} h(r) n_a \tag{3.16}$$

$$h(r) = \frac{\overline{\phi(r)}\lambda}{2\pi}, \tag{3.17}$$

where $n_a = 1$ is the refractive index of the air. Figure 3.14(b) shows a comparison between the expected spherical profile of the lens, calculated from its data sheet, to its experimentally calculated radial average height. The blue line shows the radial average of the ptychographical reconstruction of the lens and the blue shaded region shows its standard deviation. Given that the radial average includes any dust or grease on the surface of the lens, this shows excellent agreement between the measurements taken using near-field optical ptychography and the expected profile of the lens over the whole profile.

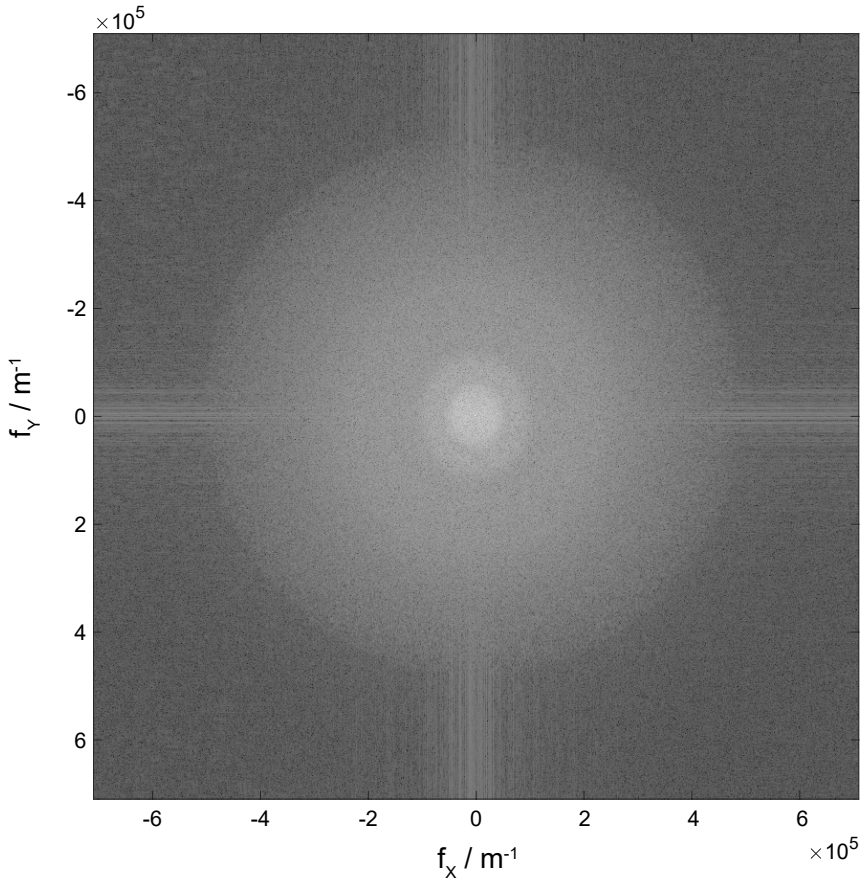

Figure 3.15: Two-dimensional Fourier transform of the reconstructed image in Figure 3.8(a) with the near-field ptychographic setup. (The log of the Fourier transform is shown here to aid clarity)

3.4.5 The numerical aperture and resolution of the microscope

Taking the two-dimensional Fourier transform of the reconstructed image from Figure 3.8(a) when using the 25× objective lens gives the plot in Figure 3.15. A clear two-dimensional passband filter, as expected for a coherent imaging system (Section 2.5.1), can be observed as the circle in the frequency domain, with a cut-off

frequency, $f_0 = 4.89 \times 10^5 \mathrm{m}^{-1}$. Using (2.60):

$$f_0 = \frac{w}{\lambda z_i} \tag{3.18}$$

$$= \frac{\sin^{-1}(\mathrm{NA})}{\lambda} \tag{3.19}$$

$$\mathrm{NA} = \sin(f_0 \lambda) \tag{3.20}$$

$$= 0.32. \tag{3.21}$$

The manufacturer's value for the NA of the objective lens is 0.4, which shows that the NA of the system is limited by the NA of the objective. Using Sparrow's criterion for coherent illumination (Section 2.5.1), the resolution of the system is:

$$d = \frac{2.976 z_i \lambda}{2\pi w} \tag{3.22}$$

$$= \frac{0.47\lambda}{\mathrm{NA}} \tag{3.23}$$

$$= 0.99\,\mu\mathrm{m}. \tag{3.24}$$

3.5 Conclusions

This work has demonstrated a novel optical QPI technique based on near-field ptychography. It has shown how to step up the technique on the optical bench, and analysed some of the key experimental parameters required to optimise the procedure. The technique is simple, and is implemented as an 'add-on' to a standard microscope. It is also simple to change the magnification of the system, without realignment. As a ptychographic technique, it does not require a reference beam, and any imperfections or aberrations in the optics are separated from the object. It is also a robust technique, working with a range of parameter values and tolerant to component misalignments.

The technique was quantitatively tested using a range of samples, from both the physical and biological domains. The tests using the singlet lens and glass

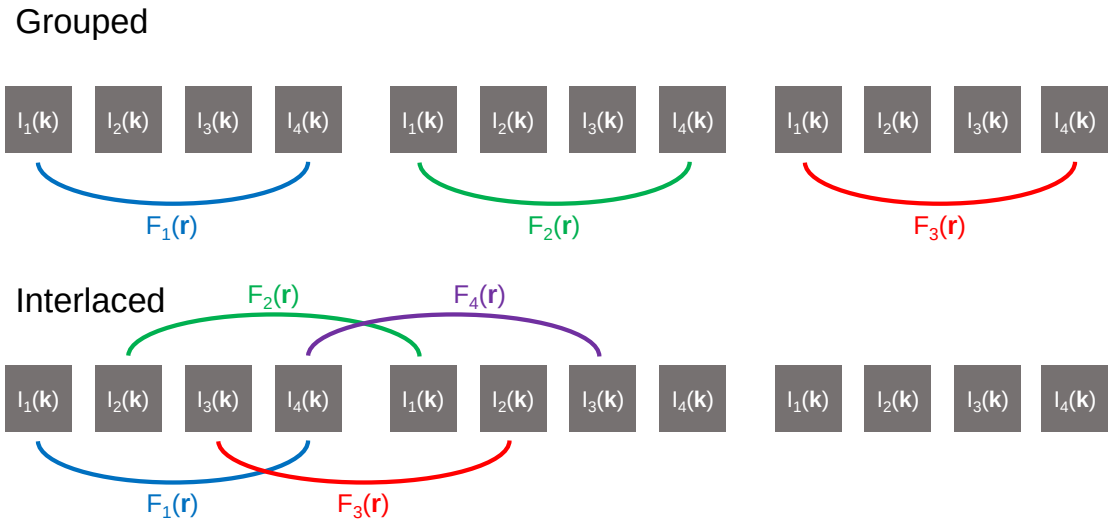

Figure 3.16: A comparison of grouped and interlaced methods for quantitative phase videos using ptychographic data. In the grouped method, all four diffraction patterns, $I_{1\leftarrow4}$, of one data acquisition cycle are used to reconstruct one quantitative phase video frame, F. Then the next cycle of ptychographic data is used to reconstruct the next frame. In the interlaced method, quantitative phase video frames are reconstructed sequentially from the combined cycles of ptychographic data.

microspheres have shown that the technique can produce high quality and accurate phase images, over a large field of view. A key result, as demonstrated with the red blood cells, is that the number of diffraction patterns required using this technique is significantly fewer than standard, and Fourier ptychography. This reduces the amount of data collection at acquisition, and hence would increase the frame rate of quantitative phase videos. It also reduces the time required to reconstruct the phase images, using ePIE. In comparison to x-ray near-field ptychography, or Fourier ptychography, our setup is also capable of imaging optically thick objects. This is because the exit wave from the diffuser is the result of the interference between the diffuser and the image of the sample, which will always satisfy the multiplicative approximation in the ptychographical reconstruction algorithms.

This work was published in the OSA's *Optics Express* [128]. It has subsequently been cited by Zhang *et al.* [135], as an inspiration for their work in near-field Fourier

ptychography.

3.5.1 Future work

There are also some improvements that can be made in a future implementation. One of the key issues in the setup is the translation stage. It takes time to move from one position to another. A first improvement would be to optimise the movement of the stage, so that it covers the least distance when going between positions, for example using the Metropolis algorithm [136] as in [130]. Faster piezo scanners would also complete the movement quicker.

For quantitative phase videos, consisting of several frames of phase images, interlaced processing could be utilised [45]. When collecting a continuous sequence of diffraction patterns, instead of processing all of one grouping of n collected diffraction patterns as a single video frame, F, before moving to next set of n diffraction patterns, the algorithm could take the first n diffraction patterns from 1 to $1 + n$. Then for the next frame, the diffraction patterns 2 through to $2 + n$ can be used, then 3 through to $3 + n$ etc.... A comparison of these grouping and interlaced methods for four diffraction patterns per cycle is given in Figure 3.16. Although this would give a $n\times$ faster frame rate than processing each n diffraction patterns as a single set, the information contained within that frame still comes from across all n diffraction patterns.

3.5.2 Further work

For live biological samples, such as cells, it would be preferable to have no sample movement at all, to prevent disruption of the sample. A suitable avenue for investigation is therefore one that speeds up the acquisition process, while removing the sample movement. An SLM would be a suitable tool for this as it is able to provide diversity between the collected diffraction patterns without physically moving. This

idea is a key part of this research and is expanded upon in Chapter 5.

Chapter 4

Characterising a Spatial Light Modulator using Ptychography

4.1 Introduction

In this Chapter, it is described how ptychography was used to characterise an SLM. Firstly it is explained why characterising an SLM is important as well as making reference to the existing techniques used to characterise an SLM given in Section 2.11.4. The novel technique for using standard ptychography to image and characterise an SLM and how the device's errors can be corrected is described. A demonstration of how the technique works is given by using ptychography to image this device, correct and calibrate it, and image it again to ensure the correction has worked. This work was published in Optics Letters [137].

4.2 Why is it necessary to characterise a Spatial Light Modulator?

As was shown in Section 2.11.3, SLMs are relatively new devices, and have several optical imperfections. Several of the QPI applications described in Section 2.7 make the assumption that the SLM is perfect. It is therefore important to assess how imperfect the SLM is, in order that we can challenge the assumptions made, but also identify ways to reduce the effect of these imperfections.

In addition, a key component of the proposed imaging system as described in Chapter 5 will be an SLM. In order to use this component correctly, it is important to calibrate it and observe its performance. Of the limitations of the SLM proposed in Section 2.11.3, the ones that can be corrected without changing the hardware are the linearisation of the phase response and the face curvature of the device. These are the areas of interest in this characterisation research.

Several different solutions (described in Section 2.11.4) were investigated to characterise SLMs, but it was shown that they can either image the SLM over a small area, or at a larger area at lower resolution. It therefore appears that standard ptychography (Section 2.8.1) may be a more suitable candidate for characterising SLMs. As a technique, it generates precise, high resolution phase images, over a large field of view. This will allow us to quantify the phase response of the SLM, as well as the curvature across the whole SLM, in great detail.

4.3 Dataset acquisition

4.3.1 Theoretical setup

Conventional ptychography, as described in Section 2.8.1 was used to measure the SLM's phase altering properties, as shown in Figure 4.1. The probe was formed using

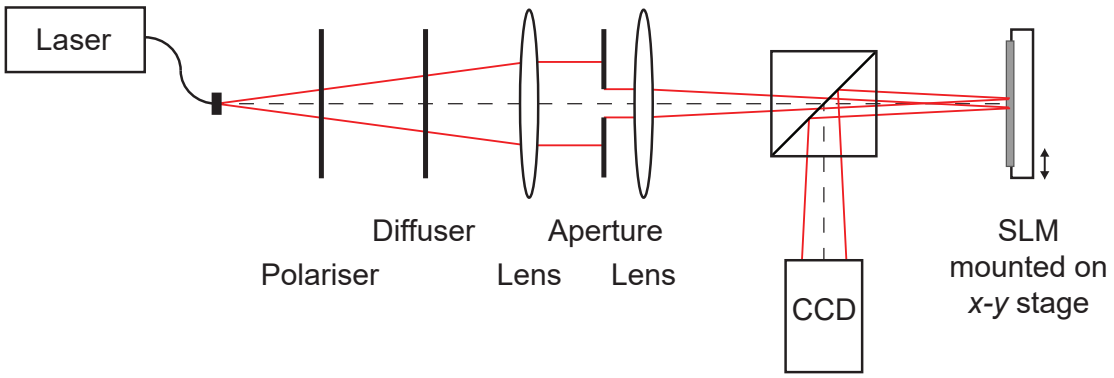

Figure 4.1: The optical setup for imaging an SLM using ptychography. The SLM is mounted on a mechanical *x*-*y* stage and moves independently to the rest of the components.

a laser which is polarised and brought to a focus. The SLM is placed slightly downstream of the focal point. The scattered probe is modulated by the SLM and reflected onto the detector.

4.3.2 Optical bench setup

The setup used for the experiments is shown in Figure 4.2. The following sections explain why each piece of equipment was used, and particular issues that arose throughout the experimental setup process.

Laser probe

A 675 nm laser was used as the illumination for the probe beam. Long exposures were used to reduce the effect of the SLM's flicker and so the laser was set to a low power. The illumination was focused and passed through an aperture so the probe size on the SLM was approximately 1 mm in diameter. When choosing the size of the probe, it is a trade off between image resolution and coverage. A spatial resolution in the reconstruction of 2 µm is required to resolve the 8 µm pixels of the SLM. For the probe to be properly sampled according to the Shannon theorem (Section 2.5.1), half of the camera's 1024 $\times$

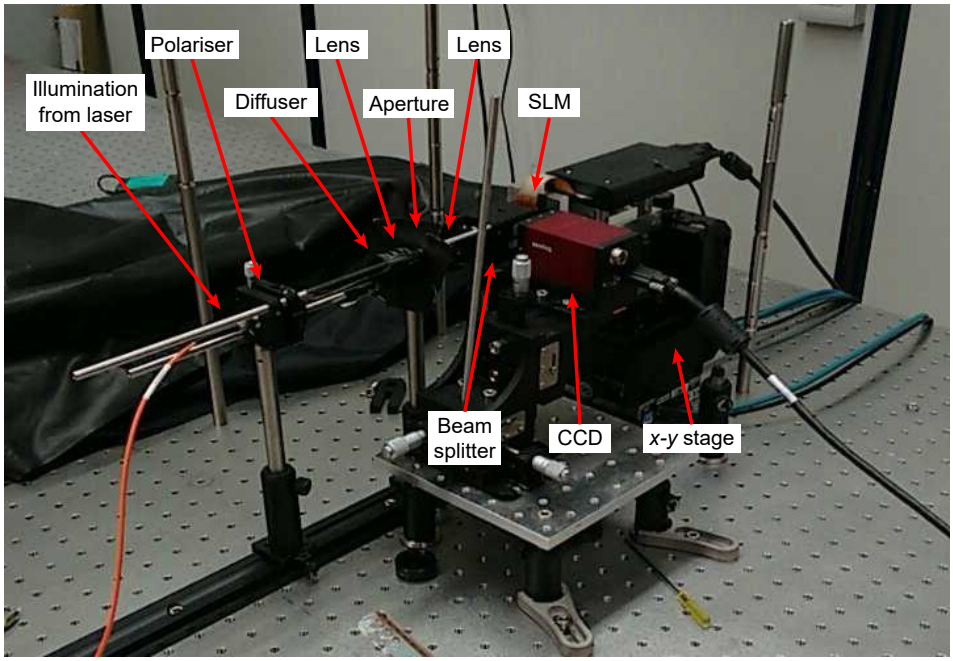

Figure 4.2: The optical bench setup used for characterising an SLM with ptychography.

1024 pixels need to be filled. This means a probe size of $2\,\mu m \times 512 \approx 1\,mm$ is needed. To cover the entire SLM, (40×70) probe positions were required.

Polariser

The incident polarisation for phase only modulation on the SLM is on the long display axis. It was therefore necessary to introduce a polariser between the light source and the SLM. Any light that is not polarised correctly when interacting with the SLM will be reflected without being modulated. To identify at which angle the polariser needed to be oriented in order to be correctly aligned with the SLM, a simple experiment was performed. Firstly, the position was roughly found by finding the orientation at which the SLM reflected no light. This is the position at which the polariser is in line with the *short* axis of the SLM. Rotating the polariser by 90° means that it is in approximately the correct orientation. Data collection and reconstructions were then performed for several orientations. The background removal code which will be described in

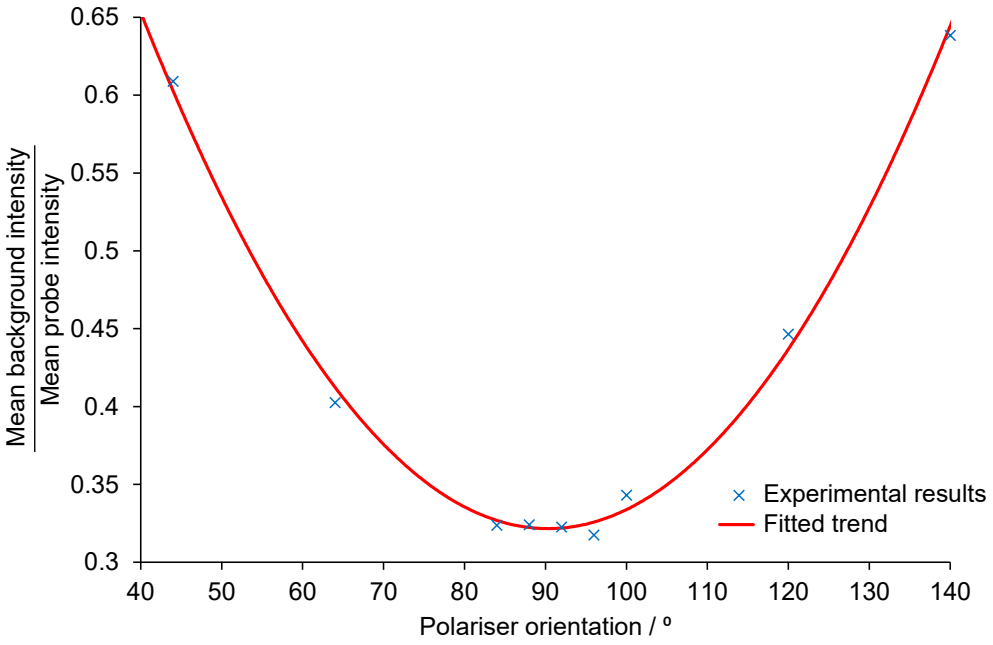

Figure 4.3: Graph of polariser's orientation against the ratio of mean background intensity to mean probe intensity. The crosses indicated measured values and the red line shows the fitted trend (Polynomial, $R^2 = 0.9966$). When the polariser is in line with the long axis of the SLM, the amount of light just reflected is at a minimum. Using this technique the minimum can be found, and so the polariser is in the correct orientation.

Section 4.4.2 was used to separate the part of the probe illumination that had just been reflected from the SLM (the background) from the part that had interacted with the SLM (the probe). The graph of orientation against the ratio of probe to background is shown in Figure 4.3. The polariser was then kept in the orientation with the smallest amount of reflection, at the minimum of the graph.

Diffuser

It was found early on in experimentation that there appeared to be reflections present in the final reconstructed image. There are many reflective surfaces in the optical components; the SLM, the front of the CCD and the faces of the beam splitter. A weak diffuser was placed in the laser beam to make the beam more dispersed. Several different diffusivity level diffusers were trialled; too weak and the reflections were present, too strong and the beam is too dispersed. The diffuser also introduced structure into the probe, which makes it easier to recover using the ePIE algorithm as it introduces higher frequencies and features into the signal.

The Spatial Light Modulator (SLM)

The SLM is a reflective optical device that modulates the phase of an incident coherent light beam. The SLM used was a Holoeye Pluto phase only spatial light modulator that operates with visible light (420 nm to 700 nm). The basic specification of the SLM used is given in Table 4.1, and a picture of the device is shown in Figure 4.4.

It is addressed using a standard DVI signal from a PC's graphics card and so behaves as an external monitor. The SLM driver unit converts an incoming 8-bit grey level signal using a LUT via a voltage level to a phase modulation value. This means that each pixel is able to impose its own independent phase change on incoming light. As the LUT needs to be set for the specific laser wavelength, it is necessary to calibrate the relationship between grey level and phase retardation. This is discussed further in

Table 4.1: Device specification for Holoeye Pluto phase only SLM [121].

Device name	Holoeye PLUTO
	Phase only spatial light modulator
Part number	HED 6010 xxx
Type	LCOS (reflective), Active Matrix LCD
Phase levels	256 grey levels
Active area	15.36 mm $\times$ 8.64 mm
Nominal resolution	1920 $\times$ 1080 pixels
Pixel pitch	8.0 µm
Fill factor	87%
Image frame rate	60 Hz
Wavelength range	420 nm to 700 nm

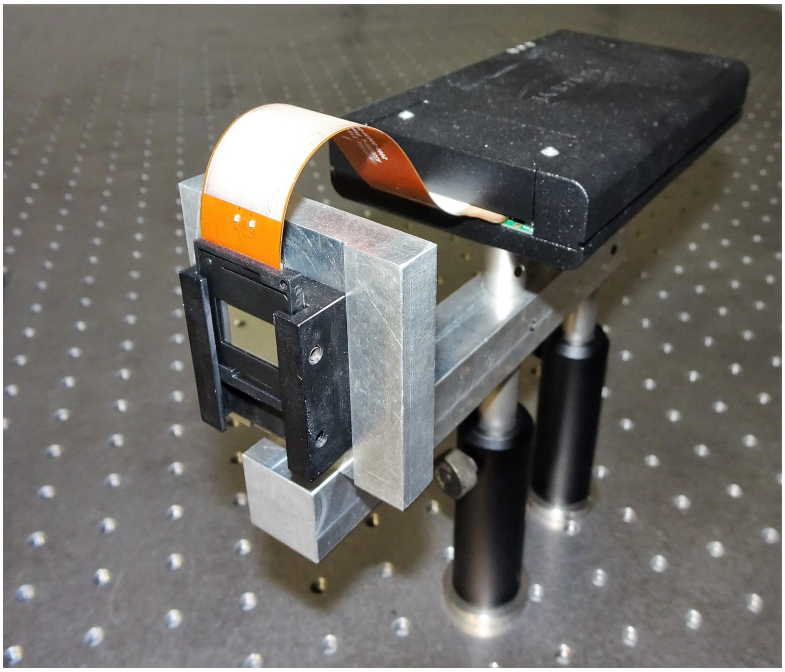

Figure 4.4: The Holoeye Pluto phase only SLM attached to the driver unit.

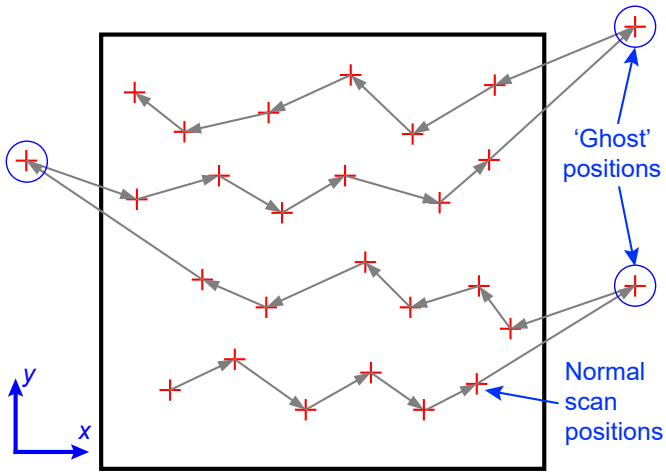

Figure 4.5: A typical scan pattern used to compensate for backlash. Diffraction patterns are not captured at the 'ghost' positions in circles, instead the probe is moved far to the side of the object to compensate for x-backlash. It is also moved up vertically and therefore can use gravity to compensate for y-backlash.

Section 4.6.1. Due to the nature of the display unit, it exhibits a slight 'flicker' [138], with a refresh rate of 60 Hz.

Translation stage

The SLM was mounted independently on a Newport XPS-Q4 $x - y$ mechanical stage such that the probe could be scanned along the surface of the SLM. The stage moved vertically in y and horizontally in x through a rectangular grid of positions with a pitch of 200 µm. To avoid the raster grid pathology [83], as outlined in Section 2.8.2, random $x - y$ offsets within the range ± 40 µm were added to each position.

Ptychography relies heavily on the *a priori* knowledge of the scan positions. In practice however, there are often imperfections in how the stage operates and therefore the positions are not physically where they have been programmed to be. One of the key issues is known as 'backlash'. This is an effect where there is no output motion when the direction of motion is reversed. This is a result of relative movement between the mechanical parts, such as the gear teeth, and so is repeatable and can be

compensated for. Instead of the standard scanning technique of moving from position to position, an additional 'ghost' position was used at the edge of each line, as shown in Figure 4.5. Additionally, work has been done in reducing the reliance on knowing the exact positions for ptychography [98], as described in Section 2.8.3 and this annealing code was included in the reconstruction procedure.

Camera

The camera used was a Allied Vision 16 bit CCD detector (2048 $\times$ 2048 pixels on a 7.4 µm pitch). To keep the NA of the system as large as possible, the camera length (the distance between the SLM and the camera) was minimised. After correcting for the refractive index of the beam splitter, the measured camera length was 4.6 cm. The NA of the system is therefore $\left(\sin\left(\tan^{-1}\left[\frac{0.75}{4.6}\right]\right)\right) = 0.16$. Using Sparrow's criterion (Section 2.5.1), the expected resolution of this setup in approximately 2.8 µm.

The detector was binned by two in order to reduce the data size and improve the Signal to Noise Ratio (SNR), and each diffraction pattern had an exposure length of 1.8s. The exposures were long to average out phase flicker caused by the SLM [138].

4.4 Image reconstruction

The ePIE algorithm [91], as described in Section 2.8.3 was used to reconstruct the phase profile produced by the SLM from collected ptychographic dataset. Additional steps were required for this particular setup, as outlined below.

4.4.1 Choice of propagator

The propagator used for this setup was the Fresnel propagator (Section 2.4.2). A known phase curvature was added before propagation in order to correct for the curvature of

the probe. The Fresnel number for the system is:

$$N_F = \frac{w^2}{\lambda z} \tag{4.1}$$

$$= \frac{((1 \times 10^{-3})/2)^2}{675 \times 10^{-9} \times 4.6 \times 10^{-2}}$$

$$= 8.05, \tag{4.2}$$

which is > 1, justifying the use of the Fresnel propagator.

4.4.2 Background removal

In order to reduce noise and reflection-like artefacts from the unmodulated polarisation states from the SLM, it is necessary to remove the 'background' signal. An approach similar to that of multimode ptychography [139]was adopted in the modulus constraint of the ePIE algorithm (2.123). The revised constraint, using the same symbols as Section 2.8.3, is:

$$\Psi'_j(\mathbf{k}) = \Psi_j(\mathbf{k}) \sqrt{\frac{I_j(\mathbf{k})}{\left|\Psi_j(\mathbf{k}, \mathbf{R}_j)\right|^2 + B(\mathbf{k})}}. \tag{4.3}$$

This assumes that the recorded diffraction pattern can be modelled as a incoherent sum of wavefront propagated from the SLM and a background that does not change between recordings. The background, $B(\mathbf{k})$ is initialised as a constant valued estimate with 5000 counts at every pixel, approximately 10% of the maximum pixel value of the captured diffraction pattern, $I(\mathbf{k})$. It is updated alongside the wavefront estimate using:

$$B'(\mathbf{k}) = B(\mathbf{k}) \left((1 - \delta) + \delta \frac{I_j(\mathbf{k})}{\left|\Psi(\mathbf{k})\right|^2 + B(\mathbf{k})} \right), \tag{4.4}$$

where δ is a adjustable constant that governs the update rate, and for all the reconstructions in this work was set to 0.01.

4.4.3 Data issues

To ensure the entirety of the SLM was scanned, 2800 (40×70) diffraction patterns were collected, which brought about a new problem for the technique. The data-dense nature of ptychography, generated from the large amount of redundancy, is something that considerably affects performance, especially for large field of views. As each diffraction pattern was over 8000KB, the total amount of data collected was approximately 21.8GB. This is obviously a considerable amount of data, especially for processing on a single GPU. Modifications were required on the algorithm to manage this; the diffraction patterns were grouped into blocks by their location, one block was loaded onto the GPU, processed and then swapped for the next block. This created a patchwork quilt effect, where each section of the final reconstruction was calculated separately and then joined together. However, the read-write times for this process are very high, as approximately 7GB are taken from disk and loaded onto the NVIDIA GTX 1080 GPU each time. A reconstruction of this size can take 6 hours to do 300 iterations of ePIE.

4.5 Physical sample reconstruction

Ptychography and ePIE were calibrated using a physical sample to assess the accuracy of the reflection mode measurements. The sample was a silicon chip, originally part of a CMOS image sensor and approximately $1\,\mathrm{cm}^2$, was covered in a thin layer of gold, and is shown in Figure 4.6. A cross section of the surface features on the chip were measured using a diamond stylus profiler as a reference measurement. The gold sample was then placed into the experimental setup shown in Figure 4.1, mounted on the x-y stage in place of the SLM. 225 (15×15) diffraction patterns were captured using the ptychography technique. The sample was reconstructed using the same ePIE algorithm. Figure 4.7a shows the resulting reconstruction of the sample. Using (2.85),

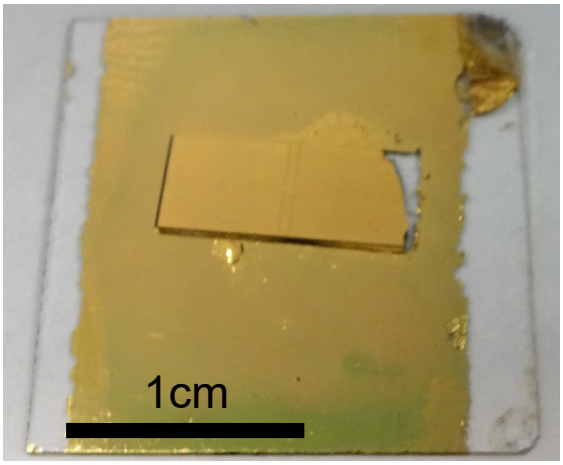

Figure 4.6: The gold-covered silicon chip, originally part of a CMOS image sensor, used as the calibration sample.

we can convert from a phase difference in the reconstructed image of the sample to feature heights $h(\mathbf{r})$:

$$\phi(\mathbf{r}) = \frac{2\pi}{\lambda} h(\mathbf{r}) n(\mathbf{r}) \tag{4.5}$$

$$h(\mathbf{r}) = \frac{\phi(\mathbf{r})\lambda}{2\pi}, \tag{4.6}$$

where $\phi(\mathbf{r})$ is the difference in phase value between position $\mathbf{r}$ and a baseline position, λ is the wavelength of the illumination, and $n = 1$ is the refractive index of the medium (air).

The location of the diamond stylus measurements was identified on the sample, and the surface profiles compared, as seen in Figure 4.7b. The two techniques match closely on the surface feature height, with a match of 4% or <10 nm. This is a good match considering that the cross section location was manually located.

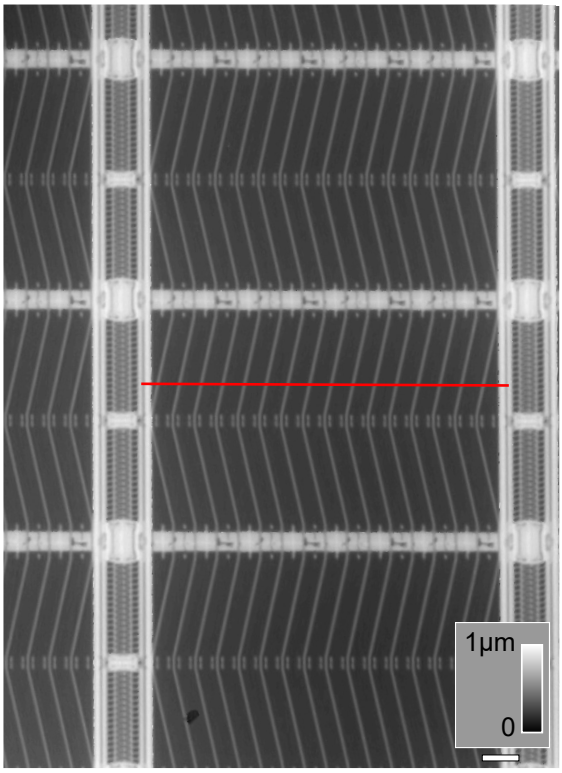

(a) Ptychographic phase reconstruction of the silicon chip. The red line indicates the approximate location of the cross-section through the sample and the grey scale indicates the feature heights. Scale bar 0.1mm.

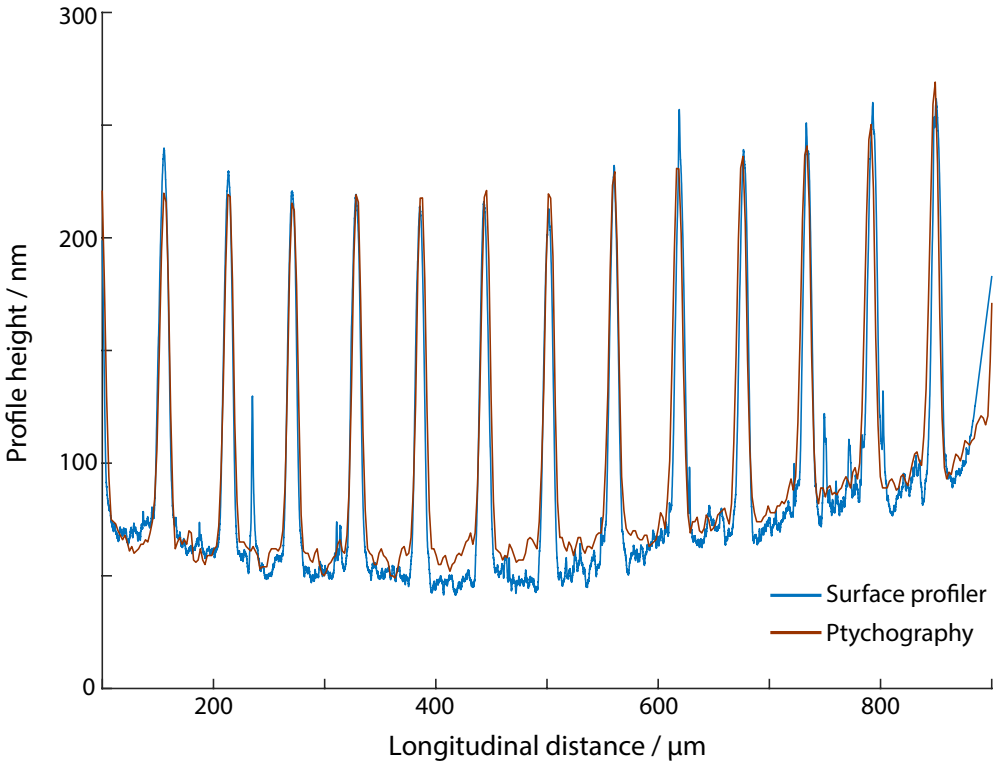

(b) Comparison of the cross section profile heights from the surface profiler and ptychography taken along the red line.

Figure 4.7: Comparison of ptychographical reconstruction and surface profile of a silicon chip.

(a) Four square patterns, each containing a random order of the 256 grey levels. Each block of identical grey levels is 16 square pixels. This did not work well as the large difference between small regions is difficult for ptychography to reproduce accurately.

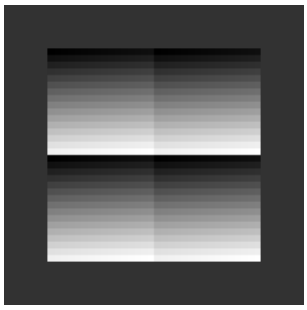

(b) Four square patterns, each containing the 256 grey levels in order from bottom left to top right. This did not work well as the curvature of the SLM influenced the phase response across each line.

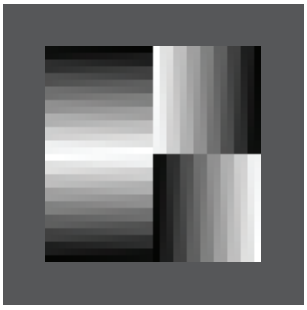

(c) The test pattern chosen to characterise the phase response of the SLM. It consists of four square patterns, formed from a snake pattern of the 256 grey levels. Each square pattern is rotated and flipped.

Figure 4.8: A variety of test patterns were tested to measure the phase response of the SLM.

4.6 Characterisation and correction procedures

Once the system was seen to be reconstructing good images of the physical sample, it was then possible to use ptychography to characterise and then to correct particular issues with the SLM. The two main issues identified were the gamma correction, which is how the SLM's phase responds when its grey levels are set, and flatness correction, which is required because the SLM is not optically flat. Both are feedback procedures, and are to a certain extent dependent on each other. It was found that it was best to perform the gamma correction before flatness correction.

4.6.1 Gamma correction

As the molecular alignment of the LCD does not follow a linear behaviour in relation to the applied voltage, the control of the phase retardation is also non-linear. The voltage levels of the SLM are mapped from the greyscale image received from the

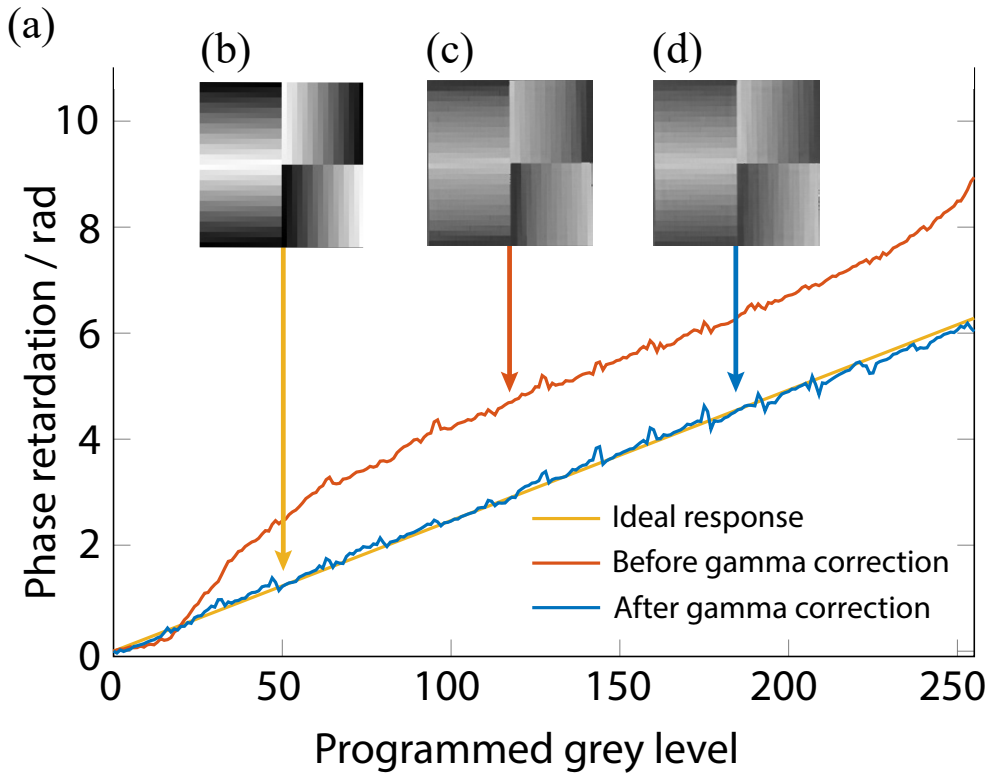

Figure 4.9: The phase response of the SLM before and after gamma correction. (a) Plots of the phase responses before and after correction. (b) Test pattern used for phase characterisation of the SLM. (c) Reconstructed phase of the SLM before gamma correction, with the red line its quantitative response. (d) Reconstructed phase of the SLM after gamma correction, with its blue line close to the yellow target response.

computer (between 0 and 255) by the driver unit using a LUT–or gamma curve [121]. An optimised gamma correction LUT is required to ensure the linearity of the phase response for the SLM for a given wavelength [120]. We can therefore establish an accurate relation between the greyscale, voltage and phase retardation by calibrating the driver's gamma curve. An ideal relation for this SLM is a linear phase over $0 - 2\pi$ for the grey levels $0 - 255$, for the wavelength of the illumination.

Calibration was achieved using a feedback mechanism. The default LUT was loaded onto the SLM's driver. Next, a test pattern was loaded onto the SLM. The purpose of the test pattern is to display all the grey levels between 0 and 255, so that their induced phase can be measured. Several different patterns were tried, as shown in Figure 4.8. As we aim for each grey level to have a step difference of 0.0245 rad, this measurement is very sensitive. The curvature of the display was a large error, and so the size of the test pattern was required to be as small as possible, whilst remaining statistically useful, so that the curvature across the pattern is small. Each grey level was assigned a box of size 16×16 SLM pixels. A snake-like order was also used, so that any two consecutive grey levels are close to each other on the display, to reduce the effect of flyback. There were 16 grey levels per line, so the test square was 256×256 SLM pixels. Finally, four test squares were used. Each test square was rotated and flipped relative to each other, so that none of them were in the same 2D orientation. Then, by averaging across all four test squares, the effect of the curvature across the display was minimised. The pattern was also placed in the centre, where the curvature is the smallest. Figure 4.8c shows the final test pattern used, with the yellow line in Figure 4.9 as the ideal linear relation between the programmed phase level and the phase retardation.

A scan of the area of the SLM on which the test patterns were displayed was achieved using the ptychographic method and the reconstruction results are shown in Figure 4.9. The mean of each of the phase levels of the reconstructed image of the SLM

was calculated and plotted in red in Figure 4.9. It can be seen that the default gamma curve produces a non-linear phase response. (The regular kinks in the plot result from the curvature of the device surface, the effect of which was not completely removed by the flip and rotation strategy due to the sensitivity of the measurements.) A best fit was computed from the phase response plot and used (with gamma curve calibration software provided by the device manufacturer) to produce a revised LUT to linearise the phase response of the SLM. This LUT was loaded onto the SLM and the same grid pattern was displayed. As before, ptychography was used to reconstruct the exit wave and the mean of each of the phase levels was recorded. The blue line in Figure 4.9 shows that the phase response is now reasonably linear and between 0 and 2π, as required.

4.6.2 Flatness correction

Finite manufacturing tolerances for the SLM leads to a slight curvature across the front of the device. This curvature of the glass cover appears as phase aberrations of the phase response of the SLM. According to the manufacturer, the deformation can be considered as almost spherical, and not more than a few microns difference between the centre and the edges [121]. This effect, which may be significant in some applications, can be characterised by measuring the wavefront aberration over the active area. The effect then can be corrected by adding a compensating phase onto images displayed by the device.

To measure the radius of this deformity, it was necessary to reconstruct an image of the whole SLM. However, ptychography needs structure in the object in order to reconstruct an image correctly. This meant a minimal pattern needed to be displayed onto the SLM to create enough structure, but not too much detail so as to adversely effect the curvature reconstruction. Several techniques were tried; Figure 4.10 explains the reasoning behind some of them. The final chosen field pattern was displayed on

(a) An array of 2D Gaussian patterns. This pattern did not reconstruct as its structure was too minimal.

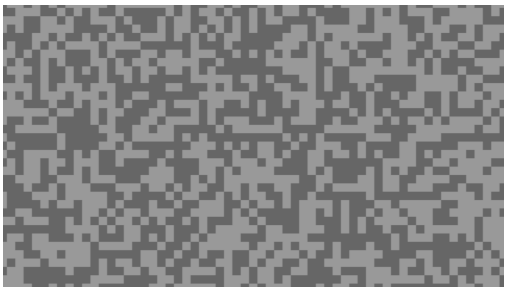

(b) A binary block pattern.

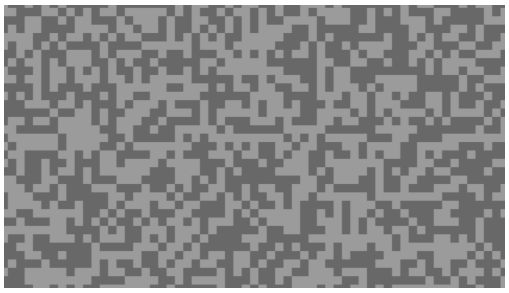

(c) A binary block pattern, the inverse of (b). Both (b) and (c) can be reconstructed separately and then their reconstructions subtracted to reveal the spherical deformity. This worked but the reconstruction of the spherical deformity was too influenced by the pattern.

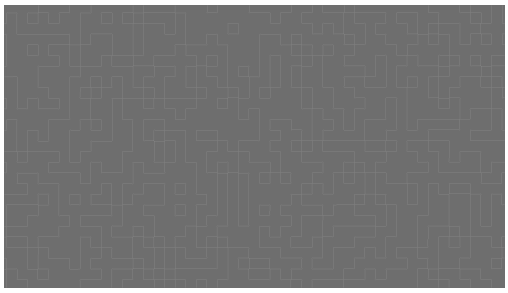

(d) A thin line pattern. This pattern reconstructs well, and only has a small influence of the reconstruction of the spherical deformity. This pattern was used to measure the spherical deformity.

Figure 4.10: Some practice test patterns used to attempt to reconstruct the spherical deformity. The patterns were displayed full screen on the SLM.

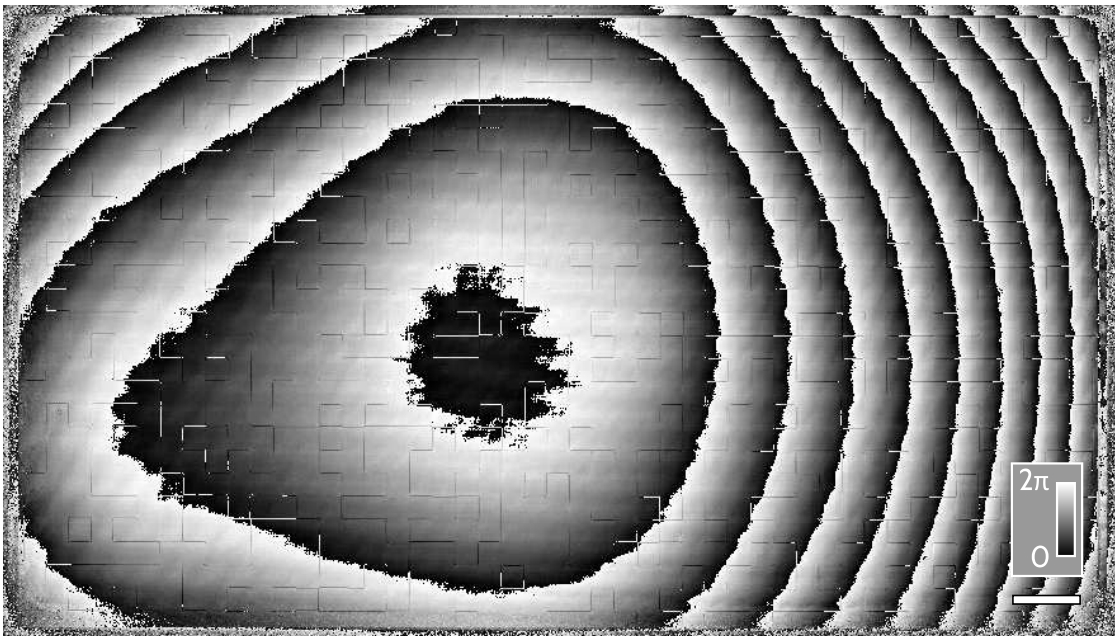

Figure 4.11: The line pattern across the whole SLM is reconstructed while showing a spherical deformity, with a slight phase ramp. Scale bar 1mm.

the SLM, as shown in Figure 4.10d. It consisted of random, one pixel wide, π phase-level lines covering the whole display, which gave sufficient structure to the diffraction data to condition the inverse problem solved by the reconstruction algorithm, without creating too much distortion in the final reconstruction. This image was reconstructed using the same ptychographic routine, giving Figure 4.11. It can be seen that the SLM is spherically deformed, with a slight phase ramp. This phase ramp could have been an artefact of the reconstruction, or a misalignment of the optical axis and detector, or from a slight tilt to the SLM mount [101]. To remove this ramp, a counter ramp was applied, before measuring the radius of each of the phase rings. The curvature of the device surface, R, was calculated with the equation:

$$R = \frac{r^2 + \left(\frac{n\lambda}{2}\right)^2}{n\lambda} \tag{4.7}$$

where r is the radius of a 2π phase wrap in the reconstruction, n is the order of that

Figure 4.12: The curvature correction added to an image before display on the SLM. The inset shows the original image.

wrap, and λ is the wavelength of light used. Averaging over several wraps, the SLM we used had a radius of curvature of 7.9 m. This corresponds to a maximum height discrepancy of 4.9 nm between the edge and centre of the SLM, well within the bounds specified by the manufacturer.

4.7 Testing the correction procedures

In order to test the effectiveness of the correction procedures, a static phase image (1920 $\times$ 1080 pixels, inset of Figure 4.12) was chosen to display, full screen, on the SLM. The gamma curve calibrated in Section 4.6.1 was loaded onto the device driver. A spherical mask was created which was the conjugate of that measured in Section 4.6.2 and added to the displayed image to compensate for the surface curvature (main image of Figure 4.12) . This mask was superimposed on to the image to be loaded on to the SLM, shown in the inset of Figure 4.12.

Figure 4.13: The phase of the reconstructed image of the SLM, with the phase range clipped to aid contrast. The inset shows a zoom where the pixel grid of the SLM can be seen. Scale bar 1 mm.

As before, a ptychographical dataset was collected of 2800 diffraction patterns, over a randomly disturbed grid of 70×40 stage translations. This gave a total field of view over the SLM of 9 mm×15 mm. ePIE was used to reconstruct the phase response of the SLM across the whole display, using the position correction and background removal as described. 300 iterations of the ePIE algorithm were required.

Figure 4.13 shows this unwrapped phase image reconstruction, with an inset showing a zoomed in portion of the image. The pixel pitch in the reconstruction is 2.04 µm, and the image contains 4500×7500 pixels. It can be seen that the spherical correction has performed well, creating a reasonably flat background to the image. Some distortions remain: a low spatial frequency ripple, around a wavelength in amplitude, which together with small unwrap errors accounts for the extension of the phase range beyond 2π. The concentric rings visible in the image correspond to phase wraps in the mask used to compensate for the SLM's surface curvature. As well as

flyback between pixels along the phase edges, from 2π to 0, the strong scatter from these phase edges goes beyond the NA of the imaging system, creating these ring distortions.

The inset shows that it is possible to resolve the individual pixels of the SLM, and that the pixel array can be seen. Each SLM pixel corresponds to approximately 16 pixels (4×4) in the reconstruction. A slight moiré effect can be seen across the reconstruction because the image pixel pitch is not an exact multiple of the SLM's pixel pitch. The reconstruction also shows an excellent phase profile. In the centre of the display, the programmed image had a phase difference between the light and dark stripes of the lighthouse building of 1.89 rad, calculated by averaging over a region on each stripe. In the reconstructed image, the difference between the same regions had a phase difference of 1.91 rad.

4.8 Conclusions

This work has demonstrated that ptychography is a useful new tool to image an SLM. Ptychography has an essentially unlimited view, so is suited for the wide field of view required to image the entire SLM. It has a high image resolution, allowing a sub-pixel reconstruction of the SLM display. Ptychography also algorithmically removes the illumination system's influence from the reconstructed image, as well as any aberrations or artefacts it may introduce, generating high quality reconstructions. It has excellent phase accuracy, as demonstrated by the physical sample. This technique also is simple to set up and doesn't require a reference arm, or imaging lenses.

This work also demonstrated how the complex images created by ptychography can be used to linearise the phase response of the SLM in a novel way. It is also able to measure the micron-sized spherical deformity of the surface of the SLM, in order that it can be compensated for high precision usage. This work was written into a letter

published in the OSA's Optics Letters [137]. It has since been cited by Wang *et al.* [140] who describe the technique as having excellent phase accuracy, but acknowledge that the mechanical stage and iterative algorithm mean that the method is not suitable for fast characterisation. Zhang *et al.* [141] also describe the technique as alternative method for physical and component measurements.

Chapter 5

Spatial light modulator based optical near-field ptychography

5.1 Introduction

This chapter explores in further detail the idea proposed at the end of Chapter 3: Can an SLM work with optical near-field ptychography to improve the technique? Chapter 4 showed how an SLM can be characterised using standard ptychography. This also gave some understanding into the operation of the SLM and its interaction with the ptychographic technique. This chapter explores two ideas that would utilise the addition of an SLM into a ptychographic technique. The first section looks at whether an SLM would make a good diffusive element in near-field ptychography, and investigates what type of pattern should be displayed on the SLM for this purpose. This forms the SLM characterisation method for the next section. The second section is the ultimate aim of this chapter: an algorithm that uses the SLM-based optical near-field ptychography without the need for a movement stage.

5.2 Using a spatial light modulator as a diffuser in optical near-field ptychography

5.2.1 Introduction

In Chapter 3, it was shown that optical near-field ptychography is a viable and versatile QPI technique to image transparent samples such as biological cells, generating high quality, accurate phase images. In Chapter 4, it was demonstrated how SLMs interact with ptychography, and how issues may be mitigated.

In optical near-field ptychography (Chapter 3), a diffuser was used as a way of creating diversity between the diffraction patterns. The diffuser used was a piece of transparent adhesive tape. In this chapter, an SLM is investigated as a suitable alternative as a diffuser. As shown in Chapter 4, the phase-only SLM used can alter the phase of the wavefield, without altering its magnitude. This is equivalent to a transparent object of varying thickness, similar to the transparent adhesive tape. It would be possible to take advantages of the SLM in near-field ptychography, such as being able to change the diffusers behaviour, and change the diffuser during the data collection stage of optical near-field ptychography. The work in this section will become the SLM reconstruction procedure in the next section, crucial for replacing the translation stage.

The reconstruction algorithm used throughout these tests is the same as for the optical near-field experiments. The modified ePIE algorithm was used (Section 2.8.3), with annealing (Section 2.8.3), background removal (Section 4.4.2), and momentum (Section 2.8.3). As was seen in the work using ptychography to characterise an SLM, the background removal step was particularly useful here to remove the mirror effect of the SLM, caused by the imperfect polarisation of the illumination (Section 4.3.2).

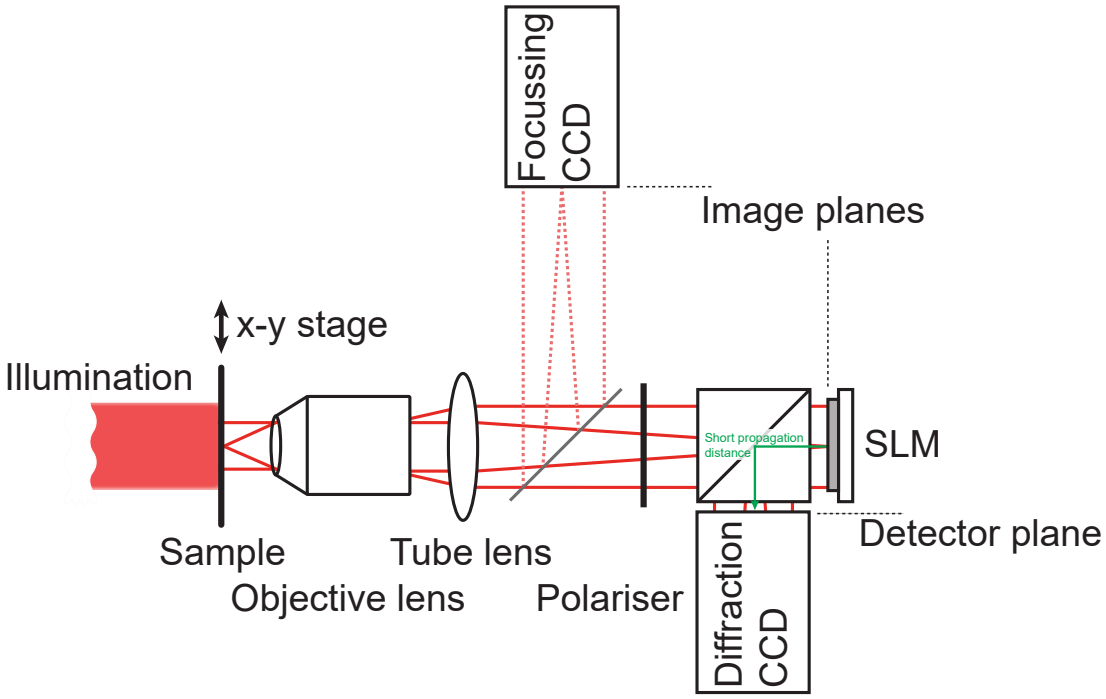

Figure 5.1: The experimental setup for optical near-field ptychography using an SLM as a diffuser. A temporary mirror can be position in the optical path, to aid focussing with the focussing CCD.

5.2.2 Dataset acquisition

Theoretical setup

The principles of optical near-field ptychography were maintained, although some adjustments were required to accommodate the SLM. The main difference between the transparent adhesive tape, and the Holoeye Pluto phase only spatial light modulator, is that the tape is a transmissive object and the SLM is a reflective object. The adjusted experimental setup is shown in Figure 5.1. As with optical near-field ptychography, the sample is uniformly illuminated over an area greater than the field of view required. The sample is mounted on the x-y translation stage in front of an objective and tube lens forming a standard microscope. The screen of the SLM is located where the transparent adhesive tape was located, at the image plane of the microscope. A

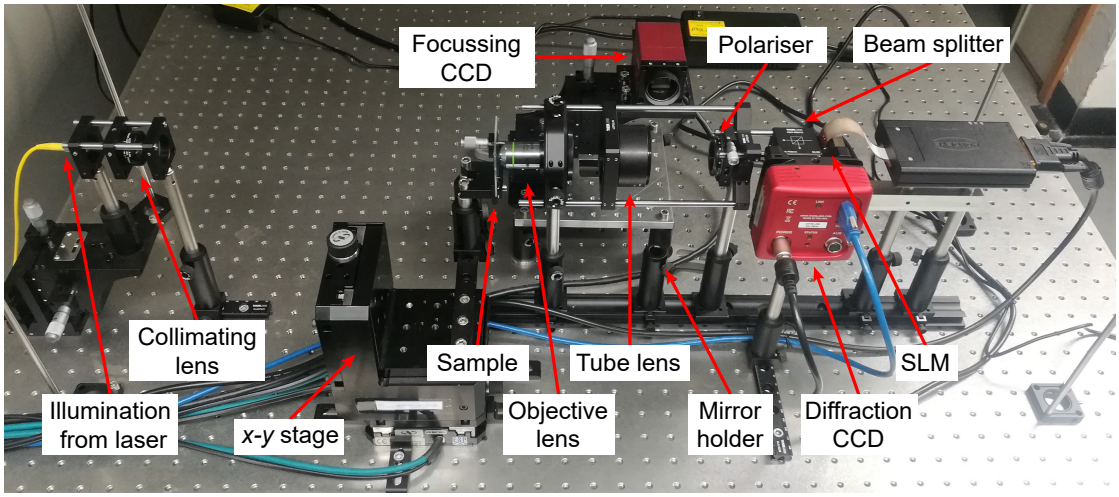

Figure 5.2: The optical bench setup used for optical near-field ptychography with an SLM.

polariser is also required when using the SLM, as explained in Section 4.3.2. The combined exit wave of the sample and the phase profile displayed on the SLM is propagated a short distance, via the beam splitter, to the detector. A temporary mirror is positioned in the optical path, for the focussing CCD, which is perpendicular to the optical path, but also located at the image plane of the microscope.

Optical bench setup

The SLM used in this experiment was the same SLM described in Section 4.3.2, the Holoeye Pluto phase only SLM. The gamma correction curve used was the one as characterised in Section 4.6.1, as the same laser wavelength was used (675 nm). The alignment was carried out in exactly the same way as in Section 3.2.4, except the SLM is now placed in the image plane of the microscope, where the transparent adhesive tape was previously. The same two objective lenses were used in this experiment, 4× and 20× magnification, although any objective magnification strength could be used. In the SLM characterisation experiment, it was shown why a polariser is required when using the SLM. The same polariser orientation technique (Section 4.3.2) was

employed in this setup so that the polarisation of the illumination is aligned with the long axis of the SLM. Because the SLM is a reflective component, it was necessary to include a beam splitter. This increased the camera length, adjusted for the change in refractive index of the glass beam splitter, to 10.2 cm. This new reflection mode optical near-field ptychography setup on the optical bench is shown in Figure 5.2.

SLM diffuser

As was discussed in Section 3.2.3, although the experiment is robust to changes, the choice of diffuser is important in getting the best image quality. One of the benefits of using an SLM as a diffuser is that its phase properties can be changed easily. Several different examples of patterns to be displayed on the SLM were tested, and there is further room for testing which patterns work best for different samples. The following are ptychographic reconstructions of SLMs using experimental data gathered using the reflective mode near-field setup. In an analogy to the original formulation of ptychography, these images can be thought of as the 'probe', unchanging throughout the data acquisition process. The test object used for these reconstructions is shown later in the experiment. As the SLM phase profile had been linearised using the characterisation of the gamma curve in Section 4.6.1 the $0 - 255$ grey levels of the SLM patterns should correspond to $0 - 2\pi$ phase delay on the SLM.

- **Picture patterns:** Figure 5.3 is a demonstration of the SLM acting as a normal display device. Because it can display any 1920×1080 pixel greyscale image on its LCD, it is possible to use any picture to act as a diffuser. Figure 5.3a is the grey scale image that was loaded to be displayed on the SLM. On the left side of the image, amongst the trees, are high spatial frequency components. On the right side, in the clouds, are low spatial frequency components. In the phase reconstruction of the SLM's display while showing this image, Figure 5.3b, it can be seen that the central part of this image has been clearly reconstructed. It is

(a) The original beach scene photograph displayed on the SLM.

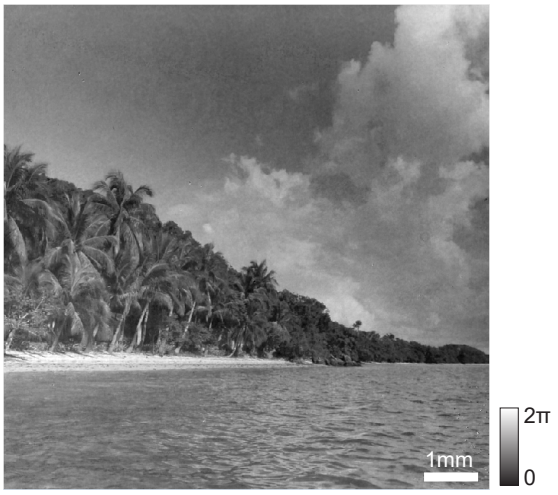

(b) The reconstructed phase image from the SLM showing the beach scene.

Figure 5.3: Any picture can be displayed onto the SLM to be used as a diffuser.

(a) The original grass photograph displayed on the SLM.

(b) The reconstructed phase image from the SLM showing the grass image. Many issues with large phase jumps and vortices can be observed.

Figure 5.4: The grass picture contains high frequencies and large phase jumps.

(a) The original cloud photograph displayed on the SLM.

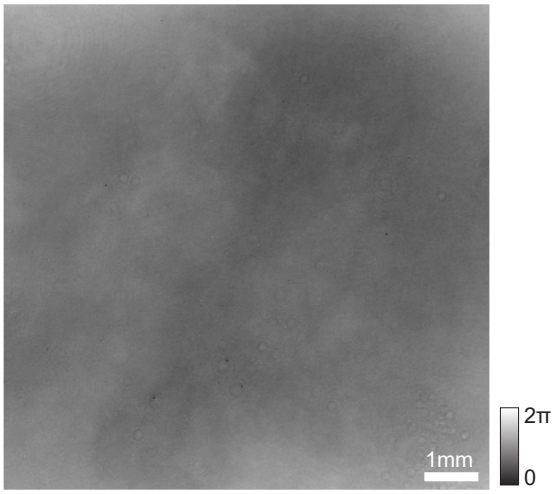

(b) The reconstructed phase image from the SLM showing the cloud image. The reconstruction does not suffer from reconstruction artefacts.

Figure 5.5: The cloud picture consists mainly of low frequencies and smooth phase changes.

also possible to identify dust in the reconstruction, causing phase wraps and unwanted artefacts.

- **High spatial frequency patterns:** To test the reconstruction of higher spatial frequency patterns, a picture of grass (Figure 5.4a) was displayed on the SLM. This image contains regions where there are large phase changes across in the image in a small amount of pixels. In the phase reconstruction shown ins Figure 5.4b, these large changes can be seen to produce phase vortices that are difficult to remove. This may be because of the large phase step change between adjacent pixels causing flyback, or by creating large phase edges that produce higher order diffractions. These aberrations in the probe reconstruction cause issues with accurate phase reconstructions of the object as they are not real phenomenon, and so images with high spatial frequencies present should be avoided as diffusers.

- **Low spatial frequency patterns:** An image of clouds was used as an example of a low spatial frequency image, in Figure 5.5. The image in Figure 5.5a shows the low spatial frequency greyscale image that was displayed on the SLM. Figure 5.5b shows the phase reconstruction of the image, without phase wraps or reconstruction artefacts, indicating that this type of image is suitable for use as a diffuser.

This work is only qualitative in nature, but it is immediately obvious that certain types of diffuser patterns are not suitable. This work could be further extended to establish with more certainty which type of pattern to display on the SLM to generate perfect results, for example by synthesising images with particular features. However, as the optical near-field ptychography still appears to be very robust, this kind of analysis is not crucial to obtaining a working outcome.

As the camera length of the setup is in the nearfield, and the propagator used is the angular spectrum propagator (Section 2.4.4), the pixel resolution of the reconstruction of the SLM is equal to the camera resolution. This means each pixel of the SLM reconstruction contains 4 (2×2) pixels of the SLM. To avoid aliasing in the final reconstruction, the Shannon sampling theorem (Section 2.5.1) says that the highest frequency in the pattern displayed on the SLM should be $1/4$ pixels.

Diffraction pattern quality

The quality of the collected diffraction patterns is crucial in obtaining a high quality reconstruction of a sample. Figure 5.6 shows a typical diffraction pattern captured using this experimental setup. Firstly, the speckle pattern is apparent and clear. However, there are issues with this diffraction pattern which will affect the final reconstruction. The bright spot in the centre of the diffraction pattern is caused by reflections in the system. Because the SLM and the CCD both have reflective glass surfaces, some light is reflected between them, causing this artefact. The size

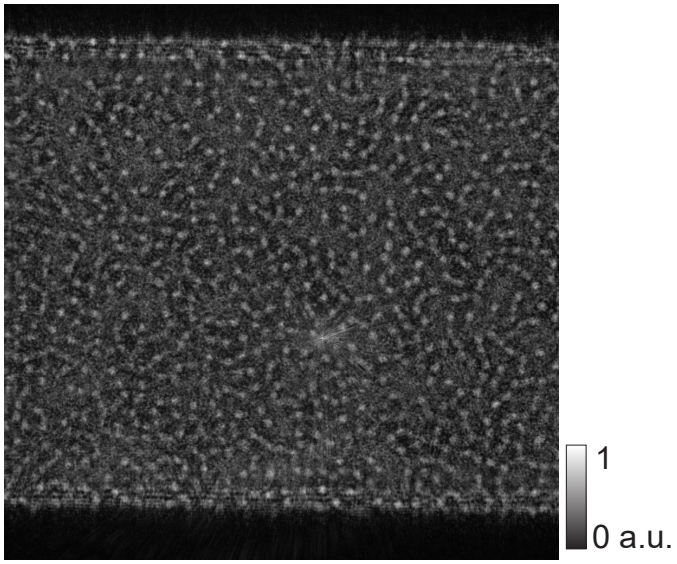

Figure 5.6: A typical diffraction pattern captured using the optical near-field setup with an SLM. This shows the full field of view of the CCD, 1.54 cm^2.

difference between the SLM and the CCD also creates issues. The SLM has an aspect ratio of 16:9, whereas the CCD sensor is square. This means that there is a 'letterbox' effect in the diffraction pattern, in the form of two black bars at the top and bottom of the image captured. Not only is this wasted data, it may actually be detrimental to the reconstruction, as the properties of the area outside the SLM's active area are unknown. In addition, the left and right edges of the SLM are not utilised.

5.2.3 Image reconstruction

The ePIE algorithm with momentum, annealing and background removal–the same as the reconstruction algorithm used for the near-field experiment with a tape diffuser in Section 3.3–was used to reconstruct the sample and SLM quantitative phase images. The background removal algorithm, as described in Section 4.4.2, was particularly useful for this experiment. As was discussed in the context of background removal while characterising an SLM (Chapter 4), some of the light field which is not exactly polarised in line with the long axis of the SLM will be unmodulated and reflected by

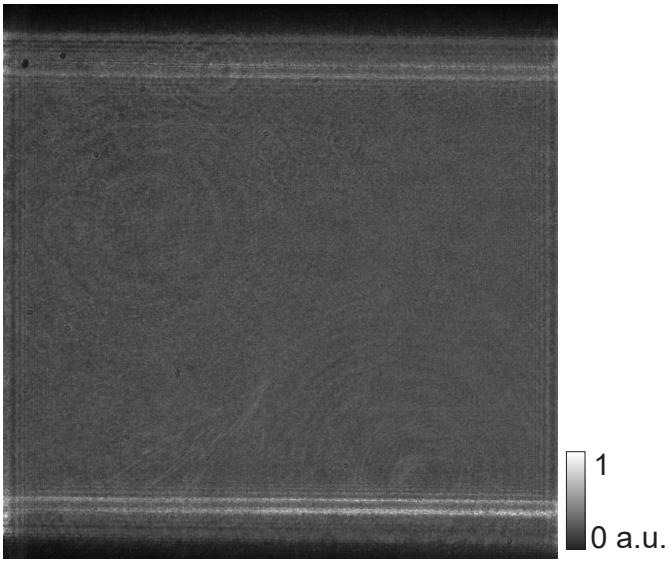

Figure 5.7: A typical intensity image of the unmodulated reflected component of the exit wave from the SLM propagated to the detector, removed using the background removal code. This shows the full field of the CCD,1.54 cm^2.

the SLM. Using the background removal code removes this unmodulated part of the exit wave from the final reconstruction. To demonstrate the extent of this, Figure 5.7 shows a typical intensity image of this unmodulated wave field that was removed by the technique.

5.2.4 Results

To demonstrate this new setup, several test data acquisitions and image reconstructions were carried out. The pattern used on the SLM was the cloud image, as the results in Section 5.2.2 indicate that it makes a suitable diffuser.

The same frog red blood cells were imaged using this setup as were imaged in Section 3.4.2. They were imaged using two objective lenses, with 20× and 4× magnification. Due to the longer camera length from the reflection mode setup, the measured magnification at the detector was 27.2× and 5.80×, respectively. 100 diffraction patterns were captured using the near-field setup and the phase images

were each reconstructed using 200 iterations of the ePIE algorithm, (as in Section 3.4.2: $\alpha = \beta = 1$). Figure 5.8a shows the phase image of the red blood cells using the $20\times$ objective lens and Figure 5.8c shows the same sample with the $4\times$ objective lens. Figure 5.8b shows the same reconstruction zoomed-in red boxed region. As with the previous optical near-field ptychography work they show high image quality over a wide field of view.

Additionally, a section of a clam's gill was imaged with the $4\times$ objective lens, the reconstructed phase image is shown in Figure 5.8d. As before, 100 diffraction patterns were used to capture this sample and 200 iterations of the ePIE algorithm were used to reconstruct the phase image. This sample contains higher spatial frequencies than the red blood cells, and the technique is able to clearly reconstruct the substructures of the gill.

Next, to investigate the performance of the system as the number of diffraction patterns was reduced, a second dataset of 25 diffraction patterns was collected of the same red blood cells sample, using the $4\times$ objective lens. Using the profile of the SLM reconstruction obtained from the first dataset to give an initial estimate of $p(\mathbf{r})$. As in Section 3.4.2, because it expected that the SLM will change very little between experiments, the step size in the probe update function was set to $\beta = 10^{-4}$. With 25 diffraction patterns, the phase reconstruction of the cells is shown is Figure 5.9a. Removing 10 diffraction patterns from the dataset and repeating the reconstruction gave the phase image in Figure 5.9b. Further reducing the number of diffractions patterns shows that the reconstruction is still good until 10 diffraction patterns in Figure 5.9c. With 8 and 6 diffraction patterns (Figure 5.9d, Figure 5.9e), the background noise becomes too great and it becomes harder to discern individual cells.

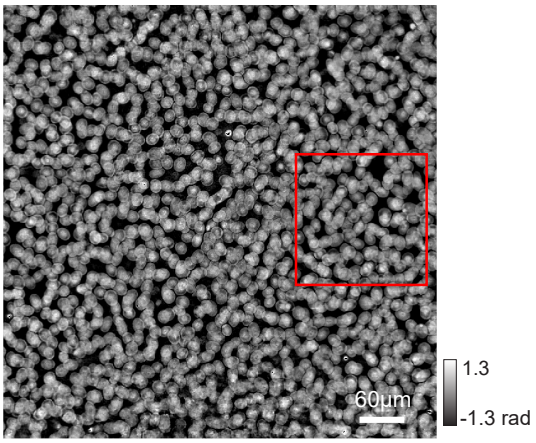

(a) Phase image of frog red blood cells imaged using a 20× objective lens.

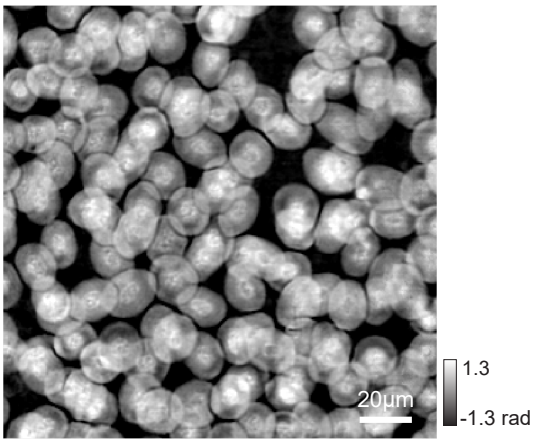

(b) The zoomed-in portion of the phase image of frog red blood cells from the red box in (a).

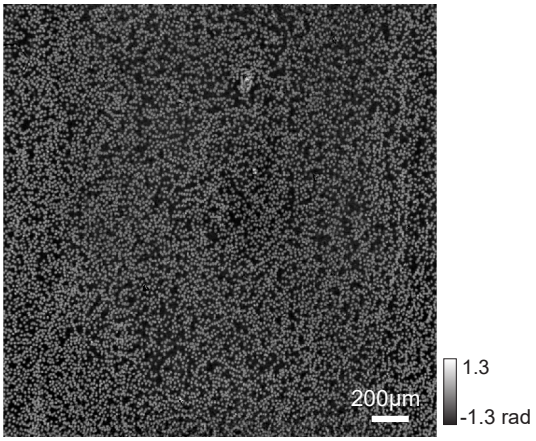

(c) Phase image of frog red blood cells imaged using a 4× objective lens.

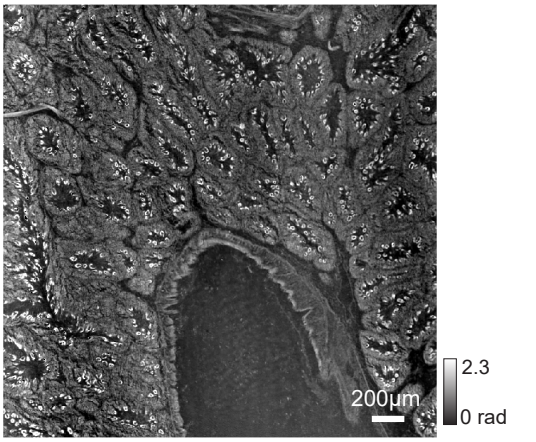

(d) Phase image of a clam's gill imaged using a 4× objective lens.

Figure 5.8: Results from optical near-field ptychography, using an SLM as a diffuser. These results were reconstructed from 100 diffraction patterns.

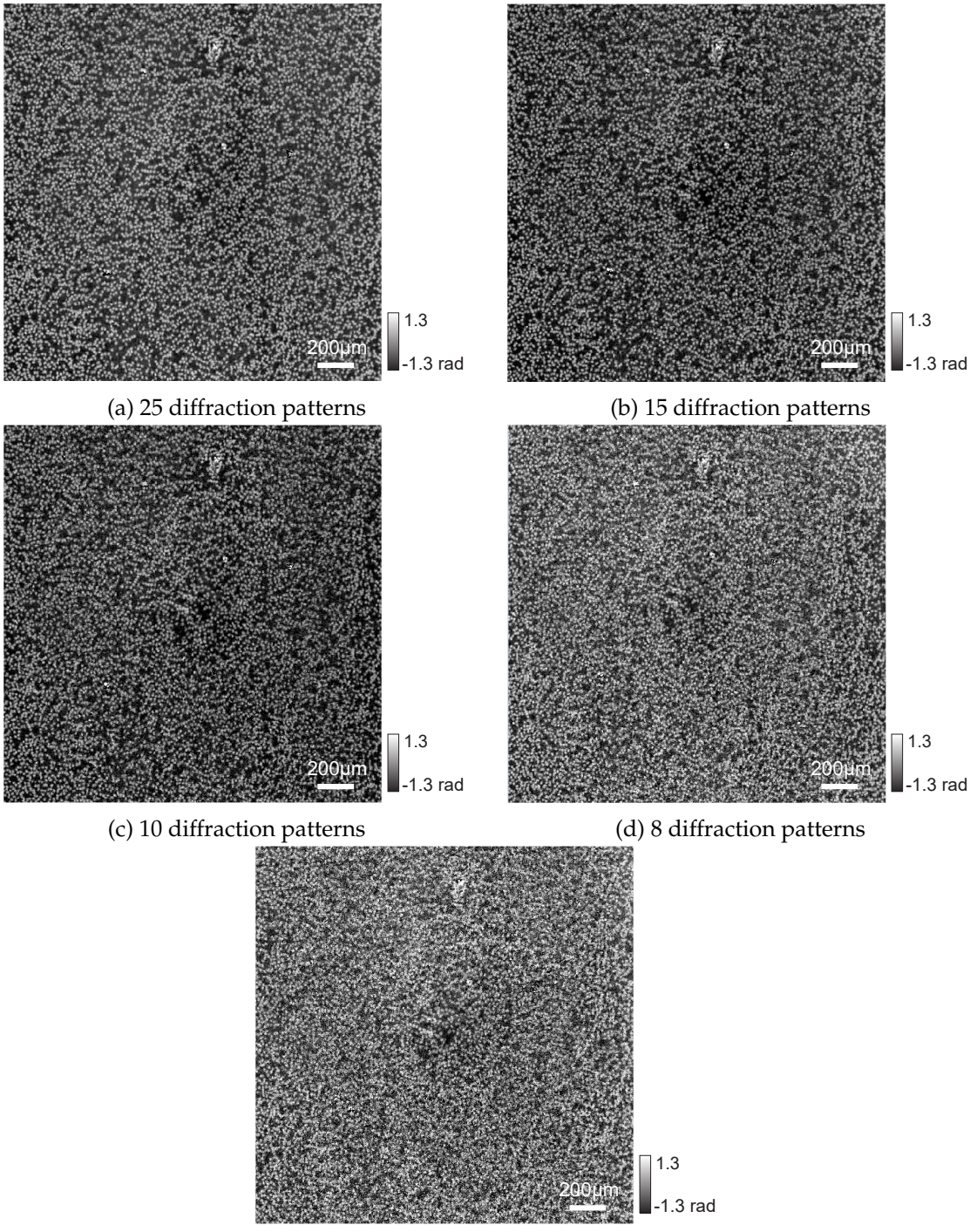

(a) 25 diffraction patterns

(b) 15 diffraction patterns

(c) 10 diffraction patterns

(d) 8 diffraction patterns

(e) 6 diffraction patterns

Figure 5.9: Comparing the quality of phase images when reducing the number of diffraction patterns acquired. 10 diffraction patterns is the minimal usable amount of diffraction patterns, where the noise in the reconstruction is low and individual cells can be clearly observed.

5.2.5 Conclusions

This work has demonstrated that an SLM is a suitable optical component that can be used as a diffuser in optical near-field ptychography. The technique was demonstrated using several standard optical test objects, red blood cells and a gill. In comparison to Section 3.4.2, the result of using fewer diffraction patterns was also investigated, suggesting that 10 diffraction patterns were the minimum required in order to discern individual red blood cells.

However, the image quality appears slightly diminished when compared to the results in Chapter 3, which use transparent adhesive tape as a diffuser. This is due to several factors. Firstly, it can be seen from the diffraction patterns captured using this setup that the data collected are of poorer quality. There are reflections caused by the reflective glass plates of the SLM and CCD, as well as the beam splitter. As shown in Section 4.3.2, it is necessary to use a polariser with the SLM to remove unmodified components of the SLM's exit wave. Additional reflection background errors can be removed from the reconstruction with the background removal procedure in Section 4.4.2. However, any imperfect polarisation from the illumination add to errors in the reconstruction. Additionally, the inherent errors encountered when using an SLM, as described in Section 2.11.3, such as the pixel grid, the fill factor and flyback can reduce the quality of the reconstruction. As a component, the SLM is also considerably more expensive than static optical diffusers.

These issues could be accepted, when the advantages of using an SLM are further considered. It is possible to change the diffractive properties of the diffuser easily. Further work could investigate which patterns displayed on the SLM provide the best reconstructions. This near-field technique could also be used as a way of quickly characterising the SLM's pattern. The key advantage that the SLM provides is the ability to change the diffuser while the data acquisition is taking place. By using this as a creator of diversity between diffraction patterns, as opposed to the movement

stage, then it will be possible to have a near-field ptychographical setup with no moving parts.

5.3 Spatial light modulator based optical near-field ptychography without using a translation stage

5.3.1 Introduction

As was concluded at the end of the work in optical near-field ptychography (Chapter 3), one of the main issues with the technique is the movement of the sample during data acquisition. Not only does this have potential to disrupt a live sample, it also is one of the bottlenecks in reducing the acquisition time, which would lead to a slower frame rate in quantitative phase videos.

In the previous section, it was shown that an SLM is a suitable diffuser for use in optical near-field setups. In this section, the ability of an SLM to change its phase altering properties is utilised to investigate whether the source of diversity between diffraction patterns can be transferred from the translation stage to an SLM. The first half of the method uses the previous section's work as an SLM calibration step. The overall aim is therefore to create a technique with the robustness and quality of optical near-field ptychography, without any moving parts.

5.3.2 Experimental setup

The optical bench setup remains the same as in the previous section, apart from the sample now is fixed in its lateral $x - y$ position, as shown in Figure 5.10. The sample is focussed correctly in z on the image plane using the focussing CCD as before, but then is locked into position.

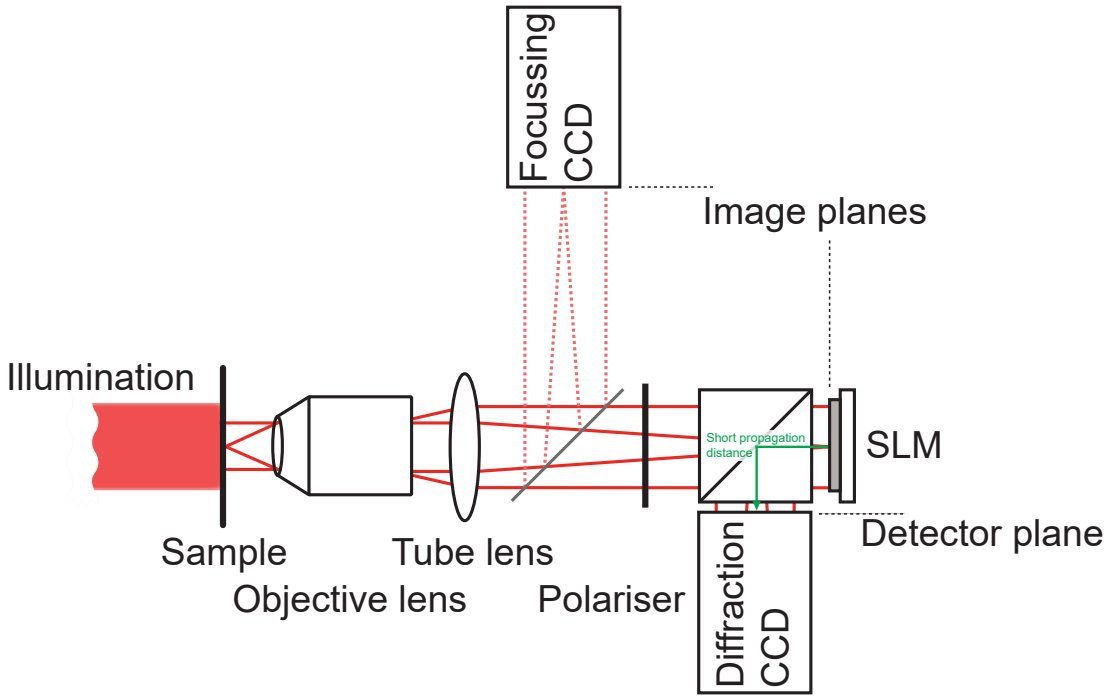

Figure 5.10: The experimental setup for optical near-field ptychography with an SLM without the use of a translation stage. The components remain in the same positions as with the previous work, but now once the sample is in focus of the focussing CCD it is fixed in position.

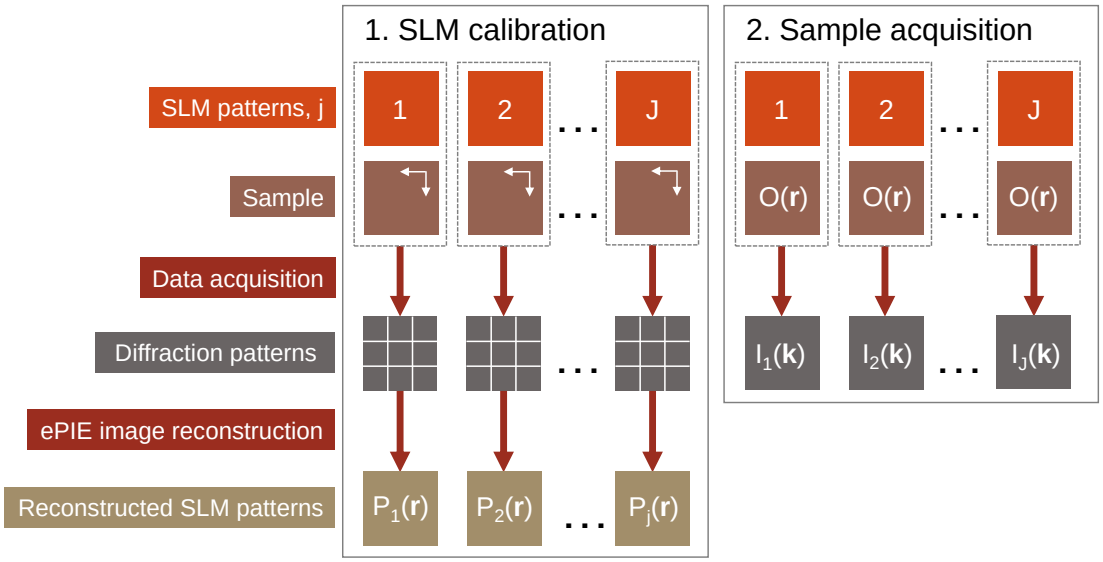

Figure 5.11: The data acquisition process consists of two main steps. The SLM calibration step only needs to be complete once. The sample acquisition step is completed when imaging a new sample.

5.3.3 Dataset acquisition

Firstly, it is important to note there is a paradigm shift with this setup, compared to the previous optical near-field setup. In that iteration of ptychography, the object moves to different positions, and the illumination profile remains static. In this iteration, the object will remain static, and the 'movement' is transferred to the SLM. The first stage is to identify how to create the movement of the illumination profile, whilst taking account of the imperfections of the SLM. The new data acquisition procedure consists of two steps:

1. **SLM calibration step:** Collect diffraction patterns using the experimental procedure in Section 5.2 for several patterns displayed on the SLM

2. **Sample data acquisition:** Collect the diffraction pattern for the sample of interest for each pattern displayed on the SLM.

The data acquisition procedure is shown graphically in Figure 5.11. For the SLM

calibration step, the method described in the previous section (Section 5.2) is used to get a set of reconstructed SLM patterns. A sample is chosen that is known to reconstruct well; in these results, the frog red blood cells were chosen. Next, J different SLM patterns were selected. In the following results, 10 different patterns were chosen, and more detail about how these patterns were selected is given below. Then J separate data acquisition processes are done, in exactly the same way as in the previous section (Section 5.2), with the movement stage. Having acquired all the data, each SLM pattern is reconstructed in the same way, using ePIE. Once this calibration step is done, all the SLM patterns, $P_j(\mathbf{r})$ have been characterised, and will become the known 'probes' in the sample reconstruction. Assuming the experimental setup doesn't change, this step does not to be repeated.

To acquire an image of a sample, $O(\mathbf{r})$, it is first brought to a focus using the focussing CCD as previously. Next, the first SLM pattern is displayed on the device. The diffraction image $I_1(\mathbf{k})$ is then captured. The next SLM pattern is displayed, and the diffraction image $I_2(\mathbf{k})$ is captured. This is repeated for all J SLM patterns. The complete dataset used for reconstruction has now been captured: $P(\mathbf{r})$ and $I(\mathbf{k})$.

It was shown in Section 5.2.2 which type of SLM patterns work well, and so the same cloud style of image was used. However, it is necessary to get sufficient diversity between each of the displayed SLM patterns. Two ways were investigated to achieve this diversity:

1. **Using the same spatial light modulator pattern, but circularly translated:** Because we have removed the sample movement from the image acquisition process, it seems logical to move the lateral translation to the SLM. An example of 10 SLM patterns created by circularly translating the same image is shown in Figure 5.12. However, the resulting reconstruction of one of the SLM patterns is shown in Figure 5.13. It can be seen that where the image has looped and joined itself, there can be large phase changes. As identified in Section 5.2.2, these large

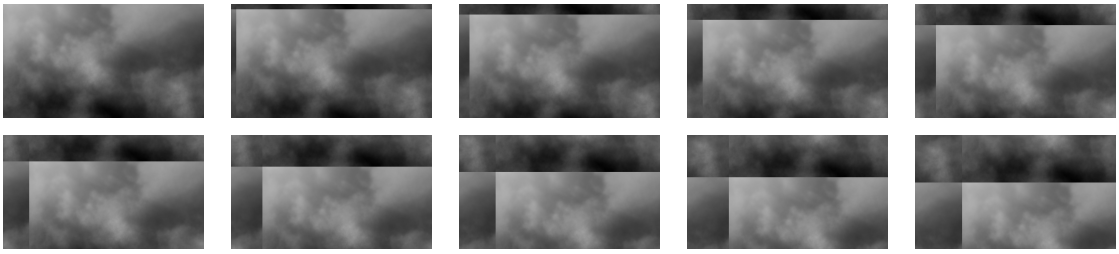

Figure 5.12: 10 different SLM patterns, created from one picture that has been translated circularly.

phase changes can cause phase vortices and other reconstruction errors which are not real. These errors, highlighted in the red box, make these unsuitable for use as SLM patterns.

2. **Using different spatial light modulator patterns:** Having performed the previous analysis, it becomes clear that any set of different pictures could be suitable to form the set of SLM patterns, as long as they can be reconstructed successfully individually. In the following experiments, the 10 different pictures of clouds as shown in Figure 5.14 were used. Once the complete SLM calibration step was completed, the 10 reconstructed SLM patterns as shown in Figure 5.15 were used for the reconstruction of the test samples.

5.3.4 Image reconstruction

The 'no-movement' reconstruction algorithm is a modification of the PIE algorithm. However, with this new algorithm there are multiple 'probes', each one being a reconstructed SLM pattern, and each one having a corresponding captured diffraction pattern.

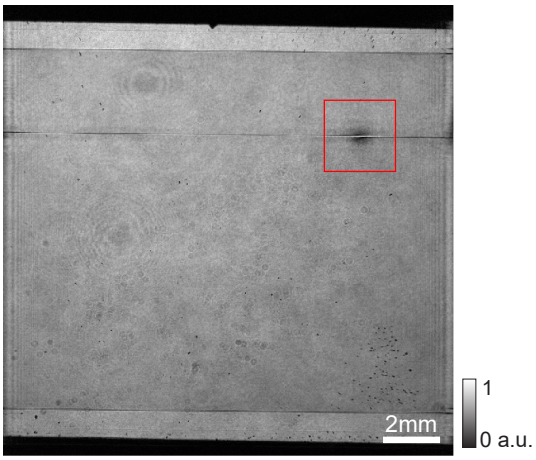

(a) The modulus of the reconstructed SLM pattern.

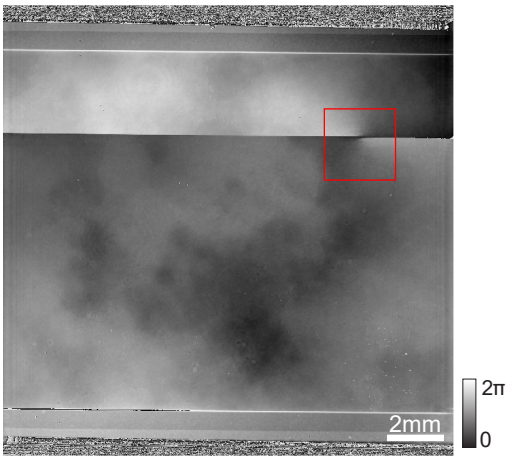

(b) The phase of the reconstructed SLM pattern.

Figure 5.13: An example reconstructed SLM pattern that has be translated circularly from top left to bottom right. It can been seen that the unnatural phase jumps where the opposite ends of the picture now meet creates vortices and errors in the reconstruction.

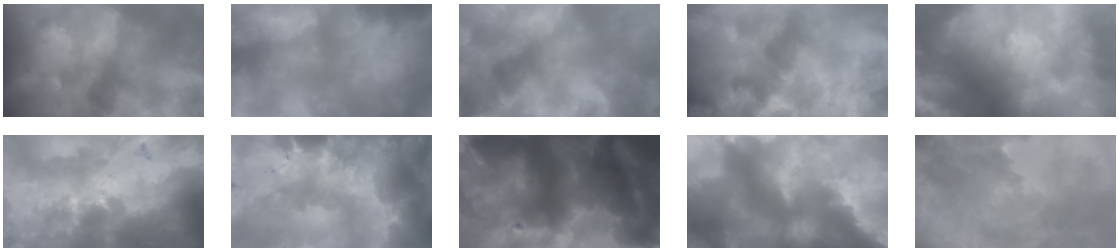

Figure 5.14: 10 different pictures of clouds to be used as the SLM patterns.

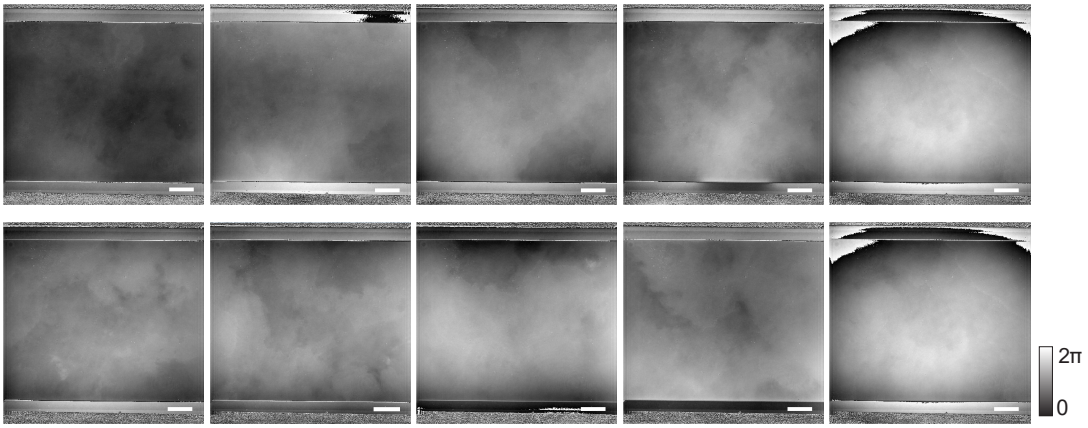

Figure 5.15: The 10 phase reconstructions of the SLM patterns that were used for further test sample reconstruction. (Scale bar 2 mm)

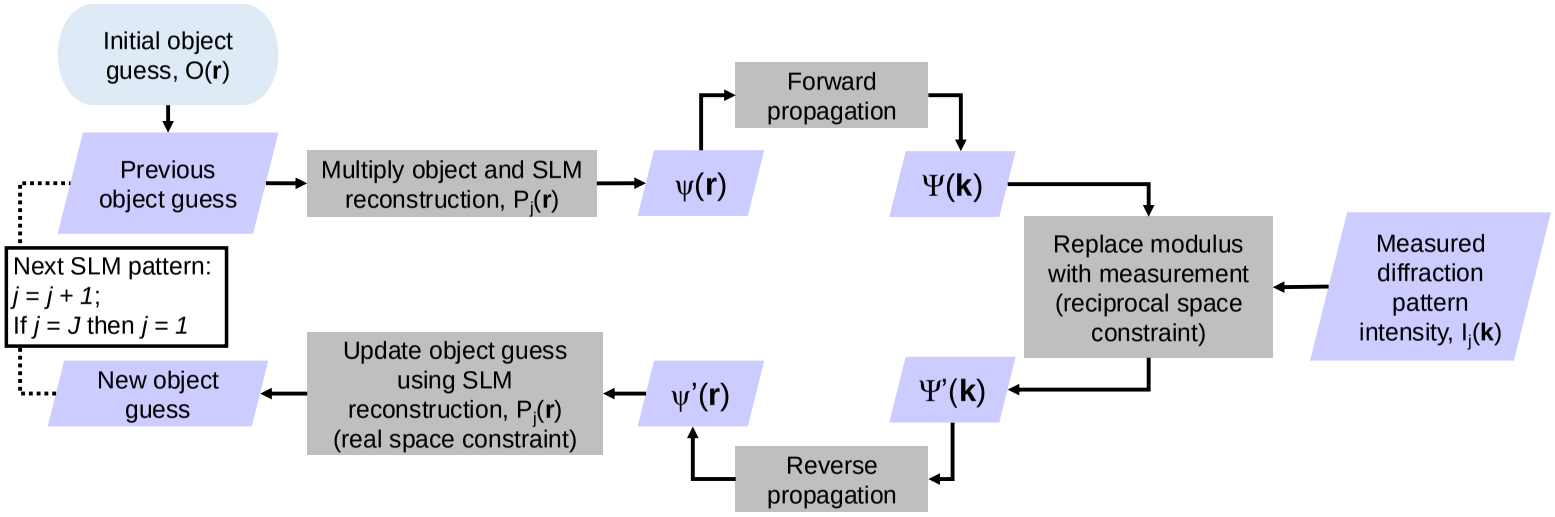

Figure 5.16: The iterative algorithm used to recover a sample from a set of reconstructed SLM patterns.

In the no-movement reconstruction algorithm, the following symbols are assigned:

$j \in [0 \dots J]$	SLM pattern number
$P_{[0 \dots J]}$	Known SLM reconstructions
O	Object transmission function
ψ	Exit wave (with ′ to indicate the updated wave)
Ψ	Diffraction pattern (with ′ to indicate the updated wave)
I	Measured intensity (from the detector)
n	Iteration number
$\mathbf{r}$	Real space coordinates
$\mathbf{k}$	Reciprocal space coordinates
$\mathcal{P}_z$	Propagator (e.g. Angular Spectrum), over a distance z
α	Object update parameter

1. For iteration $n = 0$, make initial guess of the object transmission function $O_j(\mathbf{r})$.

2. Multiply the current guess of the object by the current SLM pattern $P_j(\mathbf{r})$ to produce the guessed exit wave:

$$\psi_j(\mathbf{r}) = O_j(\mathbf{r}) P_j(\mathbf{r}). \tag{5.1}$$

3. Propagate the exit wave to the detector to create a guessed diffraction pattern. As the propagation distance is in the near-field, the angular spectrum propagator was used (Section 2.4.4).

$$\Psi_j(\mathbf{k}) = \mathcal{P}_z \left[\psi_j(\mathbf{r}) \right]. \tag{5.2}$$

4. Apply a reciprocal space constraint by replacing the modulus of the guessed diffraction pattern with the square root of the measured intensity, while retaining the phase, $\theta_j(\mathbf{k}) = \arg(\Psi_j(\mathbf{k}))$:

$$\Psi'_j(\mathbf{k}) = \sqrt{I_j(\mathbf{k})} e^{i\theta_j(\mathbf{k})}. \tag{5.3}$$

5. Reverse propagate this updated diffraction pattern to give an updated exit wave:

$$\psi'_j(\mathbf{r}) = \mathcal{P}_z^{-1}\left[\Psi'_j(\mathbf{k})\right] \tag{5.4}$$

6. Update the guess of the object, using the object update function and the known j^{th} reconstruction of the SLM, $P_j(\mathbf{r})$:

$$O_{j+1}(\mathbf{r}) = O_j(\mathbf{r}) + \alpha \frac{P_j^*(\mathbf{r})}{|P_j(\mathbf{r})|^2}\left[\psi'_j(\mathbf{r}) - \psi_j(\mathbf{r})\right] \tag{5.5}$$

   $\alpha \in [0, 1]$ is known as the object update parameter, and controls the feedback loop. A larger value of α will speed convergence, at the higher risk of being caught in a local minima.

7. Get the next reconstructed SLM pattern, $j = j + 1$, or if $j = J$ then start the next iteration:

$$n = n + 1$$
$$j = 0$$

8. Repeat steps 2-7 for a fixed number of iterations, or until the error is sufficiently

small. A suitable measure for the error is the sum squared error (SSE):

$$\text{SSE} = \frac{(I_j(\mathbf{k}) - |\Psi_j(\mathbf{k})|^2)}{N}, \tag{5.6}$$

where N is the number of pixels of the measured diffraction pattern.

For the following results 500 iterations of the algorithm were performed, using $\alpha = 1$.

5.3.5 Results

Having reconstructed the 10 SLM patterns of clouds in the calibration step, it is now possible to image the samples of interest. Two samples were used to test this method, frog red blood cells and a 1951 USAF resolution test target. Using the same SLM patterns and the sample acquisition method given in Section 5.3.3, 10 diffraction patterns were captured for each sample. As there is no requirement for the translation stage, and only 10 diffraction patterns are required, the acquisition time of this process is considerably reduced. The datasets were used in the no-movement reconstruction algorithm, and the reconstructions are shown in Figure 5.17.

Firstly, it can been seen that the technique did work, but there will need to be some improvements. Figure 5.17a shows the modulus of the image reconstruction of the resolution target, which was imaged using the 20× objective (although as before the real magnification is 27.2×). The features on the target are clear, but there are ringing shadow reconstruction artefacts. Figure 5.17b shows a phase image of the frog red blood cells. Although the locations of the cells is clear, because the contrast has been enhanced with the phase image, the phase sensitivity is not accurate due to the noise in the reconstruction. The objective lens was changed to 4× magnification (real magnification = 5.80×) and Figure 5.17c shows a phase reconstruction of the same frog red blood cells. Again, the locations of the cells is obvious, but it is a noisy image.

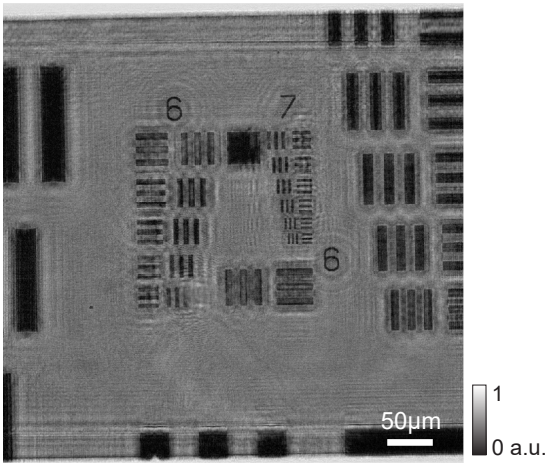

(a) Modulus image of the reconstruction of a 1951 USAF resolution test target imaged using a 20× objective lens.

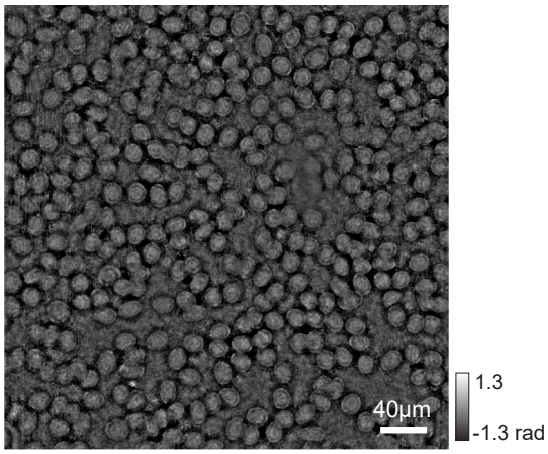

(b) Phase image of frog red blood cells imaged using a 20× objective lens.

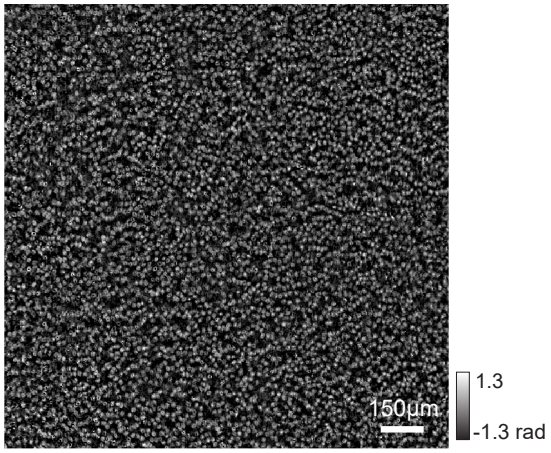

(c) Phase image of frog red blood cells imaged using a 4× objective lens.

Figure 5.17: Reconstruction results using the no-movement SLM near-field ptychography technique.

5.3.6 Conclusions

This section has shown how an SLM can be combined with optical near-field ptychography to produce a technique with a faster acquisition time, and no movement. By utilising the ability of the SLM to change its phase profile quickly, the diversity needed in the dataset can be acquired quickly, and without disturbing the sample. Reconstructed images clearly enhance the contrast of the samples, but the phase sensitivity suffers due to noise in the reconstructions.

Future work

Having demonstrated a proof of principle of the technique, it is clear that it has potential to create a technique that will generate higher quality phase images. One change that could be made is to increase the number of SLM patterns that are characterised, and so capturing more diffraction patterns of the sample. It was shown in Section 5.2.4 that 10 diffraction patterns was the minimum required to produce a clean phase reconstruction. In this technique it appears that more than ten diffraction patterns may be required. This will increase the time needed to generate the SLM characterisations for sample acquisition, which is already a lengthy process, but increasing the time of this calibration could be a necessary sacrifice to increase the overall quality of the final reconstruction.

Issues in the collected diffractions, such as unwanted reflections, should also be addressed.

Additionally, more work could be done to identify what makes the SLM a better diffuser. Different style SLM patterns could be investigated to see which is the most effective.

Further work

A strategy that constrains the values that the SLM patterns can take is proposed in Chapter 6, with the aim to speed up and improve the reconstruction.

Chapter 6

Future work: Constrained phase map spatial light modulator based optical near-field quantitative phase imaging

6.1 Introduction

Although the work in the previous chapter demonstrated that SLM-based optical near-field ptychography is a viable technique, it appears to be under-constrained, requiring a large number of previously reconstructed SLM patterns. This could be improved by adding additional constraints as to the range of values the SLM phase profile can take, and therefore reducing the number of possible solutions. This chapter lays out future work that would investigate this, by describing a new algorithm. This algorithm adds some *a priori* information to the range of values that the SLM can display, by assigning each SLM pixel's value from predefined phase maps when

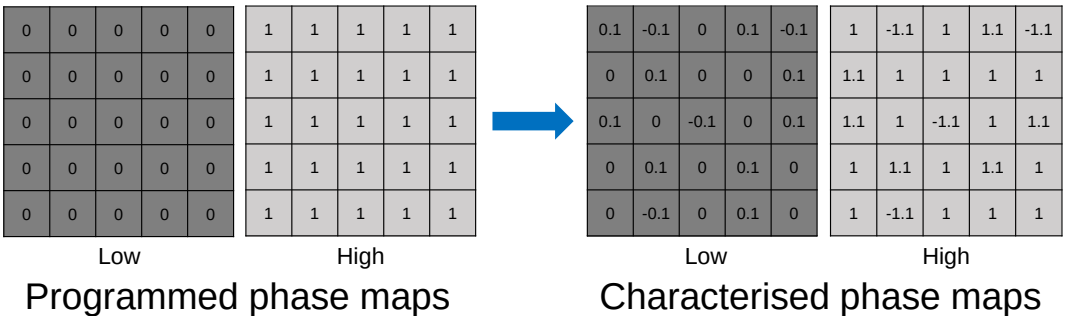

Figure 6.1: The values of the pixels for the two phase maps are characterised as the difference between the SLM's programmed values and the actual values are calculated. (Diagram scaled for visibility, each phase map has the same number of pixels as the SLM)

acquiring diffraction patterns using the SLM-based optical quantitative phase imaging setup in Section 5.3. In the reconstruction algorithm, because it has been previously shown that the programmed and actual SLM phase profiles differ, instead of characterising the entire SLM, with all the phase values that it might take, only the phase maps are corrected. The correct SLM phase maps are then used for the next iteration of the reconstruction. Figure 6.1 shows the key concept underlying the technique: starting with the predefined phase maps, each of the pixel values for each phase map are individually corrected. This additionally means that the SLM's phase profile is characterised simultaneously with the reconstruction of the sample.

The technique consists of the following steps:

1. **SLM pattern generation by random polling from phase maps**

2. **Dataset acquisition** Experimental setup is identical to the SLM-based optical quantitative phase imaging in Section 5.3.

3. **Image reconstruction**

6.2 Spatial light modulator phase profile polling

The first step is to generate a set of phase profiles that can be displayed on the SLM. These phase profiles are generated from a limited range of phase values. J random binary masks with the same number of pixels as the SLM are created, $M_{[0...J]}(\mathbf{r})$. Two phase maps, also the size of the SLM, are created: $H(\mathbf{r})$, consisting of a higher phase value, and $L(\mathbf{r})$, consisting of a lower phase value. Each SLM phase profile, $S_{[0...J]}$ is generated from the two phase maps, where each pixel of the SLM is selected from either phase map using the binary masks:

$$S_{[0...J]}(\mathbf{r}) = L(\mathbf{r}) \times [M_{[0...J]}(\mathbf{r}) == 0] + H(\mathbf{r}) \times [M_{[0...J]}(\mathbf{r}) == 1]. \tag{6.1}$$

Visually, this can be represented by Figure 6.2. It can be seen that the SLM phase profile is built up by polling the high and low phase maps using the random binary masks.

6.3 Dataset acquisition

The optical bench setup is exactly the same as that of the no-movement SLM-based optical near-field quantitative phase imaging in Section 5.3.2, with Figure 6.3 repeated here.

In order to acquire the dataset, the sample is focussed as before onto the focussing CCD. Each one of the J SLM phase profiles created earlier is displayed on the SLM and the diffraction pattern captured with the diffraction CCD. This creates a dataset of diffraction patterns, $I_{[0...J]}$.

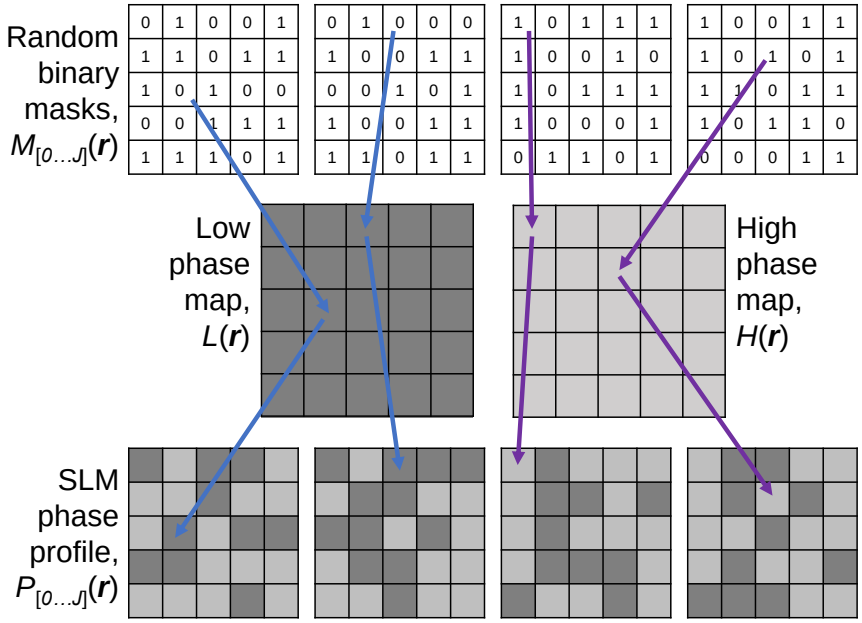

Figure 6.2: The values of the pixels for SLM phase profiles are polled from the high and low phase maps using the randomly generated binary masks. (Diagram scaled for visibility, each binary mask, phase map and SLM phase profile has the same number of pixels as the SLM.)

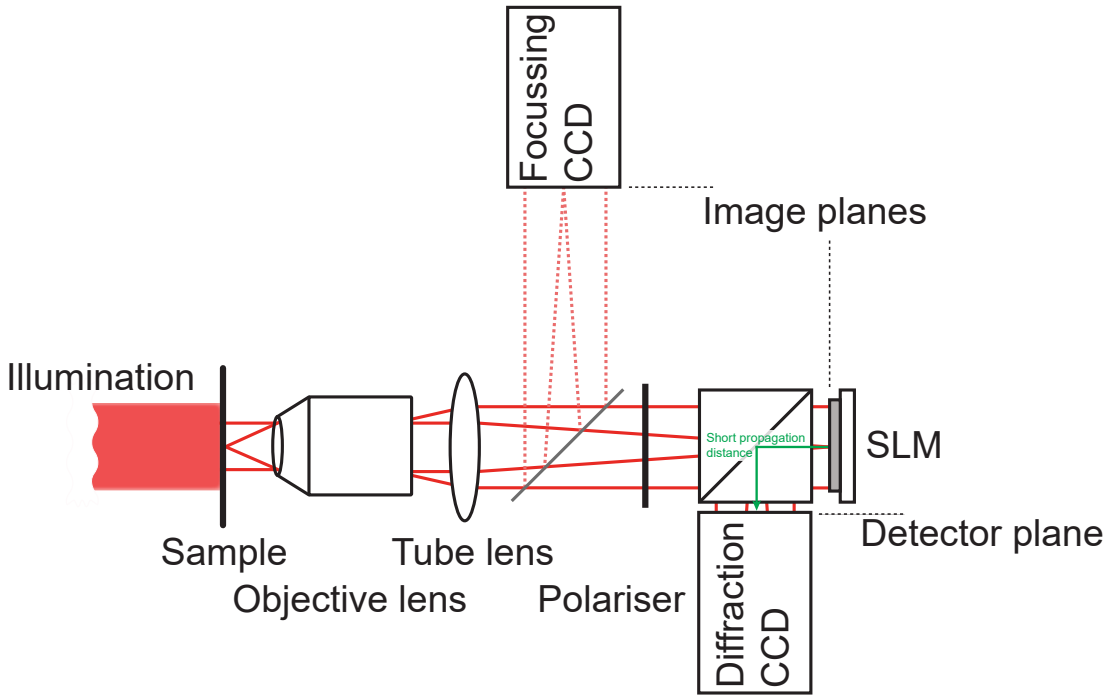

Figure 6.3: The experimental setup for this technique remains the same as the no movement SLM based optical near-field ptychography setup.

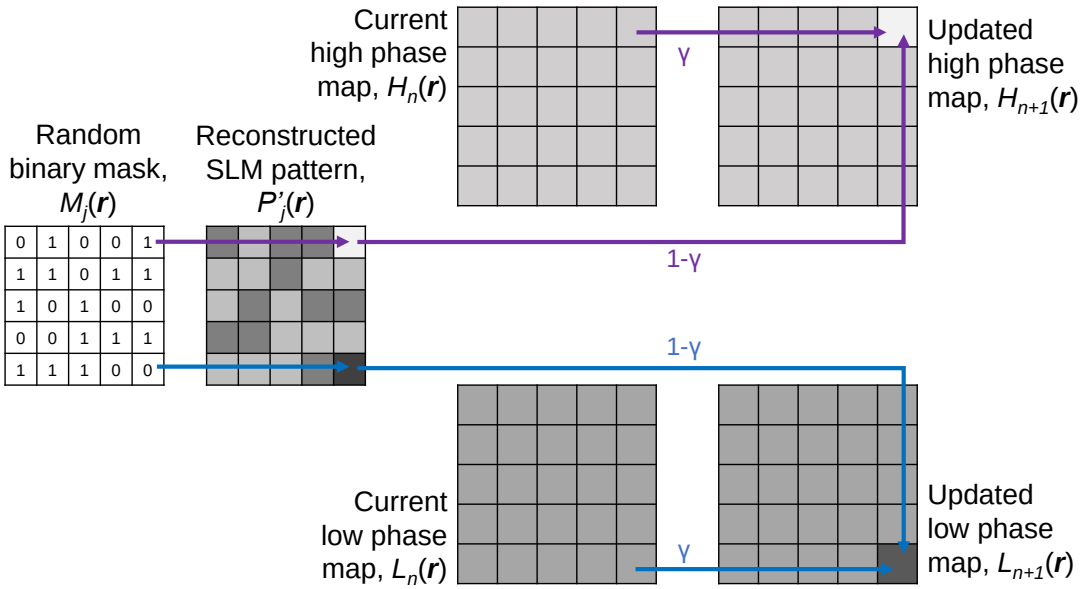

Figure 6.4: The binary mask indicates which pixel values will be updated in the high and low phase maps. The new value from the reconstructed SLM pattern is weighted and summed with the current value on the phase map to give a updated value for that pixel.

6.4 Image reconstruction

The image reconstruction algorithm is similar to that of ePIE, but the update functions are modified. Graphically, this modified algorithm is shown in Figure 6.5. Instead of updating the SLM reconstructions, the phase maps are updated, and the next SLM phase profile is created from the corrected phase maps.

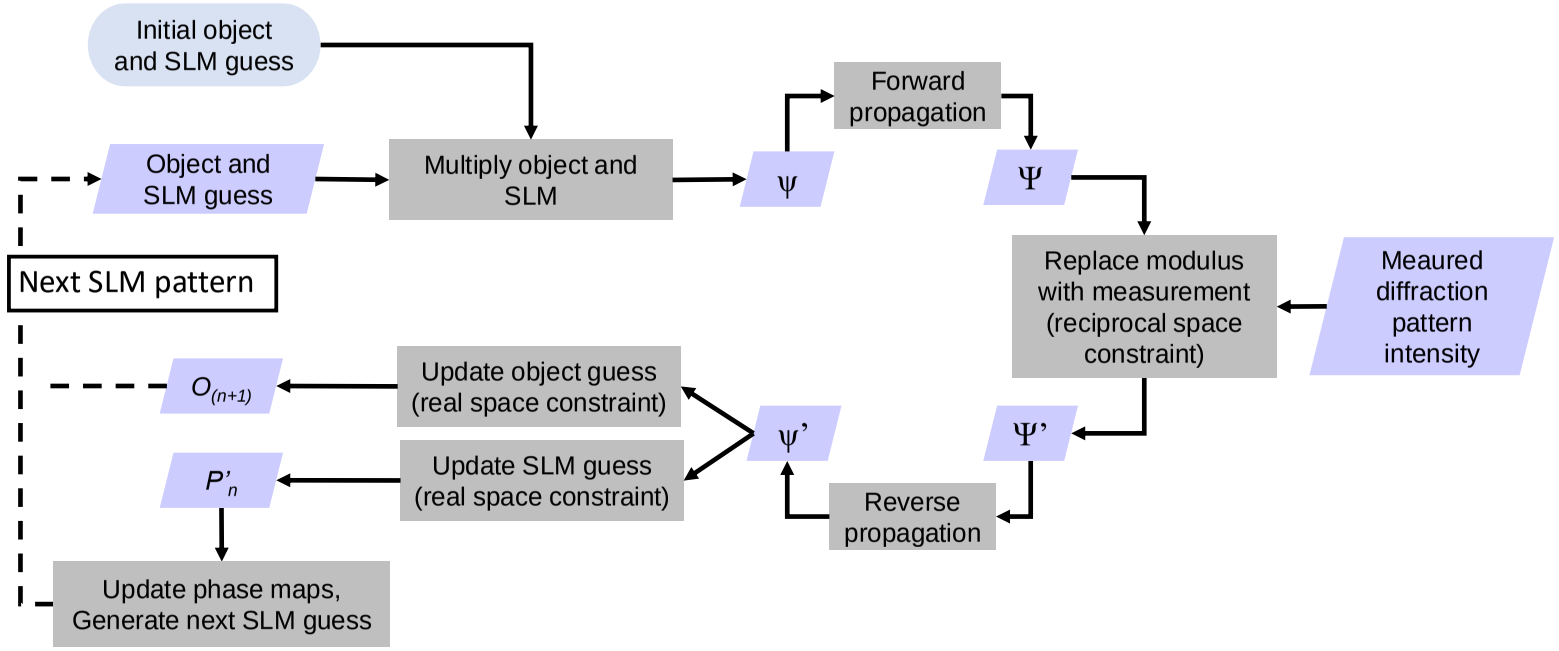

Figure 6.5: The iterative algorithm used to characterise and update the phase maps so that an image of the sample can be reconstructed.

The following symbols are assigned for the image reconstruction algorithm:

M	Random binary mask
H	High phase map
L	Low phase map
S	SLM phase profile
P	Reconstructed SLM phase profile
O	Object transmission function
ψ	Exit wave (with ′ to indicate the updated wave)
Ψ	Diffraction pattern (with ′ to indicate the updated wave)
I	Measured intensity (from the detector)
$j \in [0 \dots J]$	SLM pattern number
n	Phase map iteration number
$\mathbf{r}$	Real space coordinates
$\mathbf{k}$	Reciprocal space coordinates
$\mathcal{P}_z$	Propagator (e.g. Angular Spectrum), over a distance z
α	Object update parameter
β	Probe update parameter
γ	Phase map update parameter

1. For iteration $n = 0$, make an initial guess of the object transmission function $O_n(\mathbf{r})$. Use the first pre-generated SLM phase profile, $S_0(\mathbf{r})$, as the initial guess of the reconstructed phase profile:

$$P_0(\mathbf{r}) = 1. \exp(iS_0(\mathbf{r})) \tag{6.2}$$

2. Multiply the current guess of the object by the reconstructed phase profile to produce the guessed exit wave:

$$\psi_n(\mathbf{r}) = O_n(\mathbf{r})P_j(\mathbf{r}). \tag{6.3}$$

3. Propagate the exit wave to the detector to create a guessed diffraction pattern using the angular spectrum propagator (Section 2.4.4).

$$\Psi_n(\mathbf{k}) = \mathcal{P}_z\left[\psi_n(\mathbf{r})\right]. \tag{6.4}$$

4. Apply a reciprocal space constraint by replacing the modulus of the guessed diffraction pattern with the square root of the measured intensity for SLM pattern j, while retaining the phase, $\theta_n(\mathbf{k}) = \arg(\Psi_n(\mathbf{k}))$:

$$\Psi'_n(\mathbf{k}) = \sqrt{I_j(\mathbf{k})}e^{i\theta_n(\mathbf{k})}. \tag{6.5}$$

5. Reverse propagate this updated diffraction pattern to give an updated exit wave:

$$\psi'_n(\mathbf{r}) = \mathcal{P}_z^{-1}\left[\Psi'_n(\mathbf{k})\right] \tag{6.6}$$

6. Update the guess of the object in the area covered by the illumination, using the object update function:

$$O_{n+1}(\mathbf{r}) = O_n(\mathbf{r}) + \alpha\frac{P_n^*(\mathbf{r})}{|P_n(\mathbf{r})|^2}\left[\psi'_n(\mathbf{r}) - \psi_n(\mathbf{r})\right] \tag{6.7}$$

Update the guess of the probe, using the probe update function:

$$P'_n(\mathbf{r}) = P_n(\mathbf{r}) + \beta \frac{O^*_n(\mathbf{r})}{|O_n(\mathbf{r})|^2} \left[\psi'_n(\mathbf{r}) - \psi_n(\mathbf{r})\right] \tag{6.8}$$

$\alpha \in [0,1]$ and $\beta \in [0,1]$ are the feedback parameters for the object and probe, respectively.

7. Update the phase maps, with the newly updated reconstruction of the SLM. This is equivalent to a reverse of the polling used to generate the SLM patterns:

$$H_{n+1} = \gamma H_n + (1-\gamma) P'_n[M_j == 1] \tag{6.9}$$

$$L_{n+1} = \gamma L_n + (1-\gamma) P'_n[M_j == 0], \tag{6.10}$$

where H and L are the high and low maps respectively, and M is the random binary map associated with the current SLM pattern. $\gamma \in [0,1]$ controls the learning rate: if γ is high the rate of update is low, but more stable to errors in the SLM reconstruction. Where the binary pattern indicates that the pixel is a 'high' phase value, the current value of the pixel on the high phase map is summed (weighted by γ) with the updated value from the experiment, moving it towards its correct value. Visually, this step is demonstrated in Figure 6.4. It should be noted that not all the pixels of the phase maps will be updated, but the total number of updated pixels across both maps will equal the number of pixels on the SLM.

8. Create a guess for the next SLM phase pattern using the updated phase maps:

$$P_{(j+1)} = L_{(n+1)} \times [M_{(j+1)} == 0] + H_{(n+1)} \times [M_{(j+1)} == 1]. \tag{6.11}$$

This is equivalent to the initial polling step used to create the SLM phase profiles,

but this next phase profile uses the updated phase maps. If $j + 1 = J$ then return to $j = 0$.

9. Start the next iteration: $n = n + 1$.

10. Repeat steps 2-9 for a fixed number of iterations, or until the error is sufficiently small.

6.5 Conclusions

This chapter has outlined a new algorithm that constrains the phase values that the SLM can display. Instead reconstructing the phase image of the SLM several times, phase maps are used to store the updated phase response of each pixel of the SLM at two levels. This updated information is then used for the next iteration of the algorithm. This means that both the SLM the phase response of the SLM is characterised and the sample reconstructed simultaneously.

6.5.1 Future work

This reconstruction algorithm has several parameters and extensions which should be further investigated to improve the technique:

- **How many SLM patterns to use?** The previous QPI experiments with the SLM indicate that at least ten SLM patterns should be used. When reducing the number of SLM patterns, it should be checked whether each phase map would be updated by at least one SLM pattern. At the minimum number of SLM patterns, their corresponding binary maps would need to be the inverse of each other.

- **How many phase maps to use?** Although this work has set out the minimum number of phase maps to use: 2 (one high and one low), it is trivial to see that this

could be extended to more phase maps. At the maximum, 256 phase maps would allow the phase response for every pixel to be characterised at all its possible levels.

- **What values should the phase maps take?** If the difference between the values of the phase maps is too high, then large phase edges would be created, with the risk of flyback issues and diffraction into higher orders (Section 2.11.3). If the difference is too small, then the diffraction effect of the SLM would be reduced.

- **Do the phase maps need to be single valued?** In this work, it has been assumed that each phase map is initialised with the same value for every pixel. This does not need to be the case, and each phase map could be a picture, or other pattern.

The next part of this work would include simulating the experiment, in order to investigate the experimental parameters indicated. It can then be performed on the optical bench using the setup outlined in Section 6.3.

Chapter 7

Conclusions

This thesis has described developments in applications and methods for QPI. These developments have been used for enhancing contrast of transparent samples, as well as providing additional numerical information about a sample. The work in this thesis has used the family of QPI techniques known as ptychography as a starting point and investigated how these techniques can be improved specifically for use in high resolution, high speed optical microscopy. SLMs were also identified as an important optical component to the future of QPI techniques. This thesis investigated whether the speed and stability advantages of using an SLM in microscopy can be brought into ptychographic methods.

The background chapter started by laying out the microscopic and optical principles that form the mathematical basis of ptychography, focussing primarily around Fourier optics. Phase imaging was shown to be useful for bio-imaging in order to enhance the contrast of cells, without staining. The benefits of quantitative phase images to provide additional numerical information, such as cell thickness and refractive index, were described. The field of QPI methods was analysed, focussing particularly on the methods that use a new electro-optical device called an SLM. These techniques were shown to be experimentally simple to setup, as well as having fast

acquisition times. Ptychography was also explored in detail, as a QPI technique that produces high quality, accurate images, over a large field of view, but requires large amounts of imaging data, which decreases their frame rate. The operation of SLMs, which can modulate the phase of a light wave in two-dimensions over their surface, was described. They were shown to be able to change their phase modulation characteristics quickly, enabling new operations in microscopy. Limitations of SLMs were also identified, in particular the need to be able to characterise their signal input to phase profile response relation, and the curvature of their front surface. Different QPI techniques used to characterise these flaws were analysed, and were found to produce low quality characterisations over small field-of-views of the phase profile of the SLM.

A novel QPI technique was developed, called optical near-field ptychography, based on near-field ptychography in the x-ray domain. The setup and operation of the technique was explained and the quantitative phase images produced were tested on a range of samples. The technique is simple, and can be implemented as an 'add-on' for standard optical microscopes. The images produced are high quality – any inhomogenities in the optics are removed from the final quantitative phase image of the sample. The amount of diffraction patterns required is considerably reduced when compared to standard, or Fourier ptychography, reducing the amount of data acquisition needed, and increasing the frame rate of imaging. However, as with standard ptychography, the technique requires that the sample is mounted on a translation stage. This was identified as a bottleneck in the speed of data acquisition, as well as disruptive to biological samples. An SLM was identified as a suitable component that could be added to the technique to remove the necessity of the translation stage.

In order to use an SLM effectively, it was important that some of its behaviour was characterised, in particular the linearisation of its phase response and the curvature of

its glass surface. A novel application of standard ptychography in imaging the phase profile of the entire surface of the SLM was therefore developed. The resulting high quality quantitative phase images provided a sub-pixel reconstruction of the SLM display. The technique was shown to have excellent phase accuracy, verified with the reconstruction of a well-characterised physical test sample. A novel way to linearise the phase response of the SLM using ptychography was demonstrated and tested. The micron-sized spherical deformity of the surface of the SLM was also measured, so that it could be compensated to enable high precision usage.

An SLM was combined with optical near-field ptychography to create a novel QPI technique. The optical near-field ptychography setup required a diffuser (to modulate the image wave produced by the microscope before propagation to the detector) and a translation stage (to move the sample and create diversity between the diffraction patterns). This new technique combined both of these functions by using the SLM as a diffuser that can change its phase profile. Because there is no sample movement in this technique, the image acquisition time is quicker and the sample is not disturbed. The setup and operation of the technique was described, and some test images were analysed. However, the phase profile of the SLM required characterisation before the sample data acquisition can take place, which is a lengthy process.

Future work was anticipated with the SLM-based optical near-field ptychography setup. An algorithm was proposed that constrains the range of values the SLM's phase profile can take, meaning that it is possible to characterise the phase profile of the SLM simultaneously with the sample data acquisition. This results in a high quality and frame rate QPI technique with no moving parts, envisioned for use with quantitative phase videos of biological cells.

7.1 Major contributions

This thesis has contributed three novel methods and applications of QPI. Optical near-field ptychography was developed as a novel QPI technique, creating high quality phase images, retaining all the benefits of ptychography, while reducing the acquisition and reconstruction time. It was demonstrated on the optical bench using artificial and biological samples.

A new application of ptychography was contributed, in characterising a phase only SLM. This is an ideal application of ptychography, and produced a high-quality phase image across the entire surface of the SLM. This phase image was then used to characterise the phase response of the device, and the curvature of the glass front.

A novel combination of using a SLM with ptychography was investigated. The proposed method would remove the sample movement from the ptychographic technique, considerably increasing its acquisition rate.

Bibliography

[1] G. Smith, T. King, and D. Wilkins, *Optics and Photonics : An Introduction*, 2nd. Wiley, 2007, vol. 69, pp. 1–506.

[2] J. W. Goodman, *Introduction to Fourier Optics*, 3rd ed. Singapore: McGraw-Hill, 1996.

[3] M. Born, E. Wolf, A. B. Bhatia, P. C. Clemmow, D. Gabor, A. R. Stokes, A. M. Taylor, P. A. Wayman, and W. L. Wilcock, *Principles of Optics*, 7th ed. Cambridge: Cambridge University Press, 1999.

[4] D. G. Voelz, *Computational Fourier Optics: A MATLAB® Tutorial*. SPIE, 2011.

[5] S. Zhang, S. Zhao, L. Bai, M. Guan, J. Mo, and L. Lan, "Melatonin restores normal Bax and Bcl-2 protein expression in the subgranular zone of the dentate gyrus in pinealectomized rats," *Neural Regeneration Research*, vol. 6, no. 27, pp. 2129–2133, Oct. 2011.

[6] I. J. Bigio and S. Fantini, *Quantitative Biomedical Optics*. Cambridge: Cambridge University Press, 2016.

[7] J. Mertz, *Introduction to Optical Microscopy*. Roberts, 2010, pp. 1–45.

[8] E. Hecht, *Hecht 4th Ed Optics*, Fourth. Pearson Education, 2002, p. 204.

[9] R. Horstmeyer, R. Heintzmann, G. Popescu, L. Waller, and C. Yang, "Standardizing the resolution claims for coherent microscopy," *Nature Photonics*, vol. 10, no. 2, pp. 68–71, 2016.

[10] E. Abbe, "Beiträge zur Theorie des Mikroskops und der mikroskopischen Wahrnehmung," *Archiv für Mikroskopische Anatomie*, vol. 9, no. 1, pp. 413–418, Dec. 1873.

[11] G. O. Reynolds, J. B. DeVelis, G. B. Parrent, and B. J. Thompson, *The New Physical Optics Notebook*. 1000 20th Street, Bellingham, WA 98227-0010 USA: SPIE, Jan. 1989.

[12] E. Haustein and P. Schwille, "Trends in fluorescence imaging and related techniques to unravel biological information," *HFSP Journal*, vol. 1, no. 3, pp. 169–180, 2007.

[13] Y. K. Park, C. Depeursinge, and G. Popescu, "Quantitative phase imaging in biomedicine," *Nature Photonics*, vol. 12, no. 10, pp. 578–589, Oct. 2018.

[14] S. W. Hell and J. Wichmann, "Breaking the diffraction resolution limit by stimulated emission: stimulated-emission-depletion fluorescence microscopy," *Optics Letters*, vol. 19, no. 11, p. 780, Jun. 1994.

[15] M. G. Gustafsson, "Surpassing the lateral resolution limit by a factor of two using structured illumination microscopy," *Journal of Microscopy*, vol. 198, no. 2, pp. 82–87, 2000.

[16] E. Betzig, G. H. Patterson, R. Sougrat, O. W. Lindwasser, S. Olenych, J. S. Bonifacino, M. W. Davidson, J. Lippincott-Schwartz, and H. F. Hess, "Imaging Intracellular Fluorescent Proteins at Nanometer Resolution," *Science*, vol. 313, no. 5793, pp. 1642–1645, Sep. 2006.

[17] M. J. Rust, M. Bates, and X. Zhuang, "Sub-diffraction-limit imaging by stochastic optical reconstruction microscopy (STORM)," *Nature Methods*, vol. 3, no. 10, pp. 793–795, Oct. 2006.

[18] R. Kasprowicz, R. Suman, and P. O'Toole, "Characterising live cell behaviour: Traditional label-free and quantitative phase imaging approaches," *The International Journal of Biochemistry & Cell Biology*, vol. 84, pp. 89–95, Mar. 2017.

[19] M. Mir, B. Bhaduri, R. Wang, R. Zhu, and G. Popescu, "Quantitative Phase Imaging," in *Progress in Optics*, vol. 57, Elsevier Inc., 2012, pp. 133–217.

[20] G. Popescu, "Spatial light interference microscopy (SLIM)," *IEEE Photonic Society 24th Annual Meeting, PHO 2011*, vol. 19, no. 2, p. 797, Jan. 2011.

[21] F. Zernike, "Phase contrast, a new method for the microscopic observation of transparent objects part II," *Physica*, vol. 9, no. 10, pp. 974–986, Jul. 1942.

[22] G. Nomarski, "Microinterféromètre différentiel à ondes polarisées," *Journal de Physique et Le Radium*, vol. 16, 9S–11S, 1955.

[23] T. A. Zangle and M. A. Teitell, "Live-cell mass profiling: An emerging approach in quantitative biophysics," *Nature Methods*, vol. 11, no. 12, pp. 1221–1228, Dec. 2014.

[24] D. Boss, J. Kuehn, C. Depeursinge, P. J. Magistretti, and P. Marquet, "Dual-wavelength Digital Holography for quantification of cell volume and integral refractive index (RI)," in *OSA Biomedical Optics*, P. T. C. So and E. Beaurepaire, Eds., vol. 8086, Jun. 2011, p. 808 608.

[25] J. Marrison, L. Räty, P. Marriott, and P. O'Toole, "Ptychography-a label free, high-contrast imaging technique for live cells using quantitative phase information," *Scientific Reports*, vol. 3, no. 1, p. 2369, Dec. 2013.

[26] T. Kim, R. Zhou, L. L. Goddard, and G. Popescu, "Breakthroughs in Photonics 2013: Quantitative Phase Imaging: Metrology Meets Biology," *IEEE Photonics Journal*, vol. 6, no. 2, pp. 1–9, Apr. 2014.

[27] H. G. Davies and M. H. F. Wilkins, "Interference Microscopy and Mass Determination," *Nature*, vol. 169, no. 4300, p. 541, Mar. 1952.

[28] H. G. Davies and M. H. F. Wilkins, "Interference Microscopy and Mass Determination," *Nature*, vol. 169, no. 4300, p. 541, Mar. 1952.

[29] H. V. Pham, B. Bhaduri, K. Tangella, C. Best-Popescu, and G. Popescu, "Real Time Blood Testing Using Quantitative Phase Imaging," *PLoS ONE*, vol. 8, no. 2, I. Georgakoudi, Ed., e55676, Feb. 2013.

[30] M. Mir, T. Kim, A. Majumder, M. Xiang, R. Wang, S. C. Liu, M. U. Gillette, S. Stice, and G. Popescu, "Label-Free Characterization of Emerging Human Neuronal Networks," *Scientific Reports*, vol. 4, no. 1, p. 4434, May 2014.

[31] M. Mir, A. Bergamaschi, B. S. Katzenellenbogen, and G. Popescu, "Highly sensitive quantitative imaging for monitoring single cancer cell growth kinetics and drug response," *PLoS ONE*, vol. 9, no. 2, A. Ahmad, Ed., e89000, Feb. 2014.

[32] M. Mir, Z. Wang, Z. Shen, M. Bednarz, R. Bashir, I. Golding, S. G. Prasanth, and G. Popescu, "Optical measurement of cycle-dependent cell growth," *Proceedings of the National Academy of Sciences*, vol. 108, no. 32, pp. 13 124–13 129, Aug. 2011.

[33] G. Popescu, K. Park, M. Mir, and R. Bashir, "New technologies for measuring single cell mass," *Lab on a Chip*, vol. 14, no. 4, pp. 646–652, 2014.

[34] Y. Sung, A. Tzur, S. Oh, W. Choi, V. Li, R. R. Dasari, Z. Yaqoob, and M. W. Kirschner, "Size homeostasis in adherent cells studied by synthetic phase microscopy," *Proceedings of the National Academy of Sciences*, vol. 110, no. 41, pp. 16 687–16 692, Oct. 2013.

[35] J. Nadeau, Y. Park, and G. Popescu, "Methods in quantitative phase imaging in life science," *Methods*, vol. 136, pp. 1–3, Mar. 2018.

[36] S. Plainis, D. A. Atchison, and W. N. Charman, "Power profiles of multifocal contact lenses and their interpretation," *Optometry and Vision Science*, vol. 90, no. 10, pp. 1066–1077, Oct. 2013.

[37] Q. Weijuan, C. O. Choo, Y. Yingjie, and A. Asundi, "Microlens characterization by digital holographic microscopy with physical spherical phase compensation," *Appl. Opt.*, vol. 49, no. 33, pp. 6448–6454, Nov. 2010.

[38] A. B. Parthasarathy, K. K. Chu, T. N. Ford, and J. Mertz, "Quantitative phase imaging using a partitioned detection aperture," *Optics Letters*, vol. 37, no. 19, p. 4062, Oct. 2012.

[39] J. Kacperski and M. Kujawińska, "Active, LCoS based laser interferometer for microelements studies.," *Optics express*, vol. 14, no. 21, pp. 9664–78, Oct. 2006.

[40] J. M. Thomas, E. T. Simpson, T. Kasama, and R. E. Dunin-Borkowski, "Electron holography for the study of magnetic nanomaterials," *Accounts of Chemical Research*, vol. 41, no. 5, pp. 665–674, May 2008.

[41] D. Malacara, M. Servín, and Z. Malacara, *Interferogram Analysis for Optical Testing*. CRC Press, 2005.

[42] P. Bon, G. Maucort, B. Wattellier, and S. Monneret, "Quadriwave lateral shearing interferometry for quantitative phase microscopy of living cells," *Optics Express*, vol. 17, no. 15, p. 13 080, Jul. 2009.

[43] D. Gabor, "A New Microscopic Principle," *Nature*, vol. 161, no. 4098, pp. 777–778, May 1948.

[44] E. N. Leith and J. Upatnieks, "Reconstructed Wavefronts and Communication Theory*," *Journal of the Optical Society of America*, vol. 52, no. 10, p. 1123, Oct. 1962.

[45] G. Popescu, *Quantitative Phase Imaging of Cells and Tissues*. McGraw-Hill, 2011.

[46] P. Marquet, B. Rappaz, P. J. Magistretti, E. Cuche, Y. Emery, T. Colomb, and C. Depeursinge, "Digital holographic microscopy: a noninvasive contrast imaging technique allowing quantitative visualization of living cells with subwavelength axial accuracy," *Optics Letters*, vol. 30, no. 5, p. 468, Mar. 2005.

[47] C. L. Curl, C. J. Bellair, P. J. Harris, B. E. Allman, A. Roberts, K. A. Nugent, and L. M. Delbridge, "Single cell volume measurement by quantitative phase microscopy (QPM): A case study of erythrocyte morphology," *Cellular Physiology and Biochemistry*, vol. 17, no. 5-6, pp. 193–200, 2006.

[48] D. Paganin and K. A. Nugent, "Noninterferometric phase imaging with partially coherent light," *Physical Review Letters*, vol. 80, no. 12, pp. 2586–2589, Mar. 1998.

[49] M. R. Teague, "Deterministic phase retrieval: a Green's function solution," *Journal of the Optical Society of America*, vol. 73, no. 11, p. 1434, Nov. 1983.

[50] L. J. Allen, H. M. L. Faulkner, K. A. Nugent, M. P. Oxley, and D. Paganin, "Phase retrieval from images in the presence of first-order vortices," *Physical Review E*, vol. 63, no. 3, p. 037 602, Feb. 2001.

[51] A. Barty, K. A. Nugent, D. Paganin, and A. Roberts, "Quantitative optical phase microscopy," *Optics Letters*, vol. 23, no. 11, p. 817, Jun. 1998.

[52] G. Popescu, K. Badizadegan, R. R. Dasari, and M. S. Feld, "Observation of dynamic subdomains in red blood cells," *Journal of Biomedical Optics*, vol. 11, no. 4, p. 040 503, 2006.

[53] G. Popescu, L. P. Deflores, J. C. Vaughan, K. Badizadegan, H. Iwai, R. R. Dasari, and M. S. Feld, "Fourier phase microscopy for investigation of biological structures and dynamics," *Optics Letters*, vol. 29, no. 21, p. 2503, Nov. 2004.

[54] H. Kadono, M. Ogusu, and S. Toyooka, "Phase shifting common path interferometer using a liquid-crystal phase modulator," *Optics Communications*, vol. 110, no. 3-4, pp. 391–400, Aug. 1994.

[55] K. Creath, "V Phase-Measurement Interferometry Techniques," in *Progress in Optics*, C, vol. 26, 1988, pp. 349–393.

[56] N. Lue, W. Choi, G. Popescu, T. Ikeda, R. R. Dasari, K. Badizadegan, and M. S. Feld, "Quantitative phase imaging of live cells using fast Fourier phase microscopy," *Applied Optics*, vol. 46, no. 10, p. 1836, Apr. 2007.

[57] J. S. Gong, T. Liu, J. Chen, J. Zhu, and J. M. Xu, "Multi-slice CT virtual gastroscopy in demonstrating gastric cancer: Comparison with optical gastroscopy and pathology," *Chinese Journal of Medical Imaging Technology*, vol. 27, no. 2, pp. 345–348, Jun. 2011.

[58] Z. Wang, L. Millet, V. Chan, H. Ding, M. U. Gillette, R. Bashir, and G. Popescu, "Label-free intracellular transport measured by spatial light interference microscopy," *Journal of Biomedical Optics*, vol. 16, no. 2, p. 026 019, Feb. 2011.

[59] Z. Wang, I. S. Chun, X. Li, Z.-Y. Ong, E. Pop, L. Millet, M. Gillette, and G. Popescu, "Topography and refractometry of nanostructures using spatial light interference microscopy," *Optics Letters*, vol. 35, no. 2, p. 208, Jan. 2010.

[60] Z. Wang, D. L. Marks, P. S. Carney, L. J. Millet, M. U. Gillette, A. Mihi, P. V. Braun, Z. Shen, S. G. Prasanth, and G. Popescu, "Spatial light interference tomography (SLIT)," *Optics Express*, vol. 19, no. 21, p. 19 907, Oct. 2011.

[61] M. Mir, K. Tangella, and G. Popescu, "Blood testing at the single cell level using quantitative phase and amplitude microscopy," *Biomedical Optics Express*, vol. 2, no. 12, p. 3259, Dec. 2011.

[62] Z. Wang, "Tissue refractive index as marker of disease," *Journal of Biomedical Optics*, vol. 16, no. 11, p. 116 017, Nov. 2011.

[63] S. Sridharan, V. Macias, K. Tangella, A. Kajdacsy-Balla, and G. Popescu, "Prediction of prostate cancer recurrence using quantitative phase imaging," *Scientific Reports*, vol. 5, no. 1, p. 9976, Sep. 2015.

[64] T. H. Nguyen, M. E. Kandel, M. Rubessa, M. B. Wheeler, and G. Popescu, "Gradient light interference microscopy for 3D imaging of unlabeled specimens," *Nature Communications*, vol. 8, no. 1, p. 210, Dec. 2017.

[65] J. M. Rodenburg and A. M. Maiden, "Ptychography (in press)," in *Springer Handbook of Microscopy*, P. Hawkes and J. C. H. Spence, Eds., 1st ed., Springer International Publishing, 2019.

[66] J. M. Rodenburg, "Ptychography and related diffractive imaging methods," *Advances in Imaging and Electron Physics*, vol. 150, no. 07, pp. 87–184, 2008.

[67] W. Hoppe, "Beugung im inhomogenen Primärstrahlwellenfeld. I. Prinzip einer Phasenmessung von Elektronenbeugungsinterferenzen," *Acta Crystallographica Section A*, vol. 25, no. 4, pp. 495–501, Jul. 1969.

[68] W. Hoppe, "Beugung im inhomogenen Primärstrahlwellenfeld. III. Amplituden- und Phasenbestimmung bei unperiodischen Objekten," *Acta Crystallographica Section A*, vol. 25, no. 4, pp. 508–514, Jul. 1969.

[69] J. M. Rodenburg and H. M. Faulkner, "A phase retrieval algorithm for shifting illumination," *Applied Physics Letters*, vol. 85, no. 20, pp. 4795–4797, Nov. 2004.

[70] A. M. Maiden, J. M. Rodenburg, and M. J. Humphry, "Optical ptychography: a practical implementation with useful resolution," *Optics Letters*, vol. 35, no. 15, p. 2585, 2010.

[71] J. Sun, C. Zuo, J. Zhang, Y. Fan, and Q. Chen, "High-speed Fourier ptychographic microscopy based on programmable annular illuminations," *Scientific Reports*, vol. 8, no. 1, p. 7669, Dec. 2018.

[72] G. Zheng, R. Horstmeyer, and C. Yang, "Wide-field, high-resolution Fourier ptychographic microscopy," *Nature Photonics*, vol. 7, no. 9, pp. 739–745, Sep. 2013.

[73] X. Ou, R. Horstmeyer, C. Yang, and G. Zheng, "Quantitative phase imaging via Fourier ptychographic microscopy," *Optics Letters*, vol. 38, no. 22, p. 4845, Nov. 2013.

[74] G. Zheng, *Fourier ptychographic imaging: A MATLAB® tutorial*. IOP Publishing, 2016, pp. 1–95.

[75] L. Tian and L. Waller, "3D intensity and phase imaging from light field measurements in an LED array microscope," *Optica*, vol. 2, no. 2, p. 104, Feb. 2015.

[76] L. Tian, Z. Liu, L.-H. Yeh, M. Chen, J. Zhong, and L. Waller, "Computational illumination for high-speed in vitro Fourier ptychographic microscopy," *Optica*, vol. 2, no. 10, pp. 904–911, Oct. 2015.

[77] M. Stockmar, P. Cloetens, I. Zanette, B. Enders, M. Dierolf, F. Pfeiffer, and P. Thibault, "Near-field ptychography: Phase retrieval for inline holography using a structured illumination," *Scientific Reports*, vol. 3, no. 1, p. 1927, Dec. 2013.

[78] S. Sala, V. S. C. Kuppili, S. Chalkidis, D. J. Batey, X. Shi, C. Rau, and P. Thibault, "Multiscale X-ray imaging using ptychography," *Journal of Synchrotron Radiation*, vol. 25, no. 4, pp. 1214–1221, Jul. 2018.

[79] A. L. Robisch, K. Kröger, A. Rack, and T. Salditt, "Near-field ptychography using lateral and longitudinal shifts," *New Journal of Physics*, vol. 17, no. 7, p. 073 033, Jul. 2015.

[80] M. Stockmar, M. Hubert, M. Dierolf, B. Enders, R. Clare, S. Allner, A. Fehringer, I. Zanette, J. Villanova, J. Laurencin, P. Cloetens, F. Pfeiffer, and P. Thibault, "X-ray nanotomography using near-field ptychography," *Optics Express*, vol. 23, no. 10, p. 12 720, May 2015.

[81] M. Stockmar, I. Zanette, M. Dierolf, B. Enders, R. Clare, F. Pfeiffer, P. Cloetens, A. Bonnin, and P. Thibault, "X-ray near-field ptychography for optically thick specimens," *Physical Review Applied*, vol. 3, no. 1, p. 014 005, Jan. 2015.

[82] R. M. Clare, M. Stockmar, M. Dierolf, I. Zanette, and F. Pfeiffer, "Characterization of near-field ptychography," *Optics Express*, vol. 23, no. 15, p. 19 728, Jul. 2015.

[83] P. Thibault, M. Dierolf, O. Bunk, A. Menzel, and F. Pfeiffer, "Probe retrieval in ptychographic coherent diffractive imaging," *Ultramicroscopy*, vol. 109, no. 4, pp. 338–343, Mar. 2009.

[84] S. Marchesini, "A unified evaluation of iterative projection algorithms for phase retrieval," *Review of Scientific Instruments*, vol. 78, no. 1, p. 011 301, Jan. 2007.

[85] M. Guizar-Sicairos and J. R. Fienup, "Image reconstruction by phase retrieval with transverse translation diversity," in *Optics Express*, P. J. Bones, M. A. Fiddy, and R. P. Millane, Eds., vol. 7076, Aug. 2008, 70760A.

[86] D. R. Luke, "Relaxed averaged alternating reflections for diffraction imaging," *Inverse Problems*, vol. 21, no. 1, pp. 37–50, Feb. 2005.

[87] H. M. Faulkner and J. M. Rodenburg, "Movable aperture lensless transmission microscopy: A novel phase retrieval algorithm," *Physical Review Letters*, vol. 93, no. 2, pp. 023 903–1, Jul. 2004.

[88] P. Thibault, M. Dierolf, A. Menzel, O. Bunk, C. David, and F. Pfeiffer, "High-resolution scanning X-ray diffraction microscopy," *Science*, vol. 321, no. 5887, pp. 379–382, Jul. 2008.

[89] J. M. Rodenburg, A. C. Hurst, and A. G. Cullis, "Transmission microscopy without lenses for objects of unlimited size," *Ultramicroscopy*, vol. 107, no. 2-3, pp. 227–231, Feb. 2007.

[90] O. Bunk, M. Dierolf, S. Kynde, I. Johnson, O. Marti, and F. Pfeiffer, "Influence of the overlap parameter on the convergence of the ptychographical iterative engine," *Ultramicroscopy*, vol. 108, no. 5, pp. 481–487, Apr. 2008.

[91] A. M. Maiden and J. M. Rodenburg, "An improved ptychographical phase retrieval algorithm for diffractive imaging," *Ultramicroscopy*, vol. 109, no. 10, pp. 1256–1262, Sep. 2009.

[92] A. M. Maiden, J. M. Rodenburg, and M. J. Humphry, "A new method of high resolution, quantitative phase scanning microscopy," *Proceedings of SPIE - The International Society for Optical Engineering*, vol. 7729, no. 0, M. T. Postek, D. E. Newbury, S. F. Platek, and D. C. Joy, Eds., p. 77291I, Jun. 2010.

[93] D. Claus, A. M. Maiden, F. Zhang, F. G. R. Sweeney, M. J. Humphry, H. Schluesener, and J. M. Rodenburg, "Quantitative phase contrast optimised cancerous cell differentiation via ptychography," *Optics Express*, vol. 20, no. 9, p. 9911, Apr. 2012.

[94] K. Giewekemeyer, P. Thibault, S. Kalbfleisch, A. Beerlink, C. M. Kewish, M. Dierolf, F. Pfeiffer, and T. Salditt, "Quantitative biological imaging by ptychographic x-ray diffraction microscopy," *Proceedings of the National Academy of Sciences*, vol. 107, no. 2, pp. 529–534, Jan. 2010.

[95] F. Hüe, J. M. Rodenburg, A. M. Maiden, and P. A. Midgley, "Extended ptychography in the transmission electron microscope: Possibilities and limitations," *Ultramicroscopy*, vol. 111, no. 8, pp. 1117–1123, Jul. 2011.

[96] M. J. Humphry, B. Kraus, A. C. Hurst, A. M. Maiden, and J. M. Rodenburg, "Ptychographic electron microscopy using high-angle dark-field scattering for sub-nanometre resolution imaging," *Nature Communications*, vol. 3, no. 1, p. 730, Jan. 2012.

[97] A. Maiden, D. Johnson, and P. Li, "Further improvements to the ptychographical iterative engine," *Optica*, vol. 4, no. 7, p. 736, Jul. 2017.

[98] A. M. Maiden, M. J. Humphry, M. C. Sarahan, B. Kraus, and J. M. Rodenburg, "An annealing algorithm to correct positioning errors in ptychography," *Ultramicroscopy*, vol. 120, pp. 64–72, Sep. 2012.

[99] H. Nyquist, "Certain Topics in Telegraph Transmission Theory," *Transactions of the American Institute of Electrical Engineers*, vol. 47, no. 2, pp. 617–644, Apr. 1928.

[100] Y. L. Lee, Y. C. Lin, H. Y. Tu, and C. J. Cheng, "Phase measurement accuracy in digital holographic microscopy using a wavelength-stabilized laser diode," *Journal of Optics (United Kingdom)*, vol. 15, no. 2, p. 025 403, Feb. 2013.

[101] T. M. Godden, A. Muñiz-Piniella, J. D. Claverley, A. Yacoot, and M. J. Humphry, "Phase calibration target for quantitative phase imaging with ptychography," *Optics Express*, vol. 24, no. 7, p. 7679, Apr. 2016.

[102] Z. Zhang, Z. You, and D. Chu, "Fundamentals of phase-only liquid crystal on silicon (LCOS) devices," *Light: Science & Applications*, vol. 3, no. 10, e213, Oct. 2014.

[103] K. Nakamura, H. Takagi, T. Goto, P. B. Lim, H. Horimai, H. Yoshikawa, V. M. Bove, and M. Inoue, "Improvement of diffraction efficiency of three-dimensional magneto-optic spatial light modulator with

magnetophotonic crystal," *Applied Physics Letters*, vol. 108, no. 2, p. 022 404, Jan. 2016.

[104] H. Takagi, K. Nakamura, T. Goto, P. B. Lim, and M. Inoue, "Magneto-optic spatial light modulator with submicron-size magnetic pixels for wide-viewing-angle holographic displays," *Optics Letters*, vol. 39, no. 11, p. 3344, Jun. 2014.

[105] R. R. Thomson, A. S. Bockelt, E. Ramsay, S. Beecher, A. H. Greenaway, A. K. Kar, and D. T. Reid, "Shaping ultrafast laser inscribed optical waveguides using a deformable mirror," *Optics Express*, vol. 16, no. 17, p. 12 786, Aug. 2008.

[106] R. D. Simmonds, P. S. Salter, A. Jesacher, and M. J. Booth, "Three dimensional laser microfabrication in diamond using a dual adaptive optics system," *Optics Express*, vol. 19, no. 24, p. 24 122, Nov. 2011.

[107] H. Zhang, J. Zhang, and L. Wu, "Evaluation of phase-only liquid crystal spatial light modulator for phase modulation performance using a Twyman-Green interferometer," *Measurement Science and Technology*, vol. 18, no. 6, pp. 1724–1728, Jun. 2007.

[108] A. Jesacher, S. Bernet, and M. Ritsch-Marte, "Colour hologram projection with an SLM by exploiting its full phase modulation range," *Optics Express*, vol. 22, no. 17, p. 20 530, Aug. 2014.

[109] M. H. Schuck, D. J. McKnight, and K. M. Johnson, "Automotive head-up display using liquid-crystal-on-silicon displays," *Journal of the Society for Information Display*, vol. 5, no. 1, p. 33, 1997.

[110] M. Makowski, I. Ducin, K. Kakarenko, J. Suszek, M. Sypek, and A. Kolodziejczyk, "Simple holographic projection in color," *Optics Express*, vol. 20, no. 22, p. 25 130, Oct. 2012.

[111] W. A. Crossland, T. D. Wilkinson, I. G. Manolis, M. M. Redmond, and A. B. Davey, "Telecommunications Applications of LCOS Devices," *Molecular Crystals and Liquid Crystals*, vol. 375, no. 932491364, pp. 1–13, 2002.

[112] M. Salsi, C. Koebele, D. Sperti, P. Tran, H. Mardoyan, P. Brindel, S. Bigo, A. Boutin, F. Verluise, P. Sillard, M. Astruc, L. Provost, and G. Charlet, "Mode-division multiplexing of 2 × 100 Gb/s channels using an LCOS-based spatial modulator," *Journal of Lightwave Technology*, vol. 30, no. 4, pp. 618–623, Feb. 2012.

[113] T. Shirai, K. Takeno, H. Arimoto, and H. Furukawa, "Adaptive optics with a liquid-crystal-on-silicon spatial light modulator and its behavior in retinal imaging," *Japanese Journal of Applied Physics*, vol. 48, no. 7 PART 1, p. 070 213, Jul. 2009.

[114] D. E. Smalley, Q. Y. Smithwick, V. M. Bove, J. Barabas, and S. Jolly, "Anisotropic leaky-mode modulator for holographic video displays," *Nature*, vol. 498, no. 7454, pp. 313–317, Jun. 2013.

[115] Z. Zeng, H. Zheng, X. Lu, H. Gao, and Y. Yu, "Dynamic holographic three-dimensional projection based on liquid crystal spatial light modulator and cylindrical fog screen," *Optical Review*, vol. 22, no. 5, pp. 853–861, Oct. 2015.

[116] J. E. Curtis, B. A. Koss, and D. G. Grier, "Dynamic holographic optical tweezers," *Optics Communications*, vol. 207, no. 1-6, pp. 169–175, Jun. 2002.

[117] T. Čižmár, M. Mazilu, and K. Dholakia, "In situ wavefront correction and its application to micromanipulation," *Nature Photonics*, vol. 4, no. 6, pp. 388–394, Jun. 2010.

[118] V. Arrizón, E. Carreón, and M. Testorf, "Implementation of Fourier array illuminators using pixelated SLM: Efficiency limitations," *Optics Communications*, vol. 160, no. 4-6, pp. 207–213, Feb. 1999.

[119] X. Wang, B. Wang, P. J. Bos, J. E. Anderson, J. J. Pouch, and F. a. Miranda, "Finite-difference time-domain simulation of a liquid-crystal optical phased array," *Journal of the Optical Society of America A*, vol. 22, no. 2, p. 346, 2005.

[120] A. Lizana, A. M??rquez, I. Moreno, C. Iemmi, J. Campos, and M. J. Yzuel, "Wavelength dependence of polarimetric and phase-shift characterization of a liquid crystal on silicon display," *Journal of the European Optical Society*, vol. 3, p. 08 012, Mar. 2008.

[121] *HOLOEYE PLUTO Device Operating Instructions*, 2011.

[122] A. Bergeron, J. Gauvin, F. Gagnon, D. Gingras, H. H. Arsenault, and M. Doucet, "Phase calibration and applications of a liquid-crystal spatial light modulator," *Applied Optics*, vol. 34, no. 23, p. 5133, Aug. 1995.

[123] B. Villalobos-Mendoza, F. S. Granados-Agustín, D. Aguirre-Aguirre, and A. Cornejo-Rodríguez, "Obtaining the curve "phase shift vs gray level" of a spatial light modulator Holoeye LC2012," *Journal of Physics: Conference Series*, vol. 605, no. 1, p. 012 016, Apr. 2015.

[124] B. Villalobos-Mendoza, F. S. Granados-Agustín, D. Aguirre-Aguirre, R. Izazága-Pérez, and A. Cornejo-Rodríguez, "Measuring the phase shifts produced by transmissive spatial light modulators," *SPIE Newsroom*, pp. 4–6, Jun. 2015.

[125] S. Panezai, D. Wang, J. Zhao, and Y. Wang, "Study of the modulation characterization of phase-only liquid crystal spatial light modulator by digital holography," in *Proceedings of SPIE*, X. Lin, Y. Namba, and T. Xing, Eds., vol. 8420, Oct. 2012, 84200F–84200F–6.

[126] C. Kohler, F. Zhang, and W. Osten, "Characterization of a spatial light modulator and its application in phase retrieval," *Applied Optics*, vol. 48, no. 20, p. 4003, Jul. 2009.

[127] A. Burman, M. T. Garea, A. Lutenberg, and F. Perez Quintián, "Characterization and control of a microdisplay as a Spatial Light Modulator," *Journal of Physics: Conference Series*, vol. 274, no. 1, p. 012 102, Jan. 2011.

[128] S. McDermott and A. Maiden, "Near-field ptychographic microscope for quantitative phase imaging," *Optics Express*, vol. 26, no. 19, p. 25 471, Sep. 2018.

[129] M. Martínez-Corral and B. Javidi, "Fundamentals of 3D imaging and displays: a tutorial on integral imaging, light-field, and plenoptic systems," *Advances in Optics and Photonics*, vol. 10, no. 3, p. 512, 2018.

[130] X. Huang, H. Yan, R. Harder, Y. Hwu, I. K. Robinson, and Y. S. Chu, "Optimization of overlap uniformness for ptychography," *Optics Express*, vol. 22, no. 10, p. 12 634, May 2014.

[131] R. Clare, M. Dierolf, and I. Zanette, "Polychromatic near-field ptychography," *International Conference Image and Vision Computing New Zealand*, vol. 23, no. 15, pp. 1–6, Nov. 2017.

[132] S. Gravel and V. Elser, "Divide and concur: A general approach to constraint satisfaction," *Physical Review E*, vol. 78, no. 3, p. 036 706, Sep. 2007.

[133] P. Li and A. Maiden, "Optical ptychography with extended depth of field," *Journal of Physics: Conference Series*, vol. 902, no. 1, p. 012 015, Sep. 2017.

[134] E. H. R. Tsai, I. Usov, A. Diaz, A. Menzel, and M. Guizar-Sicairos, "X-ray ptychography with extended depth of field," *Optics Express*, vol. 24, no. 25, p. 29 089, Dec. 2016.

[135] H. Zhang, S. Jiang, J. Liao, J. Deng, J. Liu, Y. Zhang, and G. Zheng, "Near-field Fourier ptychography: super-resolution phase retrieval via speckle illumination," *Optics Express*, vol. 27, no. 5, p. 7498, Mar. 2019.

[136] N. Metropolis, A. W. Rosenbluth, M. N. Rosenbluth, A. H. Teller, and E. Teller, "Equation of State Calculations by Fast Computing Machines," *The Journal of Chemical Physics*, vol. 21, no. 6, pp. 1087–1092, Jun. 1953.

[137] S. McDermott, P. Li, G. Williams, and A. Maiden, "Characterizing a spatial light modulator using ptychography," *Opt. Lett.*, vol. 42, no. 3, pp. 371–374, Feb. 2017.

[138] J. García-Márquez, V. López, A. González-Vega, and E. Noé, "Flicker minimization in an LCoS spatial light modulator," *Optics Express*, vol. 20, no. 8, p. 8431, Apr. 2012.

[139] P. Li, T. Edo, D. Batey, J. Rodenburg, and A. Maiden, "Breaking ambiguities in mixed state ptychography," *Optics Express*, vol. 24, no. 8, p. 9038, 2016.

[140] H. Wang, Z. Dong, F. Fan, Y. Feng, Y. Lou, and X. Jiang, "Characterization of Spatial Light Modulator Based on the Phase in Fourier Domain of the Hologram and Its Applications in Coherent Imaging," *Applied Sciences*, vol. 8, no. 7, p. 1146, Jul. 2018.

[141] X. Zhang, B. Cheng, C. Liu, W. Shen, X. Dong, X. Ma, and J. Zhu, "Measurement of mid-frequency wavefront error for large optical components with ptychography," *Applied Optics*, vol. 58, no. 2, p. 264, Jan. 2019.

Appendices

Appendix A

MATLAB code examples of wave propagators

A.1 Fresnel propagation

In MATLAB, the Fresnel propagation can be achieved by:[1]

```
function propagated_image = FresnelPropagation(object_image,
    obj_plane_side_length,wavelength,propagation_distance)
%% Performs Fresnel propagation of 2D image and returns propagated
    image
%Inputs:
%   object_image: the image of the object to be diffracted
%   obj_plane_side_length: the length of the object plane (x,y)
%   wavelength: the wavelength of the simluated monochromatic light
%   propagation_distance: the distance between the source plane and
    the observation plane
```

[1] The term e^{ikz} is dropped from the transfer function, as it does not affect the transverse spatial structure, but is a constant phase delay for all the plane wave components.

```
8  %
9  %Outputs:
10 %   propgagted_image: the propagated image
11
12 %% Initialise coordinate space
13 % number of pixels of object image
14 [x_size,y_size] = size(object_image);
15
16 % sample interval of object image
17 dx = obj_plane_side_length(1)/x_size;
18 dy = obj_plane_side_length(2)/y_size;
19
20 % set up reciprocal coordinate space
21 fx = fftshift(-x_size/2:x_size/2 - 1);
22 fx = fx./(dx*x_size);
23 fy = fftshift(-y_size/2:y_size/2 - 1);
24 fy = fy./(dy*y_size);
25
26 [FX,FY] = meshgrid(fx,fy);
27
28 %% Calculate transfer function
29 H = exp(-1i*pi*wavelength*propagation_distance*(FX.^2+FY.^2));
30 H=fftshift(H);
31
32 %% Fourier transform object image
33 object_image = fftshift(fft2(fftshift(object_image)));
34
```

```
35 %% Perform convolution in Fourier space
36 convolved_image = H.*object_image;
37
38 %% Inverse Fourier transform
39 propagated_image = ifftshift(ifft2(ifftshift(convolved_image)));
40 end
```

A.2 Fraunhofer propagation

In MATLAB, the Fraunhofer propagation can be achieved by[2]:

```
1  function [propagated_image, x2, y2] = fraunhoferPropagation(
       object_image, obj_plane_side_length,wavelength,propagation_distance
       )
2  %% Performs fraunhofer propagation of 2D image and returns propagated
       image
3  % Inputs:
4  %   object_image: the image of the object to be diffracted
5  %   plane_side_length: the length of the object plane (x,y)
6  %   wavelength: the wavelength of the simluated monochromatic light
7  %   propagation distance: the distance between the object plane and
       the observation plane
8  %
9  % Outputs:
10 %   propagated_image: the propagated image
11 %   x2, y2: coordinates of observation plane
12
```

[2] As with the Fresnel propagator, the term e^{ikz} is dropped.

```
%% Initialise coordinate space
% number of pixels of object image
[x_size,y_size] = size(object_image);
% sample interval of object image
dx1 = obj_plane_side_length(1)/x_size;
dy1 = obj_plane_side_length(2)/y_size;
% the observation plane side length
obs_plane_side_length(1) = wavelength*propagation_distance/dx1;
obs_plane_side_length(2) = wavelength*propagation_distance/dy1;
% the sample size of the observation plane
dx2 = wavelength*propagation_distance/obj_plane_side_length(1);
dy2 = wavelength*propagation_distance/obj_plane_side_length(2);
% the coordinate space of the observation plane
x2 = -obs_plane_side_length(1)/2:dx2:obs_plane_side_length(1)/2-dx2;
y2 = -obs_plane_side_length(2)/2:dy2:obs_plane_side_length(2)/2-dy2;
[X2,Y2] = meshgrid(x2,y2);

%% Calculate wavenumber
k = 2*pi/wavelength;

%% Multiplicative phase factors
c = 1/(1i*wavelength*propagation_distance)*exp(1i*k*(X2.^2+Y2.^2)/(2*
    propagation_distance));

%% Fourier transform and multiply
propagated_image = c.*fftshift(fft2(fftshift(object_image)))*dx1^2;
end
```

A.3 Angular spectrum propagation

In MATLAB, the Angular Spectrum propagation can be achieved by:

```
function [propagated_image] = angularSpectrum(object_image,
    obj_plane_side_length,wavelength,propagation_distance)
%% Performs angular spectrum propagation of 2D image and returns
    propagated image
% Inputs:
%   object_image: the image of the object to be propagated
%   obj_plane_side_length: the length of the object plane (x,y)
%   wavelength: the wavelength of the simluated monochromatic light
%   propagation_distance: the distance between the source plane and
    the observation plane
%
% Outputs:
%   propagated_image: the propagated image

%% STEP 0: Initialise coordinate space
% number of pixels of object image
[x_size,y_size] = size(object_image);

% sample interval of object image
dx = obj_plane_side_length(1)/x_size;
dy = obj_plane_side_length(2)/y_size;

```

```
% set up reciprocal coordinate space
a = fftshift(-x_size/2:x_size/2 - 1);
a = a./(dx*x_size);
b = fftshift(-y_size/2:y_size/2 - 1);
b = b./(dy*y_size);

[A,B] = meshgrid(a,b);

%% Take the Fourier transform of the starting wavefield
F = fftshift(fft2(fftshift(object_image)));

%% Identify the classes of results for the phase components
mu = sqrt(1 - A.^2 - B.^2);
not_evanescent = imag(mu) == 0;

%% Calculate the phase distribution for each plane wave component
w = exp(2i*pi*propagation_distance*mu/wavelength);

%% Multiply the wavefield components by the phase shift distribution
   and inverse Fourier transform to give propagated wavefield
propagated_image = ifftshift(ifft2(ifftshift(F.*w.*not_evanescent)));
end
```